Flow in the vicinity of a moving contact line : theoretical and numerical investigations

Mijail Febres Soria

THÈSE

En vue de l'obtention du

DOCTORAT DE L'UNIVERSITÉ DE TOULOUSE

Délivré par :

Institut National Polytechnique de Toulouse (INP Toulouse)

Discipline ou spécialité :

Dynamique des fluides

Présentée et soutenue par :

M. MIJAIL FEBRES SORIA

le mercredi 29 novembre 2017

Titre :

Flow in the vicinity of a moving contact line: theoretical and numerical investigations

---

Ecole doctorale :

Mécanique, Energétique, Génie civil, Procédés (MEGeP)

Unité de recherche :

Institut de Mécanique des Fluides de Toulouse (I.M.F.T.)

Directeur(s) de Thèse :

M. DOMINIQUE LEGENDRE

Rapporteurs :

M. GUILLAUME GALLIERO, UNIVERSITE DE PAU ET DES PAYS DE L ADOUR

M. STEPHANE POPINET, CNRS PARIS

Membre(s) du jury :

M. STÉPHANE ZALESKI, UNIVERSITE PARIS 6, Président

M. DOMINIQUE LEGENDRE, INP TOULOUSE, Membre

Mme PAULINE ASSEMAT, CNRS TOULOUSE, Membre

M. STÉPHANE VINCENT, UNIVERSITE PARIS 12, Membre

M. THIERRY ONDARCUHU, CNRS TOULOUSE, Membre

M. YOHEI SATO, INSTITUT PAUL SCHERRER, Membre

Abstract

The exact mechanism with which a fluid interface interacts dynamically with a solid surface during wetting is still open to research. Among the many subjects addressed in this field in the literature, the "moving contact line problem" is one that has been ubiquitous since at least the 1970s, where a paradox in the description of the contact line was found to exist. The paradox in a few words is the next: macroscopic hydrodynamic models using the no-slip boundary condition will predict infinite shear stress close to the contact line.

The most promising studies to tackle the problem come from information provided by molecular dynamics simulations. They have confirmed that close to the contact line, the no-slip boundary condition is relaxed to some form of slip. Unfortunately, molecular simulations are still limited to very small scales in space and time, so hydrodynamic models and numerical simulations based on Navier-Stokes equations are still needed. In these simulations, the Continuum Surface Force model CSF for the calculation of the capillary contribution introduces a grid dependent contact line velocity and shear at the wall, which is a problem we proposed to solve here. In this work, we analyze the flow close to the moving contact line in the context of corner stokes-flow and explore the effects of the boundary conditions at the wall. One of these conditions offered in the literature, provides relief to the shear divergence and also opens the possibility to observe Moffatt vortices in the vicinity of the contact line, not yet seen in experiments or numerical simulations. We explore this possibility analytically and then numerically using the code *JADIM*. The latter task is constrained by the contamination of the velocity field by the so-called spurious velocities if the VOF method is used. To solved this inconvenient, a very promising version of the front-tracking method with lagrangian markers is implemented and enhanced to handle non-uniform distribution of markers without losing its spurious velocities elimination features.

Numerical tests are conducted to validate the implementation, spurious velocities are reduce close to machine precision and comparison to benchmark data is performed obtaining good agreement. Tests including contact lines are then compared with exact solutions for shape analyzing the effect of the Bond number, showing remarkable results. Numerical experiments with this implementation close to a contact line show the existence of vortical patterns during of spreading.

Finally, and based on the theoretical background developed in this work, a new sub-grid model method is proposed for macroscopic numerical simulations and implemented in the new front-tracking method of *JADIM*. Quanti-

tative data is obtained and compared to numerical and experimental spreading cases revealing improvement of grid convergence and excellent agreement.

Résumé

Les mécanismes d'interaction entre une interface fluide et une paroi solide en situation de mouillage sont encore des problèmes ouverts. Parmi les nombreuses interrogations traitées dans la littérature, le "problème de la ligne de contact en mouvement" est très étudié depuis les années 1970, lorsque le paradoxe lié au mouvement de la ligne de contact a été identifié. En quelques mots ce paradoxe est le suivant : les modèles hydrodynamiques macroscopiques utilisant une condition de non-glissement à la paroi prédisent un cisaillement infini au niveau de la ligne de contact. Des études prometteuses pour aborder ce problème se sont appuyées sur des résultats fournis par les simulations dynamiques moléculaires. Elles confirment la présence de glissement au niveau de la ligne de contact. Malheureusement, les simulations de type dynamique moléculaire sont limitées à de très petites échelles à la fois temporelles et spatiales de sorte que les modèles hydrodynamiques et les simulations numériques des équations de Navier-Stokes restent nécessaires. Dans ce type de simulation, la méthode Continuum Surface Force pour traiter le terme capillaire entraine une vitesse et un cisaillement au niveau de la ligne de contact dépendant de la résolution, problème qui est abordé dans ce travail.

L'écoulement au voisinage de la ligne de contact est analysé théoriquement dans la limite des écoulements de Stokes et l'effet des conditions limites à la paroi est exploré. Une des conditions proposées dans la littérature permet de lever la divergence du cisaillement et rend possible l'observation de tourbillons de Moffatt au voisinage de la ligne de contact ce qui reste encore à observer que ce soit expérimentalement ou numériquement. Cette possibilité est explorée de manière théorique puis numérique à l'aide du code JADIM. Sur le plan numérique, la présence de courants parasites est apparue comme limitante si la méthode VoF est utilisée. Pour remédier à cet obstacle numérique, une version très prometteuse de la méthode front-tracking utilisant des markers Lagrangien a été implémentée et améliorée pour permettre de traiter des distributions non-uniformes de markers sans perdre les performance de réduction significative des courants parasites. De nombreux tests ont été réalisés pour valider la méthode développée et montre la réduction à la précision machine des courants parasites. La méthode est également validée pour la simulation des lignes de contact statiques et dynamiques avant d'être utilisée pour l'étude de tourbillons induits par la mise en mouvement d'une ligne de contact.

Finalement, s'appuyant sur les développements théoriques de ce travail, un nouveau modèle de sous maille est proposé pour permettre la simulation de lignes de contact aux échelles macroscopiques. Il est implémenté dans la nouvelle méthode front-tracking introduite dans JADIM. Les premiers

résultats montrent une amélioration partielle de l'effet du maillage sur la vitesse de la ligne de contact mais une maitrise totale du cisaillement. Les simulations de l'étalement de gouttes permet de retrouver de manière très satisfaisante les résultats théoriques et expérimentaux de référence.

Acknowledgements

This doctoral thesis has been written during my time at the Institut de Mécanique des Fluides de Toulouse IMFT. I am grateful for a number of friends and colleagues who encourage me to persevere with it and finally finished it.

I thank Dominique Legendre for his enormous support in both academic research an day-by-day aspects of spending my first days in France. This work could not possible have begun without his encouragement and his guidance. Thanks for sharing his vast experience only comparable to his unlimited patience and for letting me conduct my research with independence.

I am grateful to Annaïg Pedrono. No work that involves *JADIM* can be conducted without her and her resourcefulness. Along with her, I thank the staff of the *Service informatique*, specially to Yannick Exposito.

My profound appreciation to Marie-Hélène Manzato, for guiding me in the complicated ways of administrative matters, though probably we both would have appreciated speaking the same language.

I thank Omer Atasi for those unending geographical, political and technical discussions (we for sure would have changed the world!). I also thank Elena, Annagrazia and Zhentong for the ambient of fraternity created, and of course Esli, it is relaxing to speak Spanish latino from time to time.

Special thanks to Marylou Garnier, for creating a nice work environment in the office and helping me to endure my adaptation to France.
I am grateful to all the colleagues, administrative and technical staff I met in one way or another at the IMFT.

Finally, I thank my family, my parents and my sister, who support me at the distance. Infinite thanks to my wife Manuela (yet another thesis ded-

icated to you) and my daughter Elina for their support, sacrifice, patience and understanding.

I gratefully acknowledge financial support from FINCyT under contract 099-FINCyT-BDE-2014.

Contents

Chapter 1

Introduction

Wetting phenomena play an important role in many industrial, environmental and biological processes like lubrication, evaporation, chemical reactions, etc. Being a physical phenomenon so omnipresent in our day-by-day life, it is ironic that our knowledge of its functioning mechanisms at all scales is very limited. In fact, literature on the subject is vast but it seems that the precise mechanism with which a fluid interface advances over a solid surface is still only partially understood (see Blake, 2006; Bonn et al., 2009) and a consistent system of equations to model this multi-scale problem is still an open question, specially for numerical simulation purposes. Special attention has been given to the "moving contact line problem" where shear stress on the wall diverges as one approach the contact line when conventional no-slip boundary condition is applied. This singularity, known sometimes as the Huh and Scriven's paradox (see Huh and Scriven, 1971; Bonn et al., 2009) can be interpreted, by simple means, as the need of a infinite force to sink a solid body into a fluid, which is physically incorrect. It is accepted that there must be a microscopic scale mechanism which must be taken into account to solve this problem, although by the time of this paradox became evident, the no-slip boundary condition was pretty well established, quoting Batchelor (2000):

"..the validity of the no-slip boundary condition at a fluid-solid interface was debated for some years during the last century, there being some doubt about whether molecular interactions at such an interface lead to momentum transfer of the same nature as that at a surface in the interior of a fluid; but the absence of slip at a rigid wall is now amply confirmed by direct observations and by the correctness of its many consequences under normal conditions...".

Among the mechanisms proposed to remove the singularity of dissipation at the contact line, a finite slippage at the solid surface has been amply investigated. This slippage consists on relaxing the no slip condition in the region of the moving contact line. In other words, we allow the fluid to have a relative velocity with respect to the wall (de Gennes, 1985).
The most simple form of the slip condition is the Navier-slip condition (Navier, 1823) or linear slip-shear in which the velocity on the wall should be a proportion of the normal velocity gradient (See equation 1.1).

$$u|_{y=0} = \lambda \left.\frac{\partial u}{\partial y}\right|_{y=0} \tag{1.1}$$

Where λ is the slip length or slip coefficient (a measure of the length over which the slip is important) and is usually considered to be extremely small for hydrophilic surfaces and tens of nanometers for hydrophobic ones (Lauga and Stone, 2003). There are however other models, less used but present in literature (see Greenspan, 1978; Haley and Miksis, 1991): The inverse linear slip and the inverse quadratic slip (See equations 1.2 and 1.3).

$$u|_{y=0} = \frac{\lambda^2}{y} \left.\frac{\partial u}{\partial y}\right|_{y=0} \tag{1.2}$$

$$u|_{y=0} = \frac{\lambda^3}{y^2} \left.\frac{\partial u}{\partial y}\right|_{y=0} \tag{1.3}$$

Note that these slip formulations are only valid for contact angles below $\pi/2$. Although the exact mechanism responsible for this slip is still open to investigation, Molecular Dynamics have confirmed its existence, or at least that the no-slip boundary condition breaks at that scale level (Thompson and Robbins, 1989; Koplik and Banavar, 1993).
Classic references on the use of slippage close to the contact line are Huh and Scriven (1971), Dussan V. and Davis (1974) and Voinov (1976). Huh and Mason (1977) analyse the case of a steady state movement of a liquid meniscus applying two different slip conditions. One consists on applying zero shear on the inner region (with size λ) and regular shear on the outer region. The other one consists on applying the slip in the whole wall as stated in equation 1.1. Analytic expresions for the shape of the interface are obtained. Hocking Hocking (1977) applied a similar solution for a general moving fluid interface using the Navier slip condition and a numerical approach is use to obtain a bounded force on the wall. He considers that the microscopic angle is sufficient to describe the phenomena. In the same line of aproximation, Hocking and Rivers (1982) obtained an analytical solution for the interface shape relating the microscopic to the macroscopic

contact angle through the capillary number when studying the spreading of a drop. Cox (1986), using matched asymptotic expansions for $Ca << 1$, obtained an equivalent expression as Hocking and Rivers (1982) but without the knowledge a priori of the interface shape. The same technique is used by Cox (1998) when Reynolds numbers outside the inner region are considered large. These analytical solutions have been used intensively in the literature and numerical codes (see Dupont, 2007; Afkhami et al., 2009; Dupont and Legendre, 2010; Legendre and Maglio, 2013; Sui and Spelt, 2013b; Legendre and Maglio, 2015; Solomenko et al., 2017, etc). The results obtained are in general in good agreement with experimental data but all of them share a common deficiency: lack of rigorous grid convergence for velocity and shear at the wall.

Kirkinis and Davis (2013, 2014), introduce a special Navier-slip condition with $\lambda = f(r)$ into the Stokes flow analysis on a corner aiming to relieve the shear unboundedness an preserve the no slip boundary conditions away from the contact line. They demonstrated that an infinite sequence of vortices should exist (Moffatt vortices), confirming what Moffatt (1964), and Anderson and Davis (1993) had found before on a similar analysis without slippage. Both findings are yet to be found experimentally, although as mentioned in those references this would be extremely difficult because of the scale and intensity of those vortices.

On the other hand, Shikhmurzaev (1993a,b, 1994, 1996, 1997a,b, 2005, 2011); Blake et al. (1999); Blake (2002) and Billingham (2008) consider that wetting is a process of forming interfaces. Basically, this model states that surface tension on the interface of two fluids is not a constant, but need to change in a finite time to the appropriate value at the solid-liquid interface. Local change in density and surface tension are responsible for the slip near the contact line and the angle deviation from its static value to a dynamic value. A very interesting feature of this model is that the dynamic contact angle becomes an output variable. Contact angle dependence with contact line velocity and other far-field variables is confirmed in Blake et al. (1999), Blake (2002), Wilson et al. (2006). Sprittles and Shikhmurzaev (2013) implemented Shikmurzaev's model into a finite element code for capillary rise, obtaining good agreement with experiments.

Another strategy to analyze the moving contact line is to use data obtained from molecular simulations. The work of Qian et al. (2003a,b) and Qian et al. (2005) proposed the Generalized Navier Boundary Condition (GNBC) for hydrodynamic models. In that study, it is theorized based on molecular simulations, that shear at the wall close to the contact line is composed of a viscous part and the non-viscous "unbalanced Young stress" giving remarkably good results in comparison with molecular dynamic simulations. The

GNBC in the context of (ALE) can be found also in Gerbeau and Lelievre (2008). More recently a model that combines sequentially macroscopic simulation and molecular dynamics is proposed in Zhang et al. (2017).

As was seen in this brief introduction, the moving contact line modeling is complex and has been studied from many fronts. A key ingredient in getting the correct physics of the contact line without resorting directly to molecular dynamics is the application of some slip model that acts locally. Robust hydrodynamic models are needed.
The main objective of this work is to make focus on the flow structure in the corner made by a moving contact line and a wall. For this purpose, we attack this problem by both analytical considerations and numerical simulations. Considering the analytical part, we analyze a moving contact line in the framework of corner stokes flow, highlighting the effects of the boundary conditions in the flow field. Special focus is dedicated to a variable slip condition proposed by Kirkinis and Davis (2013, 2014) to study the existence of Moffatt vortices in the vicinity of a moving contact line. In the numerical part, we implement in the code *JADIM* a very promising version of the front-tracking method that is capable to reduce spurious velocities close to machine precision. We enhanced the method to handle non uniform distribution of markers without losing its capability to reduce spurious velocities which is crucial to the task of confirming the presence of vortices at the contact line. Finally, we propose a new numerical subgrid model attacking the grid convergence issues (on velocity and shear) of conventional models in the literature.

Work organization

This work is organized as follows: Chapters 2 and 3, are devoted to the presentation of the numerical code *JADIM* and the description and the implementation of a new method in *JADIM*: the front-tracking method. In chapter 4 we validate the front-tracking method against classical tests for spurious velocities, bubble rising and wetting. Chapter 5 is devoted to give an analytical view of the moving contact line problem from the perspective of corner Stokes flow. Chapters 6 and 7 explore analytically and numerically the possible existence of Moffatt vortices in the vicinity of a moving contact line. Finally, we propose a subgrid model in the framework of the front-tracking method for the simulation of drop spreading in chapter 8. Conclusions and future perspectives close this work.

Chapter 2

Numerical code *JADIM*

In this work, the numerical code *JADIM* was used. This chapter dedicates some lines to describe this in-house code.

2.1 Background

JADIM was developed at *IMFT* and is in constant improvement. Among its many features, we can name the interface tracking with lagrangian adaptive grids, transport of passive scalars (like temperature), simulation of turbulence with LES and of course the treatment of moving interfaces by volume tracking methods, specifically VOF and Level-Set methods which have been addressed in the literature in Bonometti and Magnaudet (2007); Dupont and Legendre (2010); Abadie et al. (2015); Legendre and Maglio (2013, 2015).
JADIM has been formulated in a 3D general orthogonal curvilinear coordinate system and in the next section, we cover the solver of Navier-Stokes equations in the context of two-fluid phenomena using the one fluid formulation for 2D problems.

2.2 Navier Stokes equation solution

Assuming a newtonian two-fluid incompressible isothermal flow with no mass transfer at the constant surface tension interface, a one fluid formulation for the Navier-Stokes equations can be adopted:

$$\boldsymbol{\nabla} \cdot \boldsymbol{U} = 0 \tag{2.1}$$

$$\frac{\partial \boldsymbol{U}}{\partial t} + (\boldsymbol{U} \cdot \boldsymbol{\nabla})\boldsymbol{U} = -\frac{1}{\rho}\boldsymbol{\nabla} P + \frac{1}{\rho}\boldsymbol{\nabla} \cdot \boldsymbol{\Sigma} + \boldsymbol{g} + \boldsymbol{F}_\sigma \tag{2.2}$$

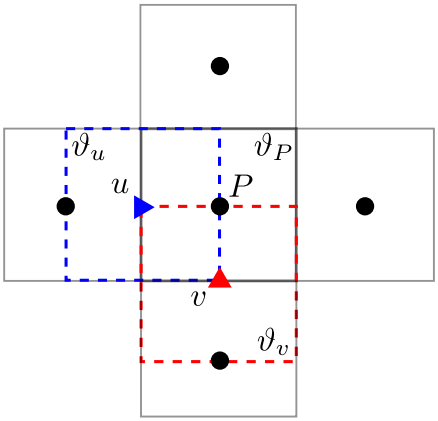

Figure 2.1: Cell center position for variables u, v and pressure P in a staggered 2D grid. Their corresponding control volumes are denoted ϑ_u, ϑ_v and ϑ_P respectively

where $\boldsymbol{U}$ stands for the velocity vector, P for the pressure, $\boldsymbol{\Sigma}$ is the viscous stress tensor, $\boldsymbol{g}$ is the acceleration due to gravity, $\boldsymbol{F}_\sigma$ is the capillary contribution, ρ and μ are the local density and dynamic viscosity, which are calculated using the classical VOF function (or volume fraction) C:

$$\rho = C\rho_1 + (1 - C)\rho_2 \tag{2.3}$$
$$\mu = C\mu_1 + (1 - C)\mu_2 \tag{2.4}$$

Calculation of C is addressed separately in section 2.3.

2.2.1 Spatial Discretization

Transport equations 2.1 and 2.2 are discretized using the finite volume method in a general orthogonal curvilinear coordinate system. Velocity components u, v and pressure P are arranged in a staggered grid having their own control volumes ϑ_u, ϑ_v and ϑ_P respectively (see figure 2.1). Continuity and momentum equations 2.1 and 2.2 are integrated in their respective control volume ϑ or depending on the case, in the surface Γ bounding their volumes:

$$\int_\Gamma \boldsymbol{U}_i \boldsymbol{n}_i d\Gamma = 0 \tag{2.5}$$

$$\int_\vartheta \frac{\partial \boldsymbol{U}_i}{\partial t} d\vartheta = -\int_\vartheta \frac{1}{\rho}\frac{\partial P}{\partial \boldsymbol{\xi}_i} d\vartheta + L[\boldsymbol{U}_i] + N[\boldsymbol{U}_i] + \int_\vartheta \boldsymbol{F}_\sigma d\vartheta \tag{2.6}$$

where $L[\boldsymbol{U}_i]$ and $N[\boldsymbol{U}_i]$ are the operators grouping terms treated implicitly and explicitly respectively. They are given by:

$$L[\boldsymbol{U}_i] = \frac{1}{\rho}\int_\Gamma \mu \frac{\partial \boldsymbol{U}_i}{\partial \boldsymbol{\xi}_j}\boldsymbol{n}_i d\Gamma \tag{2.7}$$

$$\begin{aligned} N[\boldsymbol{U}_i] = &\int_\vartheta \boldsymbol{g}_i d\vartheta + \frac{1}{\rho}\int_\Gamma \mu \frac{\partial \boldsymbol{U}_j}{\partial \boldsymbol{\xi}_i}\boldsymbol{n}_j d\Gamma - \frac{1}{\rho}\int_\Gamma \boldsymbol{U}_i\boldsymbol{U}_j\boldsymbol{n}_j d\Gamma \\ &+\frac{1}{\rho}\int_\Gamma \mu\left(2\boldsymbol{H}_i^k\boldsymbol{U}_k\boldsymbol{\delta}_{ij} - \boldsymbol{H}_j^i\boldsymbol{U}_j - \boldsymbol{H}_i^j\boldsymbol{U}_i\right)\boldsymbol{n}_j d\Gamma \\ &+\int_\vartheta \boldsymbol{H}_j^i\left(\boldsymbol{U}_j\boldsymbol{U}_j - \boldsymbol{\tau}_{jj}\right)d\vartheta - \int_\vartheta \boldsymbol{H}_i^j\left(\boldsymbol{U}_j\boldsymbol{U}_i - \boldsymbol{\tau}_{ij}\right)d\vartheta \end{aligned} \tag{2.8}$$

Where $\boldsymbol{H}$ are factors containing grid curvature, $\boldsymbol{n}$ is the normal to the control volume faces, $\boldsymbol{\delta}$ is the delta kronecker function and $\boldsymbol{\tau}$ is the viscous stress tensor, given by:

$$\boldsymbol{\tau}_{ij} = \frac{\mu}{\rho}\left(\frac{\partial \boldsymbol{U}_i}{\partial \boldsymbol{\xi}_j} + \frac{\partial \boldsymbol{U}_j}{\partial \boldsymbol{\xi}_i} - \boldsymbol{H}_j^i\boldsymbol{U}_j - \boldsymbol{H}_i^j\boldsymbol{U}_i + 2\boldsymbol{H}_i^k\boldsymbol{U}_k\boldsymbol{\delta}_{ij}\right) \tag{2.9}$$

Spacial derivatives are calculated using a second-order centered scheme.

2.2.2 Temporal Discretization

A third-order three-step Runge Kutta scheme is used to solve the advective terms time advancement, whereas a semi-implicit Crank-Nicholson method is used to treat viscous terms, giving a global precision for this numeric scheme an order Δt^2.
The Runge Kutta algorithm can be summarized as follows: at any given time step n, an intermediate velocity field $\boldsymbol{U}^m$ is calculated as:

$$\begin{aligned} \frac{\boldsymbol{U}^m - \boldsymbol{U}^{m-1}}{\Delta t}\vartheta = &-\left(\alpha_m + \beta_m\right)\frac{1}{\rho}\boldsymbol{\nabla} P\vartheta + \alpha_m L[\boldsymbol{U}^{m-1}] \\ &+\beta_m N[\boldsymbol{U}^m] + \gamma_m N[\boldsymbol{U}^m] + \zeta_m N[\boldsymbol{U}^{m-2}] + \left(\alpha_m + \beta_m\right)\boldsymbol{F}_\sigma\vartheta \end{aligned} \tag{2.10}$$

where α_m, β_m, γ_m and ζ_m are the Runge-Kutta coefficients at intermediate step m. These coefficients are:

$$\begin{aligned} \alpha_1 = \beta_1 = 4/15 \quad ; \quad \gamma_1 = 8/15 \quad ; \quad \zeta_1 = 0 \\ \alpha_2 = \beta_2 = 1/15 \quad ; \quad \gamma_2 = 5/12 \quad ; \quad \zeta_2 = -17/60 \\ \alpha_3 = \beta_3 = 1/6 \quad ; \quad \gamma_3 = 3/4 \quad ; \quad \zeta_3 = -5/12 \end{aligned}$$

At step $m = 1$, it is imposed: $\boldsymbol{U}^{m-1} = \boldsymbol{U}^n$. The velocity field at $m = 3$ contains all the vorticity of the solution but it is not divergence-free. To obtain a divergence free velocity field, a projection method is used.

Physical contribution	Criterion
Gravity	$\Delta t < \sqrt{\Delta x/g}$
Advection	$\Delta t < \sqrt{3}\Delta x/U$
Diffusion	$\Delta t < \Delta^2 x/\nu$
Capillarity	$\Delta t < \sqrt{(\rho_1+\rho_2)\Delta^3 x/8\sigma}$

Table 2.1: Time criteria used in *JADIM*.

2.2.3 Projection method

The coupling between velocity and pressure is achieved through a projection method. An auxiliary potential Ω is defined such that:

$$\rho\frac{\boldsymbol{U}^{n+1}-\boldsymbol{U}^{n,3}}{\Delta t} = -\boldsymbol{\nabla}\Omega^{n+1} \tag{2.11}$$

Given that the free-divergence condition dictates $\boldsymbol{\nabla}\cdot\boldsymbol{U}^{n+1}=0$, the potential Ω must satisfy the pseudo-Poisson equation:

$$\boldsymbol{\nabla}\cdot\left(\frac{1}{\rho}\boldsymbol{\nabla}\Omega^{n+1}\right) = \frac{1}{\Delta t}\boldsymbol{\nabla}\cdot\boldsymbol{U}^{n,3} \tag{2.12}$$

Once Ω is solved from equation 2.12, then a free-divergence velocity field $\boldsymbol{U}^{n+1}$ can be obtained from equation 2.11. Pressure is then calculated using:

$$P^{n+1} = P^n + \Omega^{n+1} \tag{2.13}$$

Further details are provided in (Cranga, 2002; Calmet and Magnaudet, 1997; Dupont and Legendre, 2010).
The time step criteria inside *JADIM* is given in table 2.1. In this work, we will be concerned with flows where capillary effects are dominant. In that case, time step is selected to be constrained with respect to the advective time where the velocity would be the maximum of a capillary wave Brackbill et al. (1992); Abadie (2013).

2.3 Volume fraction transport

In *JADIM*, two volume-tracking methods to advect the volume fraction C were available before this work: VOF (see Hirt and Nichols, 1981; Rudman, 1997; Garrioch and Baliga, 2006) and Level set (see Sussman et al., 1994;

Chang et al., 1996; van der Pijl et al., 2005). Both methods solve a conservation equation of the form:

$$\frac{\partial \chi}{\partial t} + \boldsymbol{U} \cdot \boldsymbol{\nabla} (\chi) = 0 \tag{2.14}$$

where χ represent the volume fraction C or the distance (level set) function ϕ.
The VOF method inside *JADIM* uses the algorithm based on Flux-Corrected Transport (FCT) schemes (see Zalesak, 1979; Bonometti and Magnaudet, 2007). Due to unphysical spreading of the interface, its current implementation has been improved as described in Abadie (2013). We will refer to this implementation as VOF-FCT-CSF.
On the other hand, the Level-Set method implemented in *JADIM* solves equation 2.14 using a fifth order WENO scheme. Once ϕ is known, C can be calculated through the mollified heaviside function:

$$C = \begin{cases} 0 & \text{if } \phi < -\varepsilon, \\ 0.5 \left[1 + \frac{\phi}{\varepsilon} + \frac{1}{\pi} \sin\left(\frac{\pi \phi}{\varepsilon}\right)\right] & \text{if } |\phi| \leq \varepsilon, \\ 1 & \text{if } \phi > \varepsilon \end{cases} \tag{2.15}$$

where $\varepsilon = \sqrt{2}\Delta x$ is approximately half the numerical thickness of the interface and Δx is the size of the grid. Details of this implementation can be found in Abadie (2013) and we will refer to it as Level-Set-CSF method.
When using VOF-FCT-CSF or Level-Set-CSF, the capillary contribution $\boldsymbol{F}_\sigma$ in equation 2.2 is solved using the CSF (continuum surface force) formulation Brackbill et al. (1992):

$$\boldsymbol{F}_\sigma = -\frac{\sigma}{\rho} \kappa \boldsymbol{\nabla} C \tag{2.16}$$

where σ is the constant surface tension and κ the local curvature of the interface that is calculated through:

$$\kappa = \boldsymbol{\nabla} \cdot \left(\frac{\boldsymbol{\nabla} C}{\| \boldsymbol{\nabla} C \|} \right) \tag{2.17}$$

In *JADIM*, $\boldsymbol{F}_\sigma$ is integrated in the surface of every control volume containing the interface:

$$\boldsymbol{F}_\sigma = -\frac{\sigma \overline{\boldsymbol{\nabla} C}}{\overline{\rho} \vartheta} \int_{dS} \left. \frac{\boldsymbol{\nabla} C}{\| \boldsymbol{\nabla} C \|} \right|_S \cdot \boldsymbol{n}_S dS \tag{2.18}$$

where $\boldsymbol{n}_S$ is the normal vector to the volume face, $\overline{\boldsymbol{\nabla} C}$ is the average of $\boldsymbol{\nabla} C$ at the staggered control volumes. To minimize variations in the calculation

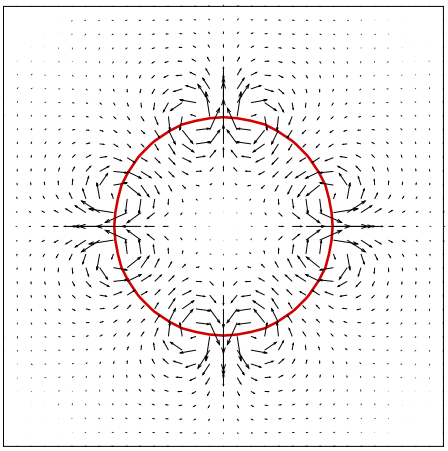

Figure 2.2: Spurious velocities for a static 2d droplet of radius $r = 0.25$ in a solid wall box of $L = 1.0$ simulated using VOF-FCT-CSF in *JADIM*. Internal and external fluids share the same density and dynamic viscosity set at $\rho = 1$ and $\mu = 0.25$ respectively and surface tension is $\sigma = 7.5$. Maximum velocity reported is $Ca \approx 5 \times 10^{-4}$. — Fluid interface

of κ, C is convoluted or "smoothed" a number of steps prior to the calculation of $\overline{\boldsymbol{\nabla} C}$ and $\boldsymbol{\nabla} C$. It is important to note that the number of convolution steps is different for $\overline{\boldsymbol{\nabla} C}$ and $\boldsymbol{\nabla} C$. Some tests for these convolution steps are given in Dupont (2007) and Dupont and Legendre (2010). Also, to reduce the intensity of spurious velocities, density at the interface is averaged as $\overline{\rho} = (\rho_1 + \rho_2)/2$ (see Brackbill et al., 1992).

2.4 Spurious velocities.

Whether we use VOF-CSF or Level-Set-CSF, the CSF formulation for the capillary force contribution has been known for its propensity to generate unphysical flow, "spurious currents" or "spurious velocities" near the interface (Francois et al., 2006). Figure 2.2 shows a typical velocity field obtained when using CSF formulation in VOF-FCT-CSF for a static droplet in a solid wall box. Ideally, in equilibrium, the velocity field for this problem should be zero. In figure 2.2, the maximum normalized velocity was found to be $Ca \approx 5 \times 10^{-4}$. This unphysical phenomenon occurs due to a numerical imbalance of the surface tension force and its associated pressure gradient, although interface advection also plays an important role in it. A comprehensive study on the coupling between surface tension force and interface

advection can be found in Abadie (2013) and Abadie et al. (2015). In those works, different discretizations of the curvature are tested, i.e. Height function and the SSF (Sharp Surface Force Cummins et al., 2005) in the VOF and Level-Set frameworks inside *JADIM*. Their results were revealing. For the case of a static bubble, the height function discretization preformed better than classical CSF model for VOF-FCT-CSF. VOF-PLIC combined with the height function performed even better, spurious velocities were close to $Ca \approx 1 \times 10^{-13}$. In the case of Level-Set, the redistancing of the Level-Set function showed to be intrusive in the reduction of spurious velocities, for the classical CSF, height function and SSF formulations, resulting in velocities close to those of classical VOF-FCT-CSF with CSF formulation, typically $Ca \approx 1 \times 10^{-4}$. When no redistancing is applied, the Level-Set combined with SSF provided an impressive $Ca \approx 1 \times 10^{-16}$, followed by Level-Set with Height function at $Ca \approx 1 \times 10^{-13}$. This results are summarize in figure 2.3a. Surprisingly, in the case of a translating bubble, all curvature discretizations reported spurious velocities above $Ca \approx 1 \times 10^{-6}$, see figure 2.3b. This is explained by the strong coupling between surface tension force and the interface advection, where errors in curvature are caused by advection errors. It is true however, that the Level-Set formulation in general allows a more precise calculation of curvature and normals due to its "smooth" nature when compared to the VOF method.
Attempts to reduce spurious velocities abound in the literature, typically improving the accuracy of curvature calculation (see for example Renardy and Renardy, 2002; Cummins et al., 2005; Popinet, 2009), a sharp surface tension force (SSF) by Francois et al. (2006), also, under energy considerations Jamet et al. (2002).
It is known, that the front-tracking method can transport interfaces more accurately compared with other methods and in most of cases, interface geometrical properties like curvature can be calculated more precisely (see Tryggvason et al., 2001). An hybrid formulation CSF-like formulation is presented in Shin et al. (2005) succeeding in reducing spurious velocities close to machine precision, though this reduction is only possible for a uniform distribution of markers at the front.

2.5 Summary

In this chapter we have described the Navier-Stokes equations solver inside *JADIM* for 2D problems in the context of a one-fluid formulation. Both methods to advect the interface (VOF-FCT-CSF and Level-Set-CSF) avail-

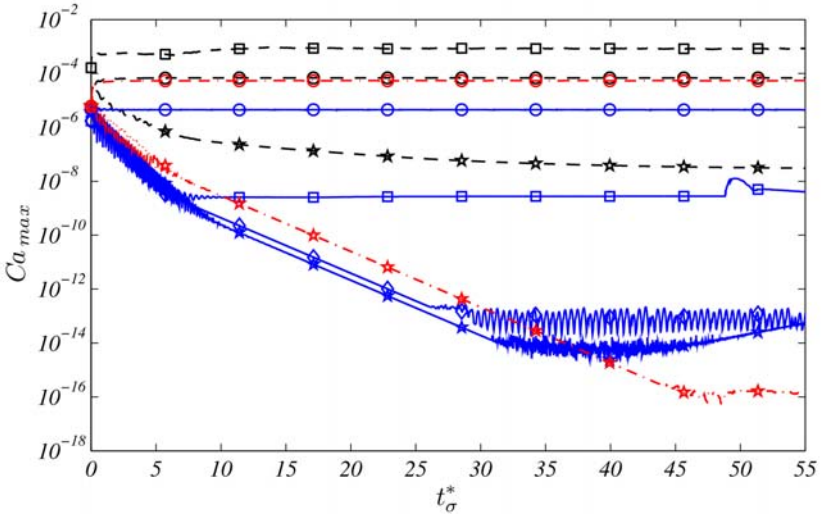

(a)

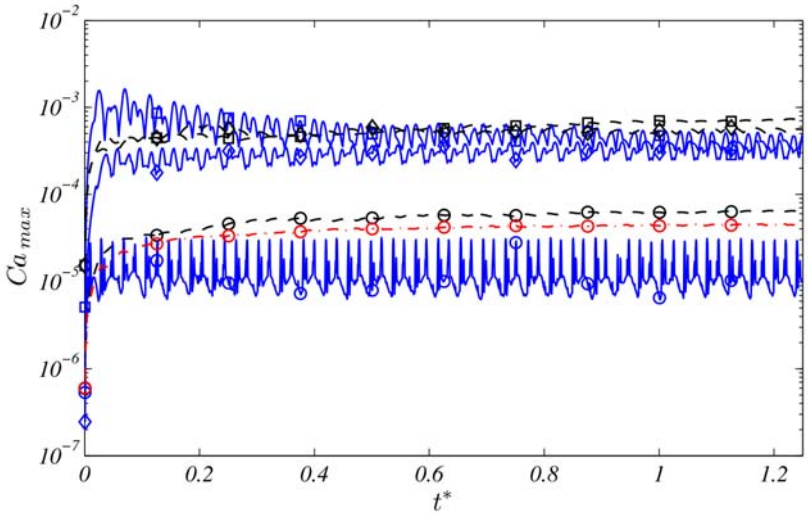

(b)

Figure 2.3: Maximum spurious velocity evolution in nodimensional time t^*. Comparison of:. VOF-FCT-CSF classic CSF; VOF-FCT-CSF Height function CSF; VOF-PLIC Height function CSF; Level-Set classic CSF; Level-Set Height function CSF; Level-Set SSF; Level-Set classic CSF, no redistancing; Level-Set Height function CSF, no redistancing; Level-Set SSF, no redistancing. a) Static bubble; b) Translating bubble. Source: Abadie et al. (2015)

able before this work were also addressed. We showed a brief demonstration of the consequences of using the CSF formulation to address the capillary force contribution (i.e. spurious velocities) and the role of the advection in spurious velocities reductions according Abadie et al. (2015). Given that the context of this work is dealing with capillary-related flows and seeing the great potential of the front-tracking method to reduce spurious velocities, we implemented it inside JADIM. This is addressed next in chapter 3.

Chapter 3

The Front-tracking method

This chapter is dedicated to give details of the implementation of the front-tracking method inside *JADIM* that was accomplished during this work. We first give some background to the method, then we list the shortcomings of it and we propose solutions and enhancements to the method.

3.1 Background

In the front-tracking method with lagrangian markers, besides the grid used to solve primitive variables like u, v and P, another grid is defined at the interface between fluids and it moves with it. This lagrangian grid or "front" is formed by discrete points or "markers" that are distributed along the fluid interface on the top of the eulerian grid (see figure 3.1a). In comparison with volume tracking methods like VOF-FCT-CSF or Level-Set-CSF, in the front-tracking method, the volume fraction is not advected through a conservation equation like 2.14, but it is calculated from the position of markers which are advected instead with the velocity field $\boldsymbol{U}$. It is possible however to solve C inside a pseudo-Poisson equation (see Unverdi and Tryggvason, 1992; Shin and Juric, 2002; Shin et al., 2005) but again, no direct role of velocity is involved in it. As a consequence and since the interface position and geometry are explicitly known, variables like curvature, normal and tangential vectors at the interface can be calculated more accurately in most cases.

At some point during a typical numerical simulation using the front-tracking method, information (i.e. surface tension force, velocity, etc) must be interchanged between the lagrangian and the eulerian grids. This is achieved through special interpolation schemes (see Peskin, 1977, 2002).
As pointed in section 2.4 and here, one of the main advantages of the front-tracking method in the numerical treatment of two-phase-flows is that surface

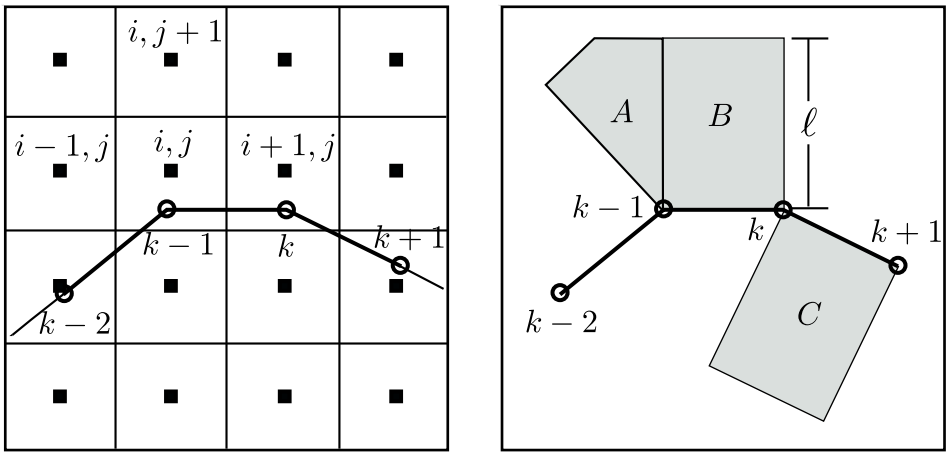

Figure 3.1: Front tracking schematics. (a) Schematic for eulerian/lagrangian grid, showing eulerian cells with subscripts i, j and lagrangian markers with subscripts k; (b) Schematic for polygon construction (for clarity, polygons on only one side are shown).

tension forces can be treated in a more natural and conservative way (see Tryggvason et al., 2001). This advantage however, comes with some shortcomings. We consider important to first dedicate some lines to the main disadvantages of the method (see section 3.2) and then we will describe the current implementation inside *JADIM* to solve them and improve the method (section 3.3).

3.2 Front-Tracking method shortcomings

Fluid interfaces can move and deform in such fashion that markers forming the front can travel in the tangential direction to the interface, accumulating in large numbers in small interface areas, or leaving large interface areas depleted of them (see figure 3.2a, where a rising bubble is simulated with no special treatment). In the former case, if care is not taken, the flow is lead to instabilities (See Popinet and Zaleski, 1999; Hou et al., 1994). In the latter, lost of precision in the interchange of information between the front and the eulerian grid is experienced. Increasing the number of markers does not solve any of this problems (see figure 3.2b, where the number of markers has been increased $\times 4$). Adding or removing elements from the front according to some threshold of element size is a relatively simple procedure (see Unverdi

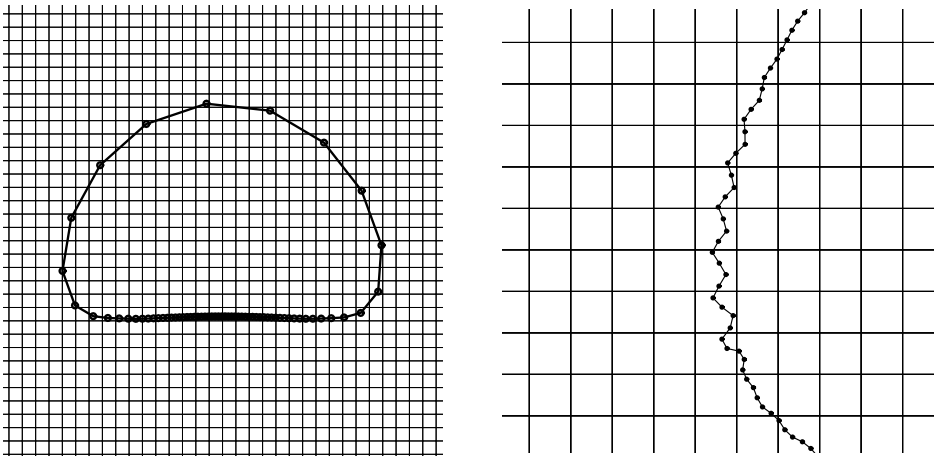

(a) (b)

Figure 3.2: Front-tracking method implemented in JADIM (present work, without any reconstruction/redistribution), applied to a rising Bubble for: $\rho_1/\rho_2 = 10$, $\mu_1/\mu_2 = 10$, $\sigma = 24.5$, $g = 0.98$, $Re = 35$, $Eo = 10$ (following Hysing et al., 2009). (a) With 63 markers and no special treatment. (b) Increasing the number of markers $\times 4$.

and Tryggvason, 1992; Juric and Tryggvason, 1998). However, it is not known how the flow is affected by it, furthermore, algorithmic complexity is expected in interface merging and break-up problems, also in 3D calculations.

Trying to keep a uniform distribution of markers work well enough in cases involving mild interface deformation (see for example the work of Ming-Chih Lai and Huang, 2011, where an artificial tangential marker velocity is applied), but for the case reported in figure 3.2, some perturbations are found on the sides of the bubble, this is shown in figure 3.3a. A similar behavior is expected when instead of an artificial velocity, polynomials/functions are fitted to the markers and then are used to keep an uniform distribution of the front (See Popinet and Zaleski, 1999; Tryggvason et al., 2001), although this has not been reported. Also, it is known that markers can suffer of small amplitude mesh-scale oscillations that are not physical in nature (See Longuet-Higgins and Cokelet, 1976). The application of smoothing filters like those found in Longuet-Higgins and Cokelet (1976) or in Savitzky and Golay (1964), seems to alleviate this situation. The combination of both artificial tangential marker velocity and smoothing filter recovers a physically relevant bubble shape (see figure 3.3b), however, for a different set of parameters of the problem, a larger number of markers may be required, rendering these two solutions useless as they will produce a uniform front with a low density

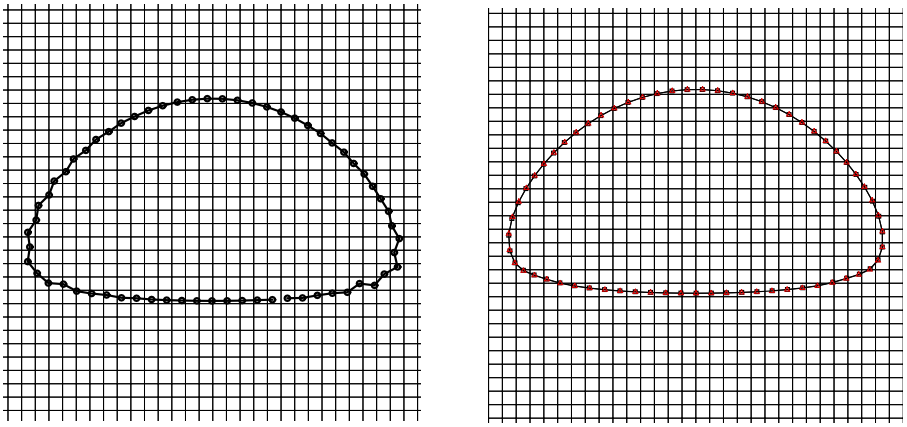

(a) (b)

Figure 3.3: Front-tracking method implemented in JADIM (present work, without reconstruction), applied to a Rising Bubble for: $\rho_1/\rho_2 = 10$, $\mu_1/\mu_2 = 10$, $\sigma = 24.5$, $g = 0.98$, $Re = 35$, $Eo = 10$ (following Hysing et al., 2009). 63 front markers treated with: (a) Artificial tangential marker velocity. (b) Artificial tangential marker velocity and ▲ Fourth order filter Longuet-Higgins and Cokelet (1976); ◘ Savitzki-Golay Savitzky and Golay (1964) filter.

of markers.
These treatments that seem to solve the front-tracking method issues are necessarily defined in the context of a uniform distribution of markers and their extension to 3D problems is not quite obvious.

On the other hand, Shin et al. (2005) introduced a new "Hybrid formulation" treatment for the surface tension forcing contribution which reported reduced spurious velocities down to machine precision and also a new reconstruction method based on an optimum indicator function contour which is intersected to the eulerian grid faces to obtain a non-uniform mass-conservative marker distribution. This approach was reported to be robust enough to solve all the issues described above. There is however an issue left to solve, the reconstruction method proposed in Shin et al. (2005) produce a non-uniform distribution of markers, which affects negatively the ability of the "Hybrid formulation" to reduce spurious velocities. We treat and solve this last problem in section 3.6.

3.3 Volume fraction advection in the front-tracking method

To calculate C from a given marker distribution, we adopt the procedure found in Ceniceros and Roma (2005); Ceniceros et al. (2010). Briefly, a set of markers identified with indexes k in figure 3.1a is distributed along the fluid interface forming the "front" over the eulerian grid identified with subscripts i, j. Around each front element e_k of length Δs_k formed by the pair of markers k and $k+1$, a rectangle (typically B and C in figure 3.1b) of width Δs_k and height ℓ can be constructed using the normal unit vector to the element pointing to both sides of the interface. The signed distance $d(\boldsymbol{x})$ from the Eulerian cell centers $\boldsymbol{x_{i,j}}$ lying inside each rectangle to the lagrangian element center $\boldsymbol{x}'_k$ can be calculated cheaply and easily by geometrical means, and also its sign can be determined depending on which side of the interface the point $\boldsymbol{x_{i,j}}$ lies.
Additionally, irregular quadrilaterals can be constructed at each marker in between two rectangles on the convex side of the interface (i.e. quadrilateral A in figure 3.1b). They are constructed because regular rectangles will not cover convex areas in between neighbor elements. Inside these irregular quadrilaterals, $d(\boldsymbol{x})$ is calculated as the distance from $\boldsymbol{x_{i,j}}$ to the marker. The distance function ϕ to the interface is then determined by:

$$\phi(\boldsymbol{x}) = \begin{cases} -\gamma & \text{if } d(\boldsymbol{x}) < -\gamma, \\ d(\boldsymbol{x}) & \text{if } |d(\boldsymbol{x})| \leq +\gamma, \\ +\gamma & \text{if } d(\boldsymbol{x}) > +\gamma \end{cases} \tag{3.1}$$

where γ is the width of the band, typically $\gamma = 2\sqrt{2}\Delta x$ (see Ceniceros and Roma, 2005). Also, ℓ is chosen such that $0 < \gamma < \ell$, so the band of width 2γ is contained in the union of all the polygons constructed before. Outside the union of all the polygons, the continuous distance function ϕ is given by $d(\boldsymbol{x}) = \pm\gamma$. This operation is repeated at each time step, and only $\phi(\boldsymbol{x})$ of eulerian points lying in the vicinity of the interface are updated (given of course that a consistent initialization of $\phi(\boldsymbol{x})$ is provided at $t = 0$). It is worth mention the simplicity of implementation of $\phi(\boldsymbol{x})$, its accuracy and economy of calculation (see Ceniceros and Roma, 2005; Ceniceros et al., 2010).

Once the field $\phi(\boldsymbol{x})$ is known, C is found through the mollified heaviside function (equation 2.15).

3.4 Capillary force contribution.

In the front-tracking method, the capillary contribution $\boldsymbol{F}_\sigma$ is calculated again through equation 2.16. Instead of approximating curvature κ as in equation 2.17 (Brackbill et al., 1992), we adopt the hybrid formulation given in Shin et al. (2005). For this, any discrete scalar information ψ_k, $\Psi_{i,j}$ from the lagrangian/eulerian grid can be transferred to the eulerian/lagrangian grid respectively through:

$$\Psi_{i,j} = \sum_k \psi_k D_{i,j} \Delta s_k \quad ; \quad \psi_k = \sum_{i,j} \Psi_{i,j} D_{i,j} \Delta x \Delta y \tag{3.2}$$

with $D_{i,j}$ the discrete form of $\delta(\boldsymbol{x} - \boldsymbol{x'})$, a function to represent interface terms that are concentrated at the boundary between fluids. To calculate $\delta(\boldsymbol{x} - \boldsymbol{x'})$ we use the distribution function reported in Peskin (2002). Taking in consideration the center cell for the x component of velocity:

$$D_{i+1/2,j} = \frac{\delta(\overline{x_{i+1/2,j} - x'_k})\delta(\overline{y_{i+1/2,j} - y'_k})}{\Delta x \Delta y} \tag{3.3}$$

where

$$\delta(r) = \begin{cases} \delta^*(r) & \text{if } |r| \leq 1, \\ 1/2 - \delta^*(2 - |r|) & \text{if } 1 < |r| < 2, \\ 0 & \text{if } |r| \geq 2 \end{cases} \tag{3.4}$$

and

$$\delta^*(r) = \frac{3 - 2|r| + \sqrt{1 + 4|r| - 4r^2}}{8} \tag{3.5}$$

variables $\overline{x_{i+1/2,j} - x'_k}$ and $\overline{y_{i+1/2,j} - y'_k}$ are the distances between centers of front elements to eulerian velocity cells, normalized by the grid size Δx and Δy respectively.
The lagrangian capillary force using markers is $\boldsymbol{F'_\sigma} = \sigma\kappa\boldsymbol{G}$, where $\boldsymbol{F'_\sigma}$ and $\boldsymbol{G}$ are given by:

$$\boldsymbol{F'_\sigma} = \int_{\Gamma(t)} \boldsymbol{f}\delta(\boldsymbol{x} - \boldsymbol{x'})ds = \sum_k \boldsymbol{f} D_{i+1/2,j} \Delta s_k \tag{3.6}$$

$$\boldsymbol{G} = \int_{\Gamma(t)} \boldsymbol{n}\delta(\boldsymbol{x} - \boldsymbol{x'})ds = \sum_k \boldsymbol{n} D_{i+1/2,j} \Delta s_k \tag{3.7}$$

where $\boldsymbol{f}$ is the local capillary force calculated at the front and $\boldsymbol{n}$ is the normal unit at the front element pointing towards the tracked fluid. Both $\boldsymbol{F'_\sigma}$ and

$\boldsymbol{G}$ are interpolated from eulerian velocity cells to eulerian pressure cells. In a uniform staggered grid, this is achieved by:

$$F'_{xi,j} = \frac{1}{2}(F'_{xi+1/2,j} + F'_{xi-1/2,j}) \tag{3.8}$$

$$F'_{yi,j} = \frac{1}{2}(F'_{yi,j+1/2} + F'_{yi,j-1/2}) \tag{3.9}$$

Similarly for $G_{xi,j}$ and $G_{yi,j}$. The curvature at eulerian pressure cells is then calculated with:

$$\kappa_{i,j} = \begin{cases} \frac{F'_{xi,j}G_{xi,j}+F'_{yi,j}G_{yi,j}}{\sigma(G^2_{xi,j}+G^2_{yi,j})} & \text{if } G^2_{xi,j} + G^2_{yi,j} > 0, \\ 0 & \text{if } G^2_{xi,j} + G^2_{yi,j} = 0 \end{cases} \tag{3.10}$$

also, a filter function is used:

$$c_{i,j} = \begin{cases} 1 & \text{if } G^2_{xi,j} + G^2_{yi,j} > 0, \\ 0 & \text{if } G^2_{xi,j} + G^2_{yi,j} = 0 \end{cases} \tag{3.11}$$

Then the curvature at velocity centers is recovered with:

$$\kappa_{i+1/2,j} = \begin{cases} \frac{\kappa_{i,j}c_{i,j}+\kappa_{i+1,j}c_{i+1,j}}{c_{i,j}+c_{i+1,j}} & \text{if } c_{i,j} + c_{i+1,j} > 0, \\ 0 & \text{if } c_{i,j} + c_{i+1,j} = 0 \end{cases} \tag{3.12}$$

$$\kappa_{i,j+1/2} = \begin{cases} \frac{\kappa_{i,j}c_{i,j}+\kappa_{i,j+1}c_{i,j+1}}{c_{i,j}+c_{i,j+1}} & \text{if } c_{i,j} + c_{i,j+1} > 0, \\ 0 & \text{if } c_{i,j} + c_{i,j+1} = 0 \end{cases} \tag{3.13}$$

Finally, the capillary force $\boldsymbol{F}_\sigma$ contribution is found with equation 2.16, discretely:

$$F_{xi+1/2,j} = -\frac{\sigma}{\rho}\kappa_{i+1/2,j}\frac{C_{i+1,j} - C_{i,j}}{\Delta x} \tag{3.14}$$

$$F_{yi,j+1/2} = \frac{\sigma}{\rho}\kappa_{i,j+1/2}\frac{C_{i,j+1} - C_{i,j}}{\Delta y} \tag{3.15}$$

It is clear that the calculation of $\kappa_{i,j}$ in equation 3.10 projects the lagrangian force $\boldsymbol{F}'_\sigma$ to the normal to the interface $\boldsymbol{G}$ in a similar procedure as the one made in the *CSF* method Brackbill et al. (1992), i.e. apply a "smoothing" or a "convolution" filter to the VOF function C.
The local force $\boldsymbol{f}$ at a front element (in 2D) is calculated following Tryggvason et al. (2001):

$$\boldsymbol{f}_{e,k} = \int_{\Delta s} \sigma\kappa\boldsymbol{n}ds \tag{3.16}$$

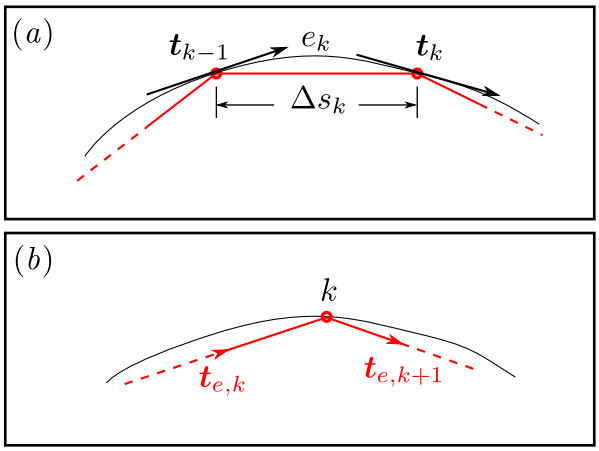

Figure 3.4: (a) Local force $f_{e,k}$ at element e_k, using equation 3.17 (present work); (b) Local force f_k at marker k, using equation 3.18.

and using the curvature of a two-dimensional line, $\kappa \boldsymbol{n} = \partial \boldsymbol{t} / \partial s$, we have:

$$\boldsymbol{f}_{e,k} = \sigma \left(\boldsymbol{t}_k - \boldsymbol{t}_{k-1} \right) \tag{3.17}$$

where $\boldsymbol{t}_k$ and $\boldsymbol{t}_{k-1}$ are the tangent vectors at markers k and $k-1$ (red circles in figure 3.4) that define the front element e_k (see red line in figure 3.4a). This approach is found in the literature (see Unverdi and Tryggvason, 1992; Juric and Tryggvason, 1998; Agresar et al., 1998; Tryggvason et al., 2001; Popinet and Zaleski, 1999; Yamamoto and Uemura, 2008; Yamamoto et al., 2013, 2014). There is however another approach to this force (see Shin and Juric, 2002; Shin et al., 2005; Lai et al., 2010; Huang et al., 2004; Ceniceros et al., 2010; Li et al., 2012) where the force is calculated at markers and is based in the difference between tangents of neighbor front elements (see figure 3.4b):

$$\boldsymbol{f}_k = \sigma \left(\boldsymbol{t}_{e,k+1} - \boldsymbol{t}_{e,k} \right) \tag{3.18}$$

Although both formulations ensure that the total force on any closed surface is equally zero, there is a crucial difference that will be addressed in section 3.6.

3.4.1 Contact angle imposition

The front tracking method has been used also to address wetting problems. Depending on the force location formulation, the contact angle can be imposed in two different but equivalent ways. If capillary force at the front

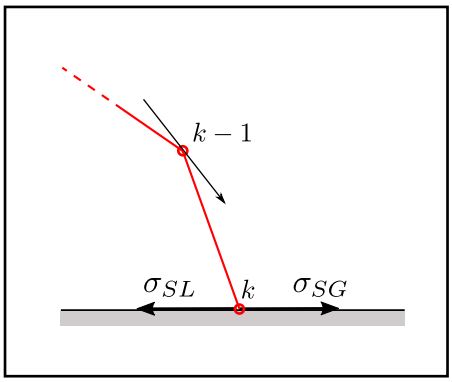

Figure 3.5: Front element adjacent to the wall.

is calculated at the front elements (as in this work), then the information missing is the unit tangent at the marker on the wall (marker k in figure 3.5). In the work of (Yamamoto and Uemura, 2008), wetting is considered a particular case of a three fluid junction (see figure 3.5), so, from Young's equation, at the front element adjacent to the wall:

$$f_{xe,k} = \sigma(\cos\alpha_s - t_{xk-1}) \qquad ; \qquad f_{ye,k} = 0 \tag{3.19}$$

where α_s is the static contact angle. The imposition of a dynamic/apparent contact angle is done in the same way. Muradoglu and Tasoglu (2010) analyzed the impact and spreading of droplets on solid walls with the front tracking method considering enough to defined a cut-off distance from the wall at which the front is fitted with a polynomial having a gradient at the wall equivalent to the dynamic contact angle obtained by the Kistlers's correlation or any equivalent, i.e. Cox's asymptotic expansions (see Cox, 1986).

When capillary force is calculated at the nodes, the static contact angle is imposed through the unbalance Young force at the node on the wall of interest:

$$\boldsymbol{f}_k = \sigma(\cos\alpha_s - \cos\alpha) \tag{3.20}$$

where σ is the constant surface tension, α_s is the static contact angle and α is the angle formed by the element at the wall and is given by:

$$\cos\alpha = \boldsymbol{t_e} \cdot \boldsymbol{t_{wall}} \tag{3.21}$$

Here, $\boldsymbol{t_{wall}}$ stands for the tangent of the wall. Works with this type of angle imposition include: Huang et al. (2004) in the front-tracking method, Manservisi and Scardovelli (2009) in a variational approach for drop spreading and the works of Lai et al. (2010) and Ming-Chih Lai and Huang (2011)

in the immersed boundary method.

3.5 Markers advection

Once equations 2.1 and 2.2 are solved and a conservative velocity field is achieved, markers are advected integrating in time:

$$\frac{d\boldsymbol{x}'_k}{dt} = \boldsymbol{U}_k \tag{3.22}$$

using an explicit first order (FO) scheme:

$$\boldsymbol{x}'^{n+1}_k = \boldsymbol{x}'^{n}_k + \boldsymbol{U}_k \Delta t \tag{3.23}$$

where n stands for the current time step. The marker velocity $\boldsymbol{U}_k$ is interpolated from the eulerian grid through:

$$\boldsymbol{U}_k = \sum_{ij} \Delta x \Delta y \boldsymbol{U}_{ij} D_{ij} \tag{3.24}$$

D_{ij} is given by equation 3.3. Typically, each time step follows the next pseudo-algorithm:

- Velocity and pressure fields are initialized along with initial markers position.
- The distance function ϕ is calculated.
- From ϕ, the VOF function C is found through equation 2.15 and fluid properties are calculated using equations 2.3 and 2.4.
- Surface tension contribution is found using the hybrid formulation in equations 3.14 and 3.15.
- The Navier-Stokes equations 2.2 are solved, using the capillary contribution (equations 3.14 and 3.15) in each Runge-Kutta cycle.
- Markers are advected using a interpolated velocity from the conservative eulerian field, equation 3.23.
- Cycle repeats at the second step.

In theory, higher order of time stepping to advect markers should improve the accuracy of marker advection (Tryggvason et al., 2006). In this work, for comparison purposes, some cases will use marker advection inside the general three-step Runge-Kutta cycle ($RK3$) as follows:

$$\frac{\boldsymbol{x}_k'^m - \boldsymbol{x}_k'^{m-1}}{\Delta t} = (\alpha_m + \beta_m)\boldsymbol{U}_k^{m-1} \tag{3.25}$$

where α_m and β_m are the Runge-Kutta coefficients of the Navier-Stokes solver (see section 2.2.2), $\boldsymbol{U}_k^m$ is the divergence-free intermediate velocity and the subscript m is the current $RK3$ step. When $m = 1$ we simply impose $\boldsymbol{x}_k'^{m-1} = \boldsymbol{x}_k'^n$. By default, in all tests of this work, advection of markers will be performed using FO, except for those cases where $RK3$ is explicitly mentioned.

3.6 Tangent calculation at markers position

Tangents at markers position have been addressed in the literature by fitting/interpolating functions on the markers and then calculating the tangents analytically (see for example Tryggvason et al., 2001; Popinet and Zaleski, 1999). In this work we consider that at any given time step, two neighbor front elements e_k and e_{k+1} share a common curvature center, as depicted in figure 3.6a. By simple geometrical means, it can be shown that the tangent at marker k can be calculated as the element length weighted average of tangents of the two neighbor elements e_k and e_{k+1}:

$$\boldsymbol{t}_k = \frac{\Delta s_{k+1}\boldsymbol{t}_{e,k} + \Delta s_k \boldsymbol{t}_{e,k+1}}{\sqrt{\Delta s_{k+1}^2 + \Delta s_k^2 + 2\Delta s_{k+1}\Delta s_k \boldsymbol{t}_{e,k} \cdot \boldsymbol{t}_{e,k+1}}} \tag{3.26}$$

Here subscript e means that the vector belongs to the front element. If Δs is constant, equation 3.26 reduces even further. This approach is based on the fact that after the fluid interface has been discretized by markers and front elements, the only remaining information of the actual interface (black curve in figure 3.6a) is preserved at markers, so, assuming that two elements share a common curvature center which is the equivalent to fitting a circle through each three consecutive markers, should be as good as any fitting function on the markers (the accuracy of this claim will be tested). Also, it is worth noticing that we only keep a list of neighbors at both sides of each element and no sorted list of markers/elements is stored, subscripts k in all cases are only given for notation. An implicit advantage when $\boldsymbol{f}$ is calculated with tangents at both ends of the front element (equation 3.17)

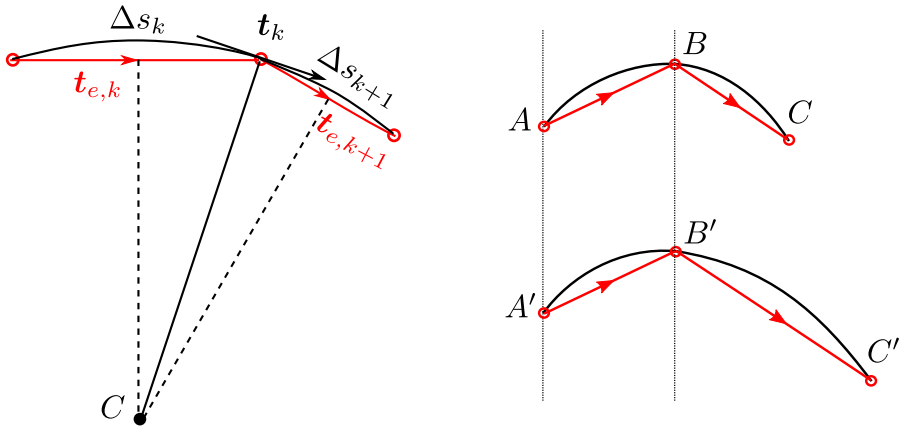

(a) (b)

Figure 3.6: Schematics of a front. The black curves represent the actual interface, in red: the discrete front. (a) Curvature center C for elements e_k and e_{k+1}; (b) Two interfaces: above with a uniform markers distribution and below, with a non-uniform marker distribution.

with respect to $\boldsymbol{f}$ calculated with tangents of neighbor elements (equation 3.18) is that the former includes geometrical information of the neighbor elements. This can be better understood in figure 3.6b. Elements AB, $A'B'$, BC, $B'C'$ have been drawn so front element pairs (AB, $A'B'$) and (BC, $B'C'$) have the same unit tangents. So, if $\boldsymbol{f}_B = \sigma\left(\boldsymbol{t}_{BC} - \boldsymbol{t}_{AB}\right)$, as in Shin and Juric (2002); Shin et al. (2005); Lai et al. (2010); Huang et al. (2004); Ceniceros et al. (2010); Li et al. (2012), both interfaces will have an identical local force $\boldsymbol{f}_B = \boldsymbol{f}_{B'}$ even though they represent different interfaces with different curvatures. The consequences of this problem were identified in Shin et al. (2005), when the elimination of spurious velocities was affected due to a non-uniform markers distribution after front reconstruction. In that work, however, using $\boldsymbol{f}$ with tangents on elements, was justified in terms that no logical connectivity between front elements was seek for simplicity in the reconstruction, since for that approach, front elements do not need to know information of their neighbors.

3.7 Front reconstruction

It is well known that markers drift along the interface. In the literature, procedures to keep a reasonable density of markers on the front consist on

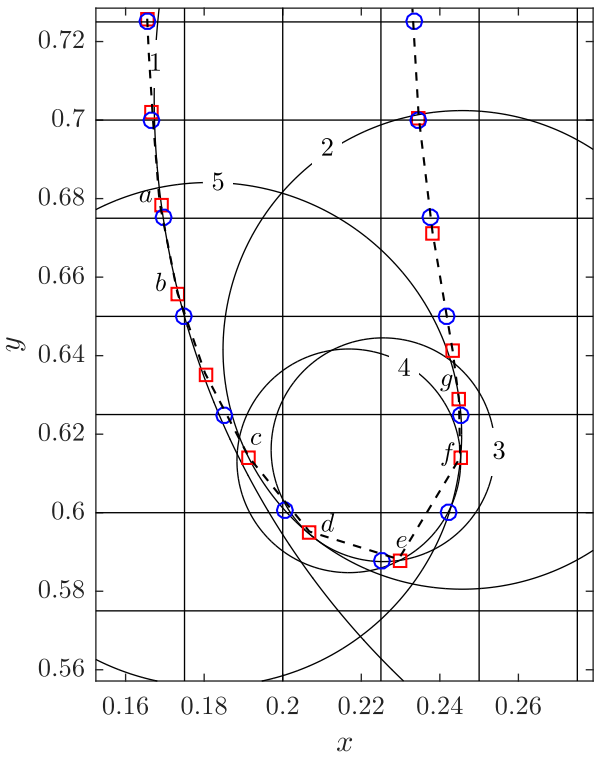

Figure 3.7: Typical reconstruction procedure for a rising bubble flow: $\rho_1/\rho_2 = 1000$, $\mu_1/\mu_2 = 100$, $\sigma = 1.96$, $g = 0.98$, $Re = 35$, $Eo = 125$, (following Hysing et al., 2009). Circles 1, 2, 3, 4 and 5 are generated with associated curvature of front elements ab, cd, de, ef and fg respectively. Markers are given: ▫ Before reconstruction; ○ After reconstruction. Details of this reconstruction are given in figure 3.8

including and removing markers given a certain element size threshold (see Unverdi and Tryggvason, 1992; Juric and Tryggvason, 1998). A more sophisticated and automated procedure can be found in Popinet and Zaleski (1999), where an interpolating curve is used to obtain an homogeneous distribution. Also, an artificial tangential velocity can be calculated and added to the marker velocity to produce a front with a uniform distribution (see Ming-Chih Lai and Huang, 2011; Ceniceros et al., 2010). A more robust procedure is proposed in Shin et al. (2005), where an optimum indicator function (to preserve mass) is found and is intersected to eulerian faces to produce a new marker. Also in Shin et al. (2005), an increase in spurious velocities is reported because of the non-uniform marker distribution obtained after reconstruction. In this work, the new procedure to calculate tangents at markers (equation 3.26), as described before, also provides tools to propose a

new front reconstruction method that solves equally all the known issues of the front-tracking method (see section 3.2) and does not affect the reduction of spurious velocities. At both ends of each front element, unit tangents can be calculated with the procedure described in 3.6. The radius R_e of a circle can then be determined for this element using the Frenet relation for local curvature $R_e^{-1}\boldsymbol{n} = d\boldsymbol{t}/ds$, or discretely:

$$R_e^{-1} = \left\| \frac{\boldsymbol{t}_{k+1} - \boldsymbol{t}_k}{\Delta s} \right\| \tag{3.27}$$

The center of this circle is found using the inner product of the normal vector of the element (which always points inside the tracked fluid) and the local surface tension force (equation 3.17):

$$\text{Circle center} = \begin{cases} \text{inside} & \text{if } \boldsymbol{n}_e \cdot \boldsymbol{f}_e > 0, \\ \text{outside} & \text{if } \boldsymbol{n}_e \cdot \boldsymbol{f}_e < 0 \end{cases} \tag{3.28}$$

Once this circle is totally defined, it is intersected with the faces of the eulerian grid generating new markers. In practice the intersection is only made to the eulerian cells in the vicinity of the element. Although an algorithm to intersect circle-line segment is used, additional verifications are applied to make sure that the intersecting point is inside the circular arc limited by the markers at both ends of the element. Since front elements do not overlap, intersecting points at each eulerian face are unique, except of course in the case that more than one front is being treated and they are about to coalesce (not addressed in this work). Also, since tangents at the markers location are unique, the circles of neighboring elements will define new smooth front and marker distribution. Figure 3.7 shows a typical reconstruction process. At the step time n_t, the front is represented by the red squares. Through selected elements ab, cd, de, ef and fg, the circles 1, 2, 3, 4 and 5 can be constructed as described before. The intersection between these circles and the eulerian grid faces, define the new front markers in blue circles. Figure 3.8 shows in detail selected elements and their associated circles for reconstruction. Except for front element ab in figure 3.8a, elements cd, de and ef in figures 3.8b, 3.8c and 3.8d respectively, have large curvature, producing relatively small circles. Small circles will intersect eulerian grid faces away from the front element. The case depicted in figure 3.8b, shows circle 2 close to a eulerian grid corner. In this situation, two markers will be generated forming a new front element of short length (see lower left in figure 3.8b, where we have enlarge the eulerian cell corner to show the preliminary markers in green). The closer the circle gets to the corner of a eulerian cell, the smaller is the front element produced (in a extreme case $\Delta s = 0$). The effect of having

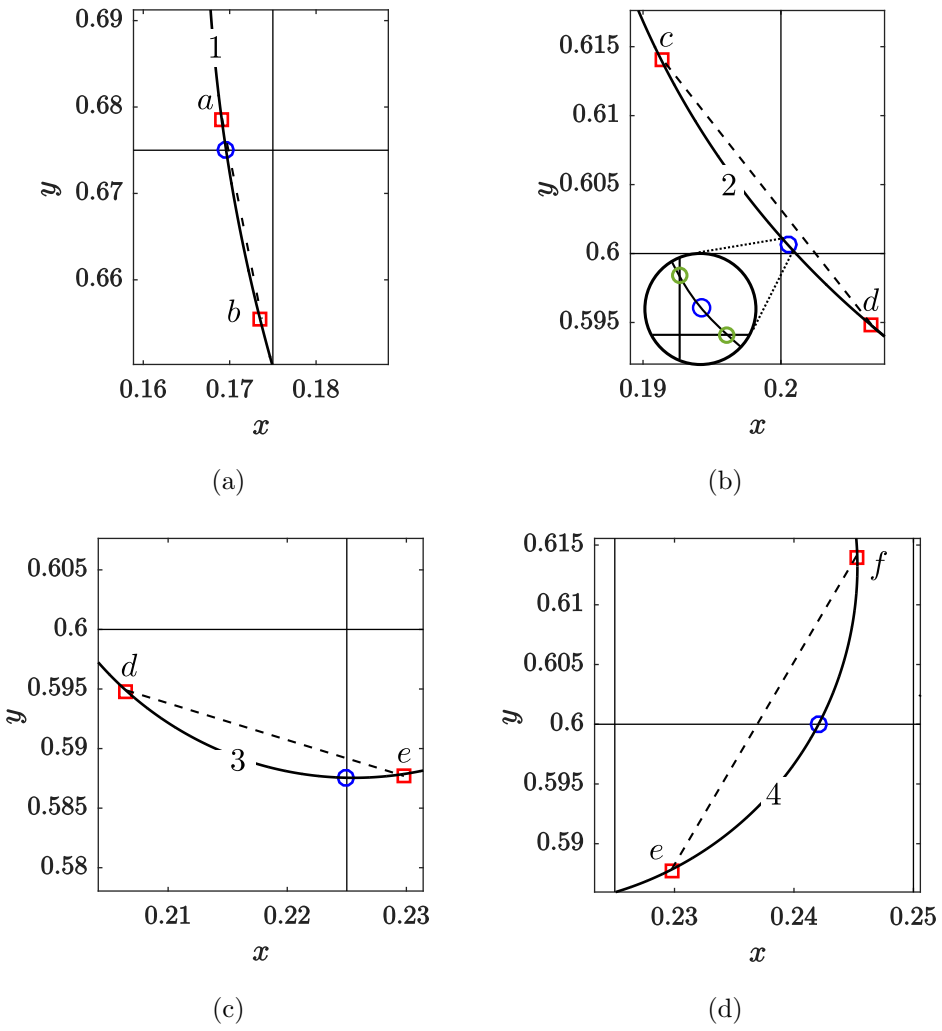

Figure 3.8: Zoom-in into figure 3.7 at front element: (a) ab. (b) cd. (c) de. (d) ef. ▫ Before reconstruction; ○ After reconstruction; ○ Preliminary markers after reconstruction.

small elements will be discussed in section 4.4. A threshold value Δs_{min} is introduced to control the minimum size of the elements. If $\Delta s_k \leq \Delta s_{min}$ the markers k and $k-1$ are fused together to avoid small elements. Following the method described above a circle of radius R_e is determined based on the two markers to fuse. They are replaced by an unique marker located at the center of the circular arc between the two markers. Figure 3.8b shows the result of such fusion.

3.8 Summary

In this chapter we have given details on how the front-tracking method has been implemented inside *JADIM* during this work. We have listed the main shortcomings and difficulties of the use of the front-tracking method. We have proposed countermeasures and enhancements to it. Both the calculation of tangents at markers and the front reconstruction need to be validated and tested to provide evidence that the spurious velocities can be maintained close to machine precision. This validation is conducted in chapter 4.

Chapter 4

Validation of the Front-Tracking Method

In this chapter we validate the current implementation of the front-tracking method inside *JADIM*, presented in the previous chapter.

4.1 Background

In the literature, it has been reported (see Shin et al., 2005) that the Hybrid formulation (equations 3.8 to 3.13) for the capillary contribution reduces spurious velocities close to machine precision when a uniform distribution of markers is used. We reproduced first the case proposed in Shin et al. (2005) for a static bubble in section 4.2 and then analyze the case of a translating bubble in section 4.3. In both cases, the reconstruction procedure described in section 3.7 is not applied and we evaluate only if the new tangent formulation proposed in this work (equations 3.17 and 3.26) for a non-uniform distribution of markers can reduce spurious velocities as in the case of a uniform distribution. In section 4.4 we evaluate the conditions under which the reconstruction process of section 3.7 can keep spurious velocities close to machine precision. We close the chapter benchmarking the method with the rising 2D bubble test and we analyze the performance of the method in the case of the equilibrium shape of a droplet spreading on a wall with effects of gravity.

4.2 Static bubble

A 2D bubble with radius $R = 0.25$ is initialized in a regular 50×50 grid of $L = H = 1$. Having all fluid properties set to 1, the corresponding Laplace

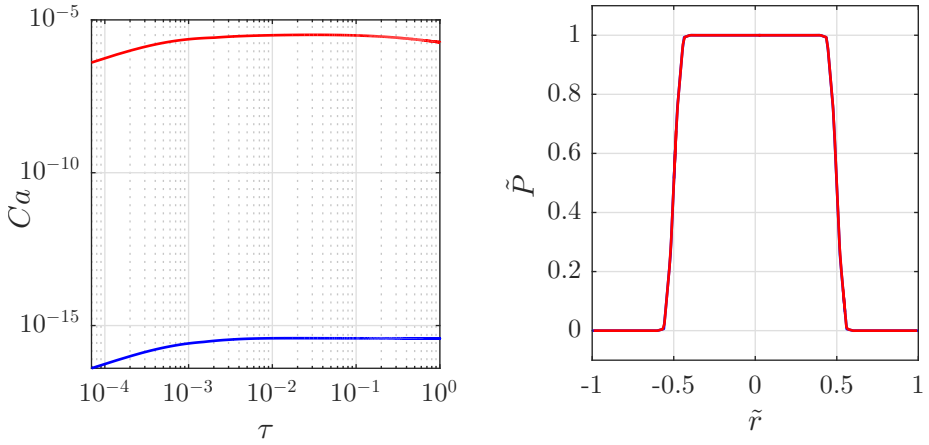

(a) (b)

Figure 4.1: Numerical simulation of a 2D static bubble in stagnant fluid (using equation 3.18). Comparison of a uniform (—) and a random distribution of markers (—). (a) Maximum normalized velocity evolution. (b) Normalized pressure at $y = 0.5$.

number is $La = \rho D\sigma/\mu^2 = 0.5$. For this test, markers are advected using a first order time integration (equation 3.23). Results are shown in figure 4.1 where two distributions of markers are compared. In blue, the interface is initialized with a uniform distribution of markers such that $\Delta s = \Delta x$. In red, the interface is initialized with a random distribution of markers, having a minimum and a maximum element size of $\Delta s_{min} = 0.3\Delta x$ and $\Delta s_{max} = \Delta x$ respectively, the reason of this choose will be clear later. Calculation of the local surface tension force $\boldsymbol{f}$ is performed using equation 3.18 as reported in Shin et al. (2005). The maximum velocity U_{max} inside the domain is reported in figure 4.1a (normalized with σ/μ) as a function of time (normalized with the capillary time scale $\tau = t/\sqrt{\rho D^3/\sigma}$). It can be seen in figure 4.1a that a non-uniform distribution of markers, increases the maximum velocity Ca up to 8 orders of magnitude with respect to the value obtained with a uniform distribution (similar to what was reported in Shin et al. (2005)). However, the pressure on a line crossing the center of the bubble seems to be unaffected and correctly predicted in both uniform and non-uniform distribution of markers. This is reported in figure 4.1b, where $\tilde{r} = (x - x_c)/x_c$, $\tilde{P} = P/(\sigma/R)$ and x_c is the x coordinate of the bubble center. The same test is repeated, now with $\boldsymbol{f}$ calculated with tangents in equation 3.26 (present approach). As can be seen in figure 4.2a, in both uniform and non-uniform distributions of makers, the maximum velocity is recovered between a margin

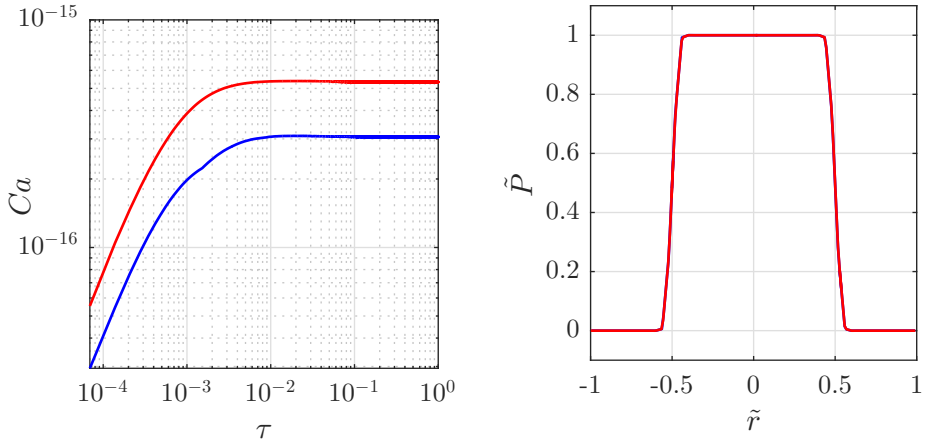

(a) (b)

Figure 4.2: Numerical simulation of a 2D static bubble in stagnant fluid (using equation 3.26). Comparison of a uniform (—) and a random distribution of markers (—). (a) Maximum normalized velocity evolution. (b) Normalized pressure at $y = 0.5$.

of 2×10^{-16} favorable to the uniform distribution. Pressure at $y = 0.5$ still shows no variation for both distributions (see figure 4.2b).
Next, the influence of Laplace number La on the spurious velocities for a non-uniform distribution is analyzed. Again we use the same numerical domain as in the previous test. Density ρ and dynamic viscosity μ of both fluids are set to 1, while surface tension is set such that $La = 0.5, 12, 120, 1200$ and 12000. Results are shown in figure 4.3a where the evolution of the maximum adimensional velocity is reported. Laplace number affects the initial evolution of the velocity, but in all cases stabilization is always achieved. Up to $La = 1200$, stabilization occurs at $\tau \sim 0.5$. For $La = 12000$, constant Ca is achieved after $\tau \sim 7$ (not shown). Figure 4.3b shows the same evolution up to $\tau = 0.2$, showing also the evolution of the RMS dimensionless velocity. The rate of convergence in time for the RMS velocity is quite similar to that of the maximum velocity and its value is 1 order of magnitude smaller. This convergence occurs from a minimum to a maximum value, the opposite to the evolution found in Popinet (2009) and Abadie et al. (2015) (from maximum to minimum). The values reached here are close to machine precision as in Popinet (2009) and also to those obtained with LS-SSF (Level Set Sharp Surface Force) reported in Abadie et al. (2015), but in a quicker velocity stabilization than both references.

We define the average pressure jump ΔP_{avg} and the maximum pressure

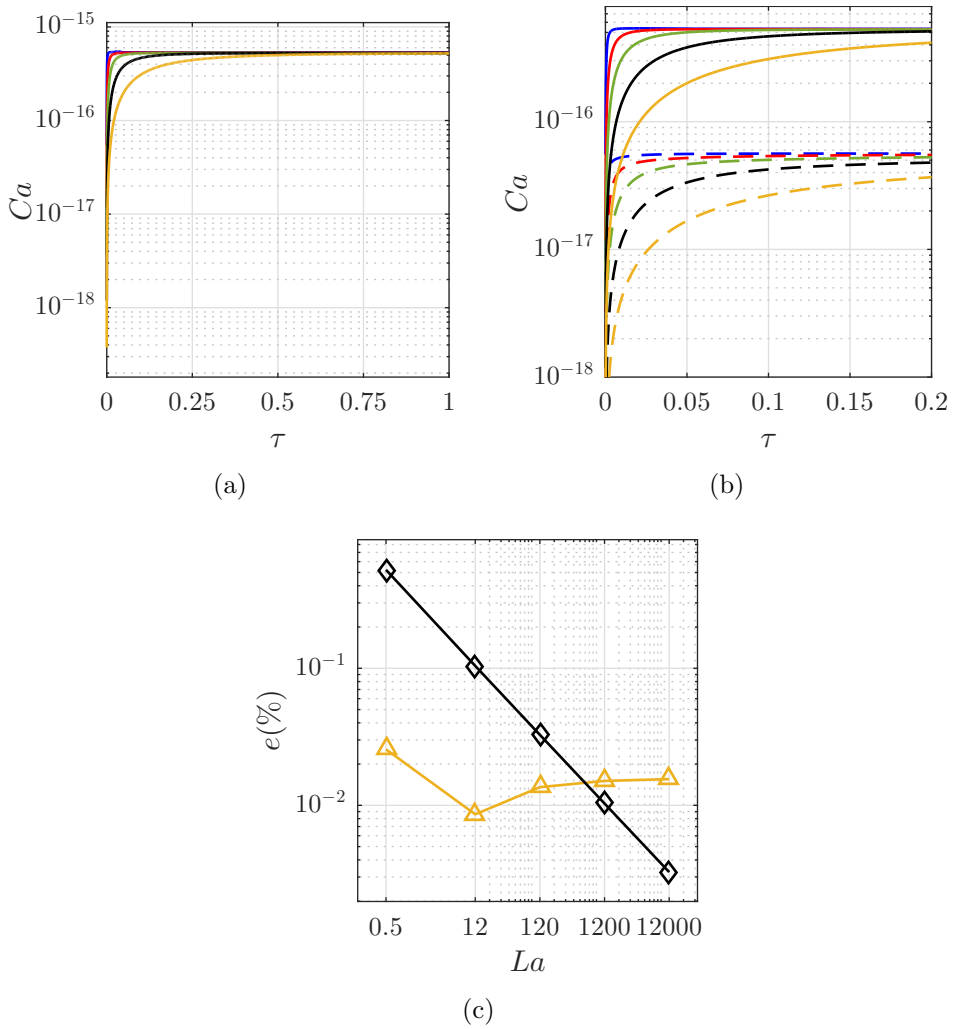

Figure 4.3: Effect of La for a non-uniform distribution of markers on: (a) Maximum velocity evolution: —, $La = 0.5$; —, $La = 12$; —, $La = 120$; —, $La = 1200$; —, $La = 12000$. (b) Maximum and RMS velocity evolution: - - -, $La = 0.5$; - - -, $La = 12$; - - -, $La = 120$; - - -, $La = 1200$; - - -, $La = 12000$. (c) Pressure Jump error: —◇—, ΔP_{max}; —△—, ΔP_{avg}.

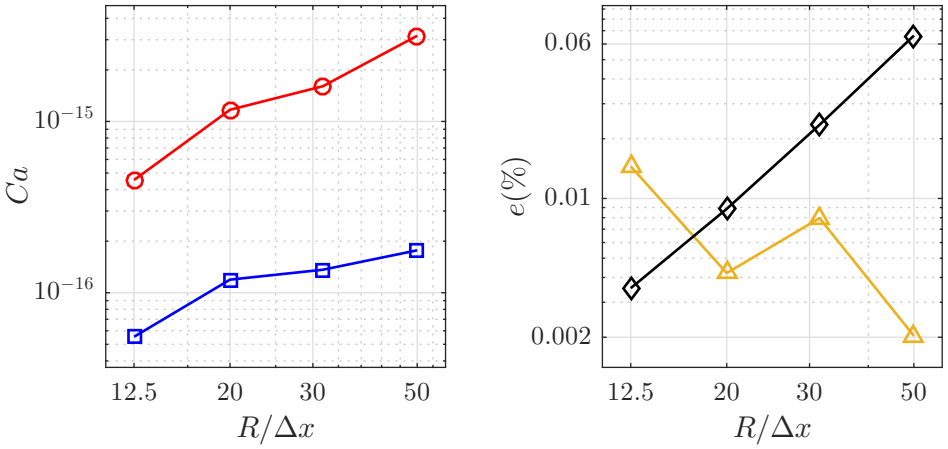

Figure 4.4: Static bubble test. Effect of $R/\Delta x$ ($\Delta\tau = 0.15$) over: (a)—○—, Maximum Velocity; —□—, RMS Velocity. (b) Percent error for —◇—, ΔP_{max}; —△—, ΔP_{avg}

jump ΔP_{max} both normalized by the Laplace pressure σ/R. The former is found by taking the difference of the area weighted average of the pressure inside and outside the bubble, while the latter is calculated by the difference between the maximum and the minimum pressure inside the domain. The influence of La on the error for ΔP_{max} and ΔP_{avg} taking 1.0 as a reference is shown in figure 4.3c. The error in ΔP_{max} has a tendency to decrease with La, while ΔP_{avg} is kept close to $\sim 0.01\%$ for any La.

A grid test dependence is shown in figure 4.4. There we see a growth in the maximum velocity with grid resolution (figure 4.4a) a similar tendency is found for the error in the maximum pressure jump (figure 4.4b). The error in the average pressure however shows a decrease with grid resolution. Next we evaluate the effect of the step of time (Δt) in the reduction of spurious velocities. The case of $La = 12000$ is chosen for this test and results are reported in figure 4.5 where the step of time has been normalized by the minimum Δt (table 2.1). A comparison between FO and $RK3$ marker advection is shown for velocity and pressure jump error. As can be seen from figure 4.5a, for all $\Delta\tau$ tested, the maximum velocity reaches $\sim 2 \times 10^{-14}$ and for both FO and $RK3$, spurious velocities converge at $\Delta\tau \sim 0.2$. Spurious velocities for $RK3$ are similar in magnitude to those for FO, except for $\Delta\tau \sim 1.8$ where the difference is about 2 orders of magnitude. This is expected given that $RK3$ is a high order scheme of advection so the difference between the two schemes will be noticeable when increasing the time step. There is virtually

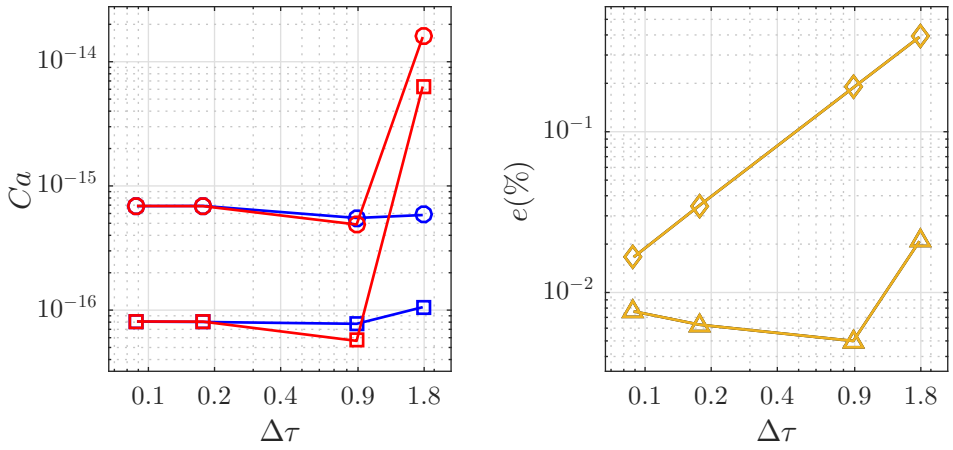

Figure 4.5: Effect of Δt ($R/\Delta x = 12.5$) over: (a) —○—, Maximum Velocity (FO); —□—, RMS Velocity (FO); —○—, Maximum Velocity ($RK3$); —□—, RMS Velocity ($RK3$). (b) Error for —◇—, ΔP_{max} (FO); —△—, ΔP_{avg} (FO); —◇—, ΔP_{max} ($RK3$); —△—, ΔP_{avg} ($RK3$).

no difference between FO and $RK3$ for error in pressure jump (figure 4.5b). Error in maximum pressure jump shows a continuous improvement and convergence with $\Delta\tau$ whereas error in average pressure is kept almost constant at $\sim 0.01\%$.

4.3 Translating bubble

This is a more aggressive test for the evaluation of spurious velocities reported in the literature (Popinet, 2009; Abadie, 2013; Abadie et al., 2015). This test is also very useful because when simulating real flows we expect the combined effects of curvature calculation and interface advection as stressed in Abadie et al. (2015). We analyze a translating bubble of $R = 0.2$ inside a unit computational square domain which is initialized with a uniform velocity field U_0. In both horizontal surfaces the symmetry boundary condition is imposed, while in vertical surfaces a periodic one is prescribed. As described in Popinet (2009), this setup introduces a new timescale $t_U = D/U_0$ with which the normalized time τ will be obtained. Here the non-uniform distribution of markers is obtained randomly, as described in section 4.2. Properties of fluids are varied to test different La and Ca numbers, keeping always the same density and viscosity inside and outside the bubble. The schematics of

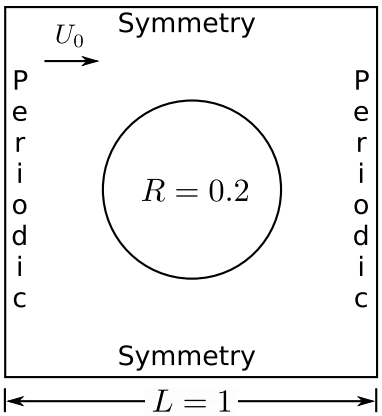

Figure 4.6: Schematic of a translating bubble test

this test are shown in figure 4.6. Theoretically, in the reference frame of the translating bubble, the velocity is zero. So, we define the normalized velocities $\tilde{U}_{max} = max(|U - U_0|)/U_0$ and $\tilde{U}_{RMS} = |U_{RMS} - U_0| / U_0$. The evolution of $\tilde{U}$ with time is shown in figure 4.7. The maximum velocity stabilizes in the late $\tau \sim 0.75$ for all La. The RMS velocity however does not converge with time, this was noticed also in Popinet (2009) where it is stated that advection will continue perturbing the shape of the interface (hence the curvature calculation) in time. Figure 4.8a shows the effect of the Laplace number over the maximum and the RMS velocity keeping $We = 0.4$. Maximum velocity reaches a peak at $\tilde{U} \sim 1 \times 10^{-13}$ and $\tilde{U}_{RMS} \sim 1 \times 10^{-14}$, showing an increase with La but still keeping spurious velocity close to machine precision, confirming the observations reported in Popinet (2009), where a $\tilde{U}_{RMS} \sim 0.0015$ was reported; percent error for the maximum pressure jump decreases with La to $\sim 0.01\%$, while the average pressure jump if kept almost constant close to ~ 0.01, this can be seen in figure 4.8*b*.

Both velocity and pressure jump are tested against the mesh quality. This is shown in figure 4.9. In the grid test, no convergence is reported for both maximum and RMS velocity, reaching remarkably a maximum of 7×10^{-13} and $\sim 4 \times 10^{-14}$ respectively, the reason for this behavior is not clear, though the order of magnitude is significantly lower than those reported in Popinet (2009) and Abadie et al. (2015) (see figure 4.9a). The Δt used for this test is about $\sim 0.15\Delta t_{min}$ from the capillarity time criteria in table 2.1 corresponding to the finest grid ($R/\Delta x = 50$). The average pressure jump error improves as $R/\Delta x$ increases, reaching $\sim 0.002\%$. This improvement in average pressure jump error is due to the way in which the average pressure is calculated, the finer the grid, the more precise the area weighted average is

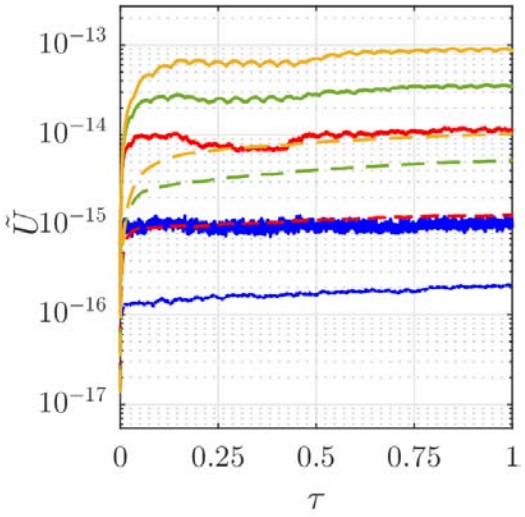

Figure 4.7: Translating bubble test. Temporal evolution of the maximum velocity for: —, $La = 1.2$; —, $La = 120$; —, $La = 1200$; —, $La = 12000$; and for RMS velocity for: - - -, $La = 1.2$; - - -, $La = 120$; - - -, $La = 1200$; - - -, $La = 12000$, while keeping $We = 0.4$ and $R/\Delta x = 12.8$.

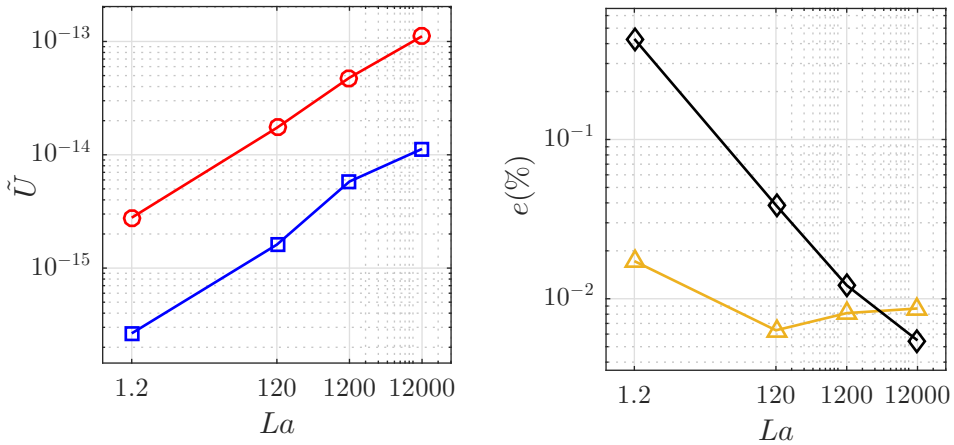

(a) (b)

Figure 4.8: Translating bubble test. Effect of La over: (a)—, Maximum Velocity; —, RMS Velocity. (b) Percent error for —, ΔP_{max}; —, ΔP_{avg}, while keeping $We = 0.4$ and $R/\Delta x = 12.8$.

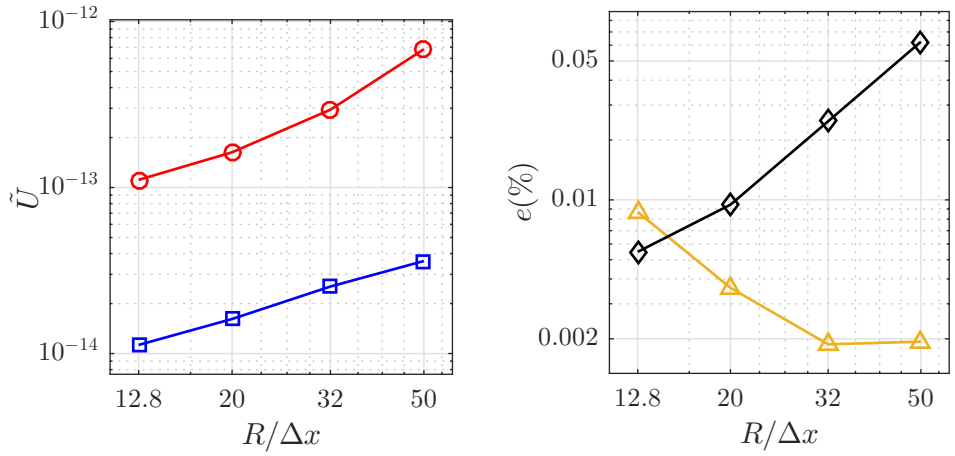

(a) (b)

Figure 4.9: Translating bubble test. Effect of $R/\Delta x$ ($\Delta\tau = 0.15$) over: (a) —o—, Maximum $\tilde{U}$; —□—, RMS $\tilde{U}$. (b) Percent error for —◇—, ΔP_{max}; —△—, ΔP_{avg}, while keeping $We = 0.4$ and $La = 12000$.

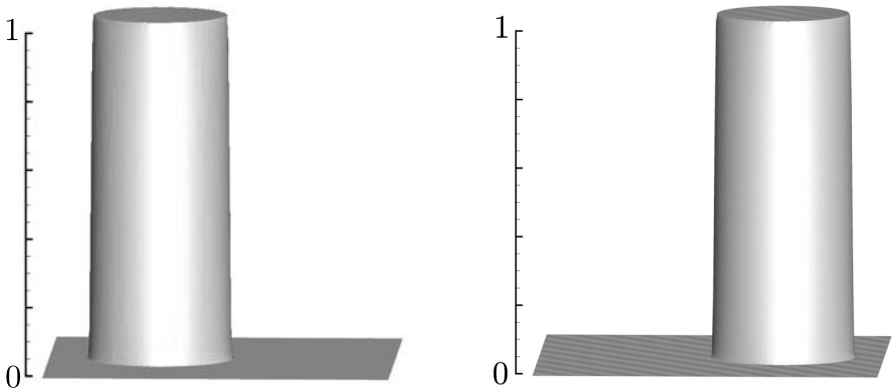

(a) (b)

Figure 4.10: Translating bubble test. Pressure profile for $R/\Delta x = 50$, $La = 12000$ and $We = 0.4$ at: (a) $\tau = 0.0804$; (b) $\tau = 1.6089$.

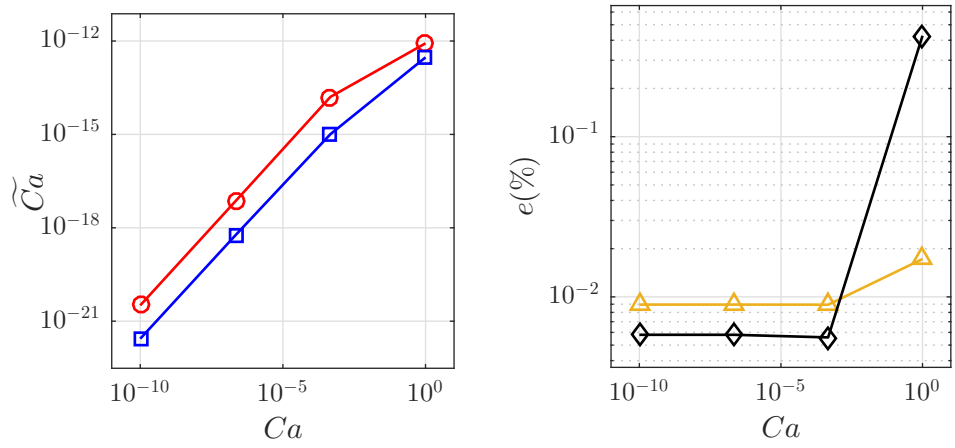

Figure 4.11: Translating bubble with $R/\Delta x = 12.8$. Effect of Ca over: (a) —○—, Maximum Velocity; —□—, RMS Velocity. (b) Percent error for —◇—, ΔP_{max}; —△—, ΔP_{avg}.

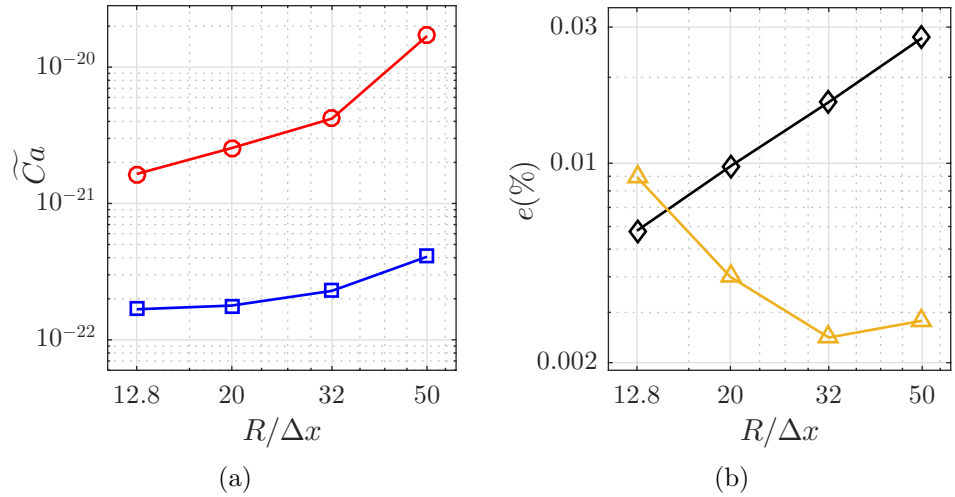

Figure 4.12: Effect of $R/\Delta x$ ($\Delta\tau = 0.15$) over: (a) —○—, Maximum Velocity; —□—, RMS Velocity. (b) Percent error for —◇—, ΔP_{max}; —△—, ΔP_{avg}, while keeping $Ca = 1 \times 10^{-10}$.

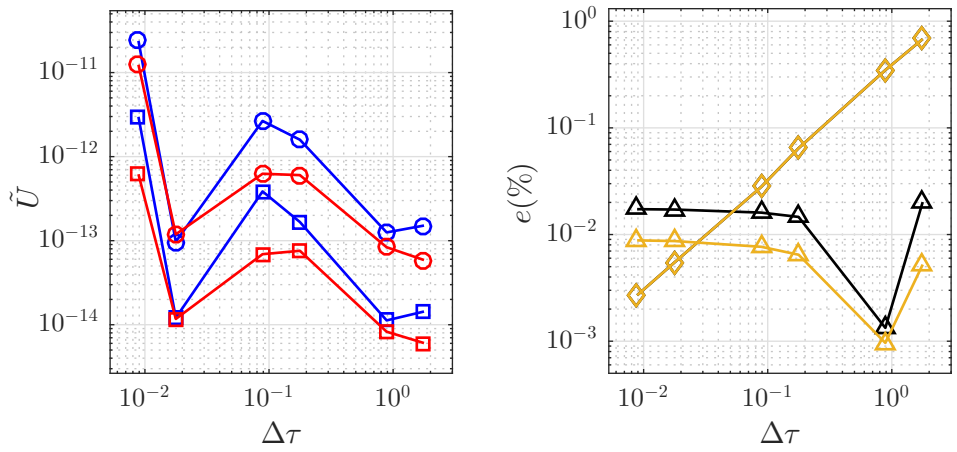

Figure 4.13: Effect of Δt ($R/\Delta x = 12.8$) over: (a) —o—, Maximum Velocity (FO); —□—, RMS Velocity (FO); —o—, Maximum Velocity ($RK3$); —□—, RMS Velocity ($RK3$). (b) Error for —◇—, ΔP_{max} (FO); —△—, ΔP_{avg} (FO); —◇—, ΔP_{max} ($RK3$); —△—, ΔP_{avg} ($RK3$).

found. The error in the maximum pressure jump shows a growing tendency with a maximum error of $\sim 0.06\%$. A similar tendency is found in Abadie et al. (2015). It is not clear why error in ΔP_{max} increases with grid quality. The pressure profile is always sharp and no perturbation in its shape could be found, this can be seen in figure 4.10, where the normalized pressure is shown at two selected time steps. Limitations in numerical simulations are related to capillary numbers under which the flow is contaminated by spurious velocities. In the next test, we use the translating bubble setup and modify properties to achieve $1 \times 10^{-10} \leq Ca \leq 1$ and check if the current implementation can reduce spurious velocities to acceptable levels. Results are shown in figure 4.11 and 4.12. We have defined $\widetilde{Ca}_{max} = max(|U - U_0|)\mu/\sigma$ and $\widetilde{Ca}_{RMS} = |U_{RMS} - U_0|\,\mu/\sigma$ as the characteristic capillary number of the spurious velocities for the maximum and the RMS velocity of each time step. From figure 4.11a, it can be deduced that spurious capillary velocities are always ~ 10 orders of magnitude lower than the main flow capillary velocity. For $Ca = 1$ we see that the maximum pressure jump starts departing from the theoretical Laplace pressure jump ($e \sim 0.4\%$). The error in the average pressure jump shows to be stable (around $\sim 0.01\%$) with Ca (see figure 4.11b). A grid test reveals a growth on the spurious velocities when the grid quality is increased (figure 4.12a) but still keeping small magnitudes. A growing tendency in the error of ΔP_{max} is also experienced (figure 4.12b),

whereas ΔP_{avg} shows improvement with grid quality as expected. Again, the profile of pressure is not perturbed (not shown here).

A test for Δt is also conducted for the translating bubble. In figure 4.13a, the normalized velocity shows no convergence with $\Delta\tau$, in fact, there is a growth in both maximum and RMS using the smallest $\Delta\tau \sim 0.01$. This can be explained with the complex coupling between surface tension force calculation and interface advection (see Abadie et al., 2015). When we use smaller Δt more time steps are required to achieve the same time of simulation, which means also that any perturbation on the general velocity field by the spurious velocities will affect successive calculations more frequently than using a larger $\Delta\tau$. This is a fact that will occur even for high order time advection schemes, in our case $RK3$, when we performed calculations of $\tilde{U}$ at a order of magnitude so small as those obtained in this work. We also performed the same tests for $\Delta\tau$, using a quadruple precision version of *JADIM*, with no better results (not shown here). In anyway, $\tilde{U}$ using FO resulted in ~ 1 order of magnitude less than $\tilde{U}$ for $RK3$ (for $\Delta\tau \sim 0.1$), this is the opposite to what was found for the static bubble, where $RK3$ performed slightly better than FO. Maximum pressure jump error (figure 4.13b) shows improvement with $\Delta\tau$ and independence of the advection method (both FO ans $RK3$ are superposed), while the average pressure jump error is kept roughly constant for any $\Delta\tau$ at $e(\%) \sim 0.01$, with FO performing slightly better.

4.4 Assessment of the reconstruction procedure

We have demonstrated so far that a non-uniform distribution of markers can achieve spurious velocities close to those obtained with a uniform distribution when care is taken calculating tangents at the ends of front elements. This section objective is to evaluate the new reconstruction process described in section 3.7. First we check the ability of the reconstruction to reproduce a known mathematical function and then we check if, after the reconstruction procedure, the spurious velocities can be kept at their low magnitude for the static and translating bubble cases. Finally, we also explore the stability of the reconstruction process in a case with large Laplace number.

4.4.1 Geometrical accuracy

To asses the accuracy of the reconstruction process described in section 3.7, we initialize the front with an ellipse of equation $x^2/9 + y^2/4 = 1$ in a 12×12

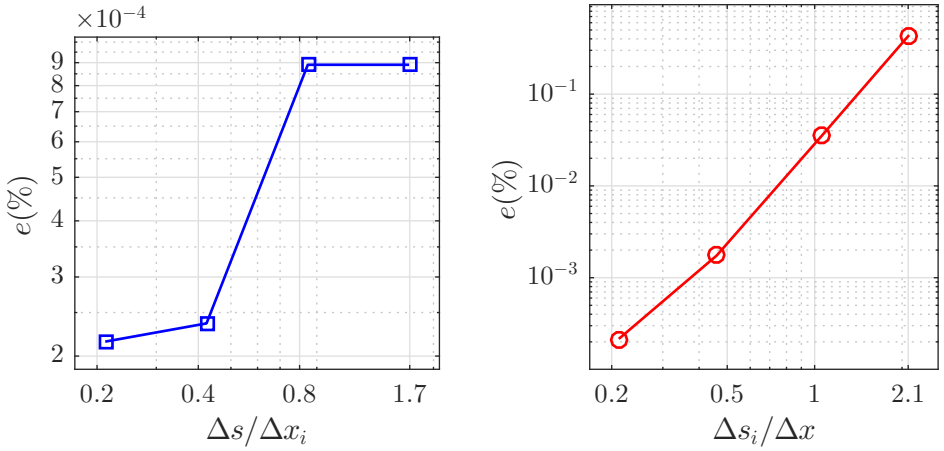

Figure 4.14: Effect of $\Delta s/\Delta x$ over the geometry of the ellipse $x^2/9+y^2/4 = 1$: (a) Varying number of eulerian elements; (b) Varying number of lagrangian markers;

box (see Torres and Brackbill, 2000, for details on the initialization). First, we construct the ellipse with 100 markers and we vary the number of cells in the eulerian grid from 16^2 to 168^2. We report the maximum percent error between markers y coordinates obtained after reconstruction and the reference value computed from the ellipse equation using each marker coordinate x. Results are shown in figure 4.14a. $\Delta s/\Delta x_i$ represents the ratio between the average element length of the initial front versus the length of a eulerian cell face. It can be seen that when the quality of the eulerian grid improves, the error on the geometry shape increases (from $\sim 2 \times 10^{-4}$ to $\sim 9 \times 10^{-4}$). The explanation for this is that when $\Delta s_i/\Delta x$ is large, less reconstructing circles can be generated so the geometry of the ellipse loses quality. This result is confirmed in 4.14b, where we repeated the test, this time keeping the eulerian grid at 16^2 cells and varying the number of elements of the initialized ellipse from 10 to 100 markers. The maximum error is $\sim 0.4(\%)$ corresponding to the maximum ratio tested ($\Delta s_i/\Delta x = 2.1$). Also, figure 4.14b shows that the error in the reconstruction procedure is ever increasing, this because we have large front elements that would intersect many eulerian faces using a unique curvature. As stated in the introduction, large front element size can also bring errors in the transfer of information between the front and the eulerian grid. So, based on figure 4.14a the maximum size ratio to have an accurate reconstruction should be kept close to 1. This raises the question on how small $\Delta s/\Delta x$ can be (see section 4.4.2).

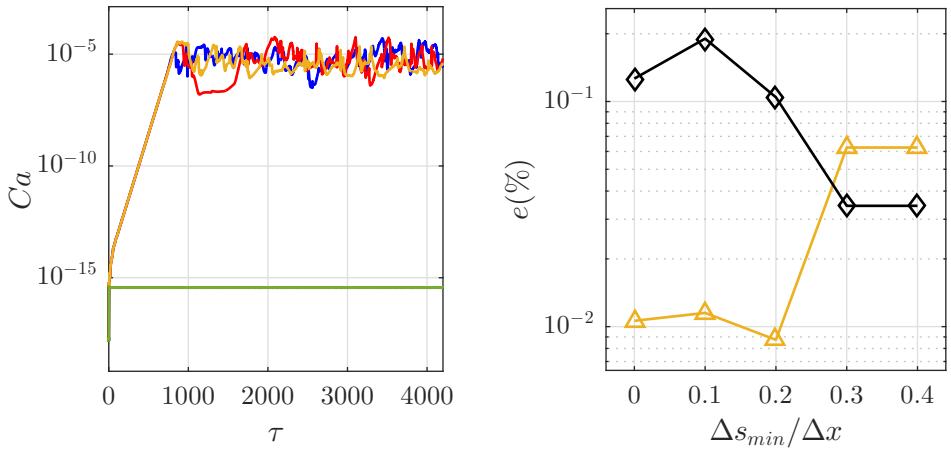

Figure 4.15: Test for minimum element size in a static drop, following Shin et al. (2005). (a) Maximum velocity; — $\Delta s_{min} = 0.0\Delta x$; — $\Delta s_{min} = 0.1\Delta x$; — $\Delta s_{min} = 0.2\Delta x$; — $\Delta s_{min} = 0.3\Delta x$; — $\Delta s_{min} = 0.4\Delta x$. (b) Percent error for pressure jump: —◇— ΔP_{max}; —△— ΔP_{avg}.

4.4.2 Stability of the spurious velocities elimination

It has been reported in Shin et al. (2005) that a non-uniform distribution of markers affects hybrid formulation capacity to reduce spurious velocities after a reconstruction process. In the preceding section we have explored the upper limit of Δs, here we explore the lower limit.

Small front elements are expected to arise when the flow groups markers in a small zone and when the reconstruction process is close to the corner of a eulerian cell. In fact, in an extreme case, since markers are reconstructed at eulerian faces, two markers forming a new element may coincide at the cell corner, producing a front element with $\Delta s = 0$.

To asses Δs_{min} we retake the static bubble test from section 4.2. A bubble of $R = 0.25$ is put in a 2D box of $L = H = 1$, having ρ and μ set to one, surface tension σ is set such that $La = 12000$. More details on the set up can be found in Shin et al. (2005). The simulation begins with a front initially uniform ($\Delta s/\Delta x = 1.0$), and the reconstruction procedure is set to be performed at each 100 time steps. The threshold Δs_{min} is defined as 0, 0.1, 0.2, 0.3, 0.4 times the uniform eulerian grid size $\Delta x = L/25$. $\Delta s_{min}/\Delta x = 0$ means that any element length Δs_k is allowed. If $\Delta s_{min}/\Delta x > 0$ then the markers are fuse together with the procedure explained in section 3.7 and depicted in figure 3.8b. A simulation is set up to $\tau \sim 4200$ such to obtain velocity

stability in time. The maximum adimensional velocity is reported in figure 4.15a. There, lines are superposed into two groups: blue ($\Delta s_{min}/\Delta x = 0$), red ($\Delta s_{min}/\Delta x = 0.1$) and orange ($\Delta s_{min}/\Delta x = 0.2$) on the top and black ($\Delta s_{min}/\Delta x = 0.3$) and green ($\Delta s_{min}/\Delta x = 0.4$) on the bottom. From there it is deduced that only if $\Delta s_{min} > 0.2\Delta x$ spurious currents results are comparable to those of a uniform distribution. For $\Delta s_{min} \leq 0.2\Delta x$, the maximum Ca stabilizes and reaches values comparable to those in Figure 4.1a (red line), which is compatible of using tangents of elements to calculate $\boldsymbol{f}$ as in Shin and Juric (2002); Shin et al. (2005); Lai et al. (2010); Huang et al. (2004); Ceniceros et al. (2010); Li et al. (2012) (equation 3.18). Figure 4.15b shows the percent error in the maximum and average pressure jump as a function of $\Delta s_{min}/\Delta x$. Maximum/average pressure jump error decrease/increase respectively with $\Delta s_{min}/\Delta x$. For $\Delta s_{min}/\Delta x > 0.2$ both errors meet roughly with an error of $\sim 0.05\%$. A similar test is conducted for the translating bubble of section 4.3, using a grid size of $\Delta x = L/25$. Again, the front is initialized with a uniform distribution of markers ($\Delta s/\Delta x = 1$). Reconstruction is performed at each 100 time steps, properties and initial velocity U_0 are set to give $La = 12000$ and $We = 0.4$. Results for this test are shown in figure 4.16. Normalized maximum velocity $\tilde{U}$ seems to converge for all cases except for the ratio $\Delta s/\Delta x = 0.0$ (any Δs is allowed). A closer look to the second half of τ of figure 4.16a is shown in figure 4.16c. There we can see that only ratios $\Delta s/\Delta x > 0.2$ in black and green lines present stability in time (up to $\tau = 1$). This confirms results obtain for the static case. On the other hand, pressure jump seems to be independent of ratio $\Delta s/\Delta x$ as can be deducted from the error in figure 4.16b. Error in the average pressure jump is $\sim 0.001\%$ and error in the maximum pressure jump is kept $\sim 0.0002\%$. To understand why a small Δs affects the spurious velocity reduction, we analyze next equation 3.17. At any given time step, the local force per surface tension unit at front element e_k (see figure 3.6a) is given by:

$$\boldsymbol{f}_{e,k}/\sigma = \boldsymbol{t}_k - \boldsymbol{t}_{k-1} \tag{4.1}$$

Substitution of equation 3.26 yields:

$$\begin{aligned} \boldsymbol{f}_{e,k}/\sigma = & \frac{\boldsymbol{t}_{e,k}\Delta s_{k+1} + \boldsymbol{t}_{e,k+1}\Delta s_k}{\sqrt{\Delta s_{k+1}^2 + \Delta s_k^2 + 2\Delta s_{k+1}\Delta s_k \boldsymbol{t}_{e,k}\cdot\boldsymbol{t}_{e,k+1}}} \\ & - \frac{\boldsymbol{t}_{e,k-1}\Delta s_k + \boldsymbol{t}_{e,k}\Delta s_{k-1}}{\sqrt{\Delta s_k^2 + \Delta s_{k-1}^2 + 2\Delta s_k\Delta s_{k-1}\boldsymbol{t}_{e,k-1}\cdot\boldsymbol{t}_{e,k}}} \end{aligned} \tag{4.2}$$

Clearly in equation 4.2, if $\Delta s_k \to 0$ then $\boldsymbol{f}_{e,k}/\sigma \to 0$, which means that small elements do not contribute to the global surface tension contribution, which

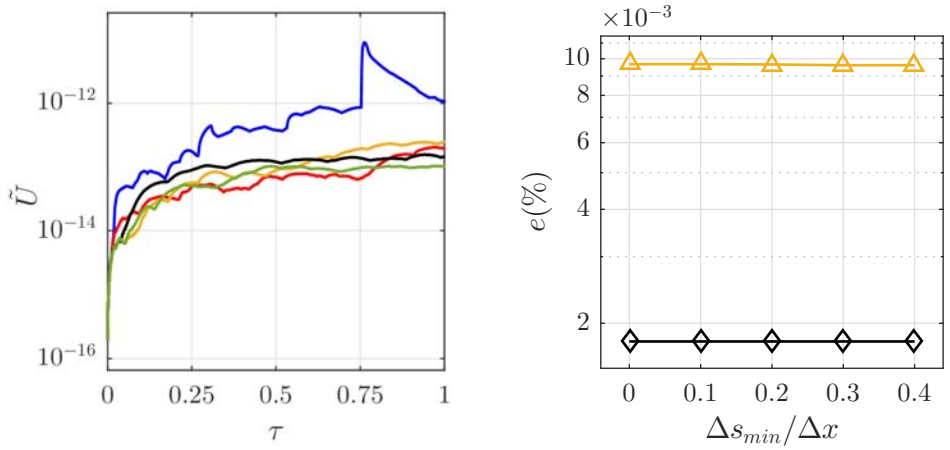

Figure 4.16: Test for minimum element size in a translating bubble. (a) Maximum velocity; — $\Delta s_{min} = 0.0\Delta x$; — $\Delta s_{min} = 0.1\Delta x$; — $\Delta s_{min} = 0.2\Delta x$; — $\Delta s_{min} = 0.3\Delta x$; — $\Delta s_{min} = 0.4\Delta x$. (b) Percent error for pressure jump; ΔP_{max}; ΔP_{avg}. (c) Zoom-in into figure 4.16a.

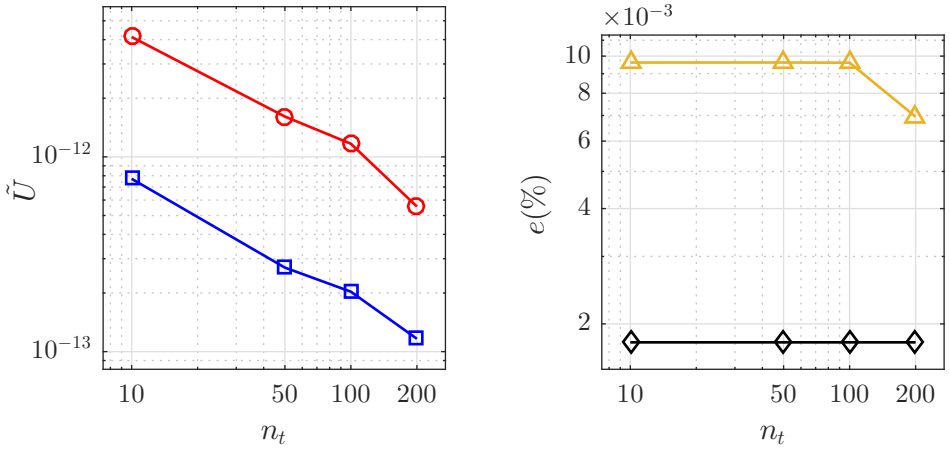

Figure 4.17: Translating bubble. Effect of frequency of reconstruction in time step units. (a) —o—, Maximum $\tilde{U}$; —□—, RMS $\tilde{U}$. (b) Percent error for pressure jump; —◇— ΔP_{max}; —△— ΔP_{avg}.

is also obvious from equation 3.6. Nevertheless, a small element may affect negatively the local force of its neighbors, i.e. if $\Delta s_{k-1} \to 0$ then the force in equation 4.2 results in:

$$\boldsymbol{f}_{e,k}/\sigma = \frac{\boldsymbol{t}_{e,k}\Delta s_{k+1} + \boldsymbol{t}_{e,k+1}\Delta s_k}{\sqrt{\Delta s_{k+1}^2 + \Delta s_k^2 + 2\Delta s_{k+1}\Delta s_k \boldsymbol{t}_{e,k} \cdot \boldsymbol{t}_{e,k+1}}} - \boldsymbol{t}_{e,k-1}$$

which shows a large contribution of the small element tangent $\boldsymbol{t}_{e,k-1}$ which undermines the calculation of the local surface tension force. A threshold of $\Delta s_{min}/\Delta x > 0.2$ ensures stability of the spurious velocities close to machine precision and it is used as the default threshold in this work. Next, the frequency of reconstruction is analyzed for the case of the translating bubble. Keeping properties to achieve $La = 12000$ and $We = 0.4$, we prescribe a reconstruction frequency of n_t equal to 10, 50, 100 and 200 time steps. Results are shown in figure 4.17. Dimensionless velocities show a decreasing tendency with decreasing frequency of reconstruction. Cut-off errors in the circle-segment line intersection calculation are introduced and accumulated in the calculations, hence the decreasing tendency. Nevertheless, magnitude of spurious velocities are kept close to machine precision (see figure 4.17a). Average pressure jump shows also its smallest value, ~ 0.007 for $n_t = 200$ time steps, while the maximum pressure jump error is independent on the reconstruction frequency, keeping its value at ~ 0.002 (figure 4.17b).

We close this spurious velocities and stability evaluation with a test proposed in Torres and Brackbill (2000) and reproduced in Shin et al. (2005) for a large La. An elliptical droplet of equation $x^2/0.003^2 + y^2/0.002^2 = 1$ is initialized inside a 0.01×0.01 box with periodic boundary conditions. Properties are set such that density and viscosity jumps are 1000 and 10 respectively. Surface tension then is 0.1 for a total $La = 500000$. Reconstruction process for this problem is set at 1000 time steps on a grid of 64^2 uniform cells. According to Scardovelli and Zaleski (1999), for large density ratios, high spurious velocities should be found. It is also mentioned that destruction of the interface is expected for large La. We experienced this latter point when trying to compared our implementation with VOF-FCT-CSF inside JADIM with catastrophic results (not shown here, but we can mention that it took only ~ 15000 time steps of the 5×10^6 planned to destroy the interface), so instead we compared the results of this test with Level-Set-CSF method in JADIM (see Abadie et al., 2015, for details on the implementation).
Figure 4.18a shows the evolution of the maximum velocity inside de domain. It can be seen that the present formulation of the front-tracking method with reconstruction has an evolution that keeps reducing the velocity, while Level-Set-CSF seems to reach its minimum value at $U_{max} \sim 10^{-2}$. Similar tendency is obtained for the kinetic energy evolution ($E_k = \int \rho \boldsymbol{U} \cdot \boldsymbol{U} dV$), Level-Set-CSF reaches a minimum of $E_k \sim 10^{-8}$ while results for front-tracking keep falling (see figure 4.18b). Figures 4.18c and 4.18d show the maximum and average pressure jump, this time normalized using σ/r_{eq}, where r_{eq} is the radius of a droplet equivalent in area to the initial ellipse. Again we see that the present front-tacking implementation evolves to reproduced the correct pressure jump. The pressure jump in the Level-set method does not converge. In fact we found out that the droplet area starts increasing with time after oscillations have ceased ($t \sim 3$). At $t \sim 5$, Level-Set-CSF reported an increase of 25% in the droplet area while the error with the front tracking method was found to be less than 1%.

4.5 Benchmarking the method

This section is devoted to compare the present implementation to data found in the literature outside the scope of the spurious velocities analysis. The test selected is the 2d rising bubble that can be found in Hysing et al. (2009). This test allows us to evaluate relatively large interface motion and deformation to asses the robustness of the new local surface tension force calculation and reconstruction methods. An initially circular bubble of $R = 0.25$ is put into a box containing a denser fluid (see figure 4.19). No slip and symmetry

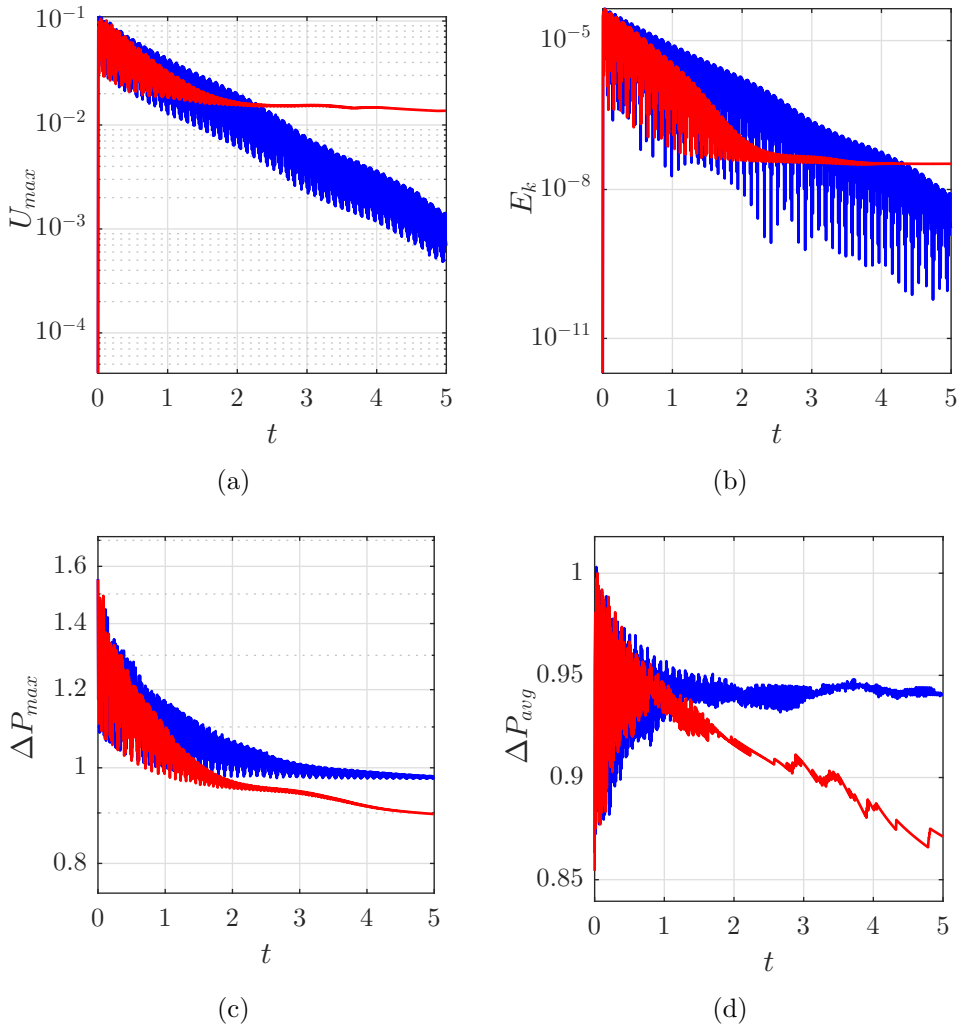

Figure 4.18: 2D oscillating droplet test using: — Front tracking (present); — Level-Set-CSF. (a) Maximum Velocity evolution. (b) Kinetic Energy evolution. (c) Maximum Pressure jump. (d) Average Pressure jump.

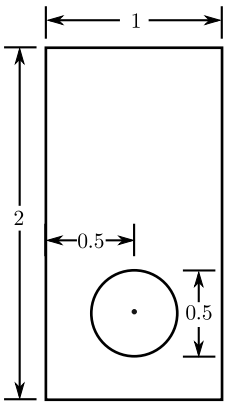

Figure 4.19: Initialization of the bubble rising test, according to Hysing et al. (2009).

Test	ρ_1/ρ_2	Γ	σ	g	Re	Eo
1	10	10	24.5	0.98	35	10
2	1000	100	1.96	0.98	35	125

Table 4.1: Rising bubble parameters

boundary conditions are applied on the two horizontal and the two vertical surfaces respectively. A constant gravity acceleration is imposed and properties for fluids are selected so two tests are analysed according to the table 4.1. Property ratios are given from the heavier to the lighter fluid. Γ stands for the viscosity ratio, σ for the surface tension. Governing numbers Reynolds and Eötvös are given by $Re = \rho_1\sqrt{g}(2R)^{3/2}/\mu$ and $Eo = 4\rho_1 g R^2/\sigma$. Four uniform grids are tested such that $\Delta x = 1/40, 1/80, 1/160$ and $1/320$ using time steps of $\Delta t = \Delta x/16$. According to Hysing et al. (2009), three groups participated in these tests: The group 1 (TU Dortmund, Inst. of Applied Math.) using a FEM-Level Set method code, the group 2 (EPFL Lausanne, Inst. of Analysis and Sci. Comp.) using a FEM-Level Set method code and the group 3 (Univ. Magdeburg, Inst. of Analysis and Num. Math.) using a FEM-ALE method code. For more details we refer the reader to Hysing et al. (2009). All test cases are initialized with a non-uniform distribution of markers (resulting from intersecting the bubble with the eulerian grid, taking care of the constrain $\Delta s/\Delta x > 0.2$). Bubble centroid position Y_c, Circularity

$\breve{c}$ and Rise velocity V_c are calculated as follows:

$$Y_c = \frac{\sum_{i,j} C_{ij} y_{ij} A_{ij}}{A_b} \tag{4.3}$$

$$\breve{c} = \frac{2\pi}{L}\sqrt{\frac{A_b}{\pi}} \tag{4.4}$$

$$V_c = \frac{\sum_{i,j} C_{ij} v_{ij} A_{ij}}{A_b} \tag{4.5}$$

In these equations, sub-index ij denote quantities at the centroid of the eulerian cell. A, A_b and L denote the cell area, total bubble area and the bubble perimeter. They are calculated as follows:

$$A_b = \sum_{ij} C_{ij} A_{ij} \tag{4.6}$$

$$L = \sum_{k} \Delta s_k \tag{4.7}$$

Three types of error will be used to compare results (see Hysing et al., 2009).

$$e_1 = \frac{\sum_t |q_{t,ref} - q_t|}{\sum_t |q_{t,ref}|} \tag{4.8}$$

$$e_2 = \left(\frac{\sum_t |q_{t,ref} - q_t|^2}{\sum_t |q_{t,ref}|^2} \right)^{1/2} \tag{4.9}$$

$$e_3 = \frac{max_t |q_{t,ref} - q_t|}{max_t |q_{t,ref}|} \tag{4.10}$$

where q_t is some quantity to be compared and $q_{t,ref}$ is the quantity of reference. If a grid tests is performed, the reference quantity is understood to be the one on the finest grid level. Benchmark quantities are given at `http://www.featflow.de/en/benchmarks/cfdbenchmarking/bubble.html`.

4.5.1 Results for Test 1

First we test the frequency at which the front reconstruction process is performed. We selected n_t to be 10, 50, 100 and 200 times steps using $\Delta x = 1/40$. Results are shown in figure 4.20. Bubble shape, circularity, centroid position and rise velocity seem to converge independently of n_t. A zoom on the final time steps in figures 4.20b and 4.20d show some perturbations caused by the reconstruction process, but in all cases the general trend is not broken (see figures 4.21a and 4.21b).

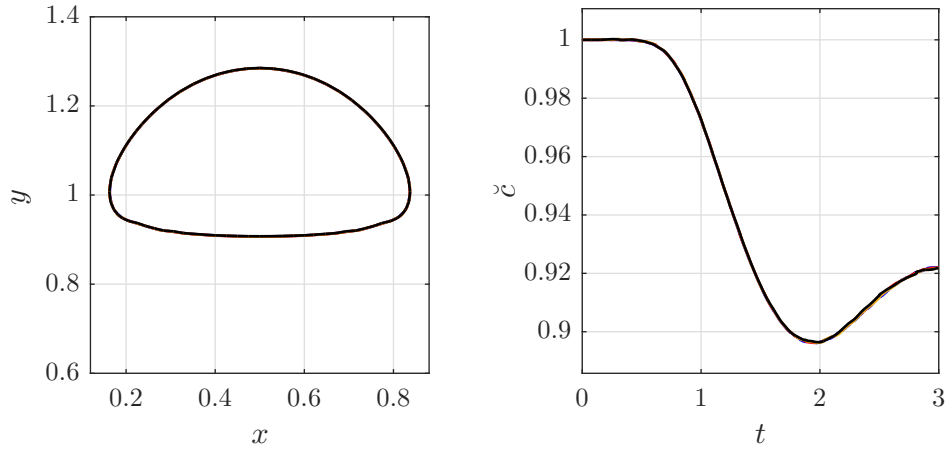

(a) Bubble shape

(b) Circularity

(c) Centroid position

(d) Rise velocity

Figure 4.20: Numerical simulation of a 2D rising bubble in stagnant fluid, Test 1 table 4.1. Frequency of front reconstruction in time steps: —, $n_t = 10$; —, $n_t = 50$; —, $n_t = 100$; —, $n_t = 200$.

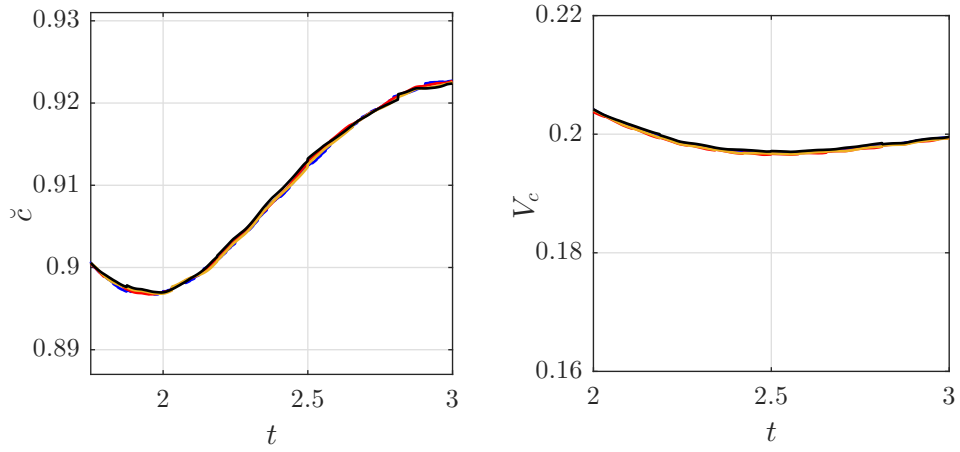

(a) Circularity (b) Rise velocity

Figure 4.21: Zoom performed in figures 4.20b and 4.20d. Frequency of front reconstruction in time steps: —, $n_t = 10$; —, $n_t = 50$; —, $n_t = 100$; —, $n_t = 200$.

Table 4.2 summarizes the errors obtained for each case, taking the same grid level data as a reference. No significant difference among the frequencies of reconstruction can be observed and no frequency gives the smallest error in every quantity evaluated. For the next tests we have chosen an intermediate frequency of reconstruction $n_t = 100$, so economy of computations can be achieve and also, we reduce the possibility of having Δs to large or to small according to the considerations described in the previous section. The process of front reconstruction can be also triggered by measuring at each time step the minimum and maximum front element size and acting accordingly. In this work however, we consider this expensive and prefer to prescribe a fixed frequency of reconstruction. Results are shown in figure 4.22. This time the solution of reference is at the finest grid. We can see convergence to the reference given in green. In fact, according to figure 4.22a, the bottom of the bubble seems to have been left behind in the case of $\Delta x = 1/40$, this however affected little the position of the bubble centroid (see figure 4.22c). Circularity seems to be the most affected variable by the coarsest grid. In figure 4.22b, at $t = 2$, $\Delta x = 1/40$ reaches its minimum $\breve{c} = 0.897$ while the reference indicates $\breve{c} = 0.901$. Contrary to this, rise velocity reports that $\Delta x = 1/40$ experiences a slight acceleration at $t = 1$ which will result in a slight larger value of V_c at the end of the simulation ($V_c = 0.199$ for a reference value of $V_c = 0.193$).

To conclude this first test, results of $\Delta x = 1/320$ are compared to its ref-

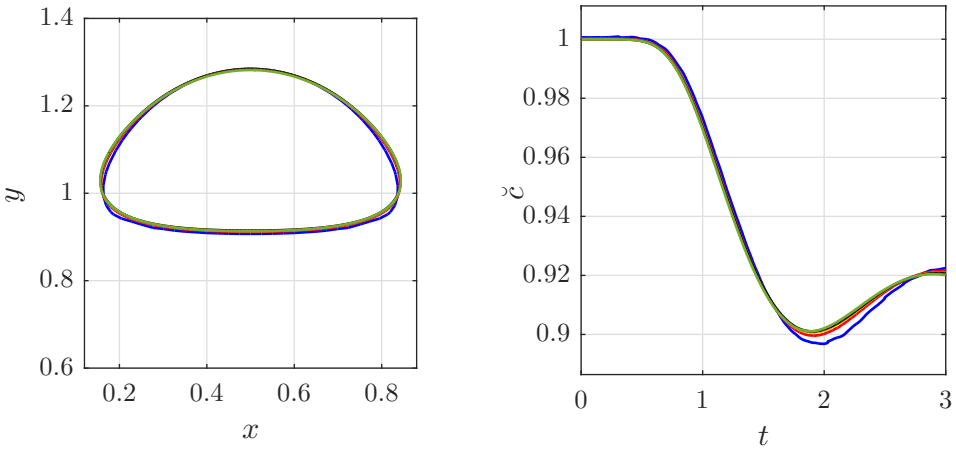

(a) Bubble shape

(b) Circularity

(c) Centroid Position

(d) Rise velocity

Figure 4.22: Evolution of a 2D rising bubble in stagnant fluid, Test 1 table 4.1, for Δx: —, 1/40; —, 1/80; —, 1/160; —, 1/320; —, Ref. 1/320.

n_t	e_1	e_2	e_3
Circularity			
10	2.80e-03	3.28e-03	6.07e-03
50	2.76e-03	3.23e-03	6.01e-03
100	2.81e-03	3.28e-03	6.18e-03
200	2.68e-03	3.11e-03	5.84e-03
Centroid position			
10	2.41e-03	3.37e-03	5.69e-03
50	2.53e-03	3.52e-03	5.96e-03
100	2.46e-03	3.43e-03	5.79e-03
200	2.38e-03	3.28e-03	5.46e-03
Rise velocity			
10	1.30e-02	1.47e-02	2.19e-02
50	1.23e-02	1.40e-02	2.17e-02
100	1.26e-02	1.43e-02	2.15e-02
200	1.34e-02	1.49e-02	2.17e-02

Table 4.2: Test for reconstruction frequency using $\Delta = 1/40$.

	e_1	e_2	e_3
Circularity	9.75e-05	1.22e-04	2.62e-04
Centroid position	8.69e-05	1.35e-04	2.58e-04
Rise velocity	1.90e-03	2.10e-03	2.75e-03

Table 4.3: Comparison of $\Delta x = 1/320$ against reference data for Test1.

erence equivalent in table 4.3. The maximum error is 2.75×10^{-3} for rise velocity.

4.5.2 Results for Test 2

Our new implementation is now evaluated in the Test 2 of table 4.1, with a frequency of reconstruction set at $n_t = 100$. As was the case of the group 3 in Hysing et al. (2009), where a FEM-ALE code was used, our implementation could not handle break-up automatically, instead, the simulation kept stretching the bubble skirt. Although we could not reproduce the break up feature, our implementation showed that the bulk of the bubble shape is in good agreement with groups of the reference data (see figure 4.23). Quantities such as Circularity, Centroid Position and Rise velocity are reported in

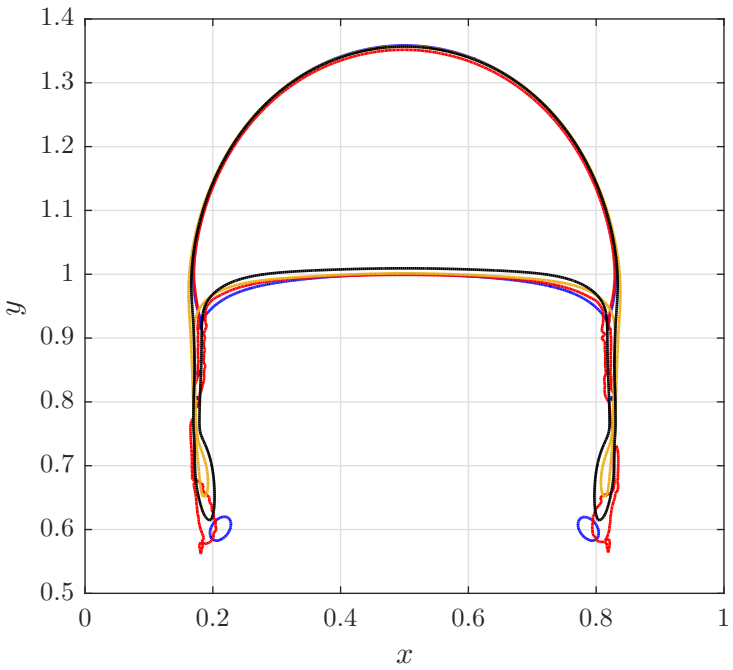

Figure 4.23: Rising Bubble, Test 2, table 4.1 at $t = 3$. Comparison with groups: —, 1; —, 2; —, 3; —, present.

	e_1	e_2	e_3
Circularity	3.75e-02	8.44e-02	2.16e-01
Centroid position	2.53e-03	4.15e-03	9.16e-03
Rise velocity	3.29e-02	3.88e-02	6.37e-02

Table 4.4: Comparison of $\Delta x = 1/130$ against reference data for Test2.

figure 4.24. Remarkably, circularity evolution for the present implementation is nearly identical to that of group 1 (up to $t \sim 2.3$), from there, the circularity will be affected by the shape of the small bubble in the interface that has undergone a break-up (see figure 4.24a). The Centroid position shown in figure 4.24b is virtually independent of the break up process. Rise velocity is the most affected quantity for all groups and the present implementation. It can be said in general that it follows the same trend (see figure 4.24c). The norm error of our implementation is now compared to that of group 1 and reported in table 4.4. Confirming what figure 4.24, the largest norm errors are obtained for Circularity.

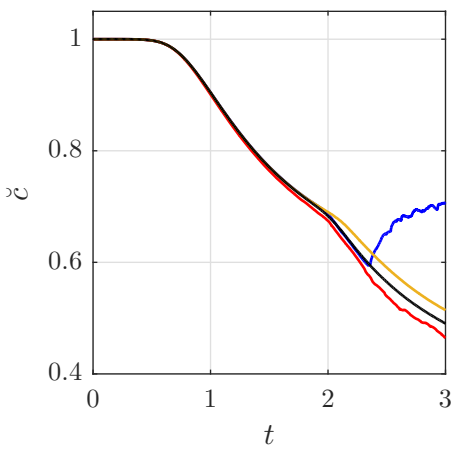

(a) Circularity

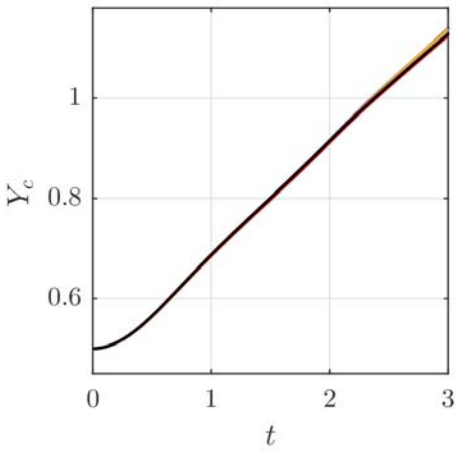

(b) Centroid Position

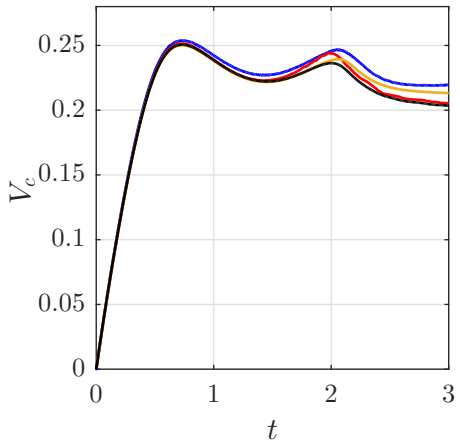

(c) Rise velocity

Figure 4.24: Evolution of a 2D rising bubble, Test 2, table 4.1, in stagnant fluid for $\Delta x = 1/320$. Comparison of: —, Group 1; —, Group 2; —, Group 3; —, Present.

4.6 Validation in wetting cases

In this section we assess the ability of the front-tracking method with lagrangian markers in cases where a moving contact line is found. In principle, we need to addressed on how to tread velocity advection of markers close to a solid wall.

4.6.1 Advection of markers close to the wall

The discrete form of the integral property of the Dirac function is:

$$\sum_{ij} D_{i,j} = 1 \tag{4.11}$$

This property is true if the marker in question is away from any solid wall, or better said, whenever is surrounded completely by eulerian cells containing fluids. For markers that are close to solid boundaries, a value of $\sum_{ij} D_{i,j} < 1$ is expected. The immediate effect of this value is that markers close to walls will move slower than those away from it. Physically this is a natural effect, since close to a wall we expect slower velocities. In the simulation of contact lines (with the front-tracking method), this would mean however, that a marker in contact to the wall should remain static, though in the practice, because of the influence of the velocity away from the wall, the marker will move but at a unacceptable low rhythm. Methods like VOF-FCT-CSF and LevelSet-CSF are not affected by this, since there is no interpolation of velocity to the interface, but rather a direct advection by conservation means. We dramatize this effect with a small numerical experiment. A 2D viscous drop spreading on a wall is set up in a square solid domain with a radius of $R_0 = 0.25$ and fluid properties set up as $\rho_1 = \rho_2 = 1$, $\mu_1 = \mu_2 = 0.25$ and $\sigma = 7.5$ according to Afkhami et al. (2009). The initial configuration forms an initial contact angle of 90° with the wall and a constant static contact angle of 60° is prescribed. A 32×32 grid is used and VOF-FCT-CSF is compared against the current front-tracking implementation in JADIM. Results for selected time steps ($\tau = t\mu/\rho R_0^2$) are given in figure 4.25, where the black curve represent the fluid interface for VOF-FCT-CSF (0.5 contour of VOF function) and the red line with triangular symbols represent the interface found with the front-tracking method. As can be seen in the sequence of figures 4.25a to 4.25d, markers close to the wall move slower with respect to the VOF-FCT-CSF method, being the slowest the marker at the wall. This produces an interface strongly curved at the wall and will affect negatively the kinematics of the bubble, we see that already at $\tau = 0.4$ (figure 4.25d) the contact line of the front-tracking method has been left behind around one

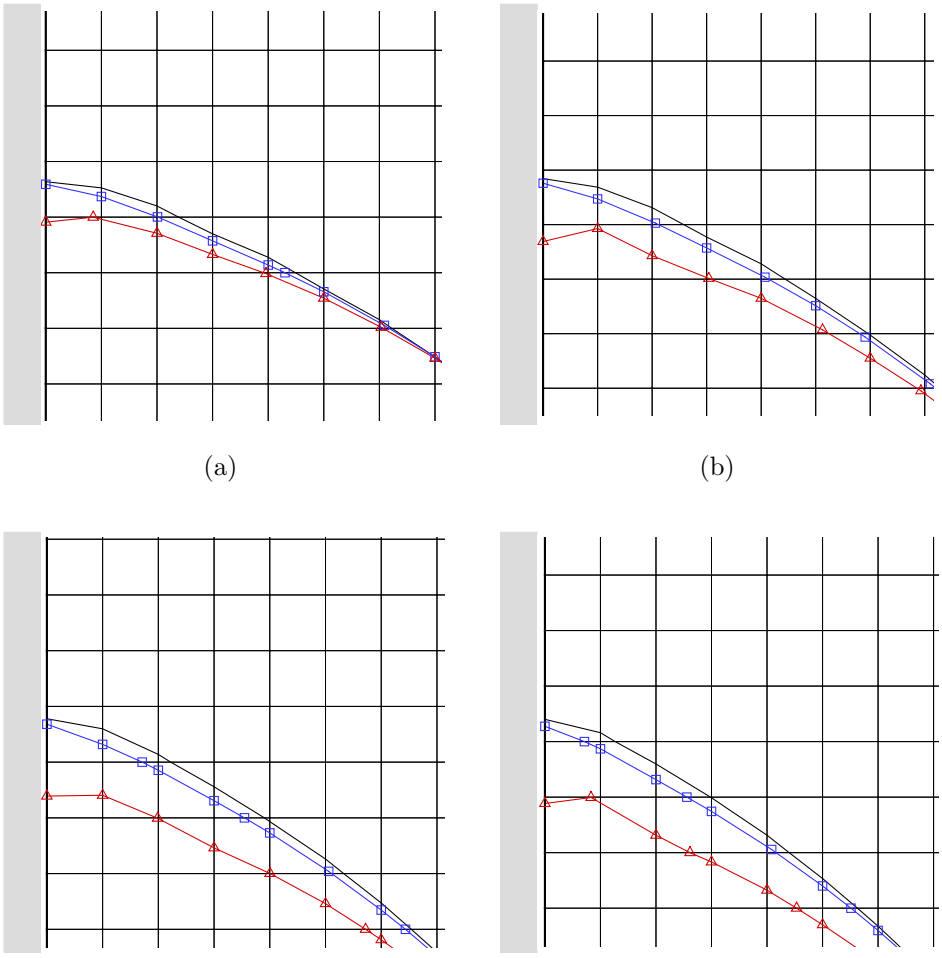

(a) (b)

(c) (d)

Figure 4.25: Hemispherical 2D viscous drop spreading, comparing: —— VOF-FCT-CSF; —△— Front-tracking no treatment at contact line; —□— Front-tracking special treatment at contact line at: a) $\tau = 0.1$; b) $\tau = 0.2$; c) $\tau = 0.3$ and d) $\tau = 0.4$.

and half computational cell. Eventually of course, when $\tau \to \infty$, both interfaces for the methods will converge because the static angle will be reached, but the transition to this state is significantly affected. Uzgoren et al. (2009) proposed a solution for this advection issue: since $\sum_{ij} D_{i,j} = 1$ is expected, then the advection of markers must be made according to:

$$\boldsymbol{U}_k = \frac{\sum_{ij} \boldsymbol{U}_{ij} D_{ij}}{\sum_{ij} D_{i,j}} \tag{4.12}$$

Using 4.12 does not affect markers away from the wall, since $\sum_{ij} D_{i,j} = 1$, but it corrects the summation to 1 for markers close to it. The results of this correction are shown in figure 4.25 with a blue line and square symbols representing the markers. It can be seen that this new interface follows correctly the one obtained with VOF-FCT-CSF allowing a smooth configuration close to the wall. The evolution of the contact line position $\tilde{r} = r/R_0$ is reported in figure 4.26. VOF-FCT-CSF (in black) and the front-tracking with special advection at the wall (equation 4.12), in black, evolve similarly and reach the static theoretical configuration (see equation 4.13) $\tilde{L} = 1.385$ at $\tau \approx 3$, giving a percent error of 0.8% and 0.1% respectively. The small difference between the final position between VOF-FCT-CSF and front-tracking is due to the way in which it is post processed. In the case of the front-tracking, the position is given by the marker at the wall, while in VOF-FCT-CSF, the volume fraction contour of 0.5 is used as a reference. The front-tracking without any treatment (red line) shows a slower evolution and at $\tau = 4$ has not yet reached the final configuration but it is towards to it. It is important to make clear that the special procedure to advect markers close to the wall in no way imposes the contact angle, only provides enough relaxation to the velocity of the markers close to a wall. The angle is imposed in this part by equation 3.19. After solving the issue of marker advection close to the wall, we present tests destined to assess the ability of the implementation to reproduce the shape and pressure jump of a drop spreading at equilibrium and compare it with analytical solutions if available. Specifically we will use the tests reported in Dupont and Legendre (2010).

4.6.2 Drop spreading to a equilibrium state

First we conduct the test in the absence of gravitational effects. The test is a viscous drop with properties $\rho_l = 1$, $\rho_g = 0.1$, $\mu_l = 0.25$, $\mu_g = 0.00025$ and $\sigma = 7.5$. The drop of initial radius $R_0 = 0.5$ is initially in contact with the wall forming 90° (see figure 4.27 a)). Ten static contact angles are tested ranging from 10° to 170° in steps of 20°. Only one half of the drop is simulated in a computational domain of uniform 160×120 cells that corresponds

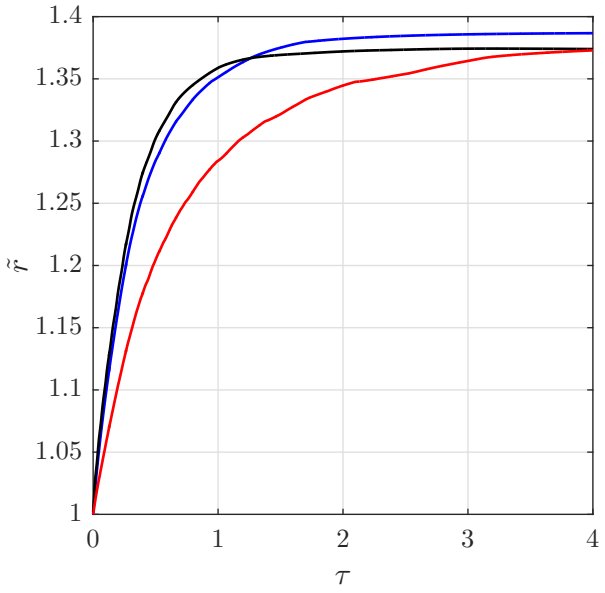

Figure 4.26: Contact line evolution for a 2D drop following Afkhami et al. (2009), using the the static contact angle model and the noslip boundary condition. — Front-tracking using equation 4.12; — Front-tracking using standard markers advection (equation 3.24); — VOF-FCT-CSF (the line corresponds to the 0.5 volume fraction contour)

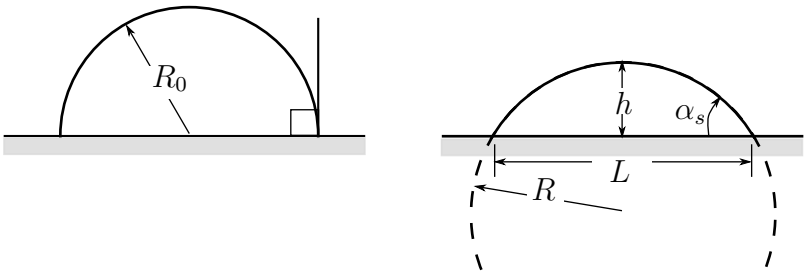

(a) (b)

Figure 4.27: a) Initialization of a viscous drop released at a wall; b) Final configuration parameters in the absence fo gravity

to $R_0/\Delta x = 40$. We define $\tilde{L}$ and $\tilde{h}$ to be half the length of the bubble projection on the horizontal wall and the height of the drop respectively, both normalized by R_0. We denominate ΔP to the Laplace pressure jump. Numerically we define ΔP_{max} and ΔP_{avg} as the maximum pressure jump (the difference between the maximum and the minimum pressure in the whole domain) and the average pressure jump (the difference between the average pressure inside and outside the drop), both normalized by σ/R_0. In the absence of gravity and at equilibrium, $\tilde{L}$, $\tilde{h}$ and ΔP are given analytically by (Dupont and Legendre, 2010):

$$\tilde{L} = \frac{R}{R_0}\sin\alpha_s \tag{4.13}$$

$$\tilde{h} = \frac{R}{R_0}(1-\cos\alpha_s) \tag{4.14}$$

$$\Delta P = \sigma/R \tag{4.15}$$

where R is the radius of the circle defining the interface at equilibrium:

$$R = R_0\sqrt{\frac{\pi}{2(\alpha_s - \sin\alpha_s\cos\alpha_s)}} \tag{4.16}$$

The interface is set to be reconstructed at each 100 time steps.
Results for the equilibrium $\tilde{h}$ and $\tilde{L}$ are shown in figure 4.28. It can be seen in figure 4.28a, that with exception of static angles close to 0° and 180°, the agreement obtained is remarkable in both $\tilde{h}$ and $\tilde{L}$. Similar agreement is obtained when comparing both numerical pressure jumps against its analytical value, with exception of angles 150° and 170°. Next we test the influence of a gravitational field on the shape obtained by the solver for two static angles, $\alpha_s = 50°$ and $\alpha_s = 130°$. Using again the initialization of figure 4.27(a) and fluid properties of the last test, a gravity acceleration is imposed such to produce an Eötvös number ($Eo = \rho_l R_0^2 g/\sigma$) ranging between 0.001 and 50. For low Eötvös numbers ($Eo \ll 1$), the non-dimensional analytical height can be used as a reference (equation 4.14), however, when $Eo \gg 1$, height of the drop is proportional to the capillary length:

$$\tilde{e} = \frac{2}{\tilde{h}R_0}\sqrt{\frac{\sigma}{\rho_l g}}\sin\left(\frac{\alpha_s}{2}\right) \tag{4.17}$$

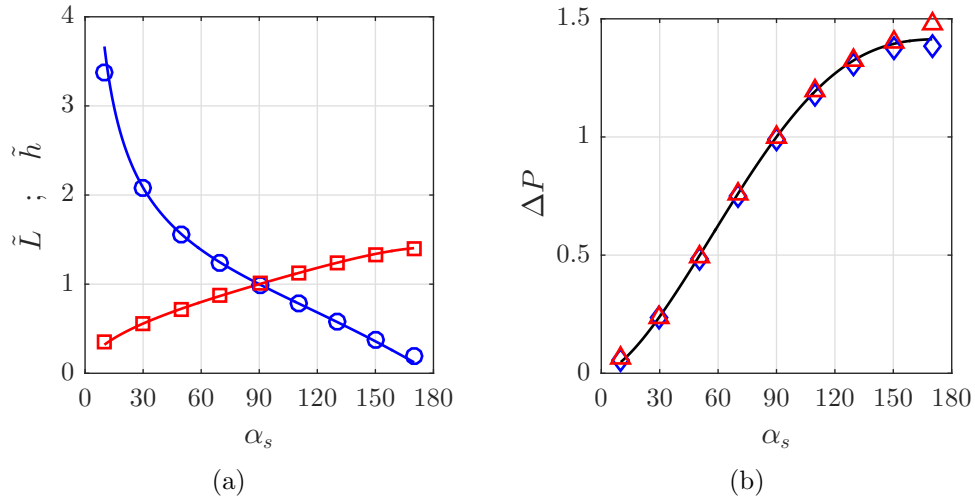

Figure 4.28: $\tilde{h}$, $\tilde{L}$ and ΔP for a Drop at equilibrium with $\rho_l = 1$, $\rho_g = 0.1$, $\mu_l = 0.25$, $\mu_g = 0.00025$, $\sigma = 7.5$ and $R_0 = 0.5$. a) Normalized drop length and height at equilibrium: — Analytical $\tilde{L}$, equation 4.13; ○ Numerical $\tilde{L}$; — Analytical $\tilde{h}$, equation 4.14; □ Numerical $\tilde{h}$. b) Normalized pressure jump: — Analytical ΔP, equation 4.15; ◇ Numerical ΔP_{avg}; △ Numerical ΔP_{max}.

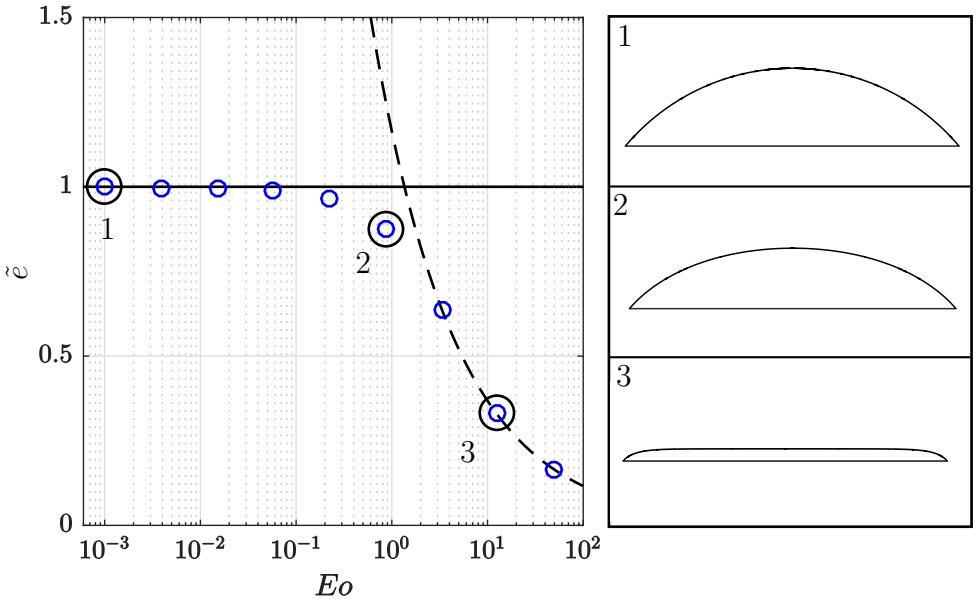

Figure 4.29: Normalized drop height under the influence of gravity for a static contact angle of $\alpha_s = 50°$ as a function of Eötvös number. — Equation 4.14; - - - Equation 4.17; ○ Numerical simulation. On the right panel: drop interface for selected Eötvös numbers. 1: $Eo = 0.001$; 2: $Eo = 0.865$; 3: $Eo = 13$.

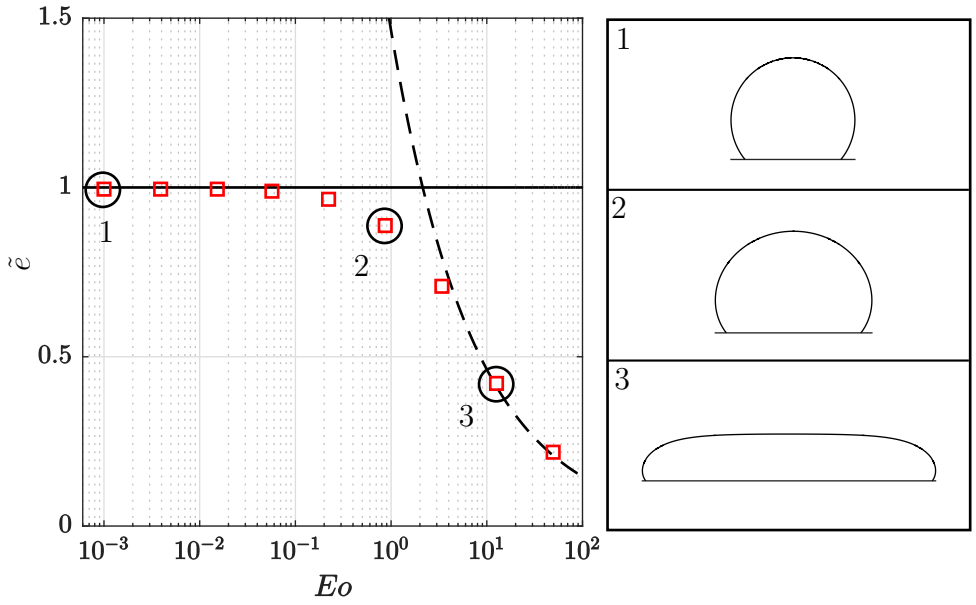

Figure 4.30: Normalized drop height under the influence of gravity for a static contact angle of $\alpha_s = 130°$ as a function of Eötvös number. —— Equation 4.14; - - - Equation 4.17; ▫ Numerical simulation. On the right panel: drop interface for selected Eötvös numbers. 1: $Eo = 0.001$; 2: $Eo = 0.865$; 3: $Eo = 13$.

Results are shown in figures 4.29 and 4.30. For both the angles tested, results are remarkably good when compared to the analytical descriptions in equations 4.14 shown in a solid black lines and 4.17 shown in a dashed black line. The right panel in figures 4.29 and 4.30 contains the actual non-scaled interface configuration at equilibrium for selected Eötvös numbers.

Normalized drop thickness $\tilde{e}$ for $Eo < 0.2$ follow almost exactly the circular cap exact solution for both contact angles. Above $Eo \approx 0.2$ drop thickness departs from the circular cap configuration to become flatter, reaching the shape shown in the right panel of figure 4.29, item number 3 for $Eo \approx 10$ and $\alpha_s = 50°$. Similarly, Eötvös number ($Eo \approx 0.2$) mark the transition between a circular cap configuration to a flattened drop for $\alpha_s = 130°$. In the right panel of figure 4.30, item 3, it is reported the final shape configuration of the drop for $Eo \approx 10$. As expected, $\tilde{e}$ for $Eo \approx 10$ and $\alpha_s = 130°$ is larger than that for $\alpha_s = 50°$ (0.4236 to 0.3329) because $\alpha_s = 130°$ works against gravity while $\alpha_s = 50°$ works in favor of it.

4.7 Summary

In this chapter we have reconsider the calculation of tangents at markers position, using the "classical" local force from tangents difference proposed in Unverdi and Tryggvason (1992); Juric and Tryggvason (1998); Agresar et al. (1998); Tryggvason et al. (2001); Popinet and Zaleski (1999); Yamamoto and Uemura (2008); Yamamoto et al. (2013, 2014) and we have calculated tangents with a new, simple, yet powerful element length average. This reconsideration forced the length Δs of the neighbors elements to intervene in $\boldsymbol{t}$, otherwise, local surface tension force $\boldsymbol{f}$ becomes "deaf" to front non-uniformity. It was demonstrated that this reconsideration recovers the capacity of the hybrid formulation Shin et al. (2005) for surface tension force to reduce spurious currents to a level comparable to that of a uniform marker distribution, close to machine precision in all the cases analyzed. The new implementation was tested against a static and a translating bubble for diverse La and Ca numbers showing remarkable results. It was noticed however, that in general, only velocity is affected by the new implementation, pressure jump is invariably well predicted, showing always errors below 1%.
Furthermore, test on the time step Δt was performed, achieving convergence in the case of the static bubble with better results for $RK3$ advection. When analyzing spurious velocities at order of magnitude close to machine precision as in this work, no convergence with Δt could be achieved for the translating bubble case. In fact, further reduction of Δt brought the growth of spurious velocities above those obtained using large Δt for both the high order time marker advection scheme ($RK3$) and the first order (FO). This is due to the accumulation of perturbations in the velocity field by the spurious velocities and of course, the complex coupling between curvature calculation and interface advection given in the translating bubble. For this test, FO performed slightly better than $RK3$.
This new approach to calculate tangents allowed us also to propose a new reconstruction scheme by which the front can be redistributed/reconstructed automatically at prescribed time intervals. This reconstruction scheme is based on circles whose radii are taken from curvature information in the front and then are intersected with the eulerian grid faces. The precision and stability of this reconstruction was tested and it was shown that the interval $0.2 < \Delta s/\Delta x \leq 1$ provides the most accurate reconstruction given a known geometry and also provides stability in the spurious velocity reduction for both static and translating bubble cases. Also, the new reconstruction scheme was tested for a large La number, obtaining better results than those for the Level-Set-CSF method.
Finally, this new implementation was tested against the benchmark results in

Hysing et al. (2009) for a rising 2D bubble. For a moderate interface deformation (Test 1 in table 4.1), the results showed independence to the frequency of reconstruction and small errors compared to the reference values. For Test 2, where large deformations and break up were present, the performance of the current implementation was comparable to those of the benchmark, specifically to the group 3 which was not prepare to handle break up as it is in our current implementation. Nevertheless, the quantities measured showed the same tendency as for the other groups. Also, the bubble shape for this second test was remarkably in good agreement with the benchmark data.
In cases involving wetting we have seen the power of the front-tracking method to reproduce the shape and pressure jump features of a drop spreading to a equilibrium state with and without the effects of a gravitational field after correcting the advection of markers close to a wall. Results were compared to the theoretical and analytical solutions for spherical caps and thickness of a drop under the influence of gravity.
For the spherical cap, results were always in good agreement with the theoretical height and length of the drop for static contact angles in the range of $10^\circ < \alpha < 170^\circ$. For $\alpha = 10^\circ$ and $\alpha = 170^\circ$, the results were acceptable. It is not clear why the shape is not correct anymore close to 0° and 180°. The same trend was experienced for the pressure jump, although the explanation for this variable could be that calculating it during Navier-Stokes solutions inside *JADIM* and post-processing it might be affected by the confinement of one or the other phase at angles close to 0° and 180° to the wall. Anyhow, we consider that results have improved compared to those obtained with VOF-FCT-CSF (see for example Dupont and Legendre, 2010, for the same tests). Further calculations and comparison with experimental data will be given in chapter 8.

Chapter 5

Some contact line situations in the context of corner Stokes Flow

In this chapter we explore some situations in which a contact line can be regarded in the context of corner Stokes flow. First we take a look into two boundary conditions at the wall, i.e. the no slip, and the navier-slip which will later be used as key ingredients to explore the existence of Moffatt vortices in the vicinity of the contact line in chapter 6 and for the development of a new subgrid model in the context of the front-tracking method in chapter 8. Finally we explore an original situation where the contact line is pinned on a moving wall, resulting in the variation of the angle of the interface with the wall.

5.1 Background

When approaching to the contact line formed by the interface of two fluids over a horizontal solid surface, it is possible to consider a corner flow configuration (see Figure 5.1). Considering a bidimensional flow and choosing cylindrical coordinates whose origin moves with the contact line itself, it is possible to invoke the creeping flow approximation given that as we approach the contact line $r \to 0$ then $Re \to 0$:

$$\mu_A \nabla^2 \mathbf{u}_A - \nabla p_A = 0 \tag{5.1}$$

$$\mu_B \nabla^2 \mathbf{u}_B - \nabla p_B = 0 \tag{5.2}$$

$$\nabla \cdot \mathbf{u}_A = 0 \tag{5.3}$$

$$\nabla \cdot \mathbf{u}_B = 0 \tag{5.4}$$

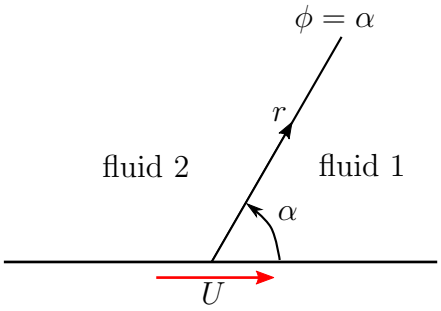

Figure 5.1: Moving contact Line sketch in the reference frame attached to it.

Taking the curl on equations 5.1 and 5.2 and replacing the velocity vector by its Lagrange's stream function equivalent (equation 5.5), the continuity equations 5.3 and 5.4 are automatically satisfied and equations 5.1 and 5.2 are reduce to the biharmonic equation (see equation 5.6).

$$u_k = \frac{1}{r}\frac{\partial \psi_k}{\partial \phi} \qquad v_k = -\frac{\partial \psi_k}{\partial r} \tag{5.5}$$

$$\nabla^4 \psi_k = 0 \tag{5.6}$$

Equation 5.6 admits separable solutions of the form:

$$\psi_k = r^{n+1} U / L^n f_k(n, \phi) \tag{5.7}$$

Choosing a convenient adimensionalization:

$$\tilde{r} = \frac{r}{L} \quad ; \quad \tilde{\psi_k} = \frac{\psi_k}{UL} \quad ; \quad \tilde{u} = \frac{u}{U} \quad ; \quad \tilde{v} = \frac{v}{U} \quad ; \quad \tilde{\tau} = \frac{\tau L}{\mu_1 U}$$
$$\tilde{p} = \frac{pL}{\mu_1 U} \tag{5.8}$$

and dropping the "tilde" notation, the stream function becomes:

$$\psi_k = r^{n+1} f_k(n, \phi) \tag{5.9}$$

where n is any number, real or complex, U is the velocity of the contact line, μ_1 is the dynamic viscosity of fluid 1, τ is the shear stress, L is a characteristic length of the flow (i.e. the radius of a drop in the case of a drop spreading) and k is 1 or 2 referring to the fluids 1 or 2 in figure 5.1. The function $f_k(n, \phi)$, is given by (Anderson and Davis, 1993):

$$\begin{aligned} f_k(n, \phi) = {} & A_k \cos\left[(n+1)\phi\right] + B_k \sin\left[(n+1)\phi\right] \\ & + C_k \cos\left[(n-1)\phi\right] + D_k \sin\left[(n-1)\phi\right] \end{aligned} \tag{5.10}$$

where A_k, B_k, C_k and D_k are constants to be determined by the appropriate boundary conditions. For the particular cases when $n = 0$ and 1, equation 5.10 takes the degenerate forms (Anderson and Davis, 1993):

$$f_k(0,\phi) = A_k \cos\phi + B_k \sin\phi + C_k\phi\cos\phi + D_k\phi\sin\phi \tag{5.11}$$

$$f_k(1,\phi) = A_k \cos(2\phi) + B_k \sin(2\phi) + C_k\phi + D_k \tag{5.12}$$

When assuming a flat interface a "partial local analysis" can be conducted considering that the flow matches with the outer flow at a large distance from the corner (typically, the bulk recirculation for a sliding drop). Partial local solutions describe situations in which all the local boundary conditions are satisfied with the exception of the normal-stress condition (see Moffatt, 1964; Anderson and Davis, 1993; Shtern, 2014). In practice, this assumption is valid for an interface in the limit of zero capillary number.
At this point is also useful to express shear, pressure and normal stress as a function of the stream function. Shear is given by:

$$\tau_1 = \left(\frac{1}{r^2}\frac{\partial^2\psi_1}{\partial\phi_1^2} - \frac{\partial^2\psi_1}{\partial r^2} + \frac{1}{r}\frac{\partial\psi_1}{\partial r}\right) \tag{5.13}$$

$$\tau_2 = \Gamma\left(\frac{1}{r^2}\frac{\partial^2\psi_2}{\partial\phi_2^2} - \frac{\partial^2\psi_2}{\partial r^2} + \frac{1}{r}\frac{\partial\psi_2}{\partial r}\right) \tag{5.14}$$

the pressure writes:

$$\frac{\partial p_1}{\partial r} = \Delta u_1 - \frac{u_1}{r^2} - \frac{2}{r^2}\frac{\partial v_1}{\partial\phi} \;\; ; \;\; \frac{1}{r}\frac{\partial p_1}{\partial\phi} = \Delta v_1 - \frac{v_1}{r^2} + \frac{2}{r^2}\frac{\partial u_1}{\partial\phi} \tag{5.15}$$

$$\frac{\partial p_2}{\partial r} = \Gamma\left(\Delta u_2 - \frac{u_2}{r^2} - \frac{2}{r^2}\frac{\partial v_2}{\partial\phi}\right) \;\; ; \;\; \frac{1}{r}\frac{\partial p_2}{\partial\phi} = \Gamma\left(\Delta v_2 - \frac{v_2}{r^2} + \frac{2}{r^2}\frac{\partial u_2}{\partial\phi}\right) \tag{5.16}$$

and the normal stress is:

$$\boldsymbol{\sigma}_1 = -p_1 + \frac{2}{r}\left(\frac{1}{r}\frac{\partial\psi_1}{\partial\phi} - \frac{\partial^2\psi_1}{\partial r\partial\phi}\right) \quad ; \quad \boldsymbol{\sigma}_2 = -p_2 + \frac{2\Gamma}{r}\left(\frac{1}{r}\frac{\partial\psi_2}{\partial\phi} - \frac{\partial^2\psi_2}{\partial r\partial\phi}\right) \tag{5.17}$$

where Γ is the viscosity ratio μ_2/μ_1 and the operator Δ is given by:

$$\Delta = \frac{\partial^2}{\partial r^2} + \frac{1}{r}\frac{\partial}{\partial r} + \frac{1}{r^2}\frac{\partial^2}{\partial\phi^2} \tag{5.18}$$

5.2 The no-slip boundary condition for a moving contact line.

Considering a clean and impermeable wall and no interchange of mass at the fluid interface, the boundary conditions for the problem depicted in figure

5.1 are given as follows. At the wall, no-slip and no-penetration boundary conditions:

$$\text{At} \quad \phi = 0 \quad \rightarrow \quad u_1 = U \quad ; \quad v_1 = 0 \tag{5.19}$$
$$\text{At} \quad \phi = \pi \quad \rightarrow \quad u_2 = -U \quad ; \quad v_2 = 0 \tag{5.20}$$

At the fluid interface ($\phi = \alpha$), continuity of tangent velocity to the interface, no penetration and shear stress equilibrium:

$$u_1 = u_2 \tag{5.21}$$
$$v_1 = v_2 = 0 \tag{5.22}$$
$$\tau_1 = \tau_2 \tag{5.23}$$

Substitution of equations 5.5 and 5.9 yields at the wall:

$$r^n \, f_1'|_{\phi=0} = 1 \quad ; \quad -(n+1) r^n f_1|_{\phi=0} = 0 \tag{5.24}$$
$$r^n \, f_2'|_{\phi=\pi} = -1 \quad ; \quad -(n+1) r^n f_2|_{\phi=0} = 0 \tag{5.25}$$

which can only be satisfied if $n = 0$. Then f is given by equation 5.11. Substitution of n leaves:

$$f_1'|_{\phi=0} = 1 \quad ; \quad f_1|_{\phi=0} = 0 \tag{5.26}$$
$$f_2'|_{\phi=\pi} = -1 \quad ; \quad f_2|_{\phi=0} = 0 \tag{5.27}$$

And at the fluid interface: conditions 5.21-5.23 become

$$f_1'|_{\phi=\alpha} = f_2'|_{\phi=\alpha} \tag{5.28}$$
$$f_1|_{\phi=\alpha} = 0 \tag{5.29}$$
$$f_2|_{\phi=\alpha} = 0 \tag{5.30}$$
$$f_1''|_{\phi=\alpha} = \Gamma \, f_2''|_{\phi=\alpha} \tag{5.31}$$

where f_k' and f_k'' stand for the first and second derivatives of f_k with respect to ϕ. The system of equations 5.26 to 5.31 can be solved by regular means

yielding the next set of constants:

$$A_1 = 0 \tag{5.32}$$

$$B_1 = \frac{\alpha\Gamma\left(\sin\alpha(\sin\alpha + \pi\cos\alpha) - \alpha(\alpha-\pi)\right) + (\alpha-\pi)^2 - \sin(\alpha)^2}{\Upsilon} \tag{5.33}$$

$$C_1 = \frac{\begin{array}{r}\Gamma(\sin\alpha\cos\alpha(\alpha(\alpha-\pi) - \sin^2\alpha) - \pi\sin^2\alpha) \\ +\sin\alpha\cos\alpha(\sin^2\alpha - (\alpha-\pi)^2)\end{array}}{\Upsilon} \tag{5.34}$$

$$D_1 = \frac{\sin^2(\alpha)((\alpha(\alpha-\pi) - \sin^2(\alpha))\Gamma - (\alpha-\pi)^2 - \sin^2(\alpha))}{\Upsilon} \tag{5.35}$$

$$A_2 = \frac{\begin{array}{r}-\pi\sin\alpha\left(\Gamma\cos\alpha(\alpha^2 - \sin^2\alpha) - \pi\sin\alpha\right. \\ \left.-\cos\alpha(\sin^2\alpha + \alpha(\pi-\alpha))\right)\end{array}}{\Upsilon} \tag{5.36}$$

$$B_2 = \frac{\begin{array}{r}((\alpha-\pi)(\sin\alpha(\pi(cos\alpha + \alpha\sin\alpha) - \sin\alpha) + \alpha(\alpha-\pi)) \\ -((\alpha-\pi) + \pi\sin^2\alpha)(\alpha^2 - \sin^2\alpha)\Gamma - \pi\sin^4\alpha\big)\end{array}}{\Upsilon} \tag{5.37}$$

$$C_2 = \frac{\begin{array}{r}\sin\alpha\left(\cos\alpha(\alpha^2 - \sin^2\alpha)\Gamma\right. \\ \left.+\cos\alpha(\alpha(\pi-\alpha) + \sin^2\alpha) - \pi\sin\alpha\right)\end{array}}{\Upsilon} \tag{5.38}$$

$$D_2 = \frac{-(\sin^2\alpha(\sin^2\alpha - \alpha^2))\Gamma + \sin^2\alpha(\alpha(\pi-\alpha) + \sin^2\alpha)}{\Upsilon} \tag{5.39}$$

with:

$$\begin{aligned}\Upsilon = {} & \Gamma(\alpha^2 - \sin\alpha^2)(\pi - \alpha + \cos\alpha\sin\alpha) \\ & +(\alpha - \cos\alpha\sin\alpha)((\alpha-\pi)^2 - \sin\alpha^2)\end{aligned} \tag{5.40}$$

It is immediately evident that substitution of $n = 0$ into equation 5.5 leaves the velocity field as:

$$u_k = f_k' \quad ; \quad v_k = -f_k \tag{5.41}$$

which is independent of r. This means that the velocity field at $r = 0$ has multiple values. This is known as the "multivaluedness" of the velocity field (see Dussan V. and Davis, 1974). This inconsistency of the velocity field is explained if we look at the shape of the shear, which is given by:

$$\tau_1 = \frac{1}{r}\left(f_1|_{\phi=0} + f_1''|_{\phi=0}\right) \quad ; \quad \tau_2 = \frac{\Gamma}{r}\left(f_2|_{\phi=\pi} + f_2''|_{\phi=\pi}\right) \tag{5.42}$$

so, at $r = 0$, $\tau_k \to \infty$, which constitutes an unphysical quantity. This unbounded shear at the wall means that any solid surface would require an

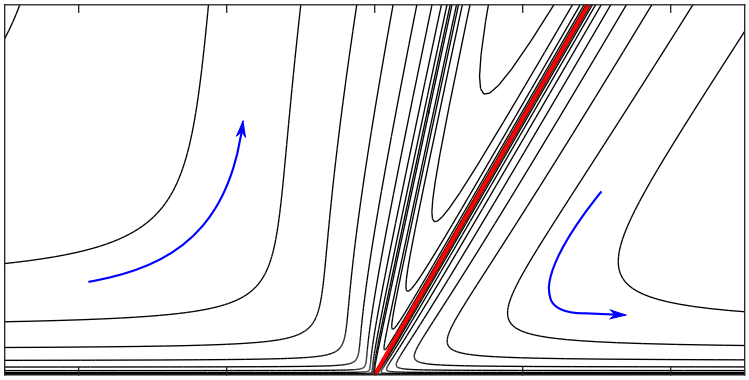

(a)

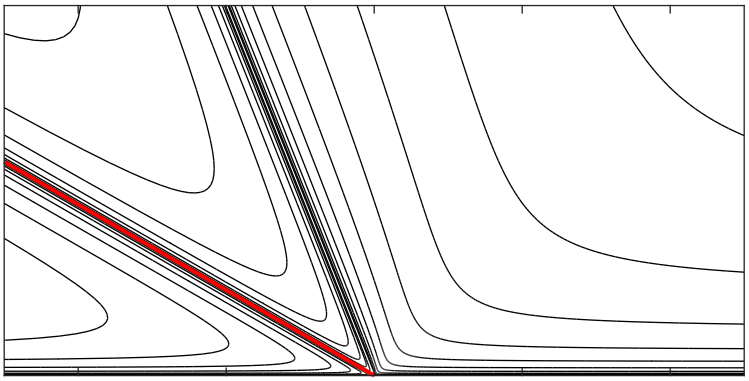

(b)

Figure 5.2: Stream function (equation 5.9) for the flow in the corner formed by two viscous fluids ($\Gamma = 1$) using the no-slip boundary condition, forming an angle of: (a) $\alpha = 60°$ and (b) $\alpha = 150°$

infinite force to be wetted by a liquid, clearly, this is not a physical behavior. This was first noticed by Huh and Scriven (1971) and by Moffatt (1964) before them, although in the later reference the focus of their work was directed to vortices. Similarly, the pressure field diverges as $r \to 0$:

$$p_1 = -\frac{1}{r}\left(f_1'''|_{\phi=0} + f_1'|_{\phi=0}\right) \quad ; \quad p_2 = -\frac{\Gamma}{r}\left(f_2'''|_{\phi=\pi} + f_2'|_{\phi=\pi}\right) \tag{5.43}$$

Normal stress balance at the interface will also vary as r^{-1} and as noticed by Huh and Scriven (1971), as $r \to 0$ a highly curved interface should be found. Perhaps at this point they were predicting the effects of viscous bending in hydrodynamic models without noticing it. The stream functions of the flow produced by the no-slip boundary condition for $\Gamma = 1$ (fluids of equal viscosity), $\alpha = 60°$ and $\alpha = 150°$ can be seen in figure 5.2. The

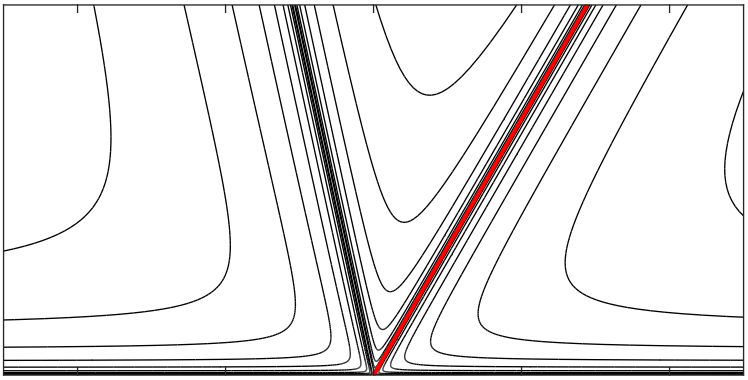

(a)

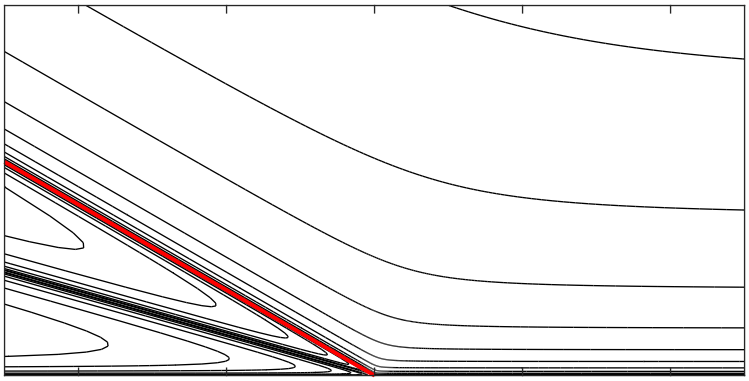

(b)

Figure 5.3: Stream function (equation 5.9) for the flow in the corner formed by two viscous fluids ($\Gamma = 1 \times 10^{-5}$) using the no-slip boundary condition, forming an angle of: (a) $\alpha = 60°$ and (b) $\alpha = 150°$. — Fluid interface.

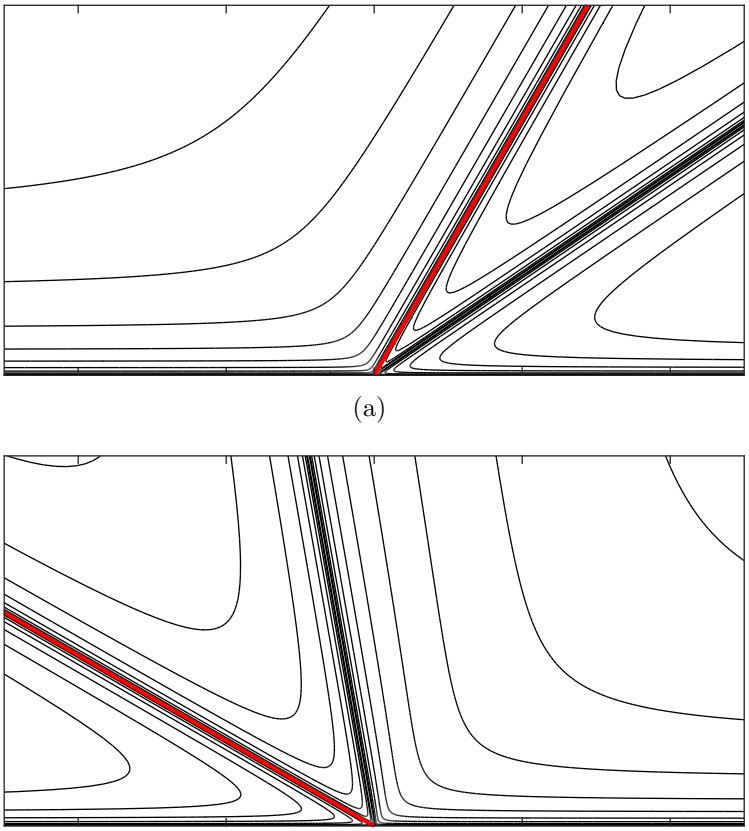

(a)

(b)

Figure 5.4: Stream function (equation 5.9) for Stokes flow in the corner formed by two viscous fluids ($\Gamma = 1 \times 10^5$) using the no-slip boundary condition, forming an angle of: (a) $\alpha = 60°$ and (b) $\alpha = 150°$. — Fluid interface.

first feature of the flow that calls for attention is the "rolling" motion of the advancing fluid (fluid 1) from the top to the bottom of the figures as shown with blue arrows in figure 5.2a, hence wetting the solid surface. The opposite motion is expected for fluid 2 as it is displaced by fluid 1. At the interface, the flow splits to match velocity fields of both fluids. A similar pattern is observed for $\alpha = 150°$ in figure 5.2b. As noted by Moffatt (1964), in the reference frame of the contact line, a "fluid 1 particle" traveling at the liquid interface (red line) will approach the contact line, whose velocity is zero, and instantly will accelerate to U. This would require of course, infinity shear and pressure. Figure 5.3, shows the stream lines for angles $\alpha = 60°$ and $\alpha = 150°$ for a viscosity ratio $\Gamma = 1 \times 10^{-5}$ (i.e. a viscous fluid spreading in a gaseous environment). Again the direction of the stream lines follows the pattern shown in figure 5.2. For $\alpha = 60°$ the flow splits, covering a larger angle

than that shown in figure 5.2a, and for $\alpha = 150°$ the splitting occurs inside fluid 2 (see figure 5.3b). This was observed also in Huh and Scriven (1971) and they gave no explanation for this splitting pattern, but it was observed that it occurs mostly in the less viscous fluid. Finally, figure 5.4, shows the stream functions for $\Gamma = 1 \times 10^5$, confirming the splitting in the less viscous fluid. Although this makes sense in terms of matching velocity fields of both fluids at the interface, there is no experimental/numerical confirmation of such patterns.

5.3 The Navier-slip boundary condition for a moving contact line.

As was seen in section 5.2, the no slip boundary condition yields unphysical shear and a multivalued velocity field at a moving contact line. To relax the no-slip boundary condition, some slip at the wall can be allowed. The most simple form of this slippage is the Navier-slip law. In the reference frame of the contact line it writes:

$$u - U = \frac{\lambda}{r}\frac{\partial u}{\partial \phi} \tag{5.44}$$

The boundary conditions at the wall are then, at $\phi = 0$:

$$\text{At} \quad \phi = 0 \quad \rightarrow \quad u_1 - U = \frac{\lambda}{r}\frac{\partial u_1}{\partial \phi} \quad ; \quad v_1 = 0 \tag{5.45}$$

$$\text{At} \quad \phi = \pi \quad \rightarrow \quad u_2 + U = -\frac{\lambda}{r}\frac{\partial u_2}{\partial \phi} \quad ; \quad v_2 = 0 \tag{5.46}$$

and the other boundary conditions at the fluid interface remain as shown in equations 5.21 to 5.23. Substitution of equations 5.5 and 5.9 yield at the wall:

$$r^n \, f_1'|_{\phi=0} - 1 = \lambda r^{n-1} \, f_1''|_{\phi=0} \quad ; \quad f_1|_{\phi=0} = 0 \tag{5.47}$$

$$r^n \, f_2'|_{\phi=\pi} + 1 = -\lambda r^{n-1} \, f_2''|_{\phi=\pi} \quad ; \quad f_2|_{\phi=0} = 0 \tag{5.48}$$

Here, the slip length λ has been non-dimensionalized using $\tilde{\lambda} = \lambda / L$. Two important considerations must be made to solve terms containing r in equations 5.47 and 5.48. First, by order of magnitude, it can be seen that if $r \rightarrow 0$, then $r^n \, f_k'|_{\text{wall}}$ decays quicker than $\lambda r^{n-1} \, f_k''|_{\text{wall}}$ so the former can be neglected altogether. Secondly, the only value of n, satisfying 5.47 and 5.48 (after the neglected terms) is $n = 1$. Conditions at the wall are given then

by:

$$-1 = \lambda\, f_1''|_{\phi=0} \quad ; \quad f_1|_{\phi=0} = 0 \tag{5.49}$$
$$1 = -\lambda\, f_2''|_{\phi=\pi} \quad ; \quad f_2|_{\phi=0} = 0 \tag{5.50}$$

and at the fluid interface:

$$f_1'|_{\phi=\alpha} = f_2'|_{\phi=\alpha} \tag{5.51}$$
$$f_1|_{\phi=\alpha} = 0 \tag{5.52}$$
$$f_2|_{\phi=\alpha} = 0 \tag{5.53}$$
$$f_1''|_{\phi=\alpha} = \Gamma\, f_2''|_{\phi=\alpha} \tag{5.54}$$

The degenerate form of f_k in equation 5.12 is used and the system of equations 5.49 to 5.54 is solved yielding the set of constants:

$$A_1 = 1/(4\lambda) \tag{5.55}$$

$$B_1 = \frac{\begin{array}{r}((\sin(4\alpha) + 4\alpha(\sin^2(2\alpha) - 1))(\alpha - \pi) + 2\pi\sin(2\alpha))\Gamma \\ +4\alpha(\sin^2(2\alpha) - 1)(\pi - \alpha) - \alpha\sin(4\alpha)\end{array}}{\Upsilon_1}$$

$$C_1 = \frac{(1-\Gamma)(\sin(2\alpha) + 2\cos(2\alpha)(\pi - \alpha))}{\Upsilon_2} \tag{5.56}$$

$$D_1 = -A_1 \tag{5.57}$$

$$A_2 = A_1 \tag{5.58}$$

$$B_2 = \frac{\begin{array}{r}(\pi - \alpha)(2\alpha - \sin(4\alpha) + 2\alpha\cos(4\alpha))\Gamma \\ +2\sin(2\alpha)(\pi - \alpha\cos(2\alpha)) + 4\alpha(\sin(2\alpha)^2 - 1)(\pi - \alpha)\end{array}}{\Upsilon_1}$$

$$C_2 = \frac{(1-\Gamma)(\sin(2\alpha) - 2\alpha\cos(2\alpha))}{4\Upsilon_2} \tag{5.59}$$

$$D_2 = \frac{\begin{array}{r}\alpha(\sin(2\alpha) - 2\alpha\cos(2\alpha)) + 2\alpha^2\cos(2\alpha) \\ -\sin(2\alpha)(\alpha + \pi)\end{array}}{4\Upsilon_2} \tag{5.60}$$

$$\begin{array}{r}\Upsilon_1 = 8\Gamma\lambda(\alpha\sin(4\alpha) - \sin^2(2\alpha))(\alpha - \pi) \\ -4\lambda\alpha(\cos(4\alpha) + 2\sin(4\alpha)(\alpha - \pi) - 1)\end{array} \tag{5.61}$$

$$\begin{array}{r}\Upsilon_2 = 4\lambda(\alpha(\sin(2\alpha) + 2\cos(2\alpha)(\pi - \alpha)) \\ -(\alpha - \pi)(\sin(2\alpha) - 2\alpha\cos(2\alpha))\Gamma)\end{array} \tag{5.62}$$

Since $n = 1$, velocity, viscous shear and pressure fields in the case of the

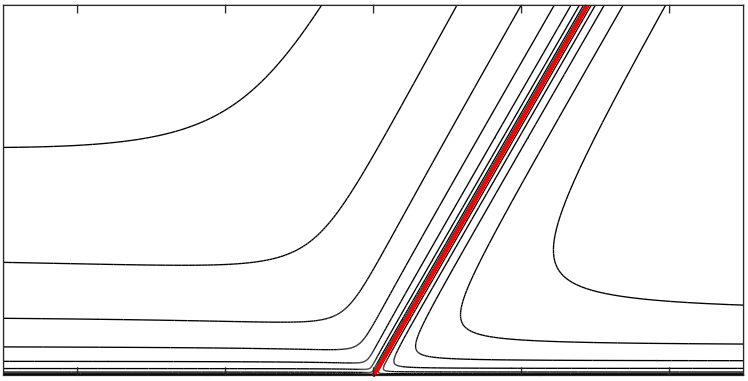

(a)

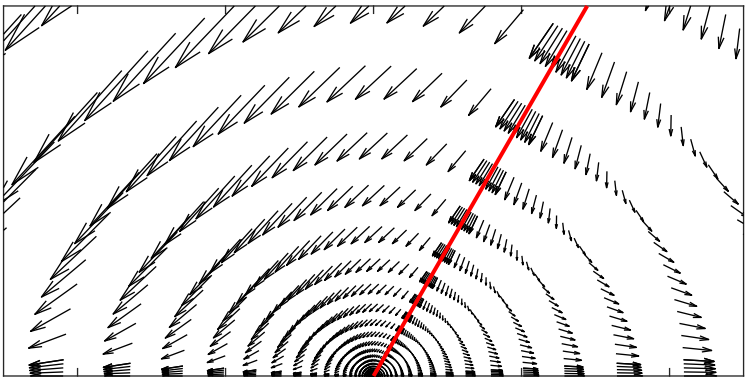

(b)

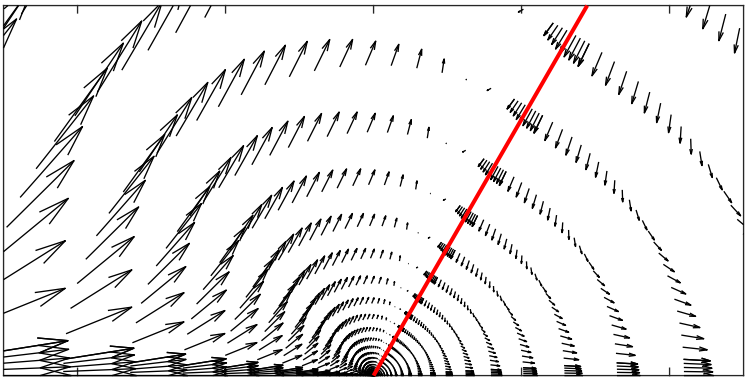

(c)

Figure 5.5: Stokes flow in the corner formed by two viscous fluids using the navier-slip boundary condition forming and angle of $\alpha = 60°$. (a) Stream function (equation 5.9) for $\Gamma = 1$, (b) Velocity field for $\Gamma = 1$ and (c) Velocity field for $\Gamma = 1 \times 10^{-5}$. — Fluid interface.

Navier-slip boundary condition are given by:

$$u_k = r f_k' \quad ; \quad v_k = -2 r f_k \tag{5.63}$$

which now is uniquely defined and vanishing as $r \to 0$. Shear and pressure at the wall result in:

$$\tau_1 = f_1''|_{\phi=0} \quad ; \quad \tau_2 = \Gamma\, f_2''|_{\phi=\pi} \tag{5.64}$$

$$p_1 = \ln r \left(f_1'''|_{\phi=0} + 4\, f_1'|_{\phi=0} \right) \quad ; \quad p_2 = \Gamma \ln r \left(f_2'''|_{\phi=\pi} + 4\, f_2'|_{\phi=\pi} \right) \tag{5.65}$$

eliminating the unphysical shear but a logarithmic singularity still remains in the pressure. As discussed in Shikhmurzaev (2006), when $r \to 0$ then $p \to -\infty$, which gives the idea of cavitation occurring at the contact line, clearly not compatible with the initial hypothesis of the problem. Normal stress balance at the interface will vary also as $\sim \ln r$, pointing to a highly curved interface close to the contact line.
Describing the characteristics of the flow obtained by a navier-slip boundary condition, in the case of fluids with the same viscosity $\Gamma = 1$, the flow "splitting" seen in the case of the no-slip boundary condition is not present here, as can be seen in figure 5.5a. Slippage allows fluid 2 to flow against U at the wall and the whole flow can be compared to an impinging jet flow. This is confirmed by the velocity field in figure 5.5b. Changing viscosity ratio to $\Gamma = 1 \times 10^{-5}$ restores the splitting as was before with the no-slip boundary condition (see figure 5.5c).
There are more complex forms of a slip boundary condition, i.e. the inverse linear slip and the inverse quadratic slip shown in equations 5.66 and 5.67 respectively. Because these conditions result in higher values of n, they solve both singularities, although they predict zero shear and pressure as $r \to 0$. A compilation of such models and the way they relieve the shear and pressure unboundedness can be found in Sibley et al. (2015).

$$u|_{\phi=0} = \frac{\lambda^2}{h} \left. \frac{\partial u}{\partial \phi} \right|_{\phi=0} \tag{5.66}$$

$$u|_{\phi=0} = \frac{\lambda^3}{h^2} \left. \frac{\partial u}{\partial \phi} \right|_{\phi=0} \tag{5.67}$$

In chapter 6, we will focus on a very special navier-slip law model proposed by Kirkinis and Davis (2013).

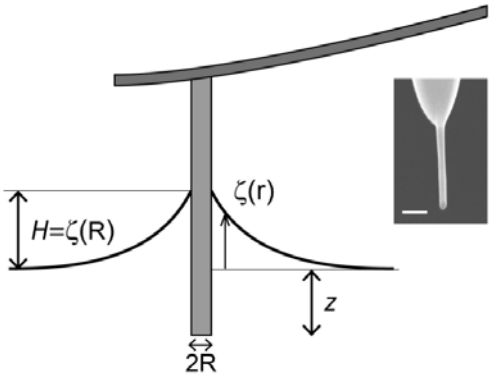

Figure 5.6: Scheme of the experiment. A nanofiber with radius R is dipped in a liquid interface leading to the formation of a meniscus with profile $\zeta(r)$ Inset: SEM image of a 60 nm in diameter silicon nanofiber (CDP55, Team Nanotec). Scale bar: 100 nm. Source: Dupré de Baubigny et al. (2015).

5.4 A pinned contact line with an oscillating interface.

The flow close to a pinned contact line with an oscillating interface can be visualized using the stokes-flow approximation. This problem has a physical precedence in Dupré de Baubigny et al. (2015) and Dupré de Baubigny et al. (2016), where the spring constant of liquid interface is determined at a nanometric scale. The schematics of the experiment is depicted in figure 5.6. In our case, of course, the lack of curvature and an appropriate length scale limits a direct comparison with experimental results.
The problem, in the reference frame of the pinned contact line can be depicted as shown in figure 5.7. The two-fluid interface forms an angle α with the solid wall. When the solid surface moves horizontally with some frequency and the contact line is assumed to be pinned, in the reference frame of the contact line the azimuthal velocity at the interface is $v = \omega r$, so α oscillates at the angular velocity $\omega = d\alpha/dt$. Since we are close to corner, such acceleration can be neglected as $Re = \omega r^2/\nu \ll 1$ (see Moffatt, 1964). In this context, the normalization of the velocity is performed using:

$$\tilde{u} = \frac{u}{\omega L} \quad ; \quad \tilde{v} = \frac{v}{\omega L} \tag{5.68}$$

The boundary conditions at the wall are then:

$$\text{At} \quad \phi = 0 \quad \rightarrow \quad u_1 = 0 \quad ; \quad v_1 = 0 \tag{5.69}$$

$$\text{At} \quad \phi = \pi \quad \rightarrow \quad u_2 = 0 \quad ; \quad v_2 = 0 \tag{5.70}$$

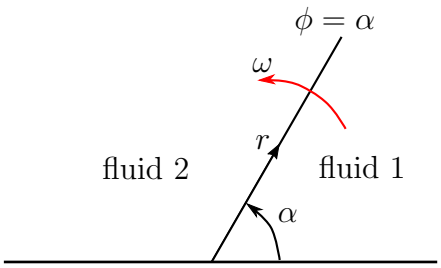

Figure 5.7: Pinned contact Line sketch in the reference frame attached to it.

At the interface:

$$\text{At} \quad \phi = \alpha \quad \rightarrow \quad u_1 = u_2 \quad ; \quad v_1 = \pm 1/2 \quad ; \quad v_2 = \pm 1/2 \qquad \tau_1 = \tau_2 \tag{5.71}$$

In equation 5.71, the sign of v_k is positive/negative for anticlockwise/clockwise direction of rotation. The substitution of the stream function yields at the wall:

$$f_1'|_{\phi=0} = 0 \quad ; \quad f_1|_{\phi=0} = 0 \tag{5.72}$$

$$f_2'|_{\phi=\pi} = 0 \quad ; \quad f_2|_{\phi=\pi} = 0 \tag{5.73}$$

and at the interface:

$$f_1'|_{\phi=\alpha} = f_2'|_{\phi=\alpha} \quad ; \quad f_1|_{\phi=\alpha} = \pm 1/2 \quad ; \quad f_2|_{\phi=\alpha} = \pm 1/2 \tag{5.74}$$

$$f_1''|_{\phi=\alpha} = \Gamma \, f_2''|_{\phi=\alpha} \tag{5.75}$$

Since, at the interface $v_k|_{\phi=\alpha} = -(n+1)r^n \, f_k''|_{\phi=\alpha} = r$, it follows that $n = 1$, so f_k in equation 5.12 is used and the system of equations 5.72 to 5.75 is solved yielding the set of constants:

$$A_1 = -\frac{\begin{array}{r} 2((\pi - 2\alpha + \sin(2\alpha)) + 2(\alpha - \pi)\sin^2(\alpha))\sin(\alpha)^2\Gamma \\ -2\sin^2(\alpha)(\sin(2\alpha) + 2\cos^2(\alpha)(\pi - \alpha)) \end{array}}{\Upsilon_1} \tag{5.76}$$

$$B_1 = \frac{\begin{array}{r} -(1/2(\Gamma - 1)(\cos(4\alpha) - 2\cos(2\alpha) \\ +\alpha\sin(4\alpha) - \pi\sin(4\alpha) + 1)) \end{array}}{\Upsilon_2} \tag{5.77}$$

$$C_1 = \frac{\begin{array}{r} -((\Gamma - 1)(\cos(4\alpha) - 2\cos(2\alpha) \\ +\alpha\sin(4\alpha) - \pi\sin(4\alpha) + 1)) \end{array}}{\Upsilon_2} \tag{5.78}$$

$$D_1 = \frac{\begin{array}{r}(\alpha(\cos(2\alpha)-1)(\cos(2\alpha)+1)-(\sin(2\alpha)+\pi\cos(2\alpha))\\ (\cos(2\alpha)-1))\Gamma-2(\sin^2(\alpha))(\sin(2\alpha)+2\cos^2(\alpha)(\pi-\alpha))\end{array}}{\Upsilon_2} \quad (5.79)$$

$$A_2 = \frac{\begin{array}{r}-(\cos(2\alpha)-1)(\alpha-\sin(2\alpha)+\alpha\cos(2\alpha))\Gamma\\ +(\cos(2\alpha)-1)(\alpha-\pi-\sin(2\alpha)+\alpha\cos(2\alpha))\end{array}}{\Upsilon_2} \quad (5.80)$$

$$B_2 = \frac{-(\cos(2\alpha)(\Gamma-1)(\cos(2\alpha)+\alpha\sin(2\alpha)-1))}{\Upsilon_2} \quad (5.81)$$

$$C_2 = \frac{2(\cos(2\alpha)(\Gamma-1)(\cos(2\alpha)+\alpha\sin(2\alpha)-1))}{\Upsilon_2} \quad (5.82)$$

$$D_2 = \frac{\begin{array}{r}(\sin(2\alpha)-\sin(4\alpha)/2+2\pi\sin^2(2\alpha)-\alpha\sin^2(2\alpha)-4\pi\sin(\alpha)^2\\ -\alpha\pi\sin(4\alpha))\Gamma-4\cos(\alpha)\sin^3(\alpha)+\alpha(\sin^2(2\alpha)+\pi\sin(4\alpha))\\ +2\pi\sin^2(\alpha)(4\sin^2(\alpha)-3)\end{array}}{\Upsilon_2} \quad (5.83)$$

$$\begin{array}{r}\Upsilon_1 = (2\pi-\alpha-8\cos(\alpha)\sin^3(\alpha)-\cos(4\alpha)(3\alpha-2\pi)+2(2\cos(2\alpha)\\ -\alpha\sin(4\alpha))(\alpha-\pi))\Gamma+2\sin(2\alpha)(\pi\sin(2\alpha)+1)\\ +8\alpha\sin^2(\alpha)(3\sin^2(\alpha)-2)-\sin(4\alpha)(2\pi\alpha-2\alpha^2+1)\end{array} \quad (5.84)$$

$$\begin{array}{r}\Upsilon_2 = (2\pi-\alpha-8cos(\alpha)\sin^3(\alpha)+4\cos(2\alpha)(\alpha-\pi)\\ -\cos(4\alpha)(3\alpha-2\pi)-2\alpha sin(4\alpha)(\alpha-\pi))\Gamma+8\cos(\alpha)\sin^3(\alpha)\\ +2(\pi-3\alpha)\sin^2(2\alpha)+8\alpha\sin^2(\alpha)+2\alpha\sin(4\alpha)(\alpha-\pi)\end{array} \quad (5.85)$$

Because $n = 1$, velocity, shear and pressure are also given by equations 5.63, 5.64 and 5.65. It is interesting to note here that although no divergence is present in shear as $r \to 0$, unbounded shear is present for two other conditions as we see next. Shear at the wall is given by:

$$\tau_1|_{\phi=0} = -4A_1 \quad ; \quad \tau_2|_{\phi=\pi} = -4A_2 \quad (5.86)$$

Substitution of constants in equations 5.76 and 5.80 into 5.86 and making the small angle approximation leaves the shear:

$$\tau_1|_{\phi=0} = 2\alpha(\alpha-\pi) + \frac{\pi}{\alpha}\left(1-\frac{1}{\Gamma-1}\right) \quad (5.87)$$

$$\tau_2|_{\phi=\pi} = -\frac{\pi}{\alpha(\Gamma-1)} - 2 \quad (5.88)$$

showing divergence for $\alpha \approx 0$ and at the same time if $\Gamma \approx 1$ (two fluids of the same viscosity). This could translate in an increasing force necessary to

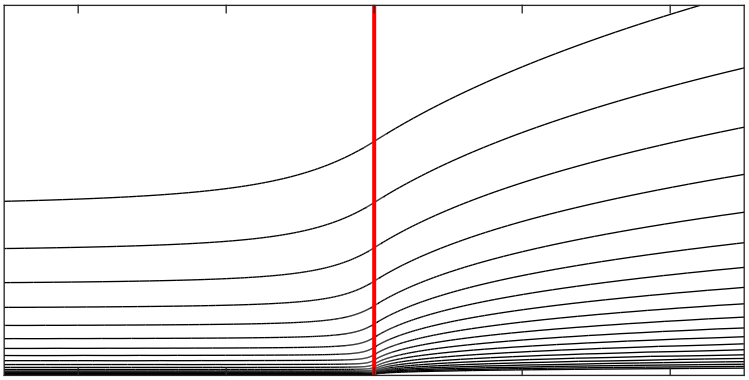

(a)

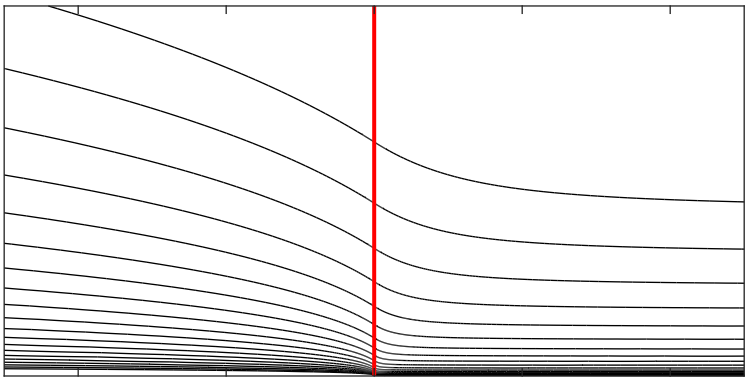

(b)

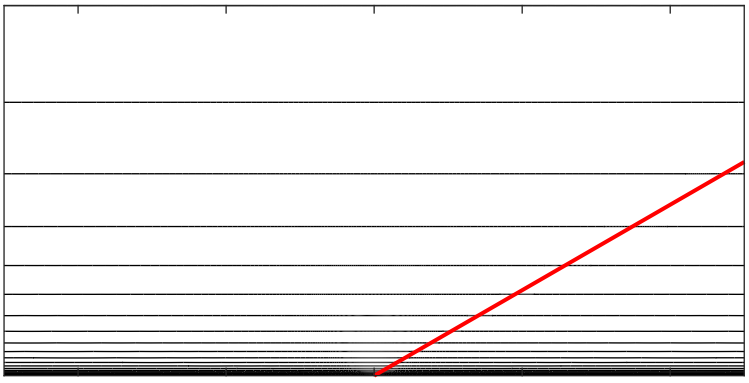

(c)

Figure 5.8: Stokes flow in the corner formed by two viscous fluids with an oscillating interface at $\alpha = 90°$ showing the Stream function (equation 5.9) for: (a) $\Gamma = 0.001$, (b) $\Gamma = 1000$ and at $\alpha = 30°$ for (c) $\Gamma = 1$. — Fluid interface.

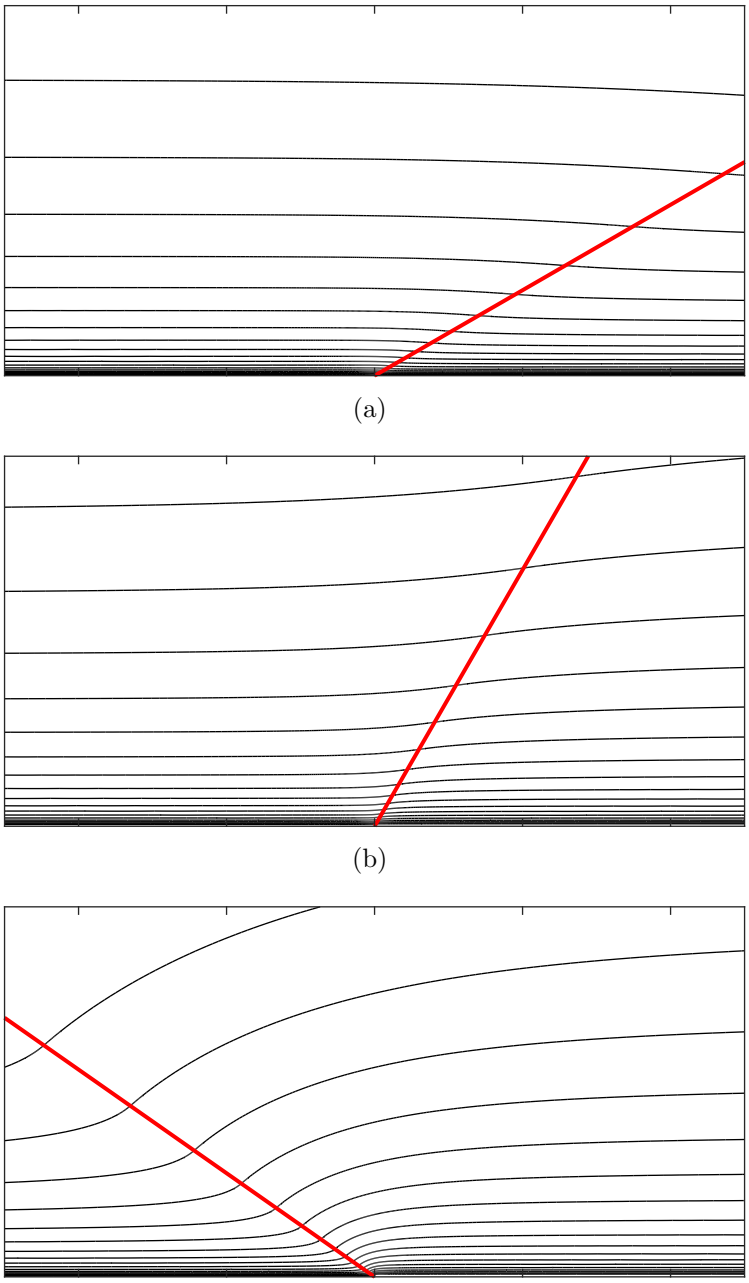

Figure 5.9: Stream function (equation 5.9) for Stokes flow in the corner formed by two viscous fluids with an oscillating interface for $\Gamma = 1 \times 10^{-5}$ at: (a) $\alpha = 30°$; (b) $\alpha = 60°$ and (c) $\alpha = 145°$. — Fluid interface.

produce the motion of the wall (the nanofiber in the experiments of Dupré de Baubigny et al. (2015, 2016)) for small values of α. This needs confirmation of experiments, although in a private communication with Thierry Ondarçuhu from CEMES, such divergence of dissipation as $\alpha \to 0$ was positively confirmed. It is also probable that for $\alpha = 0$ sets the breakdown of this similarity solution (see Moffatt and Duffy, 1980). This is also the case for the no slip boundary condition. Streamlines are given in figure 5.8a and 5.8b for the case at $\alpha = 90°$ with a viscosity ratio of $\Gamma = 0.001$ and $\Gamma = 1000$. Viscosity change symmetrically the streamlines with respect to the normal of the wall. When $\Gamma = 1$, perfect horizontal stream lines can be obtained for any angle $0° < \alpha < 180°$. This is shown in figure 5.8c for $\alpha = 30°$ as an example.
The effect of the interface angle can be seen in figure 5.9 for $\Gamma = 1 \times 10^{-5}$ at angles $\alpha = 30°$, $\alpha = 60°$ and $\alpha = 145°$. The sign of ω only reverses the direction of the velocity field but does not change the stream function pattern shown in all cases.

5.5 Summary

In this chapter we have explored a moving contact line considering it as a corner Stokes flow. We have given the analytical solutions for three different boundary conditions, two at the wall, namely, the no slip and the Navier slip conditions and one at the interface.
We have shown the effect of the no slip condition at the wall on viscous share and pressure with results known in the literature: the unbounded shear and pressure as $r \to 0$ (see Moffatt, 1964; Huh and Scriven, 1971). When using the Navier-slip condition, the unphysical shear was removed, but a logarithmic singularity still remained. In both cases, normal stress balance pointed out to a highly curved interface as we approach the contact line, clearly defying the initial flat interface hypothesis of this chapter.
Finally, we explore the case of a pinned contact line with a wall that moves at a certain frequency. In the reference frame of the contact line, the interface could be considered to oscillate with some angular velocity ω. For this case, n was determined to be 1 as in the case of the Navier slip condition. It was noticed that shear was bounded as $r \to 0$, but as $\alpha \to 0$ shear will diverge. This could translate in an increasing force necessary to produce the motion of the wall. Also, when $\alpha \to 0$, $\Gamma = 1$ produces divergence in viscous shear.
In the next chapter we analyze a special navier slip law that could open the door to the existence of Moffatt Vortices in the vicinity of the contact line.

Chapter 6

On the existence of Moffatt vortices at a moving contact line between two fluids.

In this chapter we explore the flow close to a two-fluid contact line extending the formulation of a special slip condition given in Kirkinis and Davis (2013) and Kirkinis and Davis (2014) to handle two viscous fluids and analyze the existence of Moffatt vortices in the vicinity of the contact line.

6.1 Background

In principle, molecular simulations suggest that some kind of slippage must occur close to the contact line (Thompson and Robbins, 1989; Qian et al., 2005) and at a large distance from it, the no slip-boundary condition must be recovered. Kirkinis and Davis (2013) proposed a novel slippage theory with a slip length of the form:

$$\lambda = \ell^n / r^{n-1} - b(\alpha, n) r \tag{6.1}$$

where ℓ is a macroscopic scale, $b(\alpha, n)$ is a dimensionless quantity determined by the boundary conditions. When neglecting the outer fluid influence and considering a static contact angle $\alpha_s = 0$, these parameters are related to the capillary number by the relation $Ca = \mu U/\sigma = nb(\alpha, n)(1 - \cos\alpha)$. Originally in Kirkinis and Davis (2013), n was assume to fit experimental data. Later in Kirkinis and Davis (2014), n becomes part of the solution of the flow and in general can take complex values ($n = n_R + in_I$). When n is complex, an infinite series of vortices is observed in the vicinity of the contact line

similar to those found in Moffatt (1964) for the no-slip boundary condition.

6.2 Corner Stokes flow with a variable slip length

The slip model proposed by Kirkinis and Davis (2013) for two fluids is given by:

$$\lambda_k = \ell^n / r^{n-1} - b_k(\alpha, n)\, r \quad \text{for} \quad r \leq r_k^* \tag{6.2}$$

$$\lambda_k = 0 \quad \text{for} \quad r \geq r_k^* \tag{6.3}$$

By definition this slip length vanishes at $r = r_k^* = \ell / b_k^{1/n}$ if n is a real number ($n_I = 0$), so to recover the no-slip boundary condition. Considering a characteristic velocity $U \sim 1$mm/s, Kirkinis and Davis (2013) reported $r^* \sim 0.68$ mm for glycerine and $r^* \sim 1$ μm for water. When $n_I \neq 0$, both quantities λ_k and $\ell / b_k^{1/n}$ are complex, a mistake in Kirkinis and Davis (2014) that we correct in this derivation.
Substitution of equation 6.1 and a zero azimuthal velocity on the wall for fluid 1 ($\phi = 0$) and for fluid 2 ($\phi = \pi$) gives:

$$u_1 - U = \left(\frac{\ell^n}{r^{n-1}} - b_1 r \right) \frac{1}{r} \frac{\partial u_1}{\partial \phi} \quad ; \quad v_1 = 0 \tag{6.4}$$

$$u_2 + U = - \left(\frac{\ell^n}{r^{n-1}} - b_2 r \right) \frac{1}{r} \frac{\partial u_2}{\partial \phi} \quad ; \quad v_2 = 0 \tag{6.5}$$

Zero azimuthal velocity, the continuity of both the tangential velocity and the tangential shear writes at the interface ($\phi = \alpha$):

$$v_1 = v_2 = 0 \quad ; \quad u_1 = u_2 \quad ; \quad \tau_1 = \tau_2 \tag{6.6}$$

The adimensionalization is perform using U and ℓ, so:

$$\tilde{r} = \frac{r}{\ell} \quad ; \quad \tilde{\psi_k} = \frac{\psi_k}{U \ell} \tag{6.7}$$

Dropping the notation of "tilde" for clarity and replacing the stream function form equation 5.9 and function f from equation 5.10, the boundary conditions leave at the wall:

$$f_1|_{\phi=0} = 0 \quad ; \quad r^n \, f_1'|_{\phi=0} - 1 = f_1''|_{\phi=0} - b_1 r^n \, f_1''|_{\phi=0} \tag{6.8}$$

$$f_2|_{\phi=\pi} = 0 \quad ; \quad r^n \, f_2'|_{\phi=\pi} + 1 = r^n b_2 \, f_2''|_{\phi=\pi} - \, f_2'''|_{\phi=\pi} \tag{6.9}$$

and at the interface:

$$\begin{aligned} f_1|_{\phi=\alpha} = 0 \quad ; \quad f_2|_{\phi=\alpha} = 0 \\ f_1'|_{\phi=\alpha} - \, f_2'|_{\phi=\alpha} = 0 \quad ; \quad f_1''|_{\phi=\alpha} - \Gamma \, f_2''|_{\phi=\alpha} = 0 \end{aligned} \tag{6.10}$$

The slip condition (second condition in 6.8 and 6.9) is satisfied in fluid 1 (resp. fluid 2) for any r if $f_1' = -b_1 f_1''$ and $f_1'' = -1$ (resp. $f_2' = b_2 f_2''$ and $f_2'' = -1$). In these conditions, n cannot be determined by satisfying the boundary conditions directly, instead it becomes part of the solution. The first eight equations from 6.8 to 6.10 are used to determine A_k, B_k, C_k and D_k. We find:

$$A_1 = \frac{1}{4\,n} \tag{6.11}$$

$$B_1 = \frac{\sin(n\,\alpha)\,\sin(\alpha) + n\,\left(2\,b_1\,\sin(\alpha\,\left(n-1\right)) - \sin(n\,\alpha)\,\sin(\alpha)\right)}{4\,n\,\sin(n\,\alpha)\,\cos(\alpha) - 4\,n^2\,\cos(n\,\alpha)\,\sin(\alpha)} \tag{6.12}$$

$$C_1 = -\frac{1}{4\,n} \tag{6.13}$$

$$D_1 = \frac{\sin(n\,\alpha)\,\sin(\alpha) - n\,\left(2\,b_1\,\sin(\alpha\,\left(n+1\right)) - \sin(n\,\alpha)\,\sin(\alpha)\right)}{4\,n\,\sin(n\,\alpha)\,\cos(\alpha) - 4\,n^2\,\cos(n\,\alpha)\,\sin(\alpha)} \tag{6.14}$$

and:

$$A_2 = \frac{O}{W} \tag{6.15}$$

$$B_2 = \frac{Q}{W} \tag{6.16}$$

$$C_2 = \frac{S}{W} \tag{6.17}$$

$$D_2 = \frac{-T}{W} \tag{6.18}$$

with

$$\begin{aligned} O = \sin(\alpha - n\,\left(\alpha - 2\,\pi\right)) - \sin(\alpha\,\left(n+1\right)) + 2\,n\,\cos(n\,\alpha)\,\sin(\alpha) \\ +2\,b_2\,n\,\left(\cos(\alpha\,\left(n-1\right)) - \cos(\alpha - n\,\left(\alpha - 2\,\pi\right))\right) \end{aligned} \tag{6.19}$$

$$\begin{aligned} Q = \cos(\alpha\,\left(n+1\right)) - \cos(\alpha - n\,\left(\alpha - 2\,\pi\right)) + 2\,n\,\sin(n\,\alpha)\,\sin(\alpha) \\ +2\,\mathrm{b}_2\,n\,\left(\sin(\alpha\,\left(n-1\right)) - \sin(\alpha - n\,\left(\alpha - 2\,\pi\right))\right) \end{aligned} \tag{6.20}$$

$$\begin{aligned} S = \sin(\alpha\,\left(n-1\right)) + \sin(\alpha + n\,\left(\alpha - 2\,\pi\right)) - 2\,n\,\cos(n\,\alpha)\,\sin(\alpha) \\ -2\,b_2\,n\,\left(\cos(\alpha\,\left(n+1\right)) - \cos(\alpha + n\,\left(\alpha - 2\,\pi\right))\right) \end{aligned} \tag{6.21}$$

$$\begin{aligned} T = \cos(\alpha\,\left(n-1\right)) - \cos(\alpha + n\,\left(\alpha - 2\,\pi\right)) \\ +2\,b_2\,n\,\left(\sin(\alpha\,\left(n+1\right)) + \sin(\alpha + n\,\left(\alpha - 2\,\pi\right))\right) + 2\,n\,\sin(n\,\alpha)\,\sin(\alpha) \end{aligned} \tag{6.22}$$

$$W = 8\,n\,\left(\sin(n\,\left(\alpha - \pi\right))\,\cos(\alpha) - n\,\cos(n\,\left(\alpha - \pi\right))\,\sin(\alpha)\right) \tag{6.23}$$

Since n is to be found as part of the solution, shear and pressure fields have the general form:

$$\tau_1 = r^{n-1}\left(\left(1-n^2\right)f + f''\right) \quad ; \quad \tau_2 = \Gamma r^{n-1}\left(\left(1-n^2\right)f + f''\right) \tag{6.24}$$

$$p_1 = \frac{r^{n-1}}{n-1}\left(f''' + (n+1)^2 f'\right) \quad ; \quad p_2 = \Gamma\frac{r^{n-1}}{n-1}\left(f''' + (n+1)^2 f'\right) \tag{6.25}$$

Note that only values of $n \geq 1$ relief the unboundedness for shear and pressure. One additional equation is needed to close the system and find b_k and n. This is achieved through the unbalanced Young-Force. The imposition of a contact angle α different to the static contact angle α_s produces the motion of the contact line. The force F that drives this motion is then called "non compensated Young Force" (Brochard-Wyart and de Gennes (1992)):

$$F = \sigma(\cos\alpha_s - \cos\alpha) \tag{6.26}$$

This force must overcome friction forces caused by the motion of the contact line. The shear stress at the wall, for fluids 1 and 2 (with dimensions) is given by:

$$\tau_1|_{\phi=0} = \mu_1\frac{1}{r^2}\left.\frac{\partial^2\psi_1}{\partial\phi^2}\right|_{\phi=0} \tag{6.27}$$

$$\tau_2|_{\phi=\pi} = \mu_2\frac{1}{r^2}\left.\frac{\partial^2\psi_2}{\partial\phi^2}\right|_{\phi=\pi} \tag{6.28}$$

Introducing functions f_1 and f_2 for the stream function (equation 5.10 in the manuscript):

$$\tau_1|_{\phi=0} = \mu_1\frac{Ur^{n-1}}{\ell_1^n}\, f_1''|_{\phi=0} \tag{6.29}$$

$$\tau_2|_{\phi=\pi} = \mu_2\frac{Ur^{n-1}}{\ell_1^n}\, f_2''|_{\phi=\pi} \tag{6.30}$$

The total force at the wall exerted by the two fluids is obtained by the integration of the shear in the slip region:

$$F = \int_0^{r_2^*} \tau_2|_{\phi=\pi}\, dr + \int_0^{r_1^*} \tau_1|_{\phi=0}\, dr \tag{6.31}$$

Substitution of the shear yields:

$$F = -\frac{1}{n}\left(\Gamma r_2^{*n} + r_1^{*n}\right) \tag{6.32}$$

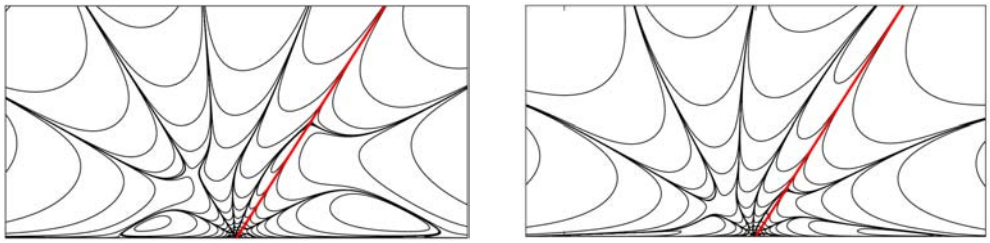

Figure 6.1: Stream function (equation 5.9) for $\alpha = 1$ rad, $Ca = 0.01$, $\Gamma = 1 \times 10^{-6}$. (a): solution obtained following Kirkinis and Davis (2014): $n = 6.999193{+}1.278230i$, (b): our corrected derivation: $n = 6.799117{+}1.648136i$.

This force must balance the non-compensated Young force:

$$\cos\alpha_s - \cos\alpha = \frac{Ca}{n}\left(\Gamma r_2^{*n} + r_1^{*n}\right) \tag{6.33}$$

where $Ca = \mu_1 U/\sigma$ is the capillary number based on the viscosity of the advancing fluid. A value of $\Gamma \to 0$ indicates that a fluid is pushing another fluid of much smaller viscosity (typically a drop spreading in a gas) while the opposite limit, $\Gamma \to \infty$, corresponds to a fluid pushing an other fluid of much larger viscosity (for example a bubble spreading in a liquid). Note that in Kirkinis and Davis (2014), the radial position r_1^* (a real number) has been replaced by $\ell/b_1^{1/n}$ in Eq. (6.33) which is not correct because if n is complex then it follows that $\ell/b^{1/n}$ is complex. The effect of this correction is shown in Figure 6.1.
Figure 6.1 reports the streamlines in the limit $\Gamma \to 0$, for $\alpha_s = 0$ and $\alpha = 1$ rad corresponding to the case reported in Kirkinis and Davis (2014). The solution shown in Figure 6.1a is obtained with the derivation proposed by Kirkinis and Davis (2014) while the streamlines shown in Figure 6.1b are obtained with our corrected solution. Following the Kirkinis and Davis (2014) derivation we obtain $n = 6.999190{+}1.278228i$ in perfect agreement with their solution. Note that considering $\Gamma = 1\times10^{-6}$ instead of $\Gamma = 0$ (this is the case shown in figure 6.1a) gives the same streamlines and a very close value for n, $n = 6.999193 + 1.278230i$. Despite noticeable changes in the streamlines shape, the flow structure in the receding fluid (not considered in Kirkinis and Davis (2014)) reveals the development of Moffatt vortices of similar shape on both sides of the interface.

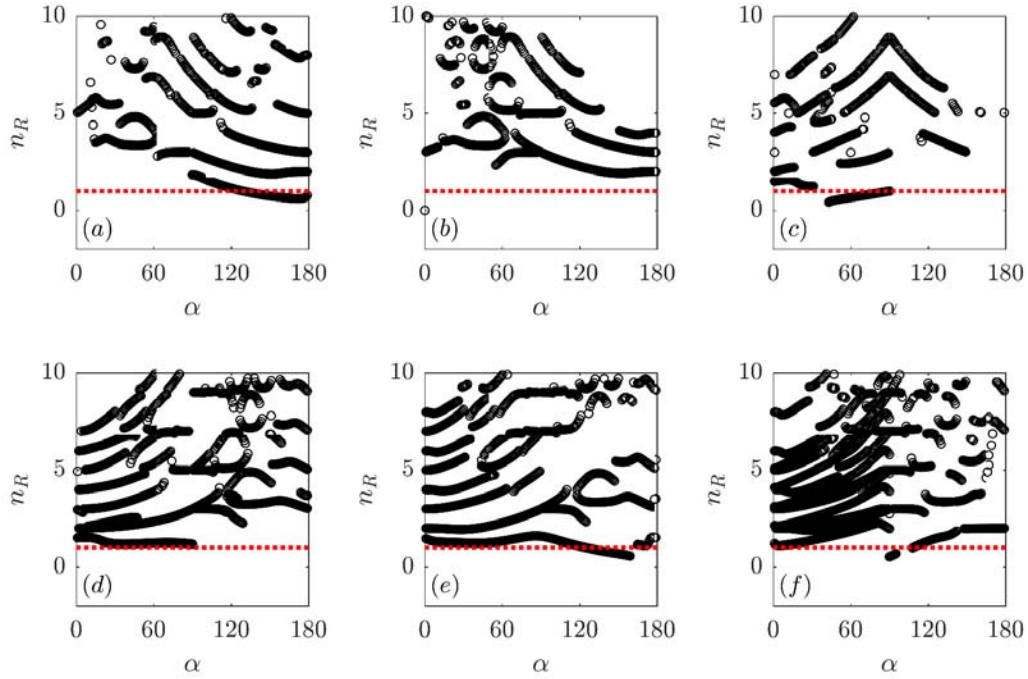

Figure 6.2: Map of real solutions for $Ca = 0.01$ and (a) $\Gamma = 0.01$, (b) $\Gamma = 0.1$, (c) $\Gamma = 1$, (d) $\Gamma = 2$, (e) $\Gamma = 10$, (f) $\Gamma = 100$.

6.3 Results

The system of equations 6.8 to 6.10 and 6.33 is solved numerically using "fsolve" inside MATLAB which uses the Levenberg-Marquardt and trust-region-reflective methods (Matlab, 2015) with default parameters. We can select the solution with the smallest positive n_R because it determines the asymptotic flow pattern at leading order (Shtern, 2014), but the solution may also be imposed by the flow far from the contact line (Kirkinis and Davis, 2014). Multiple solutions for n can be obtained for each set of parameters (Γ, α, α_s, Ca) that can be varied independently. The flow structure is significantly changed depending if n is a real or a complex number.

6.3.1 Regular corner flows (real solutions for n)

The solution with real values for n are reported in figure 6.2 as a function of α for $Ca = 0.01$ and for viscosity ratio from $\Gamma = 0.01$ to $\Gamma = 100$ in order to cover both gas/liquid and liquid/liquid interfaces. Both the density of solutions and the appropriate angle for having a solution are clearly depending on α and Γ. It seems that available solutions can be found for

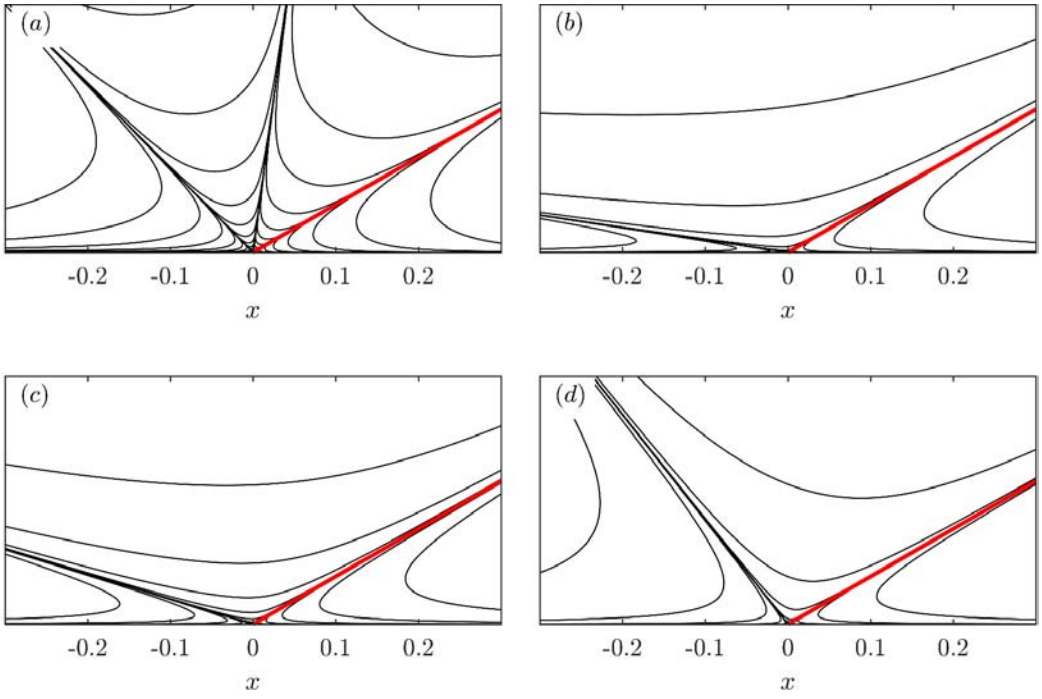

Figure 6.3: Effect of Γ. Stream function (equation 5.9) for $\alpha = 30°$, $\alpha_s = 0°$ and $Ca = 0.01$. (a) $\Gamma = 0.1$, $n = 3.490212$; (b) $\Gamma = 1$, $n = 1.253249$; (c) $\Gamma = 2$, $n = 1.202459$; (d) $\Gamma = 10$, $n = 1.246048$;

any angle. The density of the solution increases with Γ. Note that the map of solution is different between large and small Γ. Indeed Γ and $1/\Gamma$ do not play a symmetrical role in equation 6.33. Below the threshold $n_R = 1$, shown using a dotted red line, no valid description of the shear and pressure can be obtained as $r \to 0$, as it is in the case of the no-slip boundary condition, because shear and pressure are both varying as r^{n-1}. Stream lines are shown in Figure 6.3 and in Figure 6.4 where different values of Γ and α are considered, respectively. The flow behaves like a classical flow in a corner. The main feature of the flow structure is that it can be split depending on the conditions. For example, in Figure 6.3 where the effect of Γ is reported for the imposed dynamic contact angle $\alpha = 30°$, the flow only splits in fluid 2 while the flow can also be split in the two fluids as shown in Figure 6.4b. Huh and Scriven (1971) observed, with a no-slip boundary conditions for the two fluids, that there is a tendency of this splitting to appear in the fluid with the lower viscosity, while here we observe the opposite attributed to the imposed slip condition. We also have to mention that larger numbers of flow splitting appear with the increase of n. This is for example the case in figure

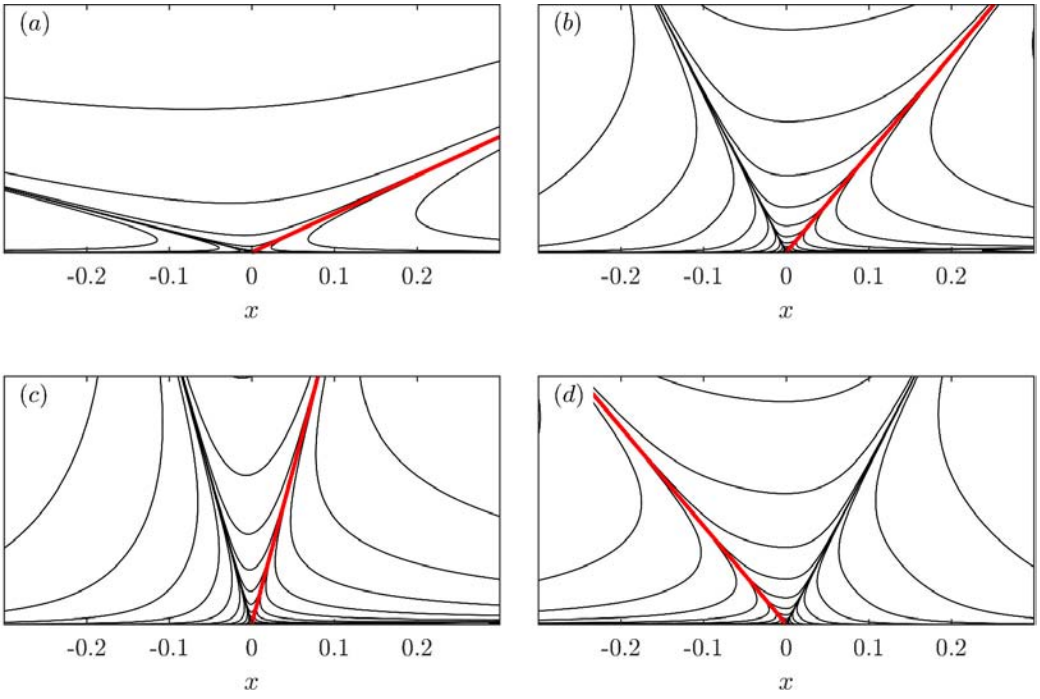

Figure 6.4: Effect of α. Stream function (equation 5.9) for $Ca = 0.01$, $\Gamma = 1$ and $\alpha_s = 0$. (a) $\alpha = 25°$, $n = 1.272566$; (b) $\alpha = 50°$, $n = 3.556807$; (c) $\alpha = 75°$, $n = 2.613791$; (d) $\alpha = 130°$, $n = 3.560146$.

6.3a where two splits are present in fluid 2.

6.3.2 Moffatt vortices (complex solutions for n)

Moffatt vortices are observed for complex solution for n. Because of the continuity of the velocity at the interface, each vortex in the advancing fluid is connected at the interface to its counterpart in the receding fluid 2, so that a pair of vortices can be identified and infinite series of Moffatt vortices are observed on both sides of the interface. In the following we call vortices 1 and 2 the vortices in the advancing fluid 1 and in the receding fluid 2, respectively. Examples of stream lines are reported in Figure 6.5 and in Figure 6.6 where the effect of the dynamic contact angle and the viscosity ratio are shown respectively. Comparing the streamlines in these figures, it is clear that their shape are very sensitive to these two parameters. Different types of Moffatt vortices can be identified: the "corner vortex" (see figure 6.5b in the advancing fluid), the "detached corner vortex" (see figures 6.6c to 6.6d in the receding fluid), the "wall vortex" (see figure 6.5a in the advancing

fluid) and the "interface vortex" (see Figure 6.5b for the receding fluid). In addition, it is also clear from these figures that the vortex size is different when comparing fluid 1 and fluid 2. For example in Figure 6.5a a zoom is necessary to visualize the vortex 2 that matches to its corresponding vortex 1 at the interface: vortex 2 is here more than one order of magnitude smaller than vortex 1. The velocity being continuous at the interface, a smaller vortex reveals a vortex of stronger vorticity. In Figure 6.6, we observe that vortex 1 becomes significantly much smaller than vortex 2 when Γ increases. This is consistent with the consideration that the motion is easier in the less viscous fluid than in the more viscous fluid. The inspection of the effect of both the Capillary number Ca and the static angle α_s (not shown here) reveals that the fluid structure is preserved when varying independently these two parameters. In fact considering the system of equations (6.10-6.33), Ca and α_s are both impacting the solution by relation 6.33 so that the relevant parameter to consider is $\widetilde{Ca} = Ca/(\cos\alpha_s - \cos\alpha)$ which measures the ratio of viscous force to the non compensated Young force. The cases for $\alpha = 90°$, $\Gamma = 1$ and $\alpha_s = 0$ (not shown here) are characterized by a perfect symmetry of the solution with respect to the interface.

6.4 Discussion

Moffatt vortices are observed for solutions where n is a complex number. As a consequence, the slip length as proposed by Kirkinis and Davis (2014) (see Eq. 6.2) used in the derivation is then a complex number. The solution of interest being given by the real part of the stream function, the slip length, as defined by Eq. (6.2) is not the effective slip experienced by the two fluids at the wall. The normalized effective slips at the wall for the advancing and receding fluids, λ_{1E} and λ_{2E}, are to be deduced from the real part of the solution for $\phi = 0$ and $\phi = \pi$ respectively as (the normalization is based on U and ℓ):

$$R\left(u_1 - 1\right) = \lambda_{1E} R\left(\frac{1}{r}\frac{\partial u_1}{\partial \phi}\right) \quad ; \quad R\left(u_2 + 1\right) = \lambda_{2E} R\left(-\frac{1}{r}\frac{\partial u_2}{\partial \phi}\right) \tag{6.34}$$

Here, $R(z)$ and $I(z)$ stand for the real and the imaginary part of the complex number z. Considering the advancing fluid ($k = 1$), the radial velocity at the wall is:

$$R\left(u_1(\phi = 0)\right) = r^{n_R}\left[\cos\left(n_I \ln(r)\right) R(f_1'|_{\phi=0}) - \sin\left(n_I \ln(r)\right) I(f_1'|_{\phi=0})\right] \tag{6.35}$$

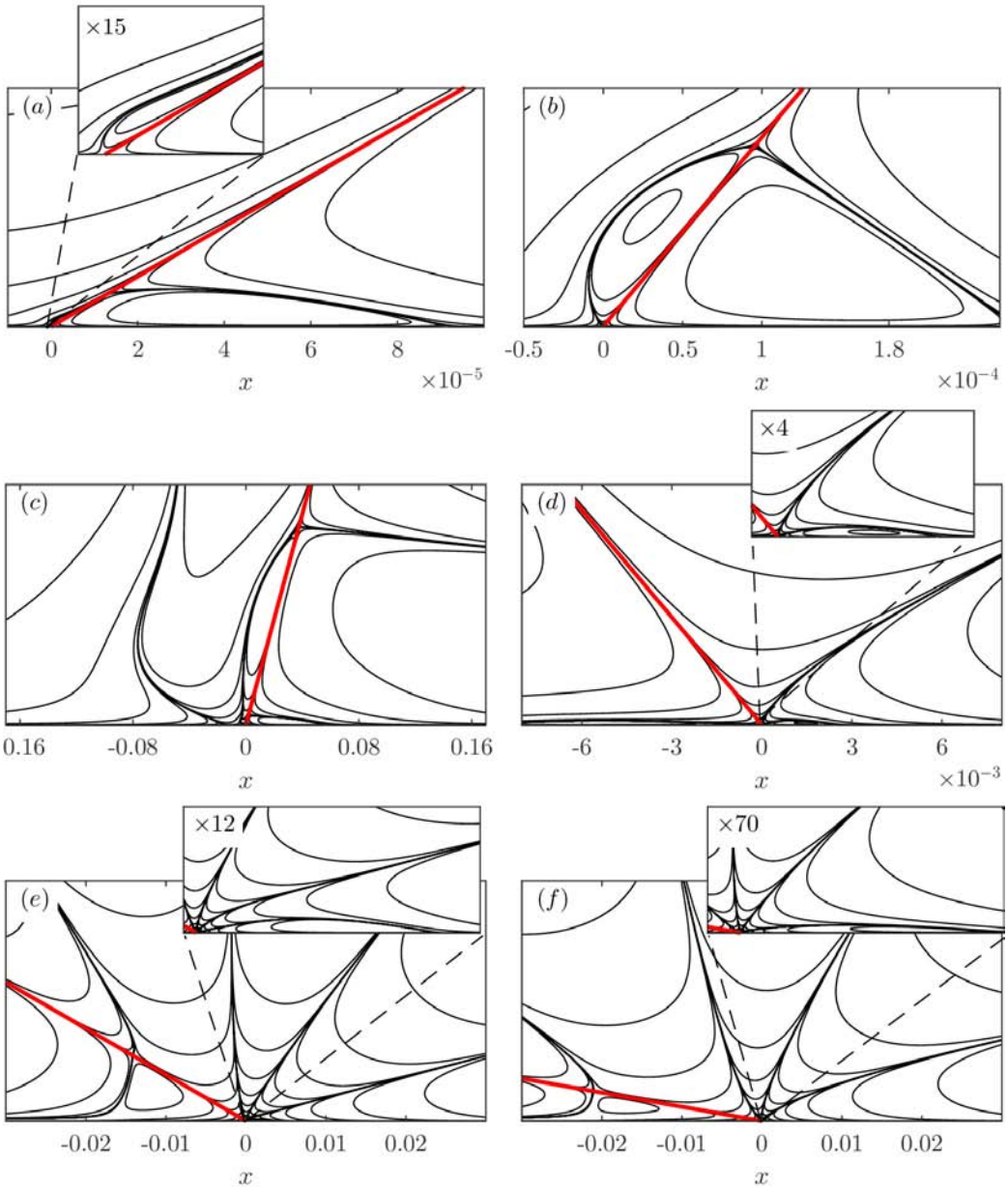

Figure 6.5: Effect of α. Stream function (equation 5.9) for $Ca = 0.01$, $\Gamma = 0.1$ and $\alpha_s = 0$. (a) $\alpha = 30°$ $(n = 2.049237 + 0.242136\,i)$; (b) $\alpha = 50°$ $(n = 2.231697 + 0.319340\,i)$; (c) $\alpha = 75°$ $(n = 2.849756 + 1.033444\,i)$; (d) $\alpha = 130°$ $(n = 2.679453 + 0.383081\,i)$; (e) $\alpha = 150°$ $(n = 4.733359 + 0.381333\,i)$; (f) $\alpha = 170°$ $(n = 4.053887 + 0.403130\,i)$;

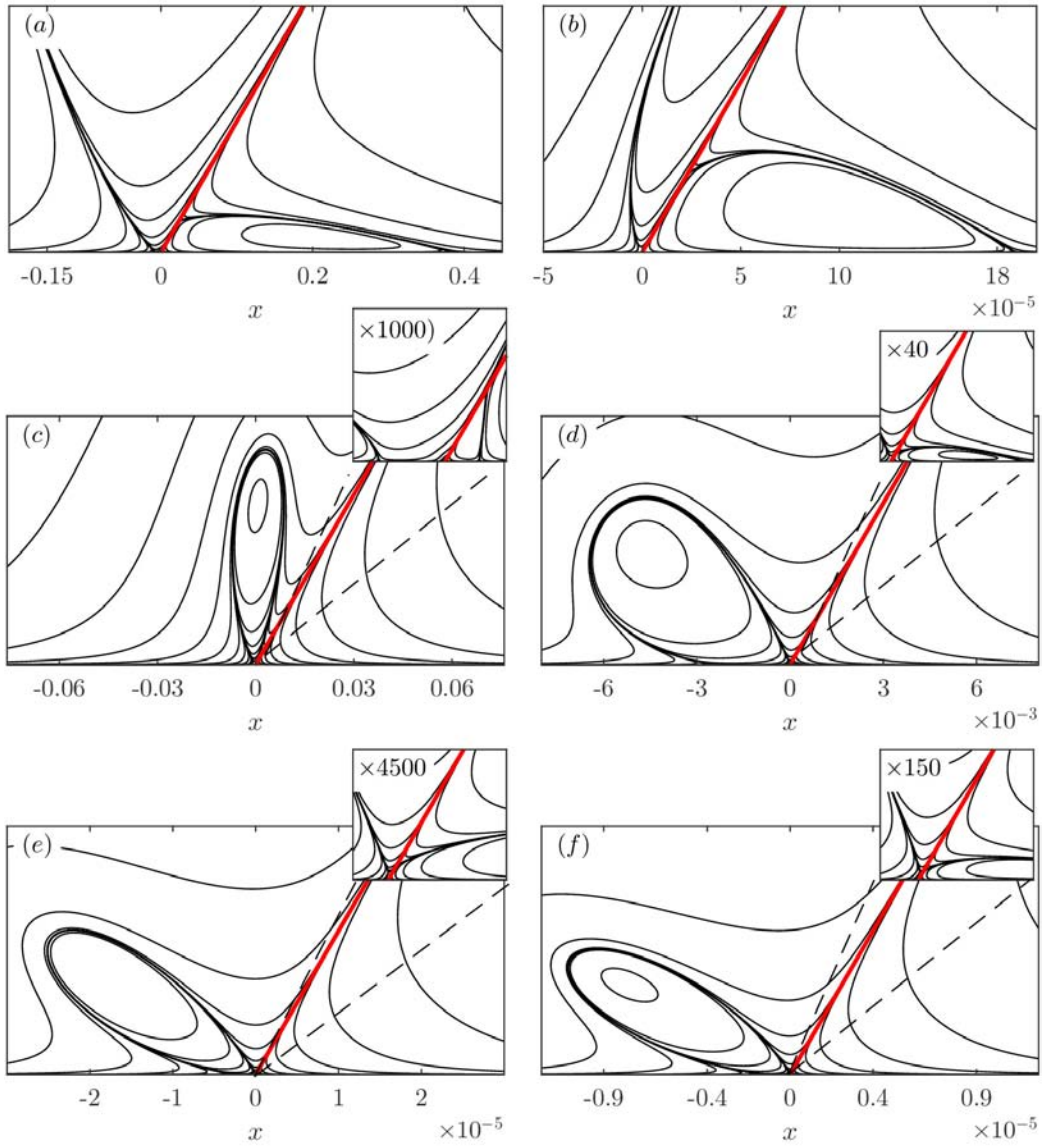

Figure 6.6: Effect of the viscosity ratio Γ. Stream function (equation 5.9) for $\alpha = 60°$, $Ca = 0.01$. (a) $\Gamma = 0.01$ $(n = 2.587148 + 0.349960\,i)$; (b) $\Gamma = 0.1$ $(n = 2.620577 + 0.334090\,i)$; (c) $\Gamma = 0.25$ $(n = 2.675627 + 0.265560\,i)$; (d) $\Gamma = 0.8$ $(n = 2.834106 + 0.400948\,i)$; (e) $\Gamma = 1$ $(n = 2.773461 + 0.210823\,i)$; (f) $\Gamma = 2$ $(n = 2.633405 + 0.209562\,i)$

while the velocity gradient at the wall is:

$$R\left(\frac{1}{r}\left.\frac{\partial u_1}{\partial \phi}\right|_{\phi=0}\right) = r^{n_R-1}\left[\cos\left(n_I \ln(r)\right) R(f_1''|_{\phi=0}) - \sin\left(n_I \ln(r)\right) I(f_1''|_{\phi=0})\right] \tag{6.36}$$

From the boundary conditions at $\phi = 0$, we get $f_1'|_{\phi=0} = b_1$, $f_1''|_{\phi=0} = -1$ and the effective slip length experienced by the fluid on the wall is then:

$$\lambda_{1E} = -rR(b_1) + r\tan\left(n_I \ln(r)\right) I(b_1) + \frac{1}{r^{n_R-1}\cos\left(n_I \ln(r)\right)} \tag{6.37}$$

Note that the value of the radial position on the wall $r = r_1^*$ where the slip length cancel (and used in Eq. 6.33) comes from this relation. Following the same derivation for the receding fluid we can show that for both fluids r_k^* is given by

$$r_k^*\left[\cos\left(n_I \ln(r_k^*)\right) R(b_k) - \sin\left(n_I \ln(r_k^*)\right) I(b_k)\right]^{1/n_R} = 1 \tag{6.38}$$

The evolution of the normalized effective slip λ_{1E} with r is shown in figure 6.7 for two cases: the case reported in Kirkinis and Davis (2014) (see Figure 6.1*b*) with $n = 6.799117 + 1.648136i$ ($\alpha = 1$ rad, $Ca = 0.01$, $\Gamma = 0$) and the case shown in Figure 6.5b with $n = 2.231697 + 0.319340\,i$ ($\alpha = 50°$, $Ca = 0.01$, $\Gamma = 0.1$). The slip length evolution is plotted here up to $r = r^*$ given by eq. 6.38 when it cancels. For clarity, the absolute value of λ_{1E} is reported with the use of a log/log scale, red lines are showing negative values of the slip while blue lines are showing positive values. For both cases, the effective slip clearly follows the general trend of the modulus of the "complex" slip λ_1 shown in green but we observe periodical changes in the sign of the effective slip length λ_{1E}. In the limit of small r with $n_R > 1$, the third term in Eq. 6.37 is dominant, and Eq. 6.37 simplifies to $\lambda_{1E} \approx 1/r^{n_R-1}\cos\left(n_I \ln(r)\right)$. This expression is reported using a black line in Figure 6.7. It clearly shows that it provides a very good description of the evolution of the effective slip with r and it reproduces the successive changes of sign. The normalized wave length Λ for the change of sign can be deduced from this relation as $\Lambda \approx \exp(\pi/n_I)$ and its magnitude is thus very sensitive to the value of the complex part n_I of the solution n. The sign of the effective slip is clearly understood to come from the shear at the wall resulting from the direction of the vortex rotation. A perfect slip (zero shear) is observed between two vortices. It is clear that such a slip behavior is questionable for real surfaces where a positive slip is expected. As shown in Figure 6.7b the slip has a positive value before it cancels while it is negative in Figure 6.7a. The case with a positive slip may be consistent with the existence of only one vortex

in the corner. Following Moffatt (1964), we can show that the ratio ρ of the distance to the corner of two successive vortices is given in each fluid by $\rho = \exp(\pi/n_I)$. We recover here the wave length Λ observed for the change of sign. This relation indicates that small values of n_I induce a relative large distance between two successive vortices. An infinite vortex observation being limited in real flow by the continuum limit, in some cases only one vortex may be observed making consistent the proposed slip. Taking for instance a millimetric drop of water moving on a plane surface in a more viscous oil, the selected solution for n has to satisfy $n_I \sim 0.2$, corresponding for example to the solution found for $\alpha = 60°$, $Ca = 0.01$ and $\Gamma = 2$ and reported in Figure 6.6f.

We end the discussion by considering a slip length of the general form $\lambda_k(r)$ for both the advancing and the receding fluids, with the imposed condition that $\lambda_k(r)$ is positive and real. Different slip models have been reported (see for example Dussan V., 1976; Sibley et al., 2015) to consider the singularity of the solution close to the contact line. Imposing a zero slip condition gets $n = 0$ and the solution has the form of equation 5.11 with both stress and pressure diverging (Huh and Scriven, 1971) as r^{-1}. A constant slip imposes $n = 1$ and removes the singularity at the contact line in the stress but not in the pressure. The function $f(\phi, n)$ has then the form (Anderson and Davis, 1993) of equation 5.12. Non-constant slip models with $n > 1$ solve both singularities and the function f has then the shape considered in this work. Replacing the stream function $\psi_k = r^{n+1} f_k$ in relations (5.45) and (5.46) we get that the the Navier-slip conditions are satisfied if the slip lengths $\lambda_k(r)$ have the form:

$$\lambda_1(r) = r\frac{f_1'|_{\phi=0}}{f_1''|_{\phi=0}} - \frac{1}{r^{n-1}}\frac{1}{f_1''|_{\phi=0}} \quad ; \quad \lambda_2(r) = -\frac{1}{r^{n-1}}\frac{1}{f_2''|_{\phi=\pi}} - r\frac{f_2'|_{\phi=\pi}}{f_2''|_{\phi=\pi}} \tag{6.39}$$

With relation (6.39), we can recover the above mentioned slip lengths and in particular the shape of the slip law introduced by Kirkinis and Davis (2013) and considered in our work. As a consequence, this slip law provides the general shape for a Navier-slip length allowing Stokes flow description in a corner. Relation (6.39) shows that a positive real slip can only be imposed on the wall if n is real but then the infinite series of Moffatt vortices is not observed. When n is a complex number then $\lambda_k(r)$ is complex and induces a solution with an effective slip as discussed above.

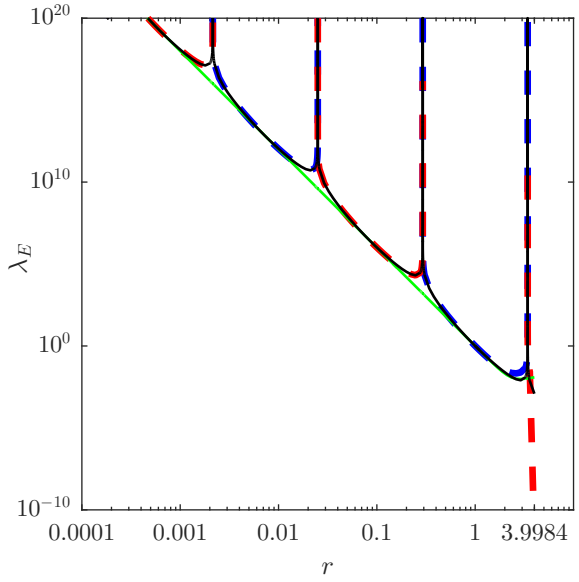

(a)

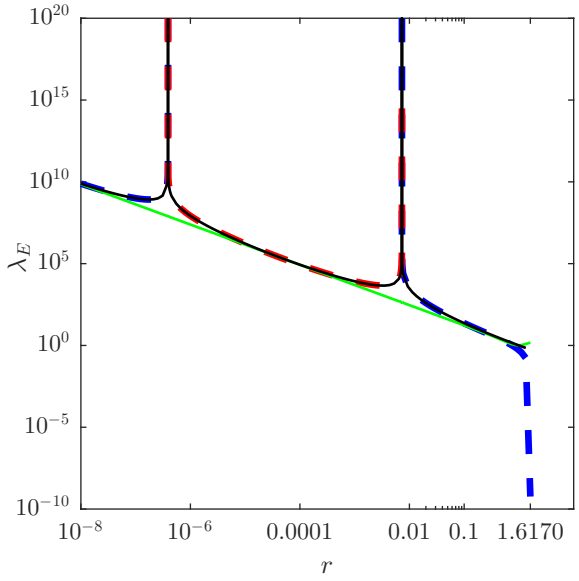

(b)

Figure 6.7: Example of effective slip length for the advancing fluid. — negative part of equation 6.37; — positive part of equation 6.37; — $\lambda_{1E} \approx \ell/r^{n_R-1}\cos[n_I \ln(r/\ell)]$; — Modulus of equation 6.37. (left) for the case reported in Kirkinis and Davis (2014) shown in Figure 6.1*b* $n = 6.999190 + 1.278228\,i$ ($Ca = 0.01$, $\Gamma = 0$, $\alpha = 1$rad); (right) for the case shown in Figure 6.5b: $n = 2.231697 + 0.319340\,i$ ($Ca = 0.01$, $\Gamma = 0.1$, $\alpha = 50°$)

6.5 Summary

In this chapter we have reconsidered the derivation proposed in Kirkinis and Davis (2014) to study the flow in the corner formed by a moving contact line between two viscous fluids. This extension makes it possible to obtain a complete view of the flow structure for any fluid/fluid and contact angle combination. Solutions for real values of n (the stream function has the form $\psi_k = r^{n+1} f_k$) provide regular flows in the corner, and flow splitting is observed depending on the parameters. Increasing the values for n, increase the number of separations. Solutions for complex values for n result in an infinite series of Moffatt vortices on both sides of the interface. The flow structure is significantly dependent on both the dynamic contact angle and the viscosity ratio while it is weakly affected by the capillary number and the static angle. Moffatt vortices can be located in the center of the wedge (the classical representation of Moffatt vortices) but they can deform and drift to the interface or to the wall. We named these structures as "corner vortices", "detached corner vortices", "interface vortices" and "wall vortices".

A slip law of the form $\lambda = \ell^n / r^{n-1} - b(\alpha, n)\, r$, as proposed by Kirkinis and Davis (2013), provides the general shape for a Navier-slip length allowing Stokes flow description in a corner. A positive slip, as observed on real surfaces, can only be imposed on the wall if n is real and then the infinite series of Moffatt vortices cannot be observed. Indeed, a solution with a complex number for n corresponds to an effective slip characterized by alternative changes of sign. However, the cutoff imposed by the continuum limit may restrict the vortex series to only one vortex in the corner. Such a situation with an imposed positive slip may then be selected by the flow. Vortices generated by the motion of a moving contact line have yet to be observed. Well controlled experiments or direct numerical simulations are required to resolve this point. Note that the presence of internal vortices is connected to a vortex organization in the receding fluid where the vortex detection may be more accessible in experiments.
Next, in chapter 7, we will look for evidence of the existence of some of these vortices numerically, discussing their origin.

Chapter 7

Numerical evidence of vortices in the vicinity of a moving contact line.

In chapter 6 we saw the possible existence of Moffatt vortices in the vicinity of the contact line, using a special slip boundary condition at the wall. In this chapter we use *JADIM* to determine if such vortical structures (Moffatt vortices) are possible in the context of the full Navier-Stokes solution since the technique used in chapters 5 and 6 did not take into consideration the curvature associated to the normal stress balance at the interface and the influence of the flow away from the contact line.

7.1 Background

In the knowledge of the author only two references have reported the flow patterns close to the contact line while using boundary conditions at the wall different from the classical no slip: (Sheng and Zhou, 1992) employing three different slip models, reported anecdotally vortices close the contact line for their third model and Sibley et al. (2012) when analyzing the interface formation model (see Shikhmurzaev, 1993a), they reported a recirculation close to the contact line and was regarded as a flow-induced Marangoni effect due to the model. An obvious constraint on this analysis is that the numerical solver must be capable of delivering a "clean" flow field. A preliminary test is conducted using VOF-FCT-CSF method against the new front-tracking method (present implementation, see chapter 3, section 4.6, figure 4.25). The test is the spreading of a viscous drop used in chapter 4 with fluids

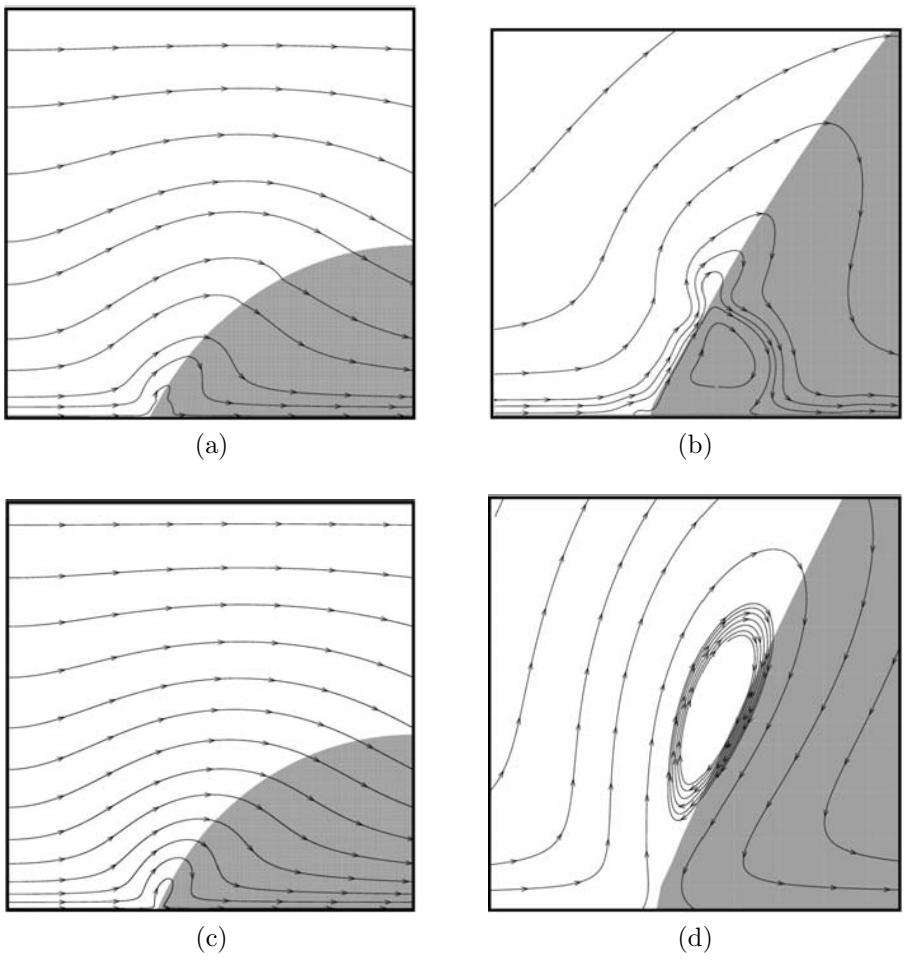

Figure 7.1: Streamlines of a viscous drop spreading as in section 4.6: $R_0 = 0.5$, $\rho = 1$, $\Gamma = 1$ and $\sigma = 7.5$. Using: a) VOF-FCT-CSF; b) zoom-in close to the contact line in a); c) Front tracking with lagrangian markers (current implementation); d) zoom-in close to the contact line in c)

having the same properties, for a relatively low Laplace number $La \sim 60$. The boundary condition at the walls used for this test for both methods is the no slip boundary condition except in the rightmost vertical boundary which is treated as a symmetry line. The dynamic contact angle model is prescribed at the contact line. The streamlines pattern at $\tau \sim 0.7$ ($\tau = t\mu/\rho R_0^2$) in the reference frame of the contact line is given in figure 7.1. It is immediately clear that the VOF-FCT-CSF method (figures 7.1a and 7.1b) provided the worst description of the flow close to the contact line if the objective is the discussion of the presence of vortices seen in chapter 6. Remarkably, the front-tracking method with lagrangian markers (figures 7.1c and 7.1d) provided a clean flow in the vicinity of the contact line, showing a recirculation at the interface. When we approach the corner ($r \to 0$), the rolling motion typical of a no slip boundary condition is recovered, and the large recirculation at the interface can be identified as the flow "splitting" shown in section 5.2 comparable to figure 5.2a for the same viscosity ratio. A similar flow pattern can be found in Sui and Spelt (2013b) for the Level-set method. As a consequence, the front-tracking method with lagrangian markers, using artificial tangential velocity Ceniceros et al. (2010) (to avoid the introduction of noise due to the reconstruction process) will be used in the following to investigate the flow close to the contact line.

7.2 Problem statement

For this numerical investigation, we apply the no slip boundary condition and the Navier-slip law in two separate conditions. The first is considering the slip length as a constant $\lambda = \ell$, so a uniform slip is expected along the wall. The second condition will use a variable slip length in the same sense as in Kirkinis and Davis (2013) and Kirkinis and Davis (2014) (see chapter 6), recovering the no slip boundary condition at some distance r^* from the contact line. Since we do not know a priori the solution an the corresponding value of n, we simply apply a sinusoidal variation of λ, of the form:

$$\lambda(r) = \begin{cases} \frac{1}{2}\ell\left(\sin\left(\phi + \frac{\pi}{2}\right) + 1\right) & \text{if } r \leq r^*, \\ 0 & \text{if } r > r^* \end{cases} \tag{7.1}$$

where ℓ is the maximum value of the slip length, r is the vertical distance from the contact line to the eulerian cell center at the wall, r^* is the vertical distance from the contact line where the no slip boundary condition is recovered and ϕ is defined as $\phi = \pi r/r^*$. The shape of this slip condition is plotted for illustrative purposes in figure 7.2a for $\ell = 100$ and $r^* = 1$ (both

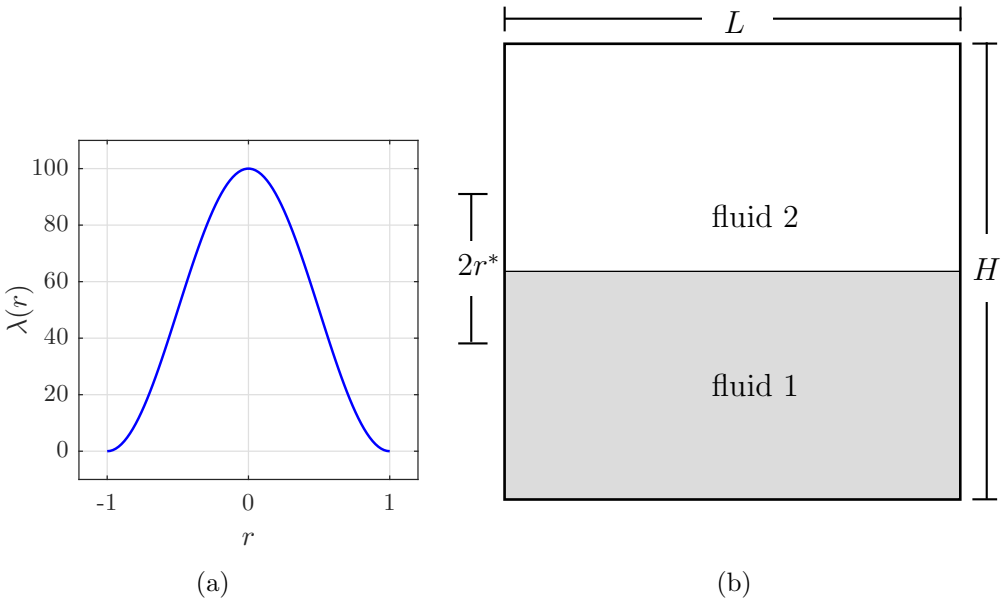

Figure 7.2: 2D Capillary rise. Properties of fluid 1 are set such that $Re < 1 \times 10^{-3}$ and $Ca < 1 \times 10^{-3}$. a) Variable slip length for $\ell = 100$ and $r^* = 1$; b) Domain definition and initial interface position.

normalized by r^*). The problem to be analyzed is a 2D capillary rise. The computational domain is a square box $L = H$ such that $L = 1.5$mm. See figure 7.2b, where we have defined also $r^* = L/6$ (this parameter will be tested). Properties of fluids are selected such that $Re = \rho U_{cl} r^*/\mu < 1 \times 10^{-3}$ to ensure Stokes flow in the corner and at the same time, to keep low capillary numbers $Ca = U_{cl}\mu/\sigma$. Both horizontal surfaces are treated as no slip walls, while the right vertical surface is a symmetry line. On the left vertical surface, different slip conditions will be applied. This configuration is selected because allows the interface to quickly acquire the contact angle imposed and also allows the interface to keep the angle longer than with other configurations (i.e. a drop). Another reason for this configuration is that for angles close to 90°, it is possible to obtain a moving contact line with an interface almost flat as considered in the analytical part in chapter 6. Since the flow inside the slip region will be solved, the static contact angle is imposed as a boundary condition for the interface at the wall.

7.3 No slip

A preliminary test is conducted in a uniform grid of 240×240. A static contact angle of $47°$ is imposed using the no slip boundary condition. A viscosity ratio of $\Gamma = 0.001$ is selected. This is done because small Γ introduced large perturbation at the interface in the test shown in section 7.4.2. Properties of fluids are taken as $\rho_1 = \rho_2 = 1000\text{kg/m}^3$, $\mu_1 = 3 \times 10^{-4}\text{Pa s}$ and $\sigma = 4 \times 10^{-9}\text{N/m}$ for $Re \approx 1 \times 10^{-4}$ and $Ca \approx 9 \times 10^{-3}$. We show this test here to have a reference of how a velocity field should look without slip (except of course the one that is numerically induced $\sim \Delta x/2$) and discard the presence of perturbations due to spurious velocities, which should increase for fluids with different viscosities. The initial configuration of the interface is a flat horizontal line (see figure 7.2b). Figure 7.3 shows a sequence of streamlines for selected times $\tau = 4.7 \times 10^{-3}$, $\tau = 3.4 \times 10^{-2}$ and $\tau = 3.6 \times 10^{-2}$ (which were normalized by characteristic time $\tau = t/t^* = t\mu/\rho r^{*2}$). Coordinates x and y are normalized by L in this case. Figure 7.3a, 7.3b and 7.3c present a recirculation at the interface as a common feature with what was shown in figure 7.1 for a viscous drop with $\Gamma = 1$ and also compatible with the no slip boundary condition in corner stokes flow shown in chapter 5 with the flow splitting in the less viscous fluid. Any departure from this pattern needs to be considered as an effect of the slip boundary condition, shown in the next sections. Note also, that no perturbation of the stream lines is present at the interface, which lead us to think that spurious velocities are being minimize by the method as expected.

7.4 Uniform slip length.

Using a uniform grid of 240×240 cells, a static contact angle of $47°$ is imposed at the interface and ℓ is set to be large enough $\ell = 100L/6$, compared to the grid size $\Delta x = L/240$, to ensure the solution of the flow inside the slip region and a viscosity ratio of $\Gamma = 1$ is selected.
Four selected times τ are reported in figures 7.4 and 7.5. Snapshots of streamlines at selected times are presented in figures 7.4a, 7.4c, 7.5a and 7.5c revealing the presence of a recirculation around the contact line that begins with an elongated form with the largest part of its area occupying fluid 2. The area occupying fluid 1 will increase in time to a point where the recirculation in fluid 2 is so small that its presence is only detected by the vorticity field (figure 7.5d). It is important to note that streamlines are crossing the interface which did not occur in the analytical part (chapter 6). This is because in this spreading interface, the velocity along the interface is not uniform.

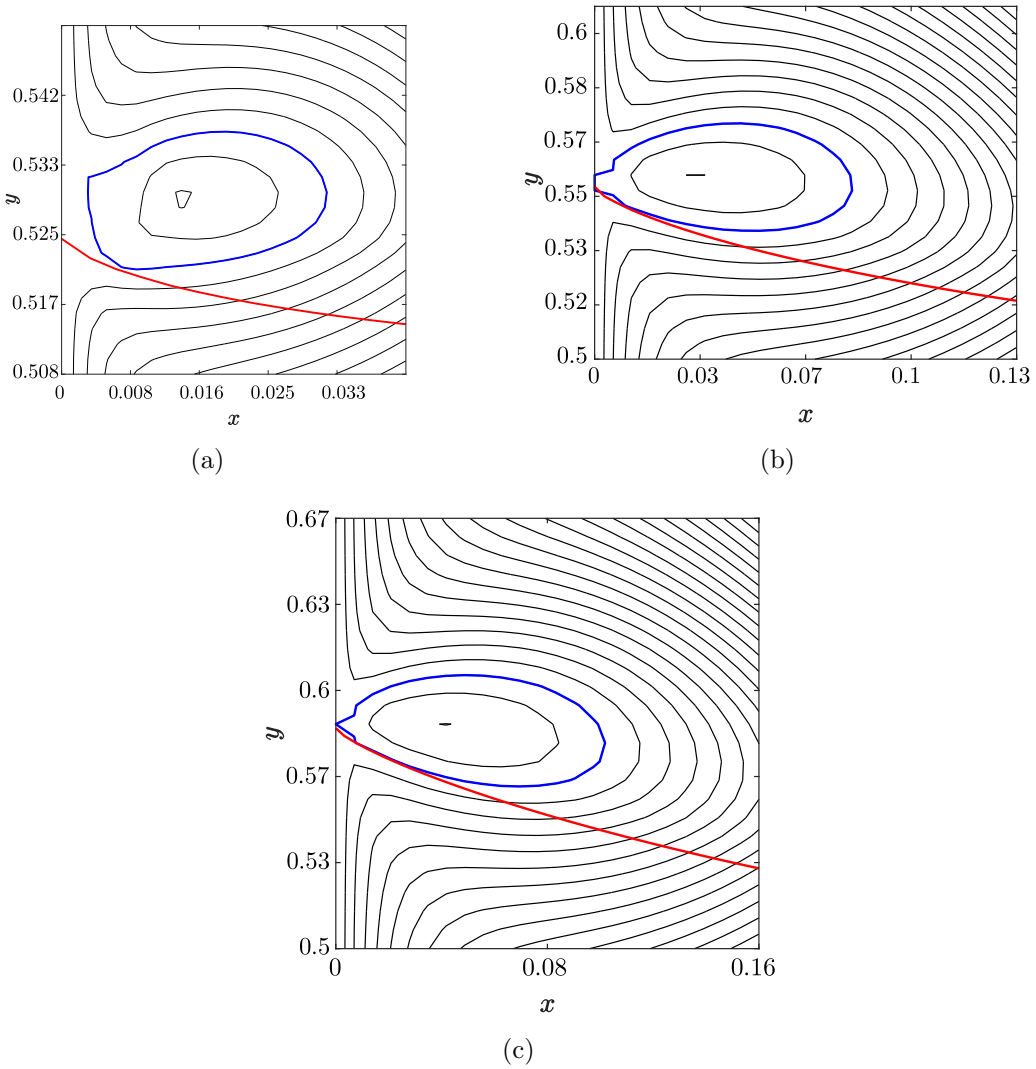

Figure 7.3: Snapshots of streamlines in the vicinity of the contact line for $\alpha_s = 47°$, $\Gamma = 0.001$ and no slip condition at the wall. Axes are normalized by L. The Streamlines sequence are reported at: a) $\tau = 4.7 \times 10^{-3}$; b) $\tau = 3.4 \times 10^{-2}$ and c) $\tau = 3.6 \times 10^{-2}$. — streamline contour $\psi = 0$; — fluid interface

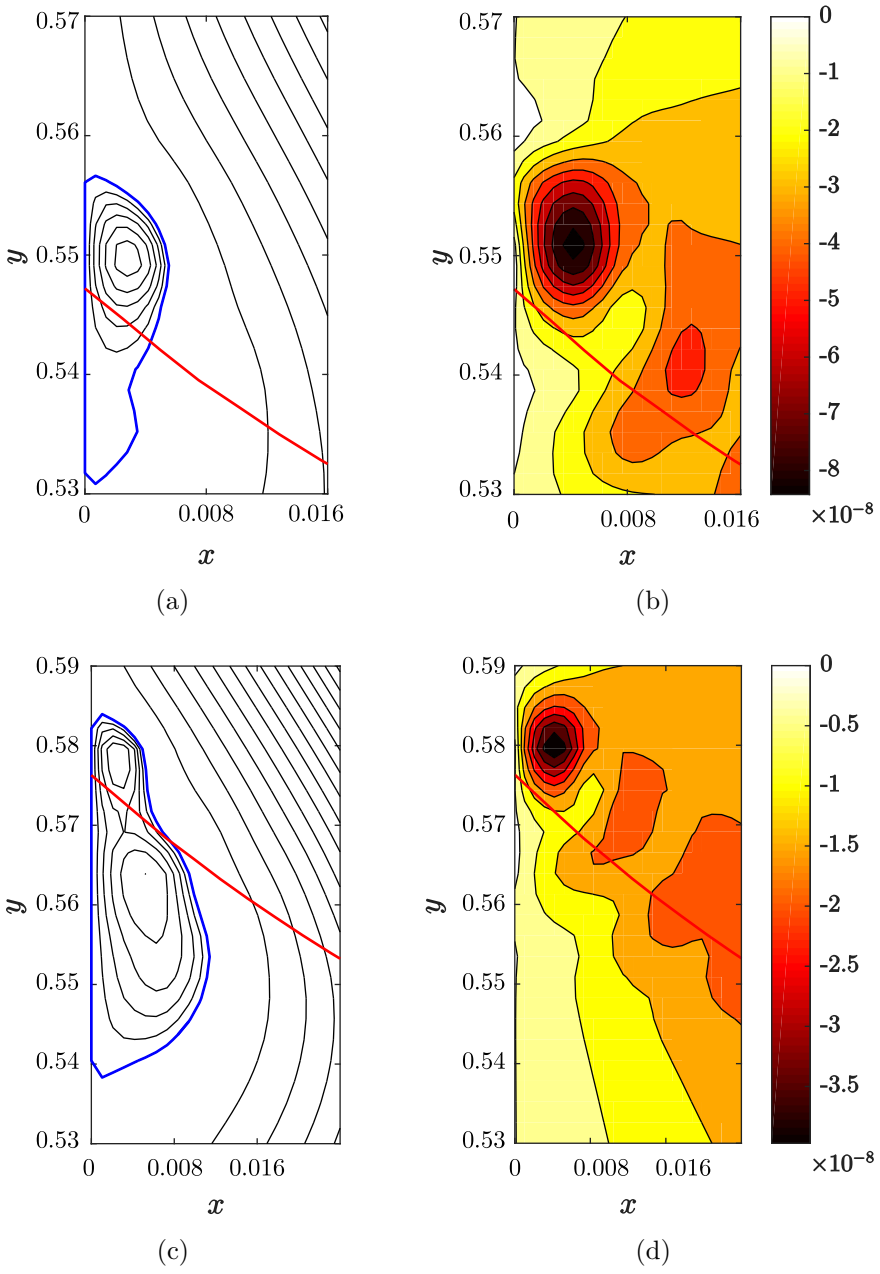

Figure 7.4: Snapshots of vortical patterns and vorticity field in the vicinity of the contact line for $\alpha_s = 47°$, $\Gamma = 1$ and a uniform slip length. Axes are normalized by L. The sequence reported is for: a) Streamlines at $\tau = 8 \times 10^{-4}$; b) vorticity field at $\tau = 8 \times 10^{-4}$; c) Streamlines at $\tau = 1.6 \times 10^{-3}$; d) Vorticity field at $\tau = 1.6 \times 10^{-3}$. — streamline contour $\psi = 0$; — fluid interface

Vorticity fields for the same sequence (figures 7.4b, 7.4d, 7.5b and 7.5d) reveal that the largest magnitudes around the contact line is concentrated in the recirculation at fluid 1. Some peaks of vorticity are also present a the interface. This might be due to small spurious velocities, still present.

7.4.1 Test for large contact angle

We change the initialization of the interface from a horizontal line to one forming 120° with the vertical and change the static contact angle to 100°, while keeping the other parameters constant for a uniform slip length. Results can be seen in figure 7.6. In this case, the interface shows only one recirculation present in fluid 2 that is always in contact to the wall. An important feature of this particular contact angle is that the velocity field is "cleaner" than that obtained with $\alpha_s = 47°$.

7.4.2 Low viscosity ratio test

Changing the viscosity ratio from $\Gamma = 1$ to $\Gamma = 0.001$ (i.e. a viscous fluid spreading in air) has immediate effects into the presence of vortices close to the contact line. Vortices are present in both sides of the interface for early spreading (figure 7.7a). Vortices will merge and invade the interface forming strange patterns as can be seen in figures 7.7b and 7.7c. As we had anticipated when performing the test for the no slip boundary condition in section 7.3, any pattern on the top of the "clean" flow obtained in section 7.3 must be due to the slip condition. It is difficult to say why such patterns are formed, specially since we have reduce spurious velocities considerably with the front-tracking method.

7.4.3 Test for the slip length ℓ

A test is conducted to evaluate the effect of ℓ on the uniform slip length formulations proposed. For this test a grid of finer resolution is used (480^2 cells) and an angle of 85° is prescribed, this is made to obtain an interface as "flat" as possible to be more in accordance to the analytical stokes solution presented in chapter 5.
In this test, we use $\ell = 1/6L$, $\ell = 10/6L$ and $\ell = 100/6L$. Results for this test at $\tau = 0.0017$ are shown in figure 7.8. When ℓ is only $1/6L$, no vortex can be identified in the field, save for a mild and elongated wiggly recirculation (see figure 7.8a). A different result is obtained when increasing ℓ to $10/6L$ and $100/6L$ in figures 7.8b and 7.8c respectively. There, vortices can be seen, one on each fluid at the corner and another one at he interface in

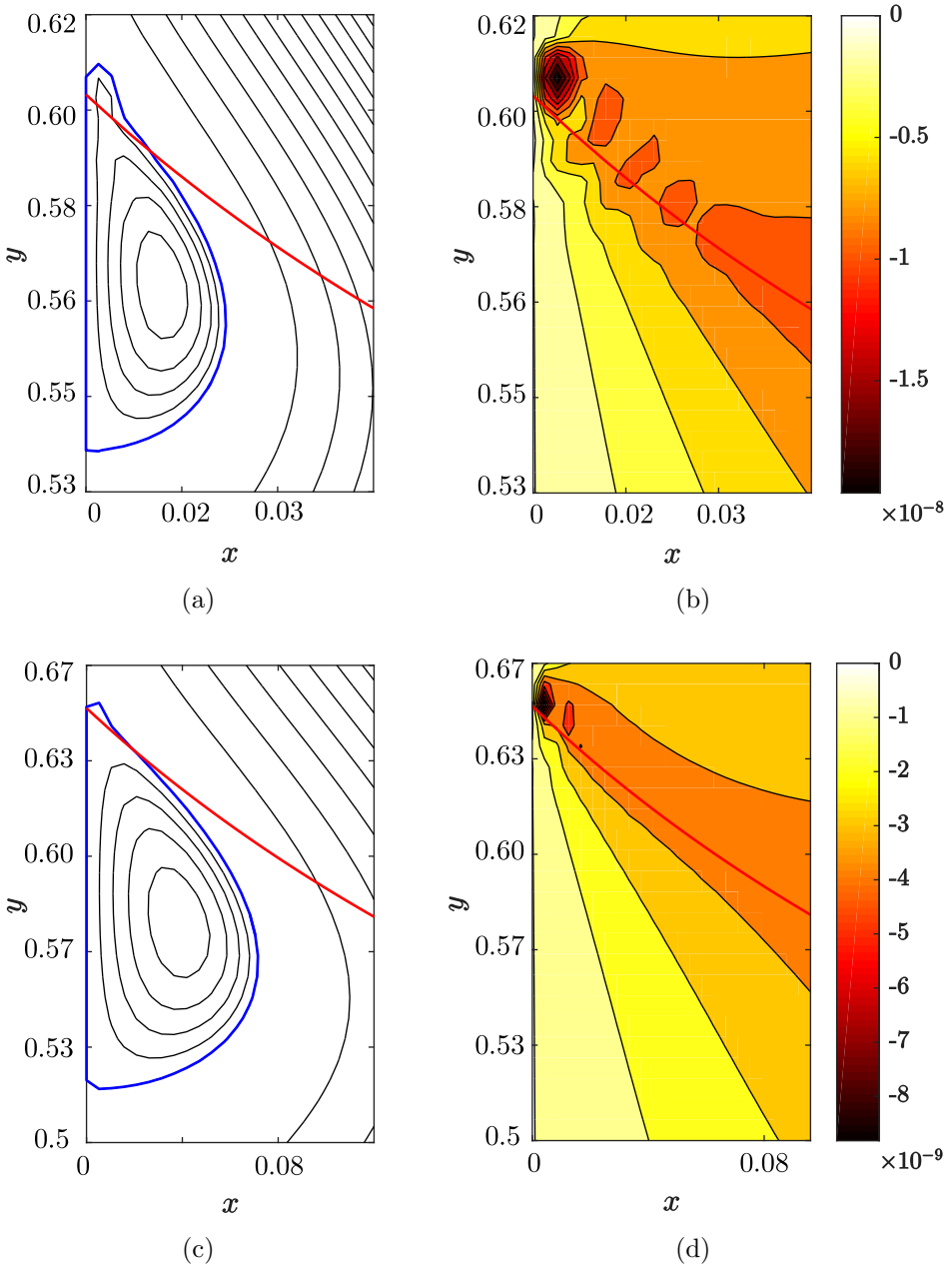

Figure 7.5: Snapshots of vortical patterns in the vicinity of the contact line for $\alpha_s = 47°$, $\Gamma = 1$ and a uniform slip length. Axes are normalized by L. The sequence reported is for: a) Streamlines at $\tau = 3.2 \times 10^{-3}$; b) Vorticity field at $\tau = 3.2 \times 10^{-3}$; c) Streamlines at $\tau = 7.8 \times 10^{-3}$; d) Vorticity field at $\tau = 7.8 \times 10^{-3}$. — streamline contour $\psi = 0$; — fluid interface

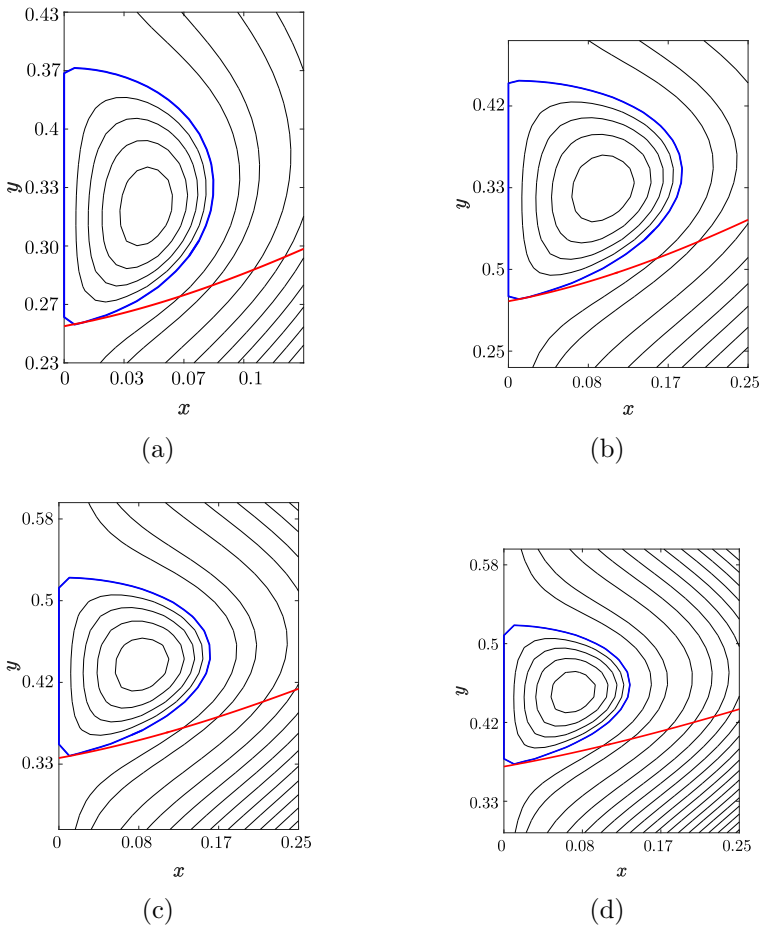

Figure 7.6: Snapshots of streamlines in the vicinity of the contact line for $\alpha_s = 100°$, $\Gamma = 1$ and a uniform slip length. Axes are normalized by L. The sequence reported is for: a) 1.6×10^{-3}; b) $\tau = 4.7 \times 10^{-3}$; c) $\tau = 7.8 \times 10^{-3}$; d) $\tau = 1.0 \times 10^{-2}$. — streamline contour $\psi = 0$; — fluid interface

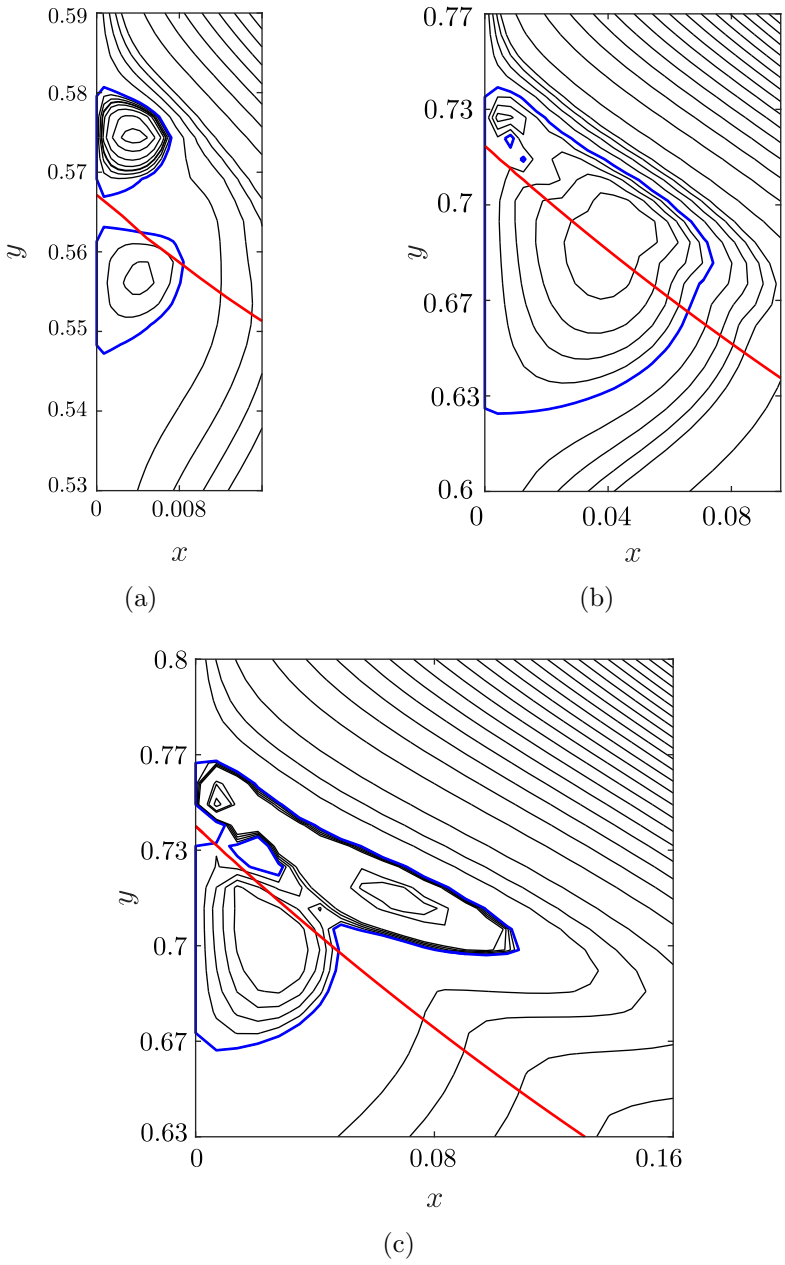

Figure 7.7: Time evolution of vortical patterns in the vicinity of the contact line for $\alpha_s = 47°$, $\Gamma = 0.001$ and a uniform slip length. Axes are normalized by L. The sequence reported is for: a) $\tau = 1.6 \times 10^{-3}$; b) $\tau = 2.0 \times 10^{-2}$; c) $\tau = 3.0 \times 10^{-2}$. — streamline contour $\psi = 0$; — fluid interface

fluid 1. When $\ell = 10/6L$ (figure 7.8b) the large vortex in fluid 1 is not in contact to the wall but "floating" away from it in a similar manner as was seen in figure 6.6 for the analytical part in chapter 6 which we denominated "detached corner vortex" ad equally similar to that for the no slip boundary condition (figure 7.3). When $\ell = 100/6L$, the large vortex is attached to the wall along with the small vortex in fluid 1. This large vortex can be considered "wall vortex" according to the definition given in chapter 5. We also see in figure 7.8 that some undulations are present at the interface, due probably to spurious velocities.

Further refinement of the grid (960^2) for the case of uniform slip does not seem to provide new flow features (see figure 7.9a), i.e. new vortices that would suggest a Moffatt vortices series. The interface still present undulations of unknown origin.

7.5 Non uniform slip length

A non uniform slip length should recover the no slip condition at some r^*. The key idea is to emulate the slip law reported in chapter 6 and references Kirkinis and Davis (2013, 2014). Also, it will tell us if vortices are present even for the case a variable slip length.

We use here a uniform grid of 240×240 cells, a static contact angle of $47°$, $\ell = 100r^*$ and $\Gamma = 1$, as was for the case in section 7.4 now using a variable slip length with $r^* = 1/6L$. A similar initial spreading as was seen for the uniform slip (figure 7.4) is seen in the case of a variable slip length in figures 7.10a and 7.10b with a unique recirculation at the contact line. In this case, the recirculation splits into two separate vortices and continues like that as time evolves (see sequence for selected times in figures 7.10c, 7.11a and 7.11b). Again in this case, the vorticity field reveals its strongest magnitude in the vortex of fluid 2 (see figures 7.10d, 7.10e, 7.10f, 7.11c and 7.11d). Since the viscosity ratio is $\Gamma = 1$, we can only speculate that vortices are generated in the receding fluid. The large recirculation in fluid 1, shows low values of vorticity. Again, some peaks of vorticity are seen at the interface pointing to some residual spurious velocities.

7.5.1 Low viscosity ratio test

Changing the viscosity ratio from $\Gamma = 1$ to $\Gamma = 0.001$ shows that there are vortices present on both sides of the interface (see figure 7.12) but the vortex/recirculation at the interface is separated from the other two vortex at the corner in a fashion compatible with the flow shown in figure 7.1d and

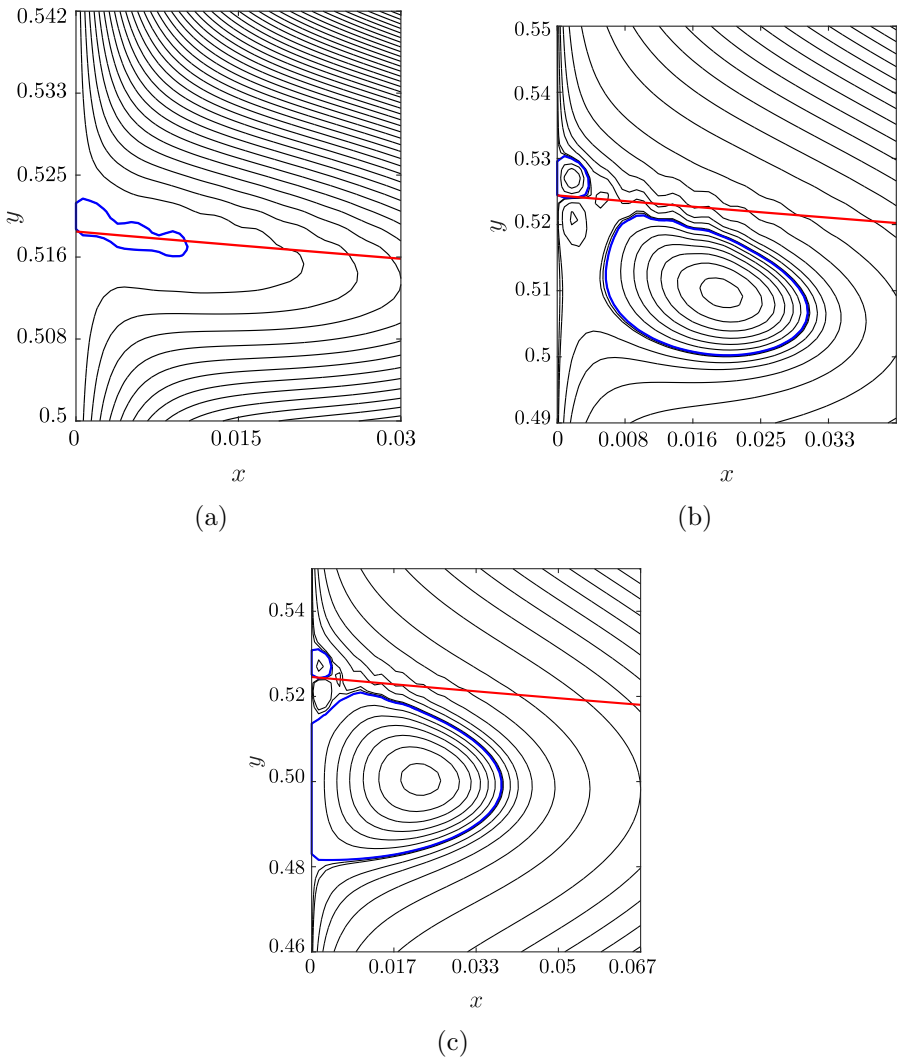

Figure 7.8: Streamlines in the vicinity of a contact line for capillary rise with $\alpha_s = 85°$, $\Gamma = 1$ and a uniform slip length at $\tau = 0.0017$, using: a) $\ell = 1/6L$; b) $\ell = 10/6L$; c) $\ell = 100/6L$. Axes are normalized by L. — streamline contour $\psi = 0$; — fluid interface

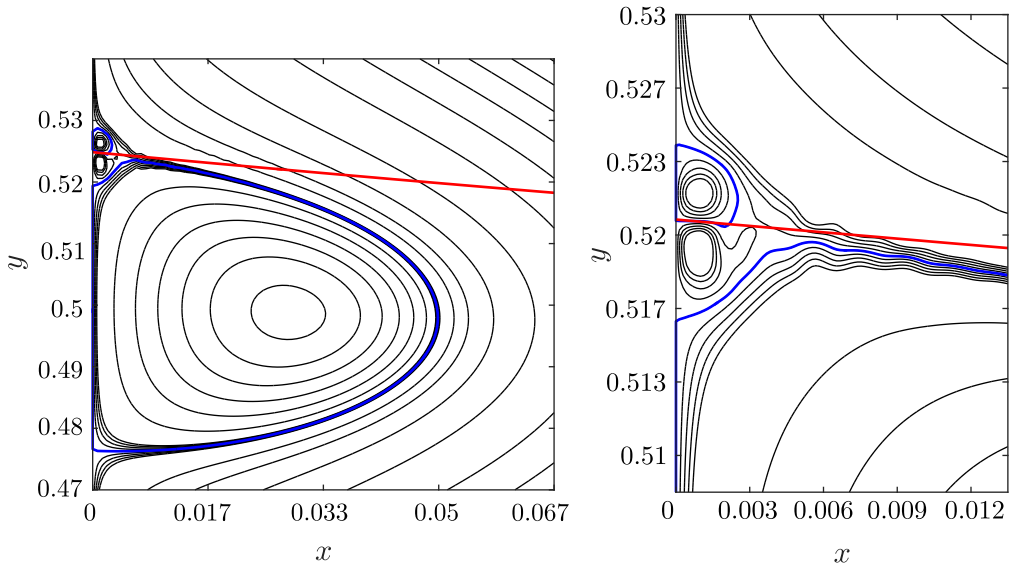

Figure 7.9: Streamlines in the vicinity of a contact line for capillary rise with $\alpha_s = 85°$, $\Gamma = 1$ at $\tau = 0.0017$, using a uniform slip with $\ell = 100/6L$. a) Large recirculation; b) zoom-in in the corner. Axes are normalized by L.

figure 6.1 using the case from Kirkinis and Davis (2014).

7.5.2 Test for slip region r^*

A second test is conducted in the variable slip formulation, we change r^* from 1 to 0.5 and see its effect on the flow using a grid of 480^2 cells. When $r^* = 1$, a configuration similar to that in figure 7.8b is identified, with vortices at the corner in both fluids and a large recirculation at the interface (see figure 7.13a). It is not clear why for this slip formula, contact angle and grid resolution, the flow presents large undulations close to the interface. Having $r^* = 0.5$, results in a field with no vortex in fluid 1 and also none at the interface (see figure 7.13b). Even at this level of refinement, there exist some undulations of the stream lines at the interface.

7.6 Evolution of vortices in time

The evolution of the size of vortices/recirculations that developed at the contact line is reported in figure 7.14. $\tilde{d}$ represents the average of height

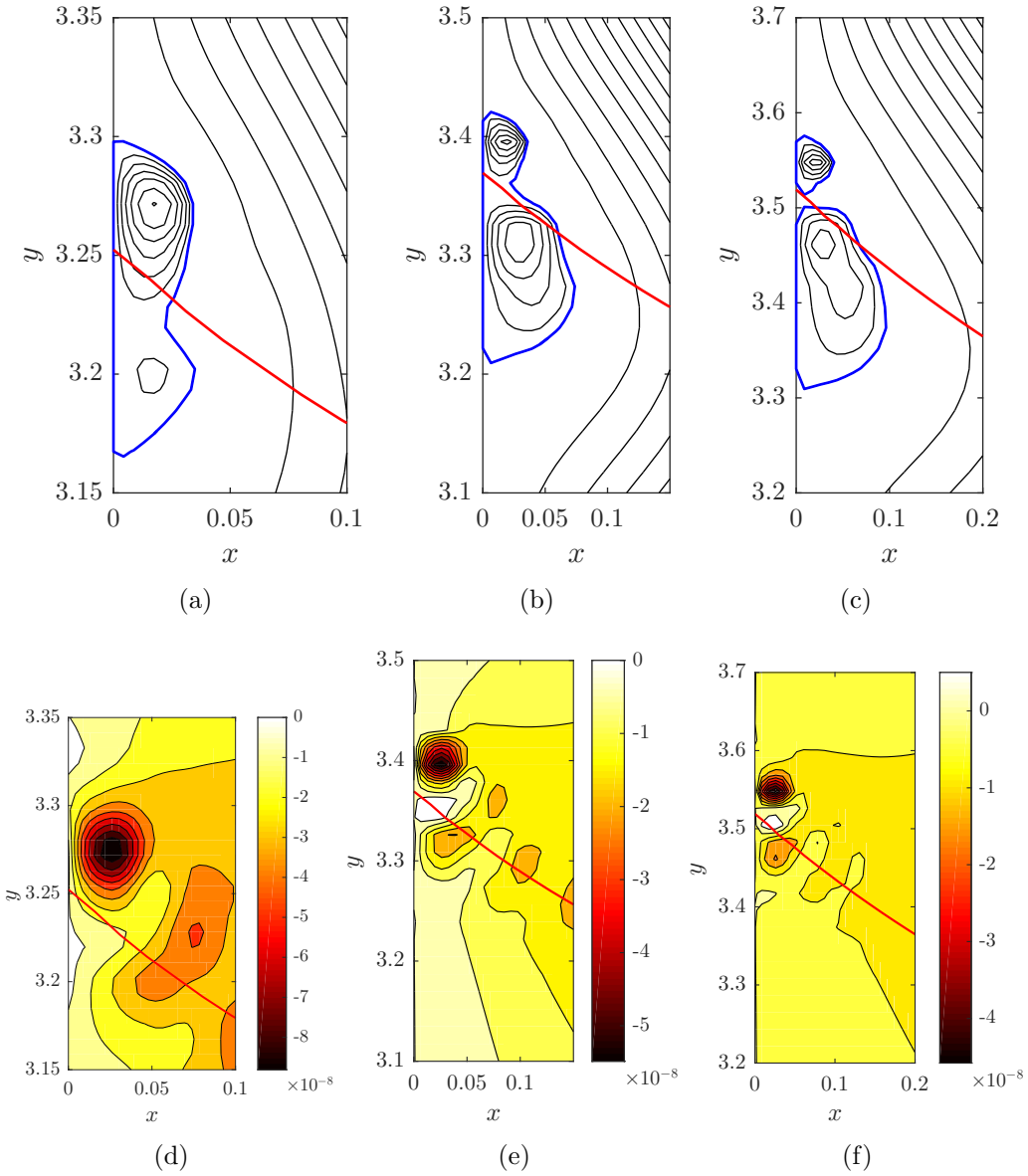

Figure 7.10: Snapshots of vortical patterns in the vicinity of the contact line for $\ell = 100/6L$, $\alpha_s = 47°$, $\Gamma = 1$ and a slip length calculated using equation 7.1. Axes are now normalized by r^*. The sequence reporting Streamlines is for: a) $\tau = 8 \times 10^{-4}$; b) $\tau = 1.6 \times 10^{-3}$; c) $\tau = 3.2 \times 10^{-3}$; reporting Vorticity field: d) $\tau = 8 \times 10^{-4}$; e) $\tau = 1.6 \times 10^{-3}$; f) $\tau = 3.2 \times 10^{-3}$;. — streamline contour $\psi = 0$; — fluid interface

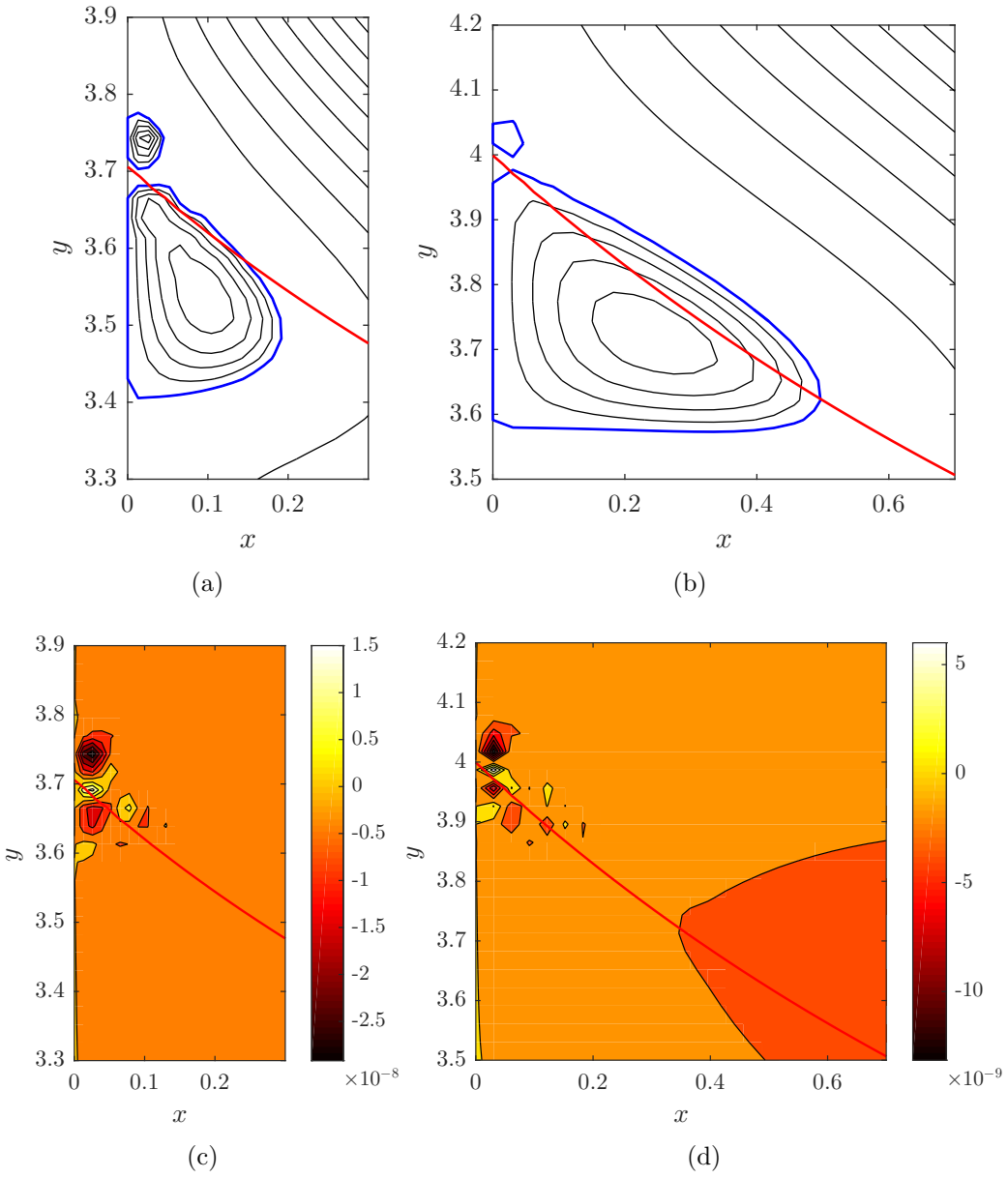

Figure 7.11: Snapshots of vortical patterns in the vicinity of the contact line for $\ell = 100/6L$, $\alpha_s = 47°$, $\Gamma = 1$ and a slip length calculated using equation 7.1. Axes are normalized by r^*. The sequence reporting Streamlines is for: a) $\tau = 6.4 \times 10^{-3}$; b) $\tau = 1.5 \times 10^{-2}$; reporting Vorticity field: c) $\tau = 6.4 \times 10^{-3}$; d) $\tau = 1.5 \times 10^{-2}$. — streamline contour $\psi = 0$; — fluid interface

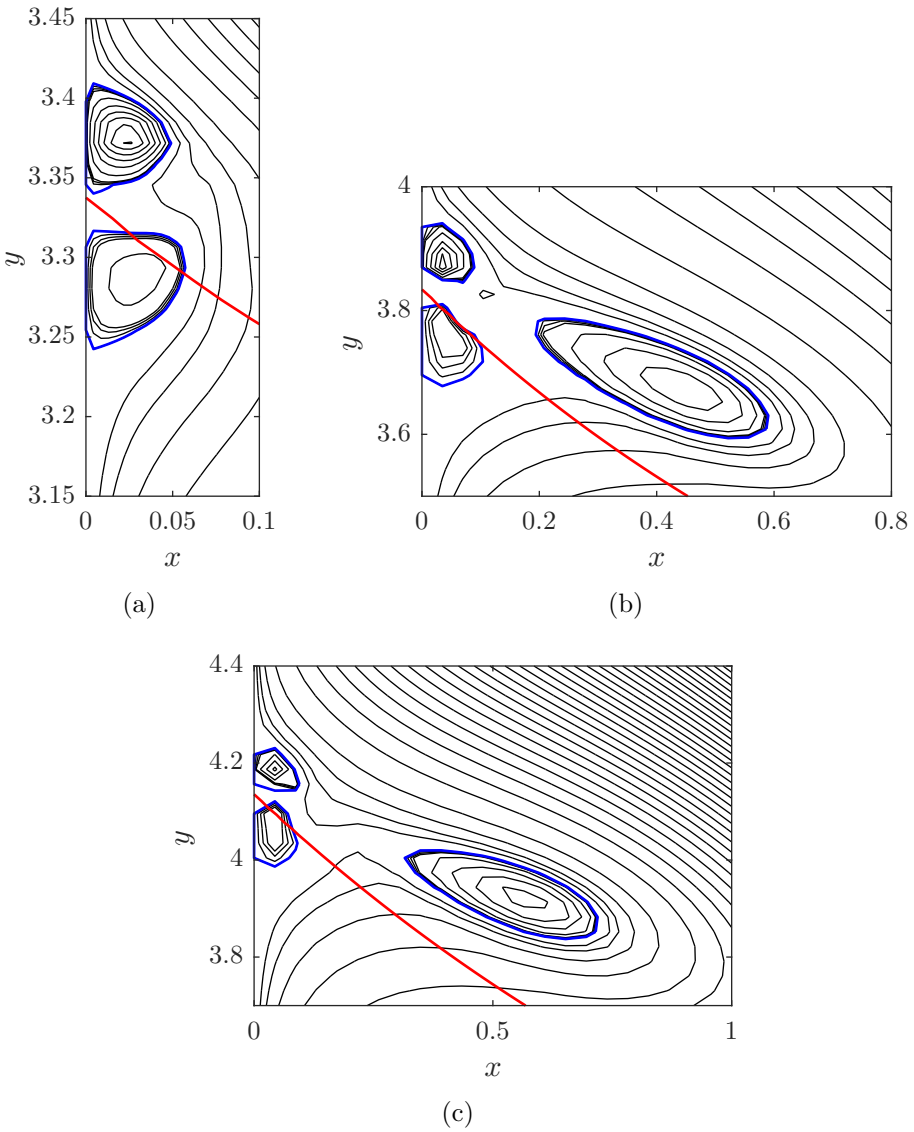

Figure 7.12: Time evolution of vortical patterns in the vicinity of the contact line for $\alpha_s = 47°$, $\Gamma = 0.001$ and a variable slip length (equation 7.1). Axes are normalized by r^*. The sequence reported is for: a) 1.6×10^{-3}; b) $\tau = 9.5 \times 10^{-3}$; c) $\tau = 2.0 \times 10^{-2}$. — streamline contour $\psi = 0$; — fluid interface

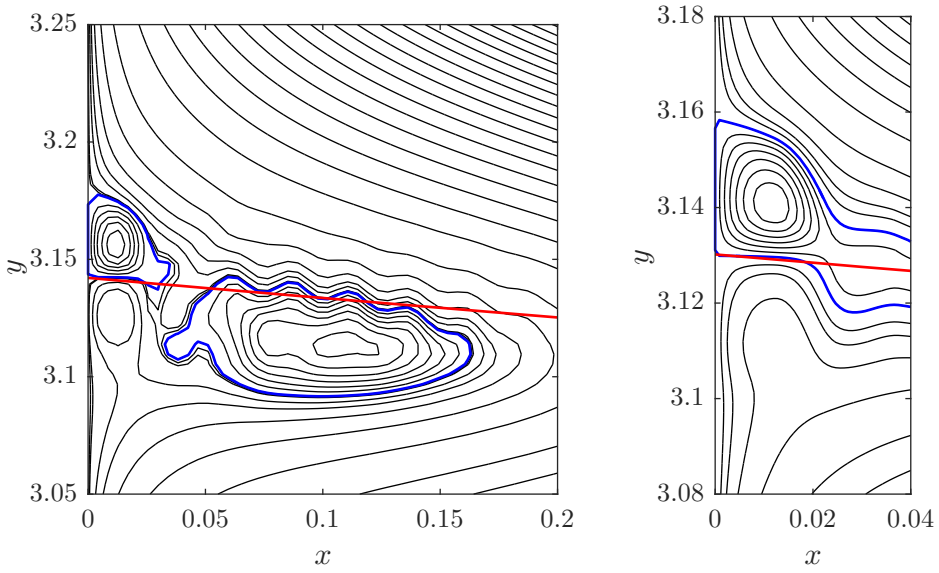

Figure 7.13: Streamlines in the vicinity of a contact line for capillary rise with $\alpha_s = 85°$, $\Gamma = 1$ and a variable slip length following equation 7.1 at $\tau = 0.0017$, using: a) $r^* = 1$; b) $r^* = 0.5$. Axes are normalized by r^*. — streamline contour $\psi = 0$; — fluid interface

and width of the vortex, normalized by ℓ. For the case of uniform slip length, $\Gamma = 1$ and $\alpha = 47°$, an increasing size of the unique recirculation is reported (figure 7.14a), this is pretty standard since we are in the early stage of spreading while for the case of variable slip length, three sizes are found. In blue, vortex size in fluid 1 (the advancing fluid), in red vortex size in fluid 2 (the receding fluid) and in green vortex size occupying both fluids (see figure 7.14b). Vortex size in fluid 2 seems to remain almost constant at $\tilde{d} \sim 0.5 \times 10^{-3}$ (or $\sim 10\mu$m in physical dimensions), while vortex size in fluid 1 oscillates in time, but it is always larger than in fluid 2 and larger as time evolves ($\sim 100\mu$m). The vortex occupying both fluids is only present at initial stages of spreading. Considering a low viscosity ratio, vortices size evolution for the case of constant and variable slip length are shown in figures 7.14c and 7.14d. In the case of uniform slip, it can be seen that vortices in the less viscous fluid (in red) keep their size relatively constant, while vortices size in the most viscous fluid 1 (in blue) oscillates up to a maximum of $\tilde{d} \sim 6 \times 10^{-3}$. There are places where both vortices fuse together in a large recirculation, this is shown in green circles. For the variable slip length (figure 7.14d), vortices on both fluids are present in almost the same size $\tilde{d} \sim 1 \times 10^{-3}$ and there are two places where an additional vortex/recirculation is present at the interface, they were shown in figures 7.12b and 7.12c.
In all tests for $\alpha_s = 85°$, the smallest vortex at the corner is about $\tilde{d} \approx 1.8 \times 10^{-4}$ or $\approx 5\mu$m in physical units. Further refinement of the grid (960^2) for the case of uniform slip did not provide new flow features (see figure 7.9a), except perhaps that the large recirculation has grown, reaching $x \approx 0.05$ in comparison with the coarser grid $x \approx 0.035$. Also, the size of the smallest vortices are kept at $\tilde{d} \approx 0.003$.

The evolution of of maximum vorticity in the vortex is presented in figures 7.15 and 7.16 for contact angles of $\alpha = 47°$ and $\alpha = 85°$ respectively for a viscosity ratio of $\Gamma = 1$ and a uniform slip length. In the case of $\alpha = 47°$, vorticity of vortex in fluid 2 is reported, while for $\alpha = 85°$, vorticity for vortices on both fluids are shown. In both cases the magnitude of vorticity decays in time. In the logarithmic scale, the trend of decay is according to a slop of ~ -1. It is difficult to characterize the vortices found here. One interesting comparison is the Lamb-Oseen (Lamb, 1932) vortex defined with:

$$U_\phi(r,t) = \frac{C}{2\pi r}\left(1 - \exp^{-\frac{r^2}{4\nu t}}\right) \tag{7.2}$$

$$\omega_z = \frac{C}{4\pi\nu t}\exp^{-\frac{r^2}{4\nu t}} \tag{7.3}$$

where U_ϕ is the azimutal velocity, C is the circulation and ν the kinematic viscosity. Vorticity decay of our results seems to follow consistently the ten-

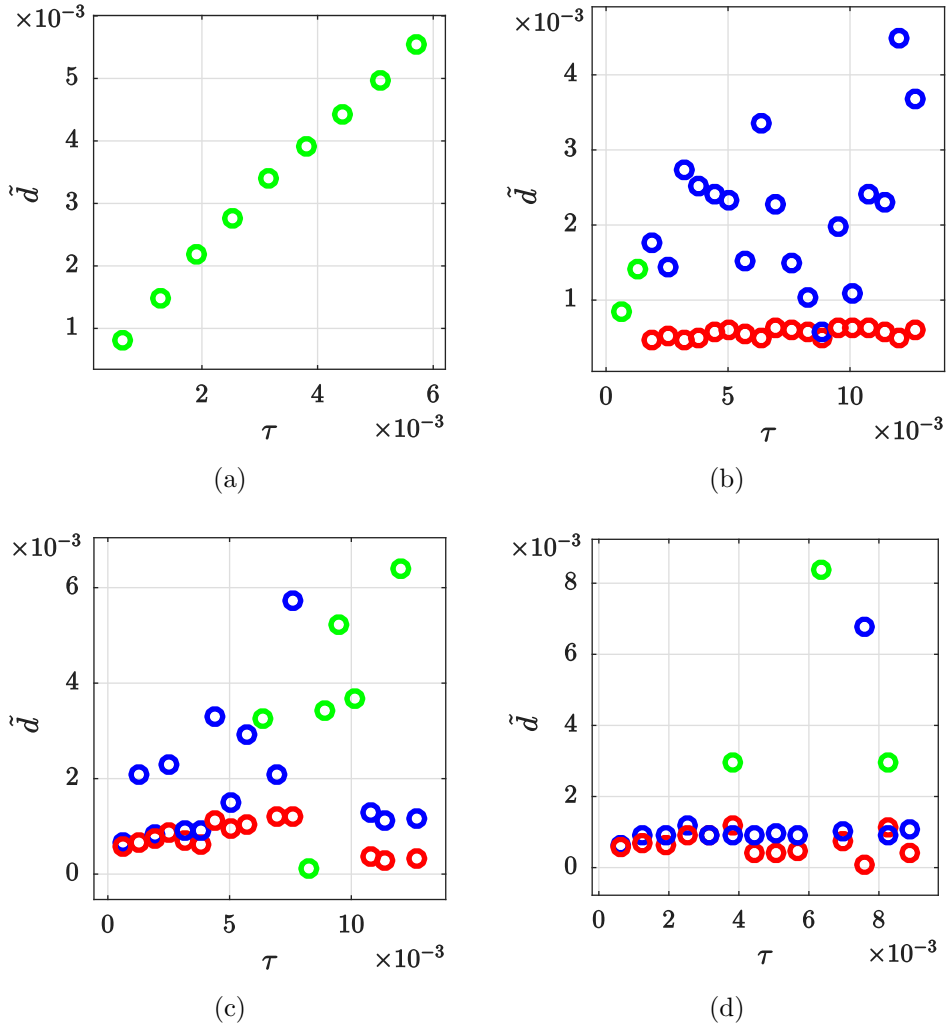

Figure 7.14: Vortices/recirculation size evolution for $\ell = 100/6L$ and $\alpha = 47°$. For $\Gamma = 1$: a) Constant slip length b) Variable slip length; For $\Gamma = 0.001$: a) Constant slip length; b) Variable slip length; ○ vortex in fluid 2; ○ vortex in fluid 1; ○ recirculation occupying both fluids or when recirculation only exists in one of them.

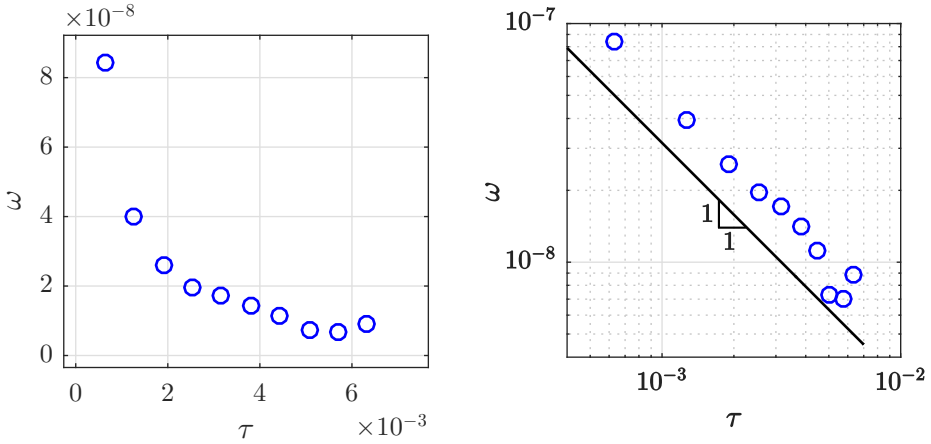

(a) (b)

Figure 7.15: Vorticity evolution in time for one vortex in fluid 2 for the case of $\alpha = 47°$, $\Gamma = 1$ and a uniform slip lenght. a) Lineal axes; b) Logarithmic axes. ○ vortex in fluid 2

dency of equation 7.3, but the size of the vortices analized here, remains almost constant. In the case of Moffatt vortices, both size and intensity are stabilized. Further tests are needed to determine the true nature of these vortices.

7.7 Summary

A preliminary investigation on the existence of vortices at a moving contact line has been presented. The numerical experiments reported in this chapter helped us to determined if vortices can be found in the vicinity of a moving contact line. We can say safely that the presence of these vortical patterns is enhanced by the use of some slip law at the wall. Using the no slip boundary condition creates a large vortex (which we called recirculation minding that this might be the mechanism selecting n in the analytical part) at the fluid interface that is coherent to what was seen in the analytical part (section 5.2, figures 5.2, 5.3 and 5.4) and the numerical test in figure 7.1. This is consistent with the idea that slippage occurs only in the vicinity of the contact line. Away from it, the picture will be consistent with the use of the no slip boundary condition. The use of a uniform or a variable sip length with an acute angle ($\alpha = 47°$), revealed the presence of vortices in both fluids. A larger angle ($\alpha = 100°$) showed a single vortex or recirculation in the

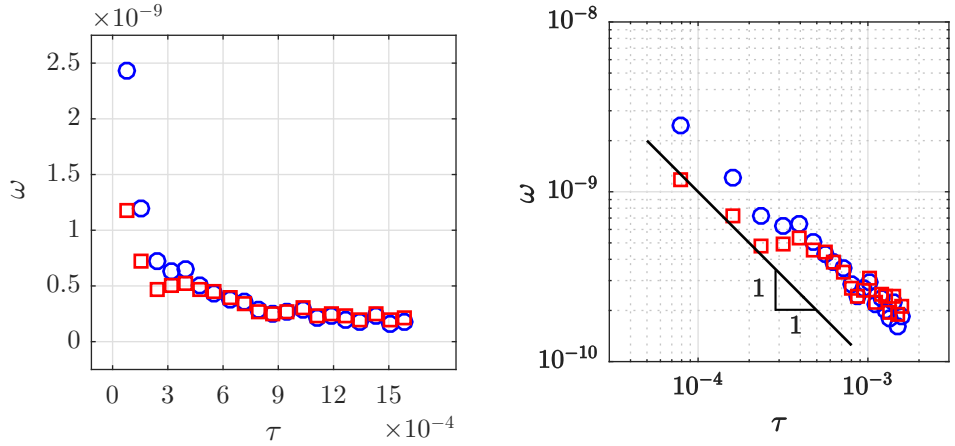

(a) (b)

Figure 7.16: Vorticity evolution in time for one vortex in fluid 2 for the case of $\alpha = 85°$, $\Gamma = 1$ and a uniform slip length. a) Lineal axes; b) Logarithmic axes. ○ vortex in fluid 2; □ vortex in fluid 1.

advancing fluid. Using a small viscosity ratio revealed in the case of uniform slip, vortices at the corner in each fluid that will merge and interact with a recirculation at the interface, making difficult the task of visualize them. In the case of variable slip length, and additional recirculation at the interface is found, and it is compatible with the case reported in the analytical part in figure 6.1 from Kirkinis and Davis (2014).

Vortices at the corner reached an equal size of $\tilde{d} \approx 0.5 \times 10^{-3}$ for $\Gamma = 1$ and $\tilde{d} \approx 0.001$ for $\Gamma = 0.001$, this was not observed in the analytical solution for complex n, there, vortices in both fluids where at least of one order of magnitude different in size. The most favorable conditions for the detection of vortices close to the contact line in this numerical experiment were observed using a contact angle of $\alpha_s = 85°$, that allowed the interface to be almost flat, and clean some undesirable features observed for $\alpha_s = 47°$. For $\alpha_s = 85°$ we found that the slip length ℓ must be larger than $\sim 10/6L$ to be able to detect vortices at the contact line, otherwise the flow field presents a wiggly recirculation pointing to an underdevelopment of the slip zone even when the grid resolution was found to be small enough ($L/\Delta x \sim 480$). For increasing values of ℓ we could identify the evolution from "detached corner vortex" to a "wall vortex" for the largest recirculation at the interface, compatible with the classification made in the analytical part in chapter 6. Using larger grid resolutions did not revealed new features, but considering figure 7.9, the connection between the two vortices in fluid 1 opens the door to consider that

we are seeing the first two vortices of a Moffatt series. Further research might give a final answer to this. The use of a variable slip length revealed also three vortices but contaminated with undulations at the interface. Decreasing r^* revealed only one vortex in fluid two. Increasing the resolution of the grid did not show any new features of the flow and the size of vortices in the corner were kept with a size of $\tilde{d} \approx 3 \times 10^{-3}$ almost one half of those observed for $\alpha_s = 47°$. Note that the large recirculation at the interface in this last test can be associated with the macroscopic motion who perhaps decide the value of n in the analytical solution in chapter 6 and setting the configuration of vortices in the corner. Grid resolution did not help in suppressing perturbations at the interface. We believe that this is a combination of the slip condition and residual spurious velocities, although, when using the no slip condition, this undulations at the interface were not observed. It was difficult to characterize this kind of vortices due to the fact that spreading is not a steady-state phenomenon. Nevertheless, it can be said that they might be caused by the initial impulse of the contact from rest, similar to the vortices generated by a bluff object against a normal flow (see Koumoutsakos and Shiels, 1996; Lian and Huang, 1989), this would explain the decay of vorticity with time reported here. We can say that a first step in the detection of vortices in the vicinity of the contact line has been taken. Further and more profound studies are needed.

Chapter 8

A new numerical model for moving contact lines

As explained in chapter 5, a full solution of Navier Stokes equations including the slip region for millimetric drops is still out of the reach of our current computational resources Maglio and Legendre (2014). We begin this chapter with a brief background statement in the state of the art of current subgrid models of the literature and the theory behind it. After that, we will describe the new subgrid model that we propose in this work in the context of the front tracking method and finally we will provide the validation against numerical tests and experiments.

8.1 Background

Although the local analysis performed in sections 5.2, 5.3 has provided great insight into the moving contact line problem, there is a factor that has not been taken into account: the influence of the external geometry (i.e. geometrical information far away from the contact line) and the effects of interface curvature (i.e. when Ca is not small to consider a flat interface). Asymptotic theories (see for example Huh and Mason, 1977; Hocking, 1977; Hocking and Rivers, 1982; Cox, 1986) provide insight in this cases. Figure 8.1 shows the moving contact line for two viscous fluids in the reference frame attached to it. From the hydrodynamic point of view there exist an inner (microscopic) region where the contact line is defined by the microscopic contact angle α_w which can be considered as the static contact angle α_w, although experimental evidence suggests otherwise (see Ramé et al., 2004). In this inner region, some slip boundary condition applies at the wall (i.e. Navier slip in section 5.3) and is valid up to a distance λ (typically slip length). At some point r^*

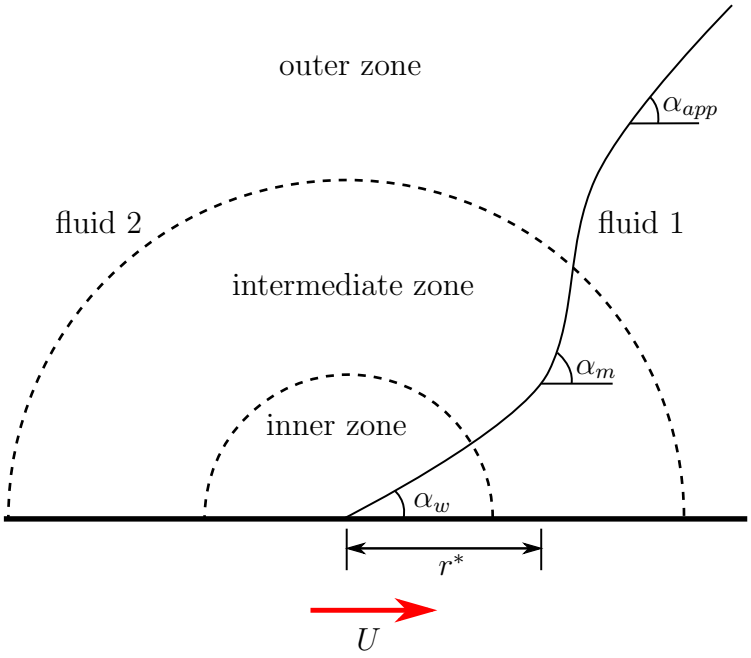

Figure 8.1: Moving contact line sketch in the reference attached to it, from the hydrodynamic point of view.

from the contact line on the wall, the effects of slip disappear and the no-slip condition is satisfied. Away from the contact line, an outer (macroscopic) region can be defined to be of scale L or some characteristic length of the flow (i.e. radius of a droplet). In this region, the interface is defined by the "apparent" contact angle α_{app}, which is not known a priori. Solutions of the inner and the outer zones can be matched at an intermediate zone where the contact angle is α_m and a characteristic scale L_m. The procedure of matching is described in Cox (1986), boundary conditions are those treated in section 5.2 (even for the inner region the normal stress to be matched to the outer zone must be that satisfying no-slip boundary conditions) including additionally the normal stress balance at the interface. From equation 5.17 we have:

$$-p_1 + \frac{2}{r}\left(\frac{1}{r}\frac{\partial\psi_1}{\partial\phi} - \frac{\partial^2\psi_1}{\partial r\partial\phi}\right) = -p_2 + \frac{2\Gamma}{r}\left(\frac{1}{r}\frac{\partial\psi_2}{\partial\phi} - \frac{\partial^2\psi_2}{\partial r\partial\phi}\right) \tag{8.1}$$

Substitution of equations 5.9 and 5.11 into 8.1, leaves at the interface:

$$-2r^{-1}\left[(\Gamma C_2 - C_1)\cos\alpha + (\Gamma D_2 - D_1)\sin\alpha\right] = -r^{-1}F(\alpha,\Gamma) \tag{8.2}$$

also, substitution of constants from equations 5.34, 5.38,5.35 and 5.39 yields the function:

$$F(\alpha,\Gamma)=\frac{\begin{array}{r}2\sin\alpha\left\{\lambda^2(\alpha^2-\sin^2\alpha)+2\Gamma\left[\alpha(\pi-\alpha)+\sin^2\alpha\right]\right.\\ \left.+\left[(\pi-\alpha)^2-\sin^2\alpha\right]\right\}\end{array}}{\begin{array}{c}\Gamma(\alpha^2-\sin^2\alpha)\left[(\pi-\alpha)+\sin\alpha\cos\alpha\right]\\ +\left[(\pi-\alpha)^2-\sin^2\alpha\right](\alpha-\sin\alpha\cos\alpha)\end{array}} \tag{8.3}$$

The matching procedure goes on (see Cox, 1986, for details), establishing relationships between angles at leading order:

$$g(\alpha_m,\Gamma)=g(\alpha_{app},\Gamma)+Ca_{cl}\ln\left(\frac{L_m}{L}\right) \tag{8.4}$$

$$g(\alpha_m,\Gamma)=g(\alpha_w,\Gamma)+Ca_{cl}\ln\left(\frac{L_m}{\lambda}\right) \tag{8.5}$$

combining equations 8.4 and 8.5, we get:

$$g(\alpha_{app},\Gamma)=g(\alpha_w,\Gamma)+Ca_{cl}\ln\left(\frac{L}{\lambda}\right) \tag{8.6}$$

where $g(\alpha,\Gamma)$ is given by:

$$g(\alpha,\Gamma)=\int_0^{\alpha}\frac{d\alpha}{F(\alpha,\Gamma)} \tag{8.7}$$

Equation 8.6 has been applied recently in the literature of numerical simulation of moving contact lines. We can mention for example the works of Dupont (2007); Afkhami et al. (2009); Dupont and Legendre (2010); Legendre and Maglio (2013); Sui and Spelt (2013a); Maglio and Legendre (2014); Legendre and Maglio (2015); Solomenko et al. (2017).
In general lines, the procedure to use equation 8.6 in numerical modeling of contact lines consists first in defining the outer zone scale L, typically, half a numerical grid distance is chosen $L=\Delta x/2$. Secondly, dimensionless contact line velocity (Ca_{cl}) must be calculated in a constant manner. Again, a good idea is to take the velocity of the control volume containing the contact line, at a distance $\Delta x/2$ from the wall (see Dupont and Legendre, 2010; Legendre and Maglio, 2013; Maglio and Legendre, 2014; Legendre and Maglio, 2015). Other ideas to calculate Ca_{cl} (see Solomenko et al., 2017), is to simply use the difference in positions of the contact line, divided by the time step. Once this quantities are defined, function $g(\alpha,\Gamma)$ in equation 8.6 is calculated numerically. In cases where the viscosity ratio is small $\Gamma\approx 0$, equation 8.7 takes the form:

$$g(\alpha,\Gamma)=\int_0^{\alpha}\frac{\alpha-\sin\alpha\cos\alpha}{2\sin\alpha}d\alpha \tag{8.8}$$

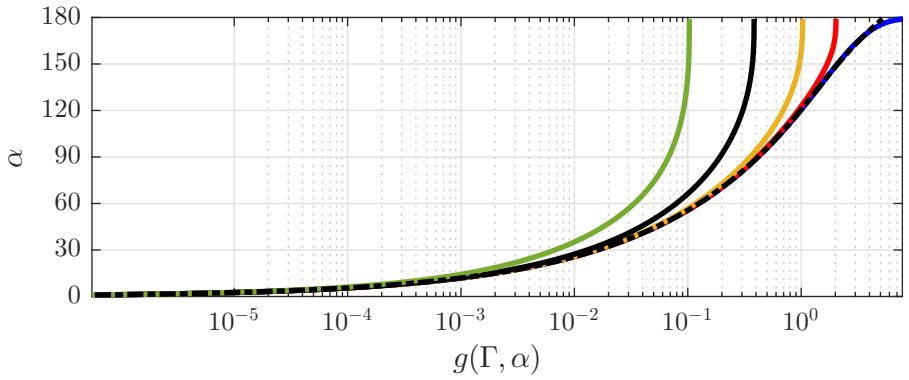

Figure 8.2: function $g(\Gamma, \alpha)$ (equation 8.7) for diverse viscosity ratios: — $\Gamma = 0$; — $\Gamma = 0.01$; — $\Gamma = 0.01$; — $\Gamma = 1$; — $\Gamma = 10$. For comparison, - - - polynomial in equation 8.9.

for simplicity in the implementation, equation 8.8 can be substituted by a polynomial form (see Mathieu, 2003):

$$g(\alpha) \approx \frac{\alpha^3}{9} - 0.00183985\alpha^{4.5} + 1.845823 \times 10^{-6}\alpha^{12.258487} \tag{8.9}$$

the inverse of this function which yields α, can also for simplicity be approximated by the polynomial:

$$g^{-1}(\alpha) \approx (9x)^{1/3} + 0.0727387x - 0.0515388x^2 + 0.00341336x^3 \tag{8.10}$$

then α becomes a numerical boundary condition that plays a role in the momentum equation. Figure 8.2 shows equation 8.7 for diverse viscosity ratios. For comparison, polynomial 8.9 is shown. We can see that the polynomial approximation matches almost perfectly equation 8.7 for $\Gamma = 0$, except for a small region near $\alpha = 180°$, but it departs from the curves for larger Γ. At $g \approx 0.1$, the difference in α between $\Gamma = 10$ and $\Gamma = 0$ is about $\sim 60°$. In the knowledge of the author, no analytical approximation for $g^{-1}(\Gamma, \alpha)$ is available in the literature for $\Gamma > 0$.

The results obtained when applying the procedure described before have yielded diverse results in the literature already mentioned. All coincide in good descriptions of the moving contact line position and shape of the interface.

Two important aspects are still missing when performing numerical simulations of the contact line. When using the dynamic contact angle model, it has been noticed that there exists a mesh dependent initial acceleration (see Legendre and Maglio, 2015) which does not allow grid convergence at

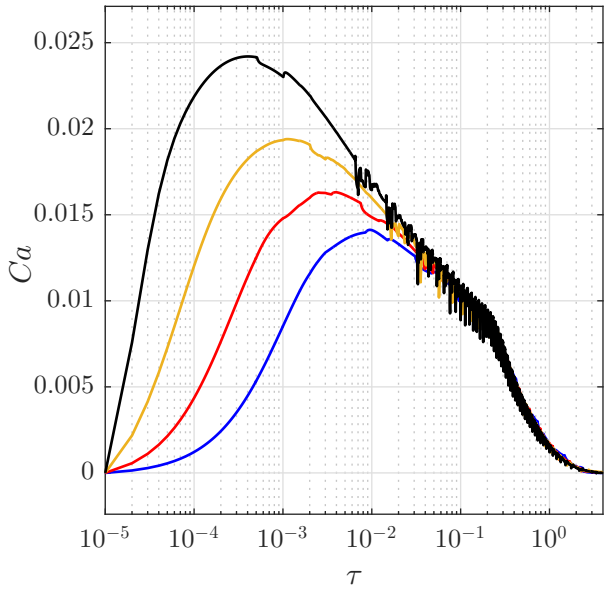

Figure 8.3: Velocity evolution for the numerical simulation of a 2D drop of radius 0.5 spreading on a solid surface using the front-tracking method, and the dynamic angle formulation (e.q. 8.6). Density and viscosity ratios are set to 1, surface tension is set to 7.5 and slip length to $\lambda = 1 \times 10^{-5}$. Colored line represent the grid resolution: — 32×32; — 64×64; — 128×128; — 256×256.

initial spreading. The integration of momentum equation at $t = 0$ using the finite volume method and the CSF formulation for the capillary contribution revealed an initial acceleration of the form:

$$a^0 \sim \frac{\sigma}{\rho}(\cos\alpha_w - \cos\alpha_d^0)\frac{1}{(\Delta x)^2} \tag{8.11}$$

Such initial acceleration for diverse grid resolutions can be seen in figure 8.3 for the spreading on a solid surface of a drop of radius $R = 0.5$, using viscosity and density ratios of 1 and a surface tension of $\sigma = 7.5$. The initial configuration for this problem was shown in figure 4.27. Non-dimensional time $\tau = t\mu/\rho R^2$ is used to normalize the time. There we can see that grid convergence cannot be achieved for initial acceleration, and also for maximum velocity of spreading. Similar results were found in Legendre and Maglio (2015). Additionally, we can see oscillations in the velocity reported, this are due to the front reconstruction process. When the reconstruction algorithm deals with the element at the wall, an additional constrain is imposed: the marker at the wall cannot be eliminated (i.e. the position of the contact line

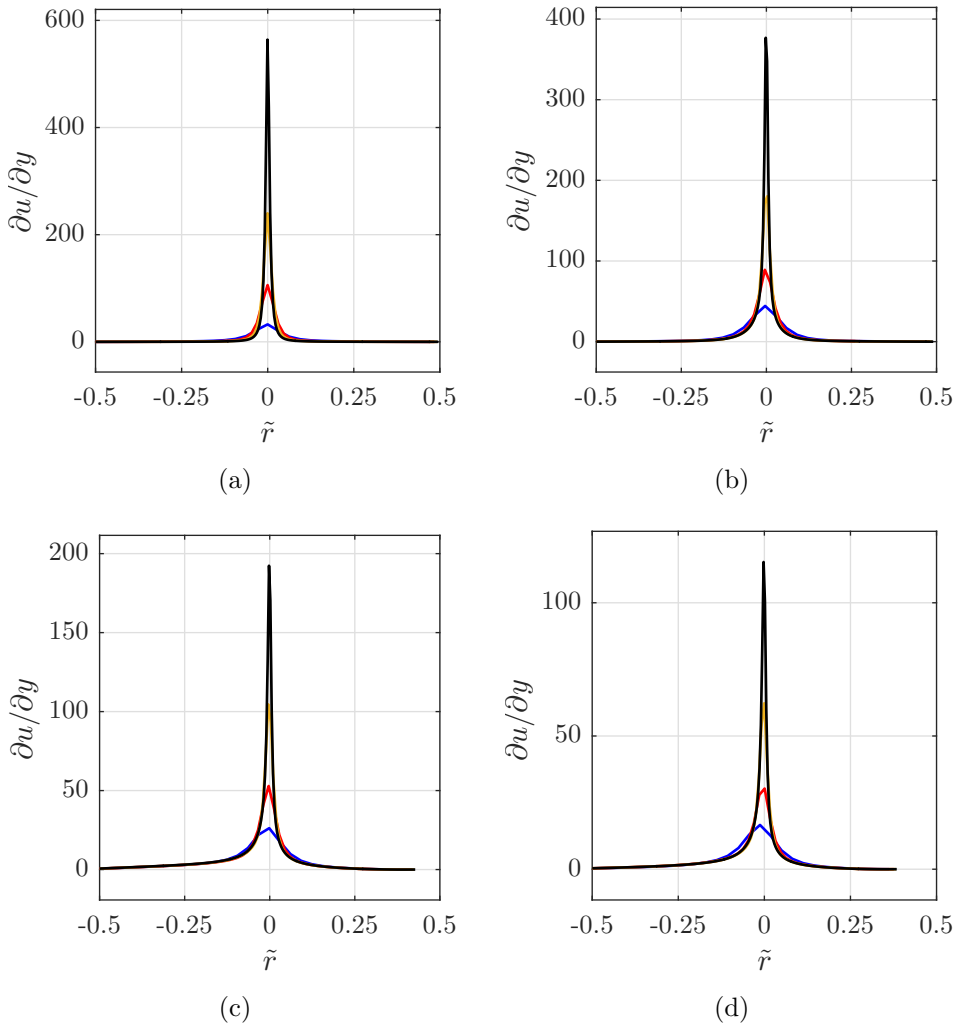

Figure 8.4: Normal velocity gradient at the wall for the case shown in figure 8.3: (a) $\tau = 0.001$; (b) $\tau = 0.05$; (c) $\tau = 0.5$. $\tilde{r}$ is the distance to the contact line. Colored line represent the grid resolution: — 32×32; — 64×64; — 128×128; — 256×256.

cannot change with the reconstruction), besides, no neighbor element is to be found to calculate a tangent at that marker. What is done currently is to assume that the tangent at the marker on the wall is equal to that of the element it belongs to. In this way the marker at the wall is preserved. This provides a circle representing a good curvature, but the new element created at the wall does not in general have the same size and direction as before, so when applying equation 3.19, a new balance of forces is created, hence the oscillations in velocity. Proposing a reconstruction process that address this particular problem is a subject of future investigation. The effect of this issue will be solved partially by the subgrid model proposed here.
The second aspect is the lack of convergence with grid refinement for shear at the wall. Figures 8.4a, 8.4b, 8.4c and 8.4d show the normal velocity gradient at the wall for $\tau = 0.001$, $\tau = 0.01$, $\tau = 0.2$ and $\tau = 0.4$ respectively. In all cases, no grid convergence was achieved. In Legendre and Maglio (2015), shear at the wall shows some convergence at $r = 0.6$, but in the late phase of spreading.
Both aspects seem to point out to a single problem: an inherent defect of the numerical method (i.e. the discretization of the CSF model close to the wall), although it is not clear how much the use of a no slip boundary condition influences the lack of convergence.
Obviously, the second aspect could be solved by direct numerical simulation, modeling the microscopic scales inclusive (down to $\sim \lambda$) with and adequate slip model. Since this kind of simulations seems still out of reach (see a rough calculation of resources necessaries for spreading of a millimeter-size droplet in Maglio and Legendre, 2014), a robust macroscopic model is still needed.

8.2 Towards a new subgrid model

In this work, we propose a subgrid model for macroscopic simulation of the contact line in the context of the front-tracking method with two clear objectives: first, eliminate the initial acceleration in simulations and second, obtained grid convergence for viscous shear.
Since the numerical discretization of the contact angle brings an initial acceleration of the type seen in equation 8.11, we stop including the contact angle inside the calculation of the capillary contribution. Instead, we fit a circle through a number of selected markers at the contact line and find the tangent at the wall (i.e. first derivative of the circle function), similar to what is done in Yamamoto et al. (2013). This is depicted in figure 8.5. The force contributing the contact angle will be embedded in the viscous

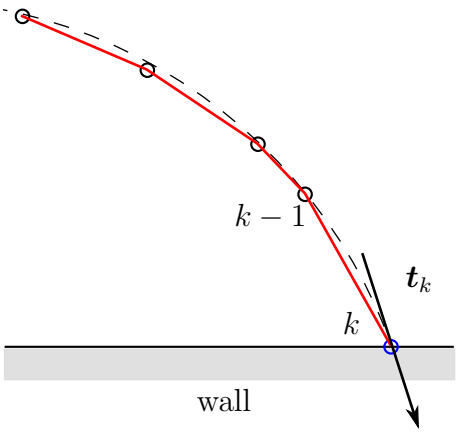

Figure 8.5: Calculation of tangent $\boldsymbol{t}_k$ of marker at the wall. - - - Fitting circle; — Front; o marker k at the wall.

shear. This is done under the next hypothesis: if the right viscous shear is obtained or modeled at the contact line, then the shape of the interface (at the macroscopic scale) characterized by α_{app} should be the physically sound (i.e. it should follow roughly 8.6). If the hypothesis is right, then θ_{app} should not be a boundary condition, but instead an output variable resulting from forces balances, a feature that this subgrid model will share with the interface formation model Shikhmurzaev (1993a, 1996, 1997a,b). The big question is: what is the right viscous shear?
The answer is not simple, but any hydrodynamic model must fulfill the next two conditions:

- shear in the immediate vicinity of the contact line, must be given by some slip law. Molecular dynamics and any models based on it suggest that the right model is the navier-slip (see Qian et al., 2003b; Gerbeau and Lelievre, 2008).
- away from the contact line, at a distance r^*, the no-slip boundary condition must be recovered.

Friction force per length unit (in 2D) f_μ results from the integration of shear along the wall. Following a two-fluid corner Stokes flow in polar coordinates:

$$f_\mu = \int_0^{r_1^*} \tau_{1,in} dr + \int_0^{r_2^*} \tau_{2,in} dr + \int_{r_1^*}^{r_m} \tau_{1,out} dr + \int_{r_2^*}^{r_m} \tau_{2,out} dr \qquad (8.12)$$

where $\tau_{k,in}$ stand for viscous shear in the inner region (where the Navier slip boundary condition applies at the wall), $\tau_{k,out}$ stands for viscous shear in

the outer region (where the no slip boundary condition applies), r_k^* stands for the distance from the contact line up to where the navier slip boundary condition is valid and r_m is some distance from the contact line up to where the current subgrid model will be applied (some proportion of the grid size Δx). We will call this parameter "subgrid zone".
According to de Gennes (1985), the logarithmic cut off region r_k^* should be of the form $r^* \cong \lambda/\theta_{app}$, here instead we find its exact value by equating viscous shear at the wall, for the slip and the no slip regions, given by equations 5.42 and 5.64, which in dimensional form are:

$$\tau_{1,in} = -\frac{\mu_1 U_{cl}}{\lambda} \quad ; \quad \tau_{2,in} = -\frac{\mu_2 U_{cl}}{\lambda} \tag{8.13}$$

$$\tau_{1,out} = \frac{\mu_1 U_{cl}}{r}\left(2D_1 - A_1\right) \quad ; \quad \tau_{2,out} = \frac{\mu_2 U_{cl}}{r}\left(A_2 - 2D_2 + \pi C_2\right) \tag{8.14}$$

parameters A_1, D_1, A_2, C_2 and D_2 are function of α_{app} and Γ and are given by equations 5.32 to 5.39. At $r = r^*$ inner and outer shear must be matched, so:

$$r_1^* = -\lambda\left(2D_1 - A_1\right) \quad ; \quad r_2^* = -\lambda\left(A_2 - 2D_2 + \pi C_2\right) \tag{8.15}$$

Since r_k^* is proportional to λ, its value is expected to be small. Note that although shear in the inner zone is extremely large due to λ (see equation 8.13), the frictional force produced in this small region will be limited by r^*. Equation 8.12 will take into account viscous shear in the small region limited by r_m. Another contribution now is added to take into account the contact angle: the non balanced young force (see equation 6.26). So, the total force f_T to be applied in the momentum equations at the wall will be given by:

$$f_T = f_\mu + f_{Young} \tag{8.16}$$

The idea of this superposition of viscous and non-viscous forces is not new. Molecular dynamics simulations show that tangential stress at the wall can be decomposed into a viscous and a non-viscous component, dominating outside and inside the interfacial region respectively (see Qian et al., 2003a; Qian et al., 2005). This non-viscous component of the shear is the non-balanced or non-compensated young stress.
Numerically, the solver (at the macroscopic scales), will not feel or distinguish both contributions for separate, but the combination of both in a unique force. In fact, to be applied in the momentum balance we will consider that this total contribution f_T comes as a unique average viscous shear. In this way:

$$f_T = \int_{-rm}^{rm} \overline{\mu}\,\overline{\frac{\partial u}{\partial y}}\,dr \tag{8.17}$$

where $\overline{\mu}$ and $\overline{\frac{\partial u}{\partial y}}$ are some consistent averaging of the viscosity and the velocity gradient at the wall, close to the contact line. So, the boundary condition to be applied in the momentum equation is:

$$\overline{\frac{\partial u}{\partial y}} = \frac{f_\mu + f_{Young}}{2 r_m \overline{\mu}} \tag{8.18}$$

8.2.1 Connecting information

To transfer information between the numerical macroscopic simulation and the subgrid region, adequate interpolation schemes must be used. The objective is to use a scheme compatible with the front-tracking method (i.e. a cosinus like interpolation function). So, to transfer viscosity from the macroscopic simulation to the subgrid region, we first calculate the viscosity at each momentum control volume on the wall (see equation 2.4) and then calculate the distance from the centroid of the control volume to the contact line using:

$$\tilde{d} = \frac{|x_{cl} - x_{i,j}|}{r_m} \tag{8.19}$$

using $\tilde{d}$, $\overline{\mu}$ can be constructed in a weighted averaged fashion:

$$\overline{\mu} = \frac{\sum w_{i,j} \mu_{i,j}}{\sum w_{i,j}} \tag{8.20}$$

where $w_{i,j}$ is calculated as:

$$w_{i,j} = \begin{cases} \cos\left(\frac{\tilde{d}\pi}{4}\right) & \text{if } \tilde{d} < 2, \\ 0 & \text{if } \tilde{d} \geq 2 \end{cases} \tag{8.21}$$

Equation 8.21 uses a cosine-like form only to make a smooth weighted average. After $\overline{\frac{\partial u}{\partial y}}$ has been calculated at the subgrid level, it must be transferred to the macroscopic simulation. This is achieved simply by:

$$\left.\frac{\partial u}{\partial y}\right|_{i,j} = w_{i,j} \overline{\frac{\partial u}{\partial y}} \tag{8.22}$$

8.2.2 Viscosity inside the subgrid region

Numerically, the interface between two fluids is not a sharp discontinuity, but a smooth transition occupying at least two control volumes (for VOF-FCT-CSF, Level-Set and the front-tracking method), so, averaging viscosity

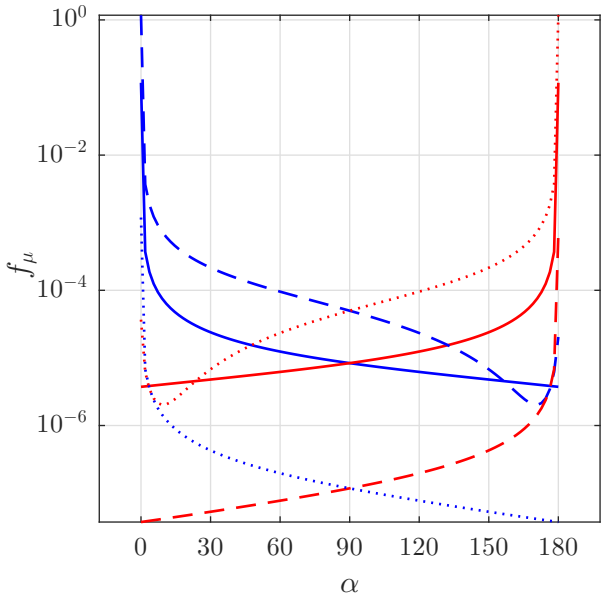

Figure 8.6: Theoretical viscous force per unit length (equation 8.12) close the contact line due to viscous shear for $\Gamma = 1$: — fluid 1, — fluid 2; $\Gamma = 0.001$: - - - fluid 1, - - - fluid 2; and $\Gamma = 1000$: ····· fluid 1, ·····fluid 2.

from the macro region to the subgrid is a natural decision. But information of the interface returning from the subgrid to the macro region will also be felt as an average, i.e. a macroscopic control volume will receive a velocity gradient that contains the imbalance between capillary and viscous forces, without knowing which of the fluids contributed more or less to the latter. The question here is: does it matter which fluid contributes more or less to the total viscous force in the subgrid model? It is a difficult question.
We do a quick analytic experiment to see the individual fluid contribution to the viscous force f_μ in equation 8.12. For this we neglect the force in the inner zone for both fluids since r_1^* and r_2^* are of order $\sim \lambda$. We select roughly $r_1^* = r_2^* \approx 1 \times 10^{-9}$ m, $0° < \alpha < 180°$ and $U_{cl} \approx 1$ mm/s. We test viscosity ratios of $\Gamma = 0.001$, $\Gamma = 1$ and $\Gamma = 1000$. Results are shown in figure 8.6, where we report $|f_\mu|$ to use a logarithmic scale. We can see there that independent of the viscosity ratio Γ, the fluid that is confined contributes in a larger part to the total viscous flow. This is in agreement with Marchand et al. (2012) for gas entrainment. We believe that this effect of the confinement is important, so instead of using individual viscosities for each fluid in equations 8.13 and 8.14, we will reinforce the dominance of the contribution from the fluid that is confined. We use the next angle dependent

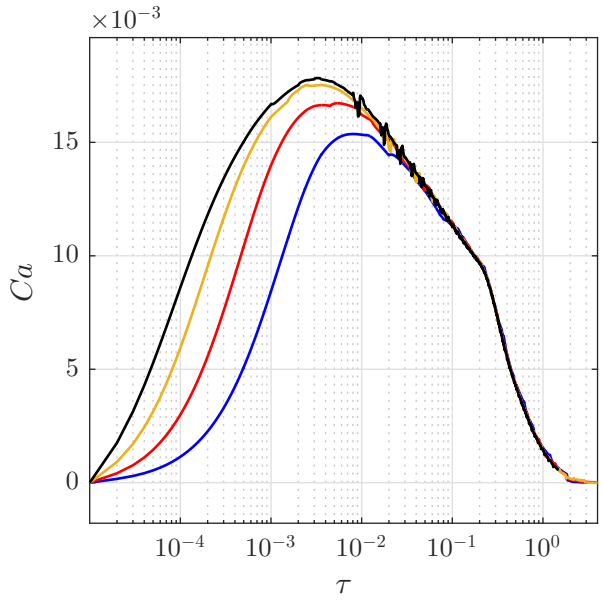

Figure 8.7: Velocity evolution for drop spreading using the subgrid model in the present work. Colored lines represent the grid resolution: — 32×32; — 64×64; — 128×128; — 256×256.

viscosity average:

$$\mu_{mod} = \frac{\alpha_{app}}{\pi}\mu_2 + \left(1 - \frac{\alpha_{app}}{\pi}\right)\mu_1 \tag{8.23}$$

This modelling viscosity μ_{mod} replaces μ_1 and μ_2. Except where the contrary is indicated explicitly as "individual viscosities", μ_{mod} is the option by default used in the subgrid model. Its formulation can in the future be treated in a more elaborated way. We will judge this assumption with results obtained in the section 8.3.

8.3 Validation

We repeat the test reported in section 8.1 with the subgrid model using $\lambda = 0.001$. Since this is a test for grid convergence, r_m is fixed at the largest grid spacing $r_m = \Delta x_{32\times32}$ for all grids and the interface is reconstructed each 50 time steps. Results for the nondimensional velocity evolution in time are shown in figure 8.7. It can be seen that grid convergence at early stage has been improved compared to figure 8.3. Additionally, the perturbations suffered in the velocity for the case using the dynamic contact angle (figure 8.3) have been smoothed, although some perturbations are still present for the grids 128×128 and 256×256. Even with this small perturbations,

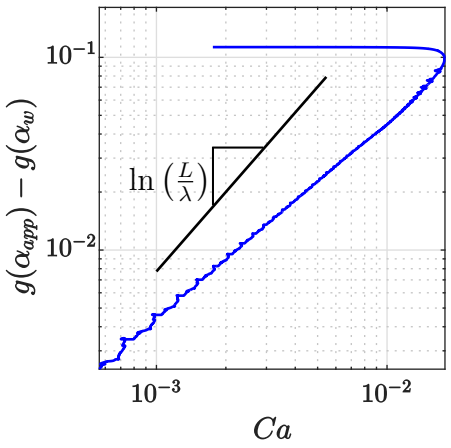

Figure 8.8: Apparent contact angle (measured from the numerical simulation) as a function of nondimensional velocity Ca.

we believe that they do not affect severely the general trend of variables of interest. The evolution of function $g(\alpha_{app}) - g(\alpha_w)$ ($g(\alpha)$ calculated through equation 8.7) with Ca is shown in figure 8.8. The log-log plot helps to see that the trend of α_{app} measured in the numerical simulation is in agreement with Cox's relations Cox (1986), where, as indicated by equation 8.6, we expect an exponent for Ca of $\ln(L/\lambda) \approx 1.37$. In this case, L was taken to be $L = 1/256$, the grid size $\Delta x_{256\times256}$. A fitting procedure revealed a exponent of ≈ 1.01 for Ca dependency of the results. Finally for this test, the normal velocity gradient at the wall is reported in figure 8.9 for selected times $\tau = 0.001$, $\tau = 0.01$, $\tau = 0.2$ and $\tau = 0.4$. As can be seen, at the initial spreading ($\tau = 0.001$ and $\tau = 0.01$ in figures 8.9a and 8.9b), shear is larger for finer grids, but with a convergent tendency in both cases. This is consistent with the value of velocity at those times. In figures 8.9c and 8.9d selected times $\tau = 0.2$ and $\tau = 0.4$ show a velocity gradient at the wall almost constant, with a small deviation for grids 128×128 and 256×256, also consistent with contact line velocity evolution in figure 8.7. It is clear that the straight shape at the top of the velocity gradient is due to the r_m selected. With this test, it is demonstrated that a subgrid model can achieve grid convergence for the maximum velocity of spreading and also has improved the initial acceleration. Shear at the wall has converge with the grid refinement and the evolution of the apparent contact angle has been described correctly.

In the viscous regime, Solomenko et al. (2017) compare their model to DNS results from Sui and Spelt (2013b) for an axisymmetric droplet of $R_0 = 0.5$ in a 1×1 domain. Properties are set such that density and viscosity

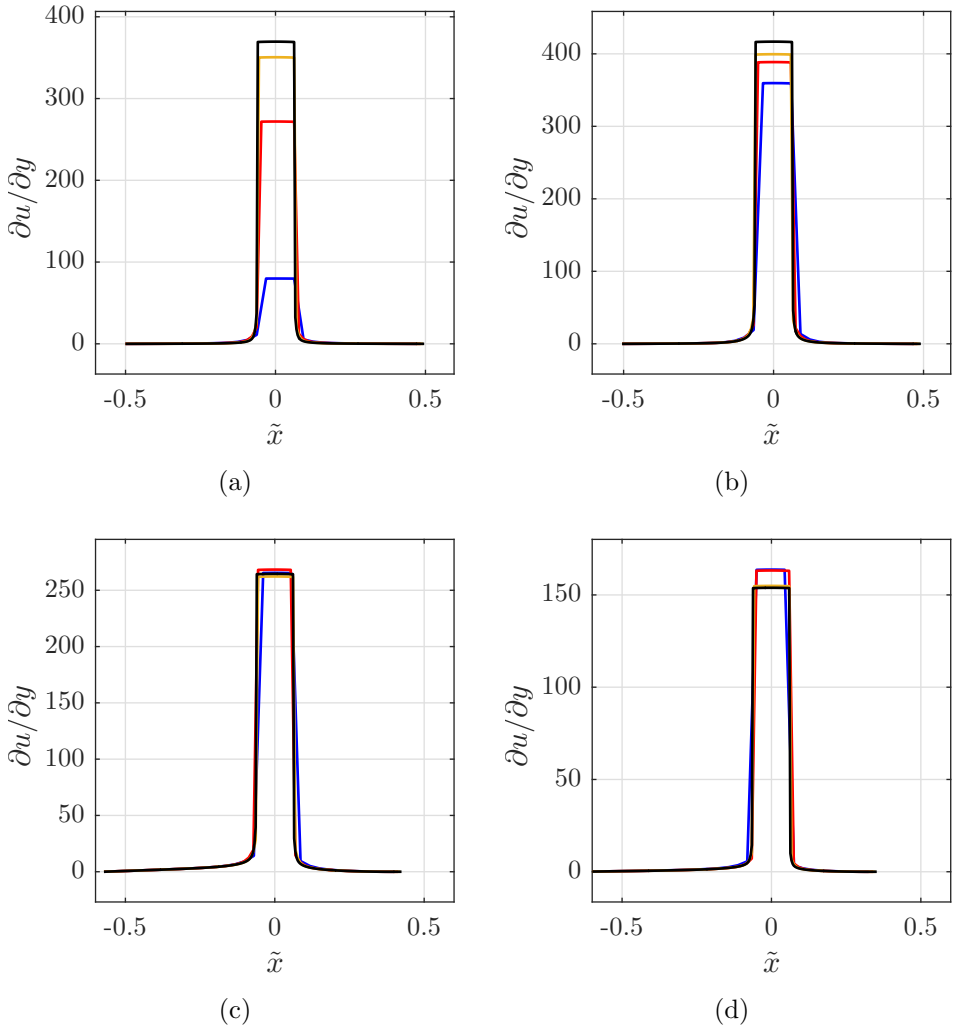

Figure 8.9: Velocity gradient at the wall for drop spreading using the present subgrid model at selected times: a) $\tau = 0.001$; b) $\tau = 0.01$; c) $\tau = 0.2$ and d) $\tau = 0.4$. Colored lines represent the grid resolution: — 32×32; — 64×64; — 128×128; — 256×256.

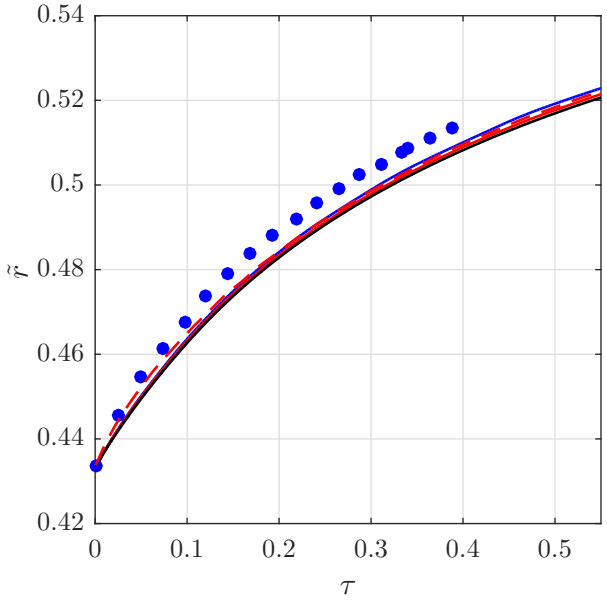

(a)

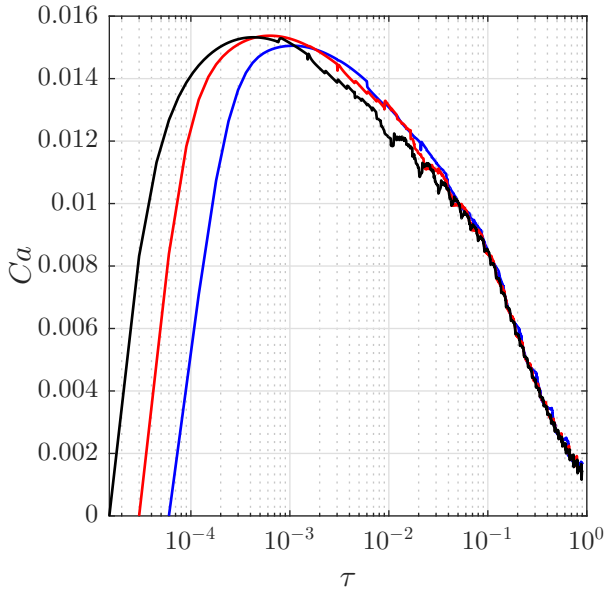

(b)

Figure 8.10: Grid convergence for drop spreading according to Solomenko et al. (2017). a) Non-dimensional contact line position. b) Non-dimensional contact line velocity. — Present study $\Delta x = 1/64$; — Present study $\Delta x = 1/128$; — Present study $\Delta x = 1/256$; •Sui and Spelt (2013b); - - - Solomenko et al. (2017) $\Delta x = 1/256$.

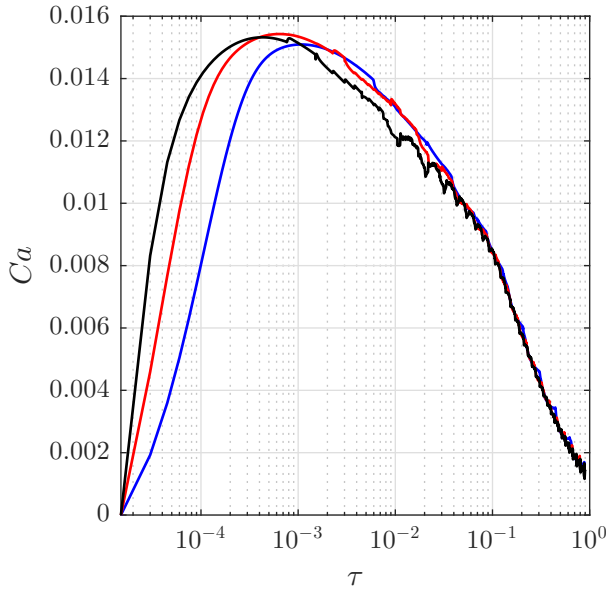

Figure 8.11: Results for the test reported in figure 8.10, using the same Δt (that for $\Delta x = 1/256$) in each grid with the new subgrid model. — $\Delta x = 1/64$; — $\Delta x = 1/128$; — $\Delta x = 1/256$;

ratios are 0.1 and numbers Re and Oh are 5 and 0.1 respectively. The initial configuration of the droplet is set to form an angle of 60° and the static configuration is set at $\alpha_w = 30°$. Three uniform grids are tested such that $\Delta x = 1/64$, $\Delta x = 1/128$ and $\Delta x = 1/256$, using a time step of $\Delta t/\Delta x = 1280 \times 10^{-6}$ and a slip length of $\lambda = 0.0001$. More details can be found in Sui and Spelt (2013b), Solomenko et al. (2017). For the subgrid model, the interface is reconstructed each 50 time steps, a subgrid zone of $r_m = 1/64$ is prescribed for all grids. In figure 8.10a the evolution in time of the contact line position is reported. Solid lines in blue, red and black represent the subgrid model position evolution for grids $\Delta x = 1/64$, $\Delta x = 1/128$ and $\Delta x = 1/256$. Dashed red line and blue dots represent the position evolution (normalized by $2R$ a $\alpha = 60°$) for $\Delta x = 1/256$ for the model used in Solomenko et al. (2017) and the DNS results of Sui and Spelt (2013b) respectively. We can see that the finest grids ($\Delta x = 1/128$ and $\Delta x = 1/256$) converge almost perfectly to the results of Solomenko et al. (2017) but still a bit below of what was obtained in the DNS. Figure 8.10b shows the evolution of the non-dimensional velocity of the contact line. There we can see that the subgrid model has achieved grid convergence of the maximum velocity of spreading.

The convergence of initial acceleration is not clear at this point since

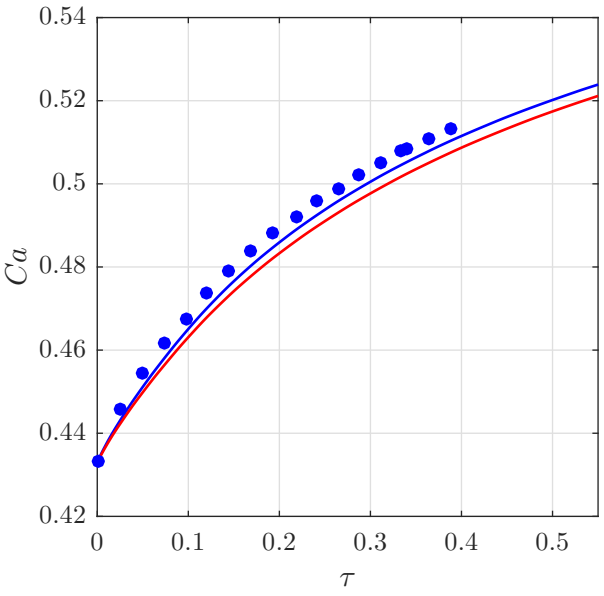

(a)

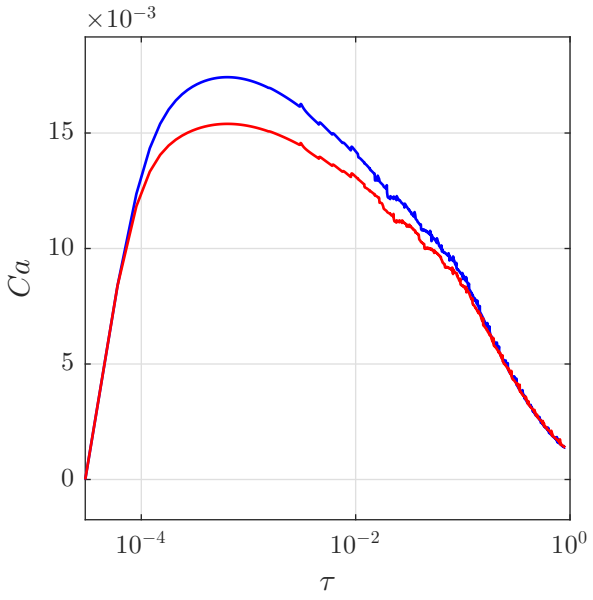

(b)

Figure 8.12: Grid convergence for drop spreading according to Solomenko et al. (2017), using $\Delta x = 1/128$. a) Non-dimensional contact line position. b) Non-dimensional contact line velocity. — Present study with individual viscosities; — Present study with modelling viscosity; •Sui and Spelt (2013b);

in this test, time step Δt is different for each grid. Contact line velocity evolution using the same Δt (that for $\Delta x = 1/256$) in each grid is reported in figure 8.11 confirming that the convergence of initial acceleration with grid refinement has been improved. Solomenko et al. (2017) did not provide the velocity evolution at this axis scale, so a direct comparison for convergence could not be made. The noise in the curves of figures 8.10b are caused by the process of front reconstruction. It can be noticed that the velocity for grid $\Delta x = 1/256$ shows some oscillations of unknown origin between $\tau = 0.01$ and $\tau = 0.1$. Both perturbations however do not affect the global tendency. Since for this test $\Gamma \neq 1$, we test the individual viscosities inside the subgrid zone. Using the grid with $\Delta x = 1/128$ We can see in figure 8.12a that using the individual viscosities in the subgrid model has improved the evolution of the contact line position towards the DNS results of Sui and Spelt (2013b). In figure 8.12b we see that the achievement of the contact line position was at the cost of an increase from ≈ 0.015 to ≈ 0.017 in the maximum spreading velocity. Without a direct comparison with velocities of Solomenko et al. (2017), nothing further can be commented. We will test the viscosity again later in comparison with experiments.

Simulations using the new subgrid model are now compared to experimental data from Lavi and Marmur (2004) for squalane drops. An squalane drop is carefully placed on a wall with no initial velocity. The centroid of the drop from the wall, is located at y_c, a distance slightly smaller than initial radius of the drop R_0. The effect of this initial configuration will be analyzed. The liquid properties of squalane are $\rho = 809$ kg/m^3; $\mu = 0.034$ Pa s, $\sigma = 0.032$ N m^{-1} and $R_0 = 0.001$m. An equilibrium angle was determined to be $\alpha_w = 41.5°$. It is assumed a slip length value of $\lambda = 1 \times 10^{-9}$ m. A square axisymmetric domain of $H = L = 0.003$ m divided uniformly in 32×32 control volumes is used, all tests are reported using the nondimensional time $\tau = t\sigma/\mu V^{1/3}$, where V is the volume of the drop. A preliminary test is conducted to determine convergence with the time step. Time steps of $\Delta t = 2 \times 10^{-5}$, $\Delta t = 1 \times 10^{-5}$, $\Delta t = 5 \times 10^{-6}$ and $\Delta t = 2 \times 10^{-6}$ s are tested and results are shown in figure 8.13. Except for 2×10^{-5} s, the contact line position $\tilde{r} = r/R_0$ converges perfectly with the time step. A second test is conducted to see the effect of r_m. As was discussed previously, this subgrid zone, needs to be a function of Δx and obviously needs to have a minimum value of $r_m = 1\Delta x$. We use the same configuration as the last test increasing the grid quality to 64×64. Subgrid zones of $r_m = 1\Delta x$, $r_m = 2\Delta x$, $r_m = 3\Delta x$, $r_m = 4\Delta x$ and $r_m = 5\Delta x$ are tested. We use a time step of 2×10^{-6} s to achieve $\tau = 100$. Results shown in figure 8.14a indicate that r_m exerts no effect in both the beginning and the end of the spreading, except for $r_m = 1\Delta x$, where an irregularity in $\tilde{r}$ evolution is found at the end

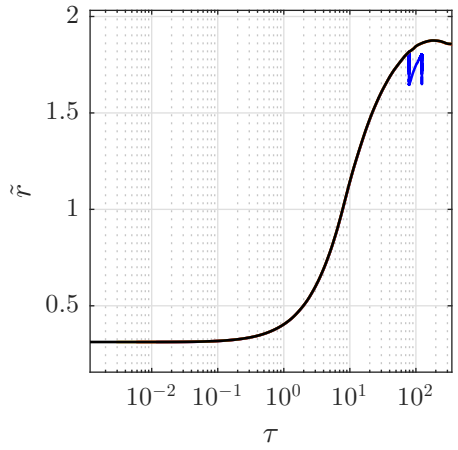

Figure 8.13: Convergence in time test of contact line position for a squalane drop according to experiments in Lavi and Marmur (2004). Time steps tested: — 2×10^{-5}; — 1×10^{-5}; — 5×10^{-6}; — 2×10^{-6}. for $r_m = 2\Delta x$

of spreading. This is expected for two reasons: numerically, if $r_m = 1\Delta x$, an abrupt change in the boundary conditions of the wall around the contact line is produced and the front-tracking method with lagrangian markers (as implemented in this work) requires a surrounding zone of at least 2 grid cells in each direction to be smooth. Figure 8.14b shows a zoom-in into figure 8.14a around $\tau \sim 10$. This is done to see the effect of r_m. According to what is reported in figure 8.14b, it seems that larger values of r_m translates the solution to the right proportionally except at the beginning and at the end of spreading. Large r_m may render the whole subgrid model meaningless (we expect r_m to be small), not to mention that away from the contact line (in the reference frame attached to it), the stokes assumption under which the model is constructed, may fail. In all the tests conducted here compared to experimental data, r_m is taken to be $r_m = 2\Delta x$, which provides stability and coherence with the subgrid model. We test next the effect of initial position of the drop. This can be expressed also in terms of the initial vertical position of the drop centroid y_c. The values tested are $y_c = 0.95R_0$ (which is used by default in other tests), $y_c = 0.98R_0$ and $y_c = 0.99R_0$. Further increase of y_c produced the divergence of the solver, the reason for this remains unclear. A 64×64 grid is used with a time step of 2×10^{-6} s. Results for the contact line position $\tilde{r}$ are shown in figure 8.15a, reporting the same evolution around $\tau \approx 10$.

$$r^* = \frac{r - R_0}{R_f - R_0} \tag{8.24}$$

Normalizing the contact line position using equation 8.24 (where R_f is the

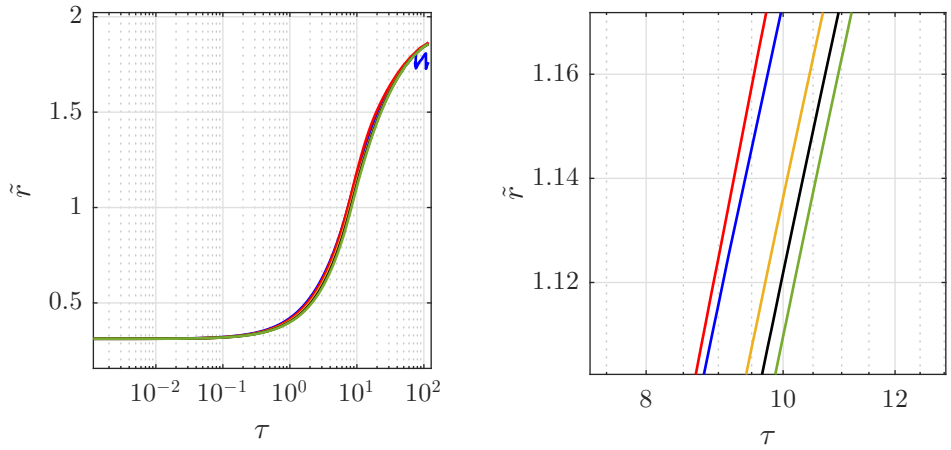

(a) (b)

Figure 8.14: Effect of r_m on the contact line position evolution for a squalane drop. a) $\tilde{r}$ evolution up to $\tau = 100$; b) Zoom-in into figure 8.14a. r_m tested: — $r_m = 1\Delta x$; — $r_m = 2\Delta x$; — $r_m = 3\Delta x$; — $r_m = 4\Delta x$; — $r_m = 5\Delta x$.

final contact line position), shows that the initial wetted area is not important for the evolution of r^* (this was also concluded in Legendre and Maglio (2015)). This is shown in figure 8.15b. In figure 8.16 we compare the evolution of wetted area normalized by the final wetted area A/A_f with the experiment reported in Lavi and Marmur (2004). It can be seen that the agreement is remarkable and it is comparable to the dynamic models used in Legendre and Maglio (2015) with the VOF-FCT-CSF model. The test based on Lavi and Marmur (2004) experiments is also a good test to report the parameters of the subgrid model since it covers a large range of α_{app}. In figure 8.17a the evolution of viscous and non-balanced Young forces per length unit inside the subgrid zone are reported. We can see clearly that the non-balance Young force is always dominant (in the subgrid region), this is consistent with the observations of Qian et al. (2003a) and Qian et al. (2005) for molecular dynamics simulations. In our case we use this dominance in our favor to introduce the capillary effects of the contact angle. Figure 8.17b shows the viscous forces for both fluids inside and outside the slip region. We can see that the viscous force in the receding fluid is always larger than in the advancing one both inside and outside the slip region. Forces outside the slip region are always larger by at least one order of magnitude than the forces inside the slip region, for both fluids. The characteristic slip region r^* in both fluids is reported in figure 8.17c. We see that initially the slip region in fluid 1 is smaller than in fluid 2, this tendency is reverted at

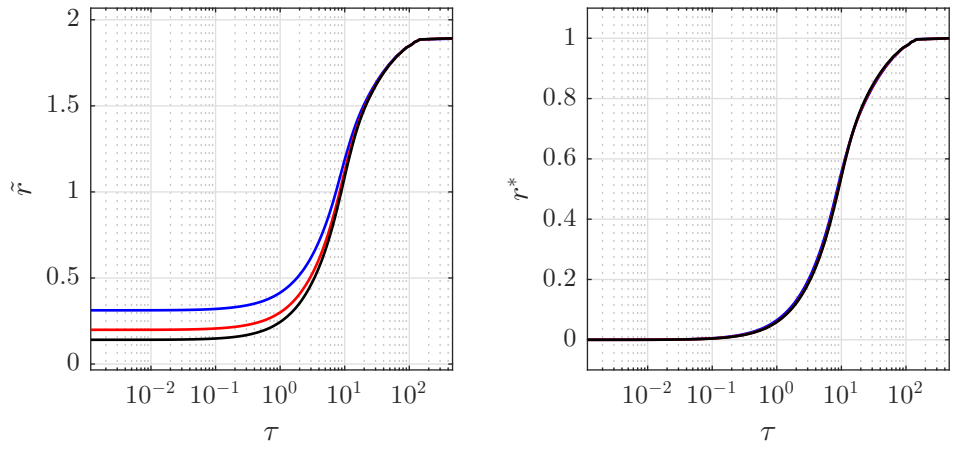

(a) (b)

Figure 8.15: Effect of the initial wetted area on the contact line position for the numerical simulation of a millimetric squalane drop. — $y_c = 0.95R_0$; — $y_c = 0.98R_0$ — $y_c = 0.99R_0$

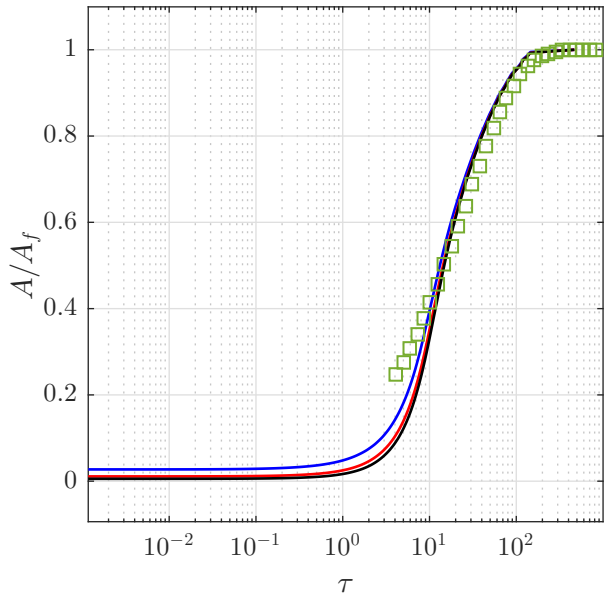

Figure 8.16: Comparison of wetted area of numerical simulation of a millimetric squalane drop against experiment reported in Lavi and Marmur (2004)

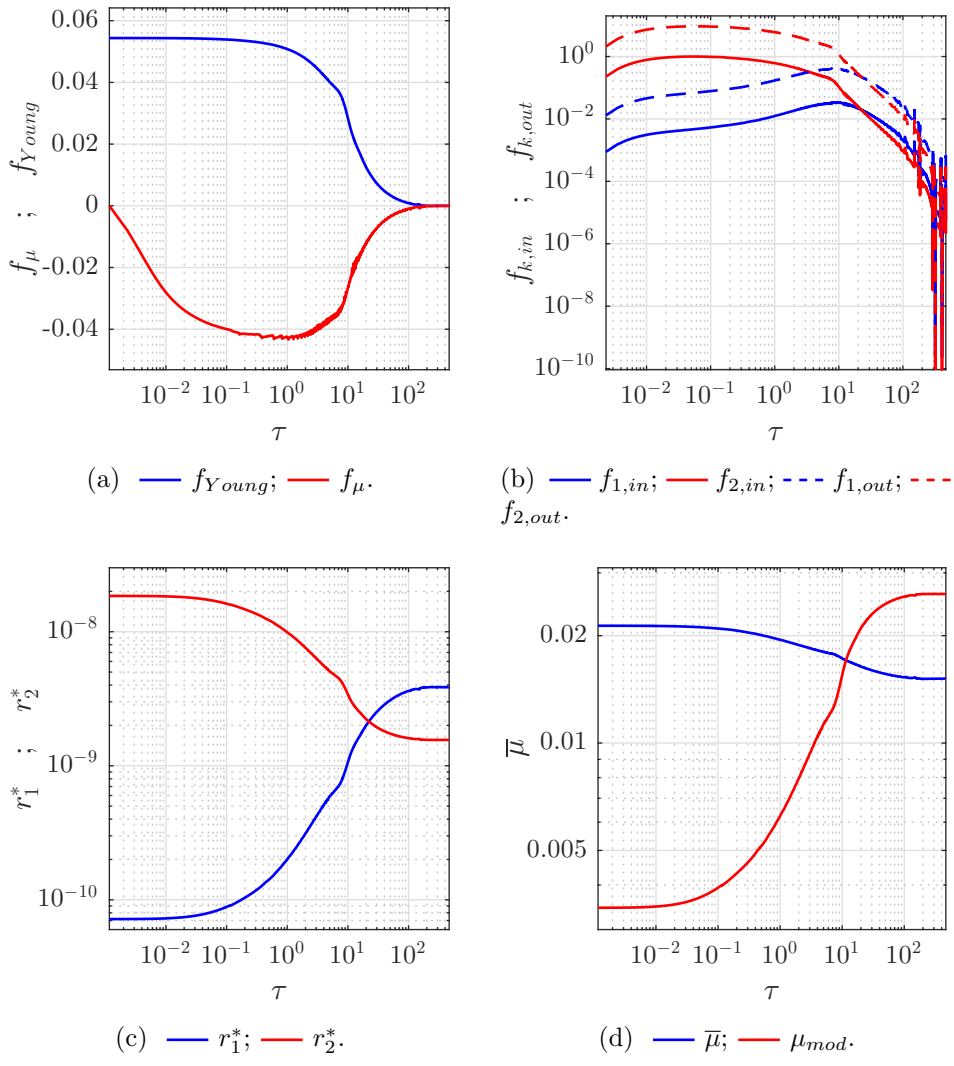

Figure 8.17: Temporal evolution of main parameters of the subgrid model for the case following Lavi and Marmur (2004).

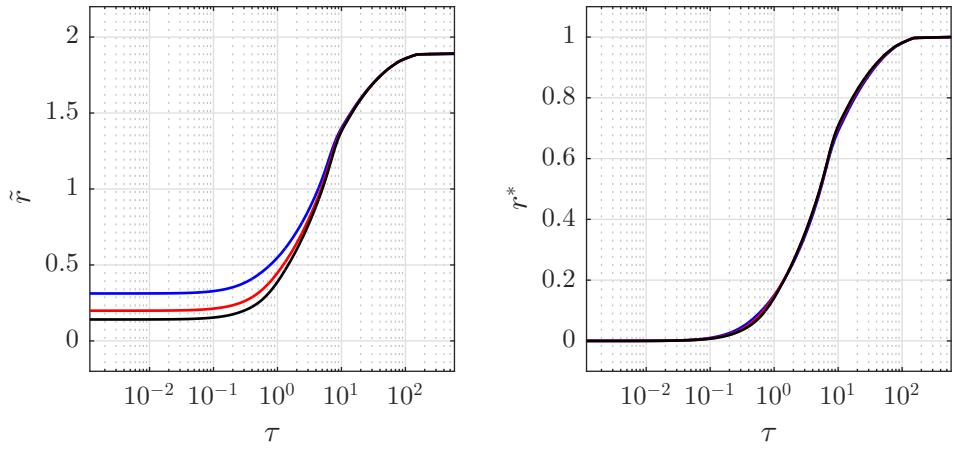

(a) (b)

Figure 8.18: Effect of the initial wetted area on the contact line position for the numerical simulation of a millimetric squalane drop, using individual viscosities. — $y_c = 0.95R_0$; — $y_c = 0.98R_0$ — $y_c = 0.99R_0$

$\tau \sim 10$. Finally, macroscopic average and modelling viscosities $\overline{\mu}$ and μ_{mod} are reported in figure 8.17d. We see that $\overline{\mu}$ is almost constant before $\tau \sim 10$, then it experiences a small fall. This is consistent with a volume fraction averaging process, while the modelling viscosity μ_{mod} increases over time in a fashion similar to the wetted area evolution. The test on initial wetted area is repeated using individual viscosities in the subgrid model. Results for the effect of the initial wetted area and comparison with experimental data are reported in figures 8.18 and 8.19. We can see that the evolution of the contact line is quite similar to that with modelling viscosity see figure 8.18. An important difference is found around $\tau = 10$, the contact line has experienced an acceleration which can be deduced from figure 8.19. This acceleration has caused a slight disagreement with experimental data at $\tau = 10$, but has improved it from $\tau = 5$ to $\tau = 9$. Further investigation regarding this modelling viscosity must still be made.

Another interesting test on partial wetting is reported in Legendre and Maglio (2015), based on the experiments of Winkels et al. (2012) for low viscosity drops. A drop of $R_0 = 0.5$ mm spreads on three different substrates with different equilibrium contact angles α_w: 0°, 65° and 115°. Properties of the liquid are $\rho = 664$ kg/m^3, $\mu = 3.64 \times 10^{-4}$ Pa s and a surface tension of $\sigma = 0.017$ N/m. Numerically, a square domain of $L = H = 3R_0$ is divided into a uniform 64×64 grid and a time step of $t = 1 \times 10^{-6}$ s is set. Again here, since the slip length is not provided by the experiment, it is assumed

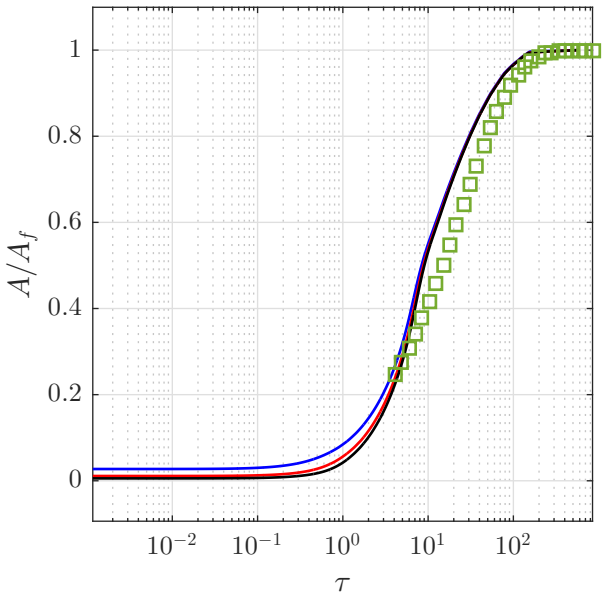

Figure 8.19: Comparison of wetted area of numerical simulation of a millimetric squalane drop against experiment reported in Lavi and Marmur (2004), individual viscosities

$\lambda = 1 \times 10^{-9}$ m. Contact line position evolution is shown in figure 8.20. For equilibrium angles of $\alpha_w = 65°$ and $\alpha_w = 115°$, the agreement with experimental data is excellent. For $\alpha_w = 0°$, the experimental evolution seems to be quicker than that of the subgrid model. This seems to be numerical artifact. In fact, a similar result can be obtained for any angles smaller than $\alpha_w = 10°$ (not shown here). Further research is needed to find the reason of why spreading with small static contact angles evolve in this fashion with the front-tracking method. Figure 8.21 shows again the same evolution, this time for $\tilde{r} = r/R_0$ in a log-log scale in a normalized time $\tau = t/\sqrt{\rho R^3/\sigma}$. The experimental initial evolution of the contact line position grows as $\tilde{r} \sim t^{1/2}$, but later (after $\tau \approx 0.1$), the growth does not follow $\sim t^{1/2}$ which was not observed in molecular dynamics (see the discussion on this aspect in Winkels et al., 2012). The numerical results obtained with the subgrid model follows remarkably the features of the experiment for $\tau > 0.1$. Similar results were obtained in Legendre and Maglio (2015) with the VOF-FCT-CSF method, showing an evolution of $\tau^{1/2}$ for initial spreading.

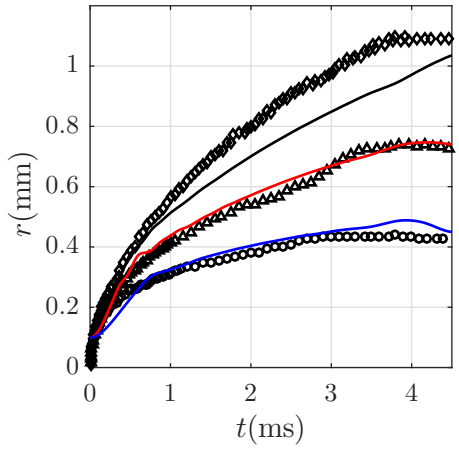

Figure 8.20: Temporal evolution of the contact line position for droplet spreading according to Winkels et al. (2012) as a function of α_w. Experimental data (see Winkels et al., 2012) with open symbols: ◊ $\alpha_w = 0°$; ▵ $\alpha_w = 65°$; ○ $\alpha_w = 115°$; Compared to numerical simulation with subgrid model: — $\alpha_w = 0°$; — $\alpha_w = 65°$; — $\alpha_w = 115°$.

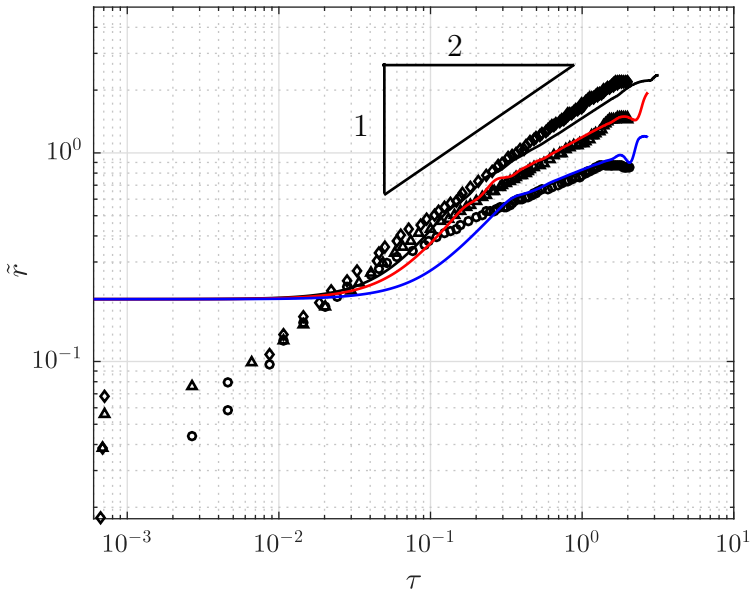

Figure 8.21: Temporal evolution of the contact line position for droplet spreading according to Winkels et al. (2012) as a function of α_w. Experimental data (see Winkels et al., 2012) with open symbols: ◊ $\alpha_w = 0°$; ▵ $\alpha_w = 65°$; ○ $\alpha_w = 115°$; Compared to numerical simulation with subgrid model: — $\alpha_w = 0°$; — $\alpha_w = 65°$; — $\alpha_w = 115°$.

8.4 Summary

We can conclude this chapter with a brief summary of our findings. First, a subgrid model was implemented inside *JADIM* in the context of the front-tracking method. Considering the drop spreading case proposed Afkhami et al. (2009), it was demonstrated that the subgrid model in this work can achieve grid convergence for both initial velocity and shear. Additionally a satisfactory evolution of the apparent contact angle was achieved, which is here an output variable and not a boundary condition, a feature only shared (in the knowledge of the author) with the interface formation model (see Shikhmurzaev, 1993a, 1996, 1997a,b). It was seen also, that the subgrid model predicted satisfactorily the contact line evolution in the viscous regime for the numerical test proposed in Solomenko et al. (2017), showing also convergence with grid refinement in the maximum spreading velocity and an improvement for the initial acceleration. The use of individual viscosities in this case improved the contact line position evolution towards DNS results in Sui and Spelt (2013b) and showed a slightly larger value for maximum spreading velocity with respect to the modelling viscosity subgrid version.
Further tests were conducted and compared to experimental data in drop spreading. Excellent agreement for wetted area evolution was found in comparison to the test on squalane drops from Lavi and Marmur (2004). Time step and initial wetted area independency was found, this is consistent with observations for the same case in Legendre and Maglio (2015). A test for r_m was conducted, no clear evidence of for the best choice of r_m could be found. It is recommended that r_m is kept as small as possible and always $r_m \geq 2\Delta x$. The evolution of parameters of the subgrid model was reported. It was shown that the non-balance Young force is always larger than its viscous counterpart in the subgrid zone. We took advantage of this to stop imposing the contact angle as boundary condition in the CSF environment. The force due to viscous shear in the receding fluid has always a dominant role during drop spreading. Also, viscous force outside the slip region were shown to be stronger than that inside it. The evolution of the modelling viscosity was compared to the average viscosity. They showed to have contrary tendencies. The same tests was conducted using individual viscosities. Similar evolutions of the contact line position were found, but a small acceleration in the contact line evolution at $\tau = 10$ was reported, producing a little disagreement when compared to experimental data. The critical factor for the use of modelling viscosity or individual viscosity seems to be the confinement of the fluids. This comes from the fact that in the test of Solomenko et al. (2017), little confinement was present, so individual viscosities performed better. On the other hand, the squalane drop spreading case (Lavi and Marmur, 2004)

possesses a large confinement of fluid 2 in the intitial spreading, so in this case, the modelling viscosity performed better. Further test are needed to determine the correct viscosity inside the subgrid region, as was commented before. Something is now for sure: the macroscopic simulation is affected by the individual contributions of each fluid to the viscous force. The subgrid model also performed well against the experiments of Winkels et al. (2012). Results were remarkably good for equilibrium contact angles of $\alpha_w = 65°$ and $\alpha_w = 115°$ and acceptable for $\alpha_w = 0°$. This latter result deserves further investigations, since similar trends can be obtained for any angles up to $\alpha_w = 10°$. For now, the subgrid model in the context of lagrangian markers seems to be unable to simulate low equilibrium contact angles. Nevertheless, in the log-log scale, the evolution of the contact line was found to be in excelent agreement with the experimental data, reproducing a changing exponent for t with α_w as discussed also in Winkels et al. (2012).
We conclude that the development of the subgrid model in the context of the front-tracking method provide a very promising approach for the macro-scale simulation of moving contact lines.

Conclusions and Future work

Conclusions

In this work we have focused on a small but challenging subject which is the numerical simulation of two-fluid flows involving the motion of a contact line. We began with a brief description of the numerical solver used in this work: *JADIM* and the methods available inside to capture the interface. We pointed out the need of a method that ensures the elimination of spurious velocities. A very promising answer to this requirement came from the work of Shin et al. (2005) in the framework of the front-tracking method, although its performance to reduce spurious velocities was negatively affected after the reconstruction procedures. A general background statement was presented on the issues related to the use of the front-tracking method i.e. markers clustering, mesh-scale oscillations, algorithmic complexity, etc. The implementation of the front-tracking method inside *JADIM* was then detailed and two important enhancements were introduced: the first is a novel technique to calculate tangents at markers positions using an element length weighted average. This technique allowed the use of a non-uniform distribution of markers at the front, a feature that is normally avoided in the literature of the front-tracking method. The second enhancement was a new front reconstruction procedure, focused on preserving the local curvature of the front by composing circles that were intersected with the eulerian grid. A battery of classical tests were performed to evaluate this new implementation and to show the reduction of spurious velocities close to machine precision. All tests for Laplace number La, Capillary number Ca and grid size $R/\Delta x$ provided low spurious velocities. A minimum element size of $\Delta s > 0.2\Delta x$ was determined to provided stability of the performance. Benchmarking results for rising bubbles were in excellent agreement with available reference data. Wetting cases using the static contact angle provided also excellent agreement to available analytical results (see Dupont and Legendre, 2010) after a correction in the advection of markers close to the wall.
Having developed a powerful tool to simulate numerically two-fluid flows, we

got immersed into the analytical analysis of a moving contact line in the context of corner Stokes flow and analyzed the effect of the different boundary conditions at the wall on the relevant flow field variables: velocity, shear and pressure. A special slip theory in the works of Kirkinis and Davis (2013) and Kirkinis and Davis (2014) was the focus of our attention, because besides relieving the shear divergence at a contact line, it provided evidence of the existence of Moffatt vortices in the vicinity of the contact line. We extended the formulation of Kirkinis and Davis (2014) to handle two fluids and generalize the calculations to non-zero static contact angle. The real results for n revealed flow patterns similar to those found with the no-slip and the navier-slip boundary conditions. Complex results for n revealed the presence of Moffatt vortices but also revealed that such presence is incompatible with a real positive slip. The cut-off imposed by the continuum limit may leave the door open for the existence of only one vortex. Next we verify the existence if such vortices numerically. Tests revealed the existence of vortices in any case were some slip scheme is applied to te wall. This vortices kept their size and showed a decreasing evolution of vorticity. The development of such vortices might be due to the initial impulse induced by the motion of the contact line, an analogy to those found for example in normal flows over plates (see Koumoutsakos and Shiels, 1996). Some perturbations on the interface were found, caused probably by spurious velocities. Further studies are needed on how to improve the front-tracking method for wetting cases.
Finally, in the last chapter, we proposed a subgrid model for the simulation of drop spreading. The motivation for this new model was the fact that in the current literature where the capillary contribution is treated through the CSF formulation (see Brackbill et al., 1992), a grid dependence is observed in contact line velocity and viscous shear at the wall. We addressed both problems proposing an imbalance of viscous and the non-balance Young forces in a microscopic numerical region. Viscous forces were formulated to follow the exact solution of corner Stokes flow from chapter 5 for the inner and outer regions. Product of this imbalance, a velocity gradient became a new boundary condition for velocity and at the same time a new boundary condition for the imposition of a macroscopic or "apparent" contact angle. Tests revealed that this subgrid model provides grid convergence for both maximum contact line velocity and shear at the wall, something not seen in the literature in the context of CSF. Additionally, improvement on the grid convergence for initial acceleration was reported. Comparisons with results from bibliography (see for example Solomenko et al., 2017) revealed similar contact line position evolution. When compared to experimental drop spreading (see Lavi and Marmur, 2004), the subgrid model performed with excellent results. Further tests results were reported to assess the effect of

substrate wettability (Winkels et al., 2012), showing excellent agreement for static contact angles larger than 10°, which seemed to be the limit for this model. Nevertheless, the trends followed by the numerical results were also in excellent agreement with the experiments.
To summarize, in this work, we have contributed in three specific aspects: the first, we have improved the front-tracking method to handle non-uniform distribution of markers, preserving its spurious velocity reduction performance and eliminating many of its subjacent issues. The second aspect, we have shown analytically that under certain conditions, a unique vortex might be found in the vicinity of the contact line. Numerically, it was shown that such vortices are sensible to the slip at the contact line. Their generation might be due to the initial impulse of the contact line motion. And finally, we have provided a new method to simulate drop spreading that achieves grid convergence for maximum velocity and shear at the wall, leaving the acceleration more difficult to converge. This aspect of grid convergence for the acceleration is little commented in the literature. Mainly, this new method, provides the apparent contact angle as an output variable and not anymore as boundary condition to be imposed. However, much is still to be studied and a lot of work is waiting in the future.

Future work

There are immediate studies that need to be conducted regarding the front tracking method. First, it is necessary to improve the reconstruction process to be compatible with problems involving contact lines. We saw some perturbations in the contact line velocity caused by it. A force balance in the vicinity of the contact line may provide a correct curvature at the wall, generating means for a correct reconstruction. Also, generalizing the subgrid model to handle low static contact angles is a point that can make this technique more robust. Further research can be conducted to achieve strict grid convergence for initial acceleration in spreading. Also, the subgrid model can be easily transfered to methods like VOF or Level-Set.
A natural and challenging step to be taken is the implementation of break-up and merging interfaces and of course, the generalization of the front-tracking method to handle 3D problems. For 3D, in preliminary tests we have experienced spurious velocities reductions to $Ca \approx 1 \times 10^{-11}$ for the static bubble test in chapter 4 extended to 3D, but a reconstruction process is still not ready. A similar extension of the subgrid model is also a natural step to be taken. More complex phenomena like hysteresis, surfactant transport and phase change at the contact line must be added to this list.

Bibliography

T. Abadie. *Hydrodynamics of Gas-Liquid Taylor Flow in Microchannels, PhD Thesis*. PhD thesis, Institut National Polytechnique de Toulouse (INP Toulouse), 2013.

T. Abadie, J. Aubin, and D. Legendre. On the combined effects of surface tension force calculation and interface advection on spurious currents within volume of fluid and level set frameworks. *Journal of Computational Physics*, 297:611 – 636, 2015. ISSN 0021-9991. doi: http://dx.doi.org/10.1016/j.jcp.2015.04.054. URL `http://www.sciencedirect.com/science/article/pii/S0021999115003113`.

S. Afkhami, S. Zaleski, and M. Bussmann. A mesh-dependent model for applying dynamic contact angles to vof simulations. *Journal of Computational Physics*, 228(15):5370–5389, 2009. ISSN 0021-9991. doi: http://dx.doi.org/10.1016/j.jcp.2009.04.027. URL `http://www.sciencedirect.com/science/article/pii/S0021999109002083`.

G. Agresar, J.J. Linderman, G. Tryggvason, and K.G. Powell. An adaptive, cartesian, front-tracking method for the motion, deformation and adhesion of circulating cells. *Journal of Computational Physics*, 143(2): 346 – 380, 1998. ISSN 0021-9991. doi: http://dx.doi.org/10.1006/jcph.1998.5967. URL `http://www.sciencedirect.com/science/article/pii/S0021999198959678`.

D. M. Anderson and S. H. Davis. Two-fluid viscous flow in a corner. *Journal of Fluid Mechanics*, 257:1–31, 12 1993. ISSN 1469-7645. doi: 10.1017/S0022112093002976. URL `http://journals.cambridge.org/article_S0022112093002976`.

G. K. Batchelor. *An Introduction to Fluid Dynamics*. Cambridge Mathematical Library. Cambridge University Press, 2000. doi: 10.1017/CBO9780511800955.

J. Billingham. Gravity-driven thin-film flow using a new contact line model. *IMA Journal of Applied Mathematics*, 73(1):4–36, 2008. doi: 10.1093/imamat/hxm042. URL http://imamat.oxfordjournals.org/content/73/1/4.abstract.

Shikhmurzaev-Y. D. Blake, T. D. Dynamic wetting by liquids of different viscosity. *Journal of Colloid And Interface Science*, 253(1):196–202, 2002. doi: 10.1006/jcis.2002.8513.

T. D. Blake, M. Bracke, and Y. D. Shikhmurzaev. Experimental evidence of nonlocal hydrodynamic influence on the dynamic contact angle. *Physics of Fluids*, 11(8):1995–2007, 1999. doi: http://dx.doi.org/10.1063/1.870063. URL http://scitation.aip.org/content/aip/journal/pof2/11/8/10.1063/1.870063.

Terence D. Blake. The physics of moving wetting lines. *Journal of Colloid and Interface Science*, 299(1):1 – 13, 2006. ISSN 0021-9797. doi: http://dx.doi.org/10.1016/j.jcis.2006.03.051. URL http://www.sciencedirect.com/science/article/pii/S0021979706002463.

Daniel Bonn, Jens Eggers, Joseph Indekeu, Jacques Meunier, and Etienne Rolley. Wetting and spreading. *Rev. Mod. Phys.*, 81:739–805, May 2009. doi: 10.1103/RevModPhys.81.739. URL http://link.aps.org/doi/10.1103/RevModPhys.81.739.

Thomas Bonometti and Jacques Magnaudet. An interface-capturing method for incompressible two-phase flows. validation and application to bubble dynamics. *International Journal of Multiphase Flow*, 33(2):109 – 133, 2007. ISSN 0301-9322. doi: https://doi.org/10.1016/j.ijmultiphaseflow.2006.07.003. URL http://www.sciencedirect.com/science/article/pii/S0301932206001315.

J.U Brackbill, D.B Kothe, and C Zemach. A continuum method for modeling surface tension. *Journal of Computational Physics*, 100(2):335 – 354, 1992. ISSN 0021-9991. doi: https://doi.org/10.1016/0021-9991(92)90240-Y. URL http://www.sciencedirect.com/science/article/pii/002199919290240Y.

F. Brochard-Wyart and P.G. de Gennes. Dynamics of partial wetting. *Advances in Colloid and Interface Science*, 39:1 – 11, 1992. ISSN 0001-8686. doi: http://dx.doi.org/10.1016/0001-8686(92)80052-Y. URL http://www.sciencedirect.com/science/article/pii/000186869280052Y.

Isabelle Calmet and Jacques Magnaudet. Large-eddy simulation of high-schmidt number mass transfer in a turbulent channel flow. *Physics of Fluids*, 9(2):438–455, 1997. doi: 10.1063/1.869138. URL http://dx.doi.org/10.1063/1.869138.

H. D. Ceniceros, A. M. Roma, A. Silveira-Neto, and Villar M. M. A robust, fully adaptive hybrid level-set/front-tracking method for two-phase flows with an accurate surface tension computation. *Commun. Comput. Phys*, 8:51–94, July 2010. doi: doi:10.4208/cicp.050509.141009a.

Hector D. Ceniceros and Alexandre M. Roma. A multi-phase flow method with a fast, geometry-based fluid indicator. *Journal of Computational Physics*, 205(2):391 – 400, 2005. ISSN 0021-9991. doi: http://dx.doi.org/10.1016/j.jcp.2004.11.013. URL http://www.sciencedirect.com/science/article/pii/S0021999104004759.

Y.C. Chang, T.Y. Hou, B. Merriman, and S. Osher. A level set formulation of eulerian interface capturing methods for incompressible fluid flows. *Journal of Computational Physics*, 124(2):449 – 464, 1996. ISSN 0021-9991. doi: http://dx.doi.org/10.1006/jcph.1996.0072. URL http://www.sciencedirect.com/science/article/pii/S0021999196900728.

R. G. Cox. The dynamics of the spreading of liquids on a solid surface. part 1. viscous flow. *Journal of Fluid Mechanics*, 168:169–194, 7 1986. ISSN 1469-7645.

R. G. Cox. Inertial and viscous effects on dynamic contact angles. *Journal of Fluid Mechanics*, 357:249–278, 2 1998. ISSN 1469-7645. doi: 10.1017/S0022112097008112. URL http://journals.cambridge.org/article_S0022112097008112.

Julie Cranga. *Simulation numérique directe d'écoulements di- et tri-phasiques engendrés par l'injection de bulles dans un bain de métal liquide*. PhD thesis, Institut National Polytechnique de Toulouse (INP Toulouse), 2002. URL http://www.theses.fr/2002INPT015H. Thèse de doctorat dirigée par Magnaudet, Jacques Mécanique des fluides Toulouse, INPT 2002, 2002INPT015H.

Sharen J. Cummins, Marianne M. Francois, and Douglas B. Kothe. Estimating curvature from volume fractions. *Computers & Structures*, 83 (6):425 – 434, 2005. ISSN 0045-7949. doi: http://dx.doi.org/10.1016/j.compstruc.2004.08.017. URL http://www.sciencedirect.com/science/

article/pii/S0045794904004110. Frontier of Multi-Phase Flow Analysis and Fluid-Structure.

P. G. de Gennes. Wetting: statics and dynamics. *Rev. Mod. Phys.*, 57:827–863, Jul 1985. doi: 10.1103/RevModPhys.57.827. URL http://link.aps.org/doi/10.1103/RevModPhys.57.827.

Jean-Baptiste Dupont. *Étude des écoulements diphasiques dans les mini-canaux d'une pile à combustible*. PhD thesis, Institut National Polytechnique de Toulouse (INP Toulouse), 2007. URL http://www.theses.fr/2007INPT044H. Thèse de doctorat dirigée par Legendre, Dominique et Fabre, Jean Dynamique des fluides Toulouse, INPT 2007,2007INPT044H.

Jean-Baptiste Dupont and Dominique Legendre. Numerical simulation of static and sliding drop with contact angle hysteresis. *Journal of Computational Physics*, 229(7):2453 – 2478, 2010. ISSN 0021-9991. doi: http://dx.doi.org/10.1016/j.jcp.2009.07.034. URL http://www.sciencedirect.com/science/article/pii/S0021999109004203.

Julien Dupré de Baubigny, Michael Benzaquen, Laure Fabié, Mathieu Delmas, Jean-Pierre Aimé, Marc Legros, and Thierry Ondarçuhu. Shape and effective spring constant of liquid interfaces probed at the nanometer scale: Finite size effects. *Langmuir*, 31(36):9790–9798, 2015. doi: 10.1021/acs.langmuir.5b02607. URL http://dx.doi.org/10.1021/acs.langmuir.5b02607. PMID: 26295187.

Julien Dupré de Baubigny, Michael Benzaquen, Caroline Mortagne, Clémence Devailly, Sébastien Kosgodagan Acharige, Justine Laurent, Audrey Steinberger, Jean-Paul Salvetat, Jean-Pierre Aimé, and Thierry Ondarçuhu. Afm study of hydrodynamics in boundary layers around micro- and nanofibers. *Phys. Rev. Fluids*, 1:044104, Aug 2016. doi: 10.1103/PhysRevFluids.1.044104. URL https://link.aps.org/doi/10.1103/PhysRevFluids.1.044104.

E. B. Dussan V. The moving contact line: the slip boundary condition. *Journal of Fluid Mechanics*, 77(4):665–684, 1976. doi: 10.1017/S0022112076002838.

Elizabeth B. Dussan V. and Stephen H. Davis. On the motion of a fluid-fluid interface along a solid surface. *Journal of Fluid Mechanics*, 65:71–95, 8 1974. ISSN 1469-7645. doi: 10.1017/S0022112074001261. URL http://journals.cambridge.org/article_S0022112074001261.

Marianne M. Francois, Sharen J. Cummins, Edward D. Dendy, Douglas B. Kothe, James M. Sicilian, and Matthew W. Williams. A balanced-force algorithm for continuous and sharp interfacial surface tension models within a volume tracking framework. *Journal of Computational Physics*, 213(1): 141 – 173, 2006. ISSN 0021-9991. doi: https://doi.org/10.1016/j.jcp.2005.08.004. URL http://www.sciencedirect.com/science/article/pii/S0021999105003748.

S. H. Garrioch and B. R. Baliga. A plic volume tracking method for the simulation of two-fluid flows. *International Journal for Numerical Methods in Fluids*, 52(10):1093–1134, 2006. ISSN 1097-0363. doi: 10.1002/fld.1217. URL http://dx.doi.org/10.1002/fld.1217.

Jean-Frédéric Gerbeau and Tony Lelievre. Generalized navier boundary condition and geometric conservation law for surface tension. Research report, 2008. URL https://hal.inria.fr/inria-00285206.

H. P. Greenspan. On the motion of a small viscous droplet that wets a surface. *Journal of Fluid Mechanics*, 84:125–143, 1 1978. ISSN 1469-7645. doi: 10.1017/S0022112078000075. URL http://journals.cambridge.org/article_S0022112078000075.

Patrick J. Haley and Michael J. Miksis. The effect of the contact line on droplet spreading. *Journal of Fluid Mechanics*, 223:57–81, 2 1991. ISSN 1469-7645. doi: 10.1017/S0022112091001337. URL http://journals.cambridge.org/article_S0022112091001337.

C.W Hirt and B.D Nichols. Volume of fluid (vof) method for the dynamics of free boundaries. *Journal of Computational Physics*, 39(1):201 – 225, 1981. ISSN 0021-9991. doi: http://dx.doi.org/10.1016/0021-9991(81)90145-5. URL http://www.sciencedirect.com/science/article/pii/0021999181901455.

L. M. Hocking. A moving fluid interface. part 2. the removal of the force singularity by a slip flow. *Journal of Fluid Mechanics*, 79:209–229, 2 1977. ISSN 1469-7645. doi: 10.1017/S0022112077000123. URL http://journals.cambridge.org/article_S0022112077000123.

L. M. Hocking and A. D. Rivers. The spreading of a drop by capillary action. *Journal of Fluid Mechanics*, 121:425–442, 8 1982. ISSN 1469-7645. doi: 10.1017/S0022112082001979. URL http://journals.cambridge.org/article_S0022112082001979.

Thomas Y. Hou, John S. Lowengrub, and Michael J. Shelley. Removing the stiffness from interfacial flows with surface tension. *Journal of Computational Physics*, 114(2):312 – 338, 1994. ISSN 0021-9991. doi: http://dx.doi.org/10.1006/jcph.1994.1170. URL http://www.sciencedirect.com/science/article/pii/S0021999184711703.

Huaxiong Huang, Dong Liang, and Brian Wetton. Computation of a moving drop/bubble on a solid surface using a front-tracking method. *Commun. Math. Sci.*, 2(4):535–552, 12 2004. URL http://projecteuclid.org/euclid.cms/1109885497.

C. Huh and S. G. Mason. The steady movement of a liquid meniscus in a capillary tube. *Journal of Fluid Mechanics*, 81:401–419, 7 1977. ISSN 1469-7645. doi: 10.1017/S0022112077002134. URL http://journals.cambridge.org/article_S0022112077002134.

C. Huh and L. E. Scriven. Hydrodynamic model of steady movement of a solid/liquid/fluid contact line. *Journal of Colloidal and Interface Science*, 35:85–101, 1971. doi: 10.1016/0021-9797(71)90188-3.

S. Hysing, S. Turek, D. Kuzmin, N. Parolini, E. Burman, S. Ganesan, and L. Tobiska. Quantitative benchmark computations of two-dimensional bubble dynamics. *International Journal for Numerical Methods in Fluids*, 60(11):1259–1288, 2009. ISSN 1097-0363. doi: 10.1002/fld.1934. URL http://dx.doi.org/10.1002/fld.1934.

Didier Jamet, David Torres, and J.U. Brackbill. On the theory and computation of surface tension: The elimination of parasitic currents through energy conservation in the second-gradient method. *Journal of Computational Physics*, 182(1):262 – 276, 2002. ISSN 0021-9991. doi: http://dx.doi.org/10.1006/jcph.2002.7165. URL http://www.sciencedirect.com/science/article/pii/S0021999102971652.

Damir Juric and Grétar Tryggvason. Computations of boiling flows. *International Journal of Multiphase Flow*, 24(3):387 – 410, 1998. ISSN 0301-9322. doi: http://dx.doi.org/10.1016/S0301-9322(97)00050-5. URL http://www.sciencedirect.com/science/article/pii/S0301932297000505.

E. Kirkinis and S. H. Davis. Hydrodynamic theory of liquid slippage on a solid substrate near a moving contact line. *Phys. Rev. Lett.*, 110:234503, Jun 2013.

E. Kirkinis and S. H. Davis. Moffatt vortices induced by the motion of a contact line. *Journal of Fluid Mechanics*, 746, 5 2014. ISSN 1469-7645. doi:

10.1017/jfm.2014.162. URL http://journals.cambridge.org/article_S0022112014001621.

Joel Koplik and Jayanth R. Banavar. Molecular dynamics of interface rupture. *Physics of Fluids A*, 5(3):521–536, 1993. doi: http://dx.doi.org/10.1063/1.858879. URL http://scitation.aip.org/content/aip/journal/pofa/5/3/10.1063/1.858879.

P. Koumoutsakos and D. Shiels. Simulations of the viscous flow normal to an impulsively started and uniformly accelerated flat plate. *Journal of Fluid Mechanics*, 328:177–227, 1996. doi: 10.1017/S0022112096008695.

Ming-Chih Lai, Yu-Hau Tsend, and Huaxiong Huang. Numerical simulation of moving contact lines with surfactant by immersed boundary method. *Commun. Comput. Phys*, 8:735–757, 2010. doi: doi:10.4208/cicp.281009.120210a.

H. Lamb. *Hydrodynamics. 6th edition.* C.U.P, 1932. URL https://books.google.fr/books?id=nOHRXwAACAAJ.

Eric Lauga and Howard A. Stone. Effective slip in pressure-driven stokes flow. *Journal of Fluid Mechanics*, 489:55–77, 2003. doi: 10.1017/S0022112003004695.

Becky Lavi and Abraham Marmur. The exponential power law: partial wetting kinetics and dynamic contact angles. *Colloids and Surfaces A: Physicochemical and Engineering Aspects*, 250(1):409 – 414, 2004. ISSN 0927-7757. doi: https://doi.org/10.1016/j.colsurfa.2004.04.079. URL http://www.sciencedirect.com/science/article/pii/S0927775704004777. In honour of the 250th volume of Colloid and Surfaces A and the 25th Anniversary of the International Association of Colloid and Interface Scientists (IACIS).

D. Legendre and M. Maglio. Numerical simulation of spreading drops. *Colloids and Surfaces A: Physicochemical and Engineering Aspects*, 432(0):29 – 37, 2013. ISSN 0927-7757. doi: http://dx.doi.org/10.1016/j.colsurfa.2013.04.046. URL http://www.sciencedirect.com/science/article/pii/S0927775713003415.

D. Legendre and M. Maglio. Comparison between numerical models for the simulation of moving contact lines. *Computers & Fluids*, 113(0):2–13, 2015. ISSN 0045-7930. doi: http://dx.doi.org/10.1016/j.compfluid.2014.09.018. URL http://www.sciencedirect.com/science/article/pii/S0045793014003557. Small scale simulation of multiphase flows.

Yibao Li, Eunok Jung, Wanho Lee, Hyun Geun Lee, and Junseok Kim. Volume preserving immersed boundary methods for two-phase fluid flows. *International Journal for Numerical Methods in Fluids*, 69(4):842–858, 2012. ISSN 1097-0363. doi: 10.1002/fld.2616. URL http://dx.doi.org/10.1002/fld.2616.

Q. X. Lian and Z. Huang. Starting flow and structures of the starting vortex behind bluff bodies with sharp edges. *Experiments in Fluids*, 8(1):95–103, Oct 1989. ISSN 1432-1114. doi: 10.1007/BF00203070. URL https://doi.org/10.1007/BF00203070.

M. S. Longuet-Higgins and E. D. Cokelet. The deformation of steep surface waves on water. i. a numerical method of computation. *Proceedings of the Royal Society of London A: Mathematical, Physical and Engineering Sciences*, 350(1660):1–26, 1976. ISSN 0080-4630. doi: 10.1098/rspa.1976.0092. URL http://rspa.royalsocietypublishing.org/content/350/1660/1.

Marco Maglio and Dominique Legendre. Numerical simulation of sliding drops on an inclined solid surface. pages 47–69, 2014. doi: 10.1007/978-3-319-00191-3_3. URL https://doi.org/10.1007/978-3-319-00191-3_3.

S. Manservisi and R. Scardovelli. A variational approach to the contact angle dynamics of spreading droplets. *Computers & Fluids*, 38(2):406 – 424, 2009. ISSN 0045-7930. doi: http://dx.doi.org/10.1016/j.compfluid.2008.05.001. URL http://www.sciencedirect.com/science/article/pii/S0045793008001102.

Antonin Marchand, Tak Shing Chan, Jacco H. Snoeijer, and Bruno Andreotti. Air entrainment by contact lines of a solid plate plunged into a viscous fluid. *Phys. Rev. Lett.*, 108:204501, May 2012. doi: 10.1103/PhysRevLett.108.204501. URL https://link.aps.org/doi/10.1103/PhysRevLett.108.204501.

Benoît Mathieu. *Études physique, expérimentale et numérique des mécanismes de base intervenant dans les écoulements diphasiques*. PhD thesis, 2003. URL http://www.theses.fr/2003AIX11039. Thèse de doctorat dirigée par Tadrist, Lounès Mécanique. Énergétique Aix-Marseille 1 2003,2003AIX11039.

Matlab. *MATLAB version 8.5.0.197613 (R2015a)*. The Mathworks, Inc., Natick, Massachusetts, 2015.

Chung-Yin Huang Ming-Chih Lai and Yi-Min Huang. Simulating the axisymmetric interfacial flows with insoluble surfactant by immersed boundary method. *International Journal Of Numerical Analysis And Modeling*, 8(1):105 – 117, 2011.

H. K. Moffatt. Viscous and resistive eddies near a sharp corner. *Journal of Fluid Mechanics*, 18:1–18, 1 1964. ISSN 1469-7645.

H. K. Moffatt and B. R. Duffy. Local similarity solutions and their limitations. *Journal of Fluid Mechanics*, 96(2):299–313, 01 1980. doi: 10.1017/S0022112080002133. URL https://www.cambridge.org/core/article/local-similarity-solutions-and-their-limitations/2AA1B11E96464D236770570D3EBFEFC4.

Metin Muradoglu and Savas Tasoglu. A front-tracking method for computational modeling of impact and spreading of viscous droplets on solid walls. *Computers & Fluids*, 39(4):615 – 625, 2010. ISSN 0045-7930. doi: http://dx.doi.org/10.1016/j.compfluid.2009.10.009. URL http://www.sciencedirect.com/science/article/pii/S0045793009001698.

C. L. M. H. Navier. Mémoire sur les lois du mouvement des fluides. *Mem. Acad. R. Sci. Paris*, 6:389–416, 1823.

Charles S Peskin. Numerical analysis of blood flow in the heart. *Journal of Computational Physics*, 25(3):220 – 252, 1977. ISSN 0021-9991. doi: http://dx.doi.org/10.1016/0021-9991(77)90100-0. URL http://www.sciencedirect.com/science/article/pii/0021999177901000.

Charles S. Peskin. The immersed boundary method. *Acta Numerica*, 11:479–517, 2002. doi: 10.1017/S0962492902000077. URL https://www.cambridge.org/core/article/immersed-boundary-method/95ECDAC5D1824285563270D6DD70DA9A.

S. Popinet and S. Zaleski. A front-tracking algorithm for accurate representation of surface tension. *International Journal for Numerical Methods in Fluids*, 30:775–793, July 1999. doi: 10.1002/(SICI)1097-0363(19990730)30:6⟨775::AID-FLD864⟩3.3.CO;2-R.

Stéphane Popinet. An accurate adaptive solver for surface-tension-driven interfacial flows. *J. Comput. Phys.*, 228(16):5838–5866, September 2009. ISSN 0021-9991. doi: 10.1016/j.jcp.2009.04.042. URL http://dx.doi.org/10.1016/j.jcp.2009.04.042.

T. Qian, X.-P. Wang, and P. Sheng. Molecular hydrodynamics of the moving contact line in two-phase immiscible flows. *Commun. Comput. Phys*, October 2005.

Tiezheng Qian, Xiao-Ping Wang, and Ping Sheng. Molecular scale contact line hydrodynamics of immiscible flows. *Phys. Rev. E*, 68:016306, Jul 2003a. doi: 10.1103/PhysRevE.68.016306. URL https://link.aps.org/doi/10.1103/PhysRevE.68.016306.

Tiezheng Qian, Xiao-Ping Wang, and Ping Sheng. Generalized navier boundary condition for the moving contact line. *Commun. Math. Sci.*, 1(2):333–341, 06 2003b. URL http://projecteuclid.org/euclid.cms/1118152074.

E. Ramé, S. Garoff, and K. R. Willson. Characterizing the microscopic physics near moving contact lines using dynamic contact angle data. *Phys. Rev. E*, 70:031608, Sep 2004. doi: 10.1103/PhysRevE.70.031608. URL https://link.aps.org/doi/10.1103/PhysRevE.70.031608.

Yuriko Renardy and Michael Renardy. Prost: A parabolic reconstruction of surface tension for the volume-of-fluid method. *J. Comput. Phys.*, 183(2): 400–421, December 2002. ISSN 0021-9991. doi: 10.1006/jcph.2002.7190. URL http://dx.doi.org/10.1006/jcph.2002.7190.

Murray Rudman. Volume-tracking methods for interfacial flow calculations. *International Journal for Numerical Methods in Fluids*, 24(7):671–691, 1997. ISSN 1097-0363. doi: 10.1002/(SICI)1097-0363(19970415)24:7⟨671::AID-FLD508⟩3.0.CO;2-9. URL http://dx.doi.org/10.1002/(SICI)1097-0363(19970415)24:7<671::AID-FLD508>3.0.CO;2-9.

Abraham. Savitzky and M. J. E. Golay. Smoothing and differentiation of data by simplified least squares procedures. *Analytical Chemistry*, 36(8): 1627–1639, 1964. doi: 10.1021/ac60214a047. URL http://dx.doi.org/10.1021/ac60214a047.

R. Scardovelli and S. Zaleski. Direct numerical simulation of free-surface and interfacial flow. *Annu. Rev. Fluid Mech.*, 31:567 – 603, 1999. doi: https://doi.org/10.1146/annurev.fluid.31.1.567.

Ping Sheng and Minyao Zhou. Immiscible-fluid displacement: Contact-line dynamics and the velocity-dependent capillary pressure. *Phys. Rev. A*, 45:5694–5708, Apr 1992. doi: 10.1103/PhysRevA.45.5694. URL https://link.aps.org/doi/10.1103/PhysRevA.45.5694.

Y. D. Shikhmurzaev. Mathematical modeling of wetting hydrodynamics. *Fluid Dynamics Research*, 13(1):45, 1994. URL http://stacks.iop.org/1873-7005/13/i=1/a=A03.

Y. D. Shikhmurzaev. Dynamic contact angles and flow in vicinity of moving contact line. *AIChE Journal*, 42(3):601–612, 1996. ISSN 1547-5905. doi: 10.1002/aic.690420302. URL http://dx.doi.org/10.1002/aic.690420302.

Y. D. Shikhmurzaev. Moving contact lines in liquid/liquid/solid systems. *Journal of Fluid Mechanics*, 334:211–249, 3 1997a. ISSN 1469-7645. doi: 10.1017/S0022112096004569. URL http://journals.cambridge.org/article_S0022112096004569.

Y. D. Shikhmurzaev. Spreading of drops on solid surfaces in a quasi-static regime. *Physics of Fluids*, 9(2):266–275, 1997b. doi: http://dx.doi.org/10.1063/1.869147. URL http://scitation.aip.org/content/aip/journal/pof2/9/2/10.1063/1.869147.

Y. D. Shikhmurzaev. Capillary breakup of liquid threads: a singularity-free solution. *IMA Journal of Applied Mathematics*, 70(6):880–907, 2005. doi: 10.1093/imamat/hxh075. URL http://imamat.oxfordjournals.org/content/70/6/880.abstract.

Y.D. Shikhmurzaev. The moving contact line on a smooth solid surface. *International Journal of Multiphase Flow*, 19(4):589 – 610, 1993a. ISSN 0301-9322. doi: http://dx.doi.org/10.1016/0301-9322(93)90090-H. URL http://www.sciencedirect.com/science/article/pii/030193229390090H.

Y.D. Shikhmurzaev. A two-layer model of an interface between immiscible fluids. *Physica A: Statistical Mechanics and its Applications*, 192 (1-2):47–62, 1993b. ISSN 0378-4371. doi: http://dx.doi.org/10.1016/0378-4371(93)90143-R. URL http://www.sciencedirect.com/science/article/pii/037843719390143R.

Y.D. Shikhmurzaev. Some dry facts about dynamic wetting. *The European Physical Journal Special Topics*, 197(1):47–60, 2011. ISSN 1951-6355. doi: 10.1140/epjst/e2011-01435-x. URL http://dx.doi.org/10.1140/epjst/e2011-01435-x.

Yulii D. Shikhmurzaev. Singularities at the moving contact line. mathematical, physical and computational aspects. *Physica D: Nonlinear Phenomena*, 217(2):121 – 133, 2006. ISSN 0167-2789. doi: http://dx.

doi.org/10.1016/j.physd.2006.03.003. URL http://www.sciencedirect.com/science/article/pii/S0167278906000844.

Seungwon Shin and Damir Juric. Modeling three-dimensional multiphase flow using a level contour reconstruction method for front tracking without connectivity. *Journal of Computational Physics*, 180(2):427 – 470, 2002. ISSN 0021-9991. doi: http://dx.doi.org/10.1006/jcph.2002.7086. URL http://www.sciencedirect.com/science/article/pii/S0021999102970865.

Seungwon Shin, S.I. Abdel-Khalik, Virginie Daru, and Damir Juric. Accurate representation of surface tension using the level contour reconstruction method. *Journal of Computational Physics*, 203(2):493 – 516, 2005. ISSN 0021-9991. doi: http://dx.doi.org/10.1016/j.jcp.2004.09.003. URL http://www.sciencedirect.com/science/article/pii/S0021999104003894.

Vladimir Shtern. Moffatt eddies at an interface. *Theoretical and Computational Fluid Dynamics*, 28(6):651–656, 2014. ISSN 1432-2250. doi: 10.1007/s00162-014-0332-7. URL http://dx.doi.org/10.1007/s00162-014-0332-7.

David N. Sibley, Nikos Savva, and Serafim Kalliadasis. Slip or not slip? a methodical examination of the interface formation model using two-dimensional droplet spreading on a horizontal planar substrate as a prototype system. *Physics of Fluids*, 24(8):082105, 2012. doi: 10.1063/1.4742895. URL http://dx.doi.org/10.1063/1.4742895.

David N. Sibley, Andreas Nold, Nikos Savva, and Serafim Kalliadasis. A comparison of slip, disjoining pressure, and interface formation models for contact line motion through asymptotic analysis of thin two-dimensional droplet spreading. *Journal of Engineering Mathematics*, 94(1):19–41, 2015. ISSN 1573-2703. doi: 10.1007/s10665-014-9702-9. URL http://dx.doi.org/10.1007/s10665-014-9702-9.

Zlatko Solomenko, Peter D.M. Spelt, and Pascal Alix. A level-set method for large-scale simulations of three-dimensional flows with moving contact lines. *Journal of Computational Physics*, 348:151 – 170, 2017. ISSN 0021-9991. doi: http://dx.doi.org/10.1016/j.jcp.2017.07.011. URL http://www.sciencedirect.com/science/article/pii/S0021999117305132.

J.E. Sprittles and Y.D. Shikhmurzaev. Finite element simulation of dynamic wetting flows as an interface formation process. *Journal of Computational*

Physics, 233(0):34 – 65, 2013. ISSN 0021-9991. doi: http://dx.doi.org/10.1016/j.jcp.2012.07.018. URL http://www.sciencedirect.com/science/article/pii/S0021999112003919.

Y. Sui and Peter D.M. Spelt. An efficient computational model for macroscale simulations of moving contact lines. *Journal of Computational Physics*, 242:37 – 52, 2013a. ISSN 0021-9991. doi: http://dx.doi.org/10.1016/j.jcp.2013.02.005. URL http://www.sciencedirect.com/science/article/pii/S0021999113001150.

Yi Sui and Peter D. M. Spelt. Validation and modification of asymptotic analysis of slow and rapid droplet spreading by numerical simulation. *Journal of Fluid Mechanics*, 715:283–313, 1 2013b. ISSN 1469-7645. doi: 10.1017/jfm.2012.518. URL http://journals.cambridge.org/article_S0022112012005186.

Mark Sussman, Peter Smereka, and Stanley Osher. A level set approach for computing solutions to incompressible two-phase flow. *Journal of Computational Physics*, 114(1):146 – 159, 1994. ISSN 0021-9991. doi: http://dx.doi.org/10.1006/jcph.1994.1155. URL http://www.sciencedirect.com/science/article/pii/S0021999184711557.

Peter A. Thompson and Mark O. Robbins. Simulations of contact-line motion: Slip and the dynamic contact angle. *Phys. Rev. Lett.*, 63:766–769, Aug 1989. doi: 10.1103/PhysRevLett.63.766. URL http://link.aps.org/doi/10.1103/PhysRevLett.63.766.

D.J. Torres and J.U. Brackbill. The point-set method: Front-tracking without connectivity. *Journal of Computational Physics*, 165(2):620 – 644, 2000. ISSN 0021-9991. doi: http://dx.doi.org/10.1006/jcph.2000.6635. URL http://www.sciencedirect.com/science/article/pii/S002199910096635X.

G. Tryggvason, B. Bunner, A. Esmaeeli, D. Juric, N. Al-Rawahi, W. Tauber, J. Han, S. Nas, and Y.-J. Jan. A Front-Tracking Method for the Computations of Multiphase Flow. *Journal of Computational Physics*, 169:708–759, May 2001. doi: 10.1006/jcph.2001.6726.

Gretar Tryggvason, Asghar Esmaeeli, Jiacai Lu, and Souvik Biswas. Direct numerical simulations of gas/liquid multiphase flows. *Fluid Dynamics Research*, 38(9):660, 2006. URL http://stacks.iop.org/1873-7005/38/i=9/a=A05.

S. O. Unverdi and G. Tryggvason. A front-tracking method for viscous, incompressible, multi-fluid flows. *Journal of Computational Physics*, 100: 25–37, May 1992. doi: 10.1016/0021-9991(92)90307-K.

E. Uzgoren, J. Sim, and W. Shyy. Marker-based, 3-d adaptive cartesian grid method for multiphase flow around irregular geometries. *Communications in Computational Physics*, 5:1–41, 2009.

S. P. van der Pijl, A. Segal, C. Vuik, and P. Wesseling. A mass-conserving level-set method for modelling of multi-phase flows. *International Journal for Numerical Methods in Fluids*, 47(4):339–361, 2005. ISSN 1097-0363. doi: 10.1002/fld.817. URL `http://dx.doi.org/10.1002/fld.817`.

O.V. Voinov. Hydrodynamics of wetting. *Fluid Dynamics*, 11(5):714–721, 1976. ISSN 0015-4628. doi: 10.1007/BF01012963. URL `http://dx.doi.org/10.1007/BF01012963`.

Mark C. T. Wilson, Jonathan L. Summers, Yulii D. Shikhmurzaev, Andrew Clarke, and Terence D. Blake. Nonlocal hydrodynamic influence on the dynamic contact angle: Slip models versus experiment. *Phys. Rev. E*, 73:041606, Apr 2006. doi: 10.1103/PhysRevE.73.041606. URL `http://link.aps.org/doi/10.1103/PhysRevE.73.041606`.

Koen G. Winkels, Joost H. Weijs, Antonin Eddi, and Jacco H. Snoeijer. Initial spreading of low-viscosity drops on partially wetting surfaces. *Phys. Rev. E*, 85:055301, May 2012. doi: 10.1103/PhysRevE.85.055301. URL `http://link.aps.org/doi/10.1103/PhysRevE.85.055301`.

Yasufumi Yamamoto and Tomomasa Uemura. Numerical experiment of drop spreading by front-tracking method. *Journal of the Japanese Society for Experimental Mechanics*, 8(Special Issue):s43–s48, 2008. doi: 10.11395/jjsem.8.s43.

Yasufumi Yamamoto, Takahiro Ito, Tatsuro Wakimoto, and Kenji Katoh. Numerical simulations of spontaneous capillary rises with very low capillary numbers using a front-tracking method combined with generalized navier boundary condition. *International Journal of Multiphase Flow*, 51:22–32, 2013. ISSN 0301-9322. doi: http://dx.doi.org/10.1016/j.ijmultiphaseflow.2012.12.002. URL `http://www.sciencedirect.com/science/article/pii/S0301932212001759`.

Yasufumi Yamamoto, Katsunori Tokieda, Tatsuro Wakimoto, Takahiro Ito, and Kenji Katoh. Modeling of the dynamic wetting behavior in a cap-

illary tube considering the macroscopic-microscopic contact angle relation and generalized navier boundary condition. *International Journal of Multiphase Flow*, 59:106–112, 2014. ISSN 0301-9322. doi: http://dx.doi.org/10.1016/j.ijmultiphaseflow.2013.10.018. URL `http://www.sciencedirect.com/science/article/pii/S0301932213001699`.

S. T. Zalesak. Fully multidimensional flux-corrected transport algorithms for fluids. *Journal of Computational Physics*, 31:335–362, June 1979. doi: 10.1016/0021-9991(79)90051-2.

Jun Zhang, Matthew K. Borg, and Jason M. Reese. Multiscale simulation of dynamic wetting. *International Journal of Heat and Mass Transfer*, 115:886 – 896, 2017. ISSN 0017-9310. doi: http://dx.doi.org/10.1016/j.ijheatmasstransfer.2017.07.034. URL `http://www.sciencedirect.com/science/article/pii/S0017931017315521`.